

Theoretical design of new materials for solar energy harvesting

Bužančić Milosavljević, Margarita

Doctoral thesis / Doktorski rad

2024

Degree Grantor / Ustanova koja je dodijelila akademski / stručni stupanj: **University of Split, Faculty of Science / Sveučilište u Splitu, Prirodoslovno-matematički fakultet**

Permanent link / Trajna poveznica: <https://um.nsk.hr/um:nbn:hr:166:891170>

Rights / Prava: [In copyright](#)/[Zaštićeno autorskim pravom.](#)

Download date / Datum preuzimanja: **2025-01-22**

Repository / Repozitorij:

[Repository of Faculty of Science](#)



University of Split
Faculty of Science
Doctoral Study of Biophysics



Doctoral thesis

**THEORETICAL DESIGN OF NEW
MATERIALS FOR SOLAR ENERGY
HARVESTING**

Margarita Bužančić Milosavljević

Split, 2024

Sveučilište u Splitu
Prirodoslovno-matematički fakultet
Doktorski studij Biofizika



Doktorski rad

**TEORIJSKI DIZAJN NOVIH
MATERIJALA ZA ISKORIŠTAVANJE
SUNČEVE ENERGIJE**

Margarita Bužančić Milosavljević

Split, 2024

Sveučilište u Splitu, Prirodoslovno-matematički fakultet
Odjel za fiziku, Doktorski studij Biofizika

TEORIJSKI DIZAJN NOVIH MATERIJALA ZA ISKORIŠTAVANJE SUNČEVE
ENERGIJE

Doktorski rad autorice Margarite Bužančić Milosavljević kao dio obaveza potrebnih da se dobije doktorat znanosti, izrađen je pod vodstvom mentorice prof. dr. dr. h. c. Vlaste Bonačić-Koutecký i komentora prof. dr. sc. Mile Dželalije.

Dobiveni akademski naziv i stupanj: doktorica prirodnih znanosti iz polja kemije.

Povjerenstvo za ocjenu i obranu doktorskog rada u sastavu:

1. izv. prof. dr. sc. Perica Bošković _____
(Prirodoslovno-matematički fakultet u Splitu, prirodne znanosti, polje kemija - predsjednik)

2. dr. sc. Emmanuelle Bignon _____
(Centre national de la recherche scientifique, LPCT UMR7019, prirodne znanosti, polje kemija - članica)

3. doc. dr. sc. Ivana Anđelić _____
(Prirodoslovno-matematički fakultet u Splitu, prirodne znanosti, polje kemija - članica)

4. izv. prof. dr. sc. Viljemka Bučević Popović _____
(Prirodoslovno-matematički fakultet u Splitu, prirodne znanosti, polje kemija - zamjenski član)

potvrđuje da je disertacija obranjena dana _____

Voditelj doktorskog studija: izv. prof. dr. sc. Damir Kovačić

Dekan: prof. dr. sc. Mile Dželalija

THEORETICAL DESIGN OF NEW MATERIALS FOR SOLAR ENERGY HARVESTING

Margarita Bužančić Milosavljević

Thesis performed at:

Center of Excellence for Science and Technology-Integration of
Mediterranean region (STIM), Faculty of Science, University of Split

Abstract:

The subject of the thesis is development of novel nanoscale materials for solar energy harvesting. The aim is to theoretically design two types of new luminescent dyes with enhanced efficiency: the first for application in dye-sensitized solar cells (DSSCs) and the second for use in transparent luminescent solar concentrators (TLSCs). More precisely, the objective is to predict photovoltaic and photochemical properties, including energy conversion efficiency and fluorescence quantum yield (QY). The first research direction focuses on novel bio-nano hybrid sensitizers for use in dye-sensitized solar cells, specifically on cyanidin-silver nanocluster hybrids. Furthermore, the influence of odd and even numbers of electrons and the impact of gold or copper doping on the efficiency and stability of these hybrids are investigated. The second research direction emphasises developing the rules for reliable theoretical prediction of fluorescence quantum yield within harmonic approximation. Additionally, it involves the theoretical design of squaraine-based J-aggregates as transparent TLSC luminophores with high QY. The calculations of structural and optical properties are based on density functional theory (DFT) and its time-dependent variant (TDDFT). Overall, the theoretical modeling of photovoltaic and photochemical properties serves to confirm and to stimulate experimental research in the field of new solar technologies.

(117 pages, 39 figures, 2 schemes, 12 tables, 181 references, 2 appendices, original in English)

Thesis deposited in:

National and University Library in Zagreb

University Library in Split

Library of the Faculty of Science, University of Split

Keywords: fluorescent dyes, bio-nano hybrids, DSSC, fluorescence QY, J-aggregates, TLSC, DFT, TDDFT

Supervisor: Prof. Vlasta Bonačić-Koutecký, dr. dr. h. c.

Co-supervisor: Prof. Mile Dželalija, Ph.D.

Reviewers:

1. Assoc. Prof. Perica Bošković, Ph.D.
2. Emmanuelle Bignon, Ph.D.
3. Asst. Prof. Ivana Anđelić, Ph.D.

Thesis accepted:

TEORIJSKI DIZAJN NOVIH MATERIJALA ZA ISKORIŠTAVANJE SUNČEVE ENERGIJE

Margarita Bužančić Milosavljević

Rad je izrađen na:

Centru izvrsnosti za znanost i tehnologiju-Integracija Mediteranske regije (STIM),
Prirodoslovno-matematički fakultet, Sveučilište u Splitu

Sažetak:

Teza istražuje razvoj novih nanomaterijala za prikupljanje solarne energije. Cilj je teoretski dizajnirati dvije vrste novih luminescentnih boja s poboljšanom učinkovitošću: jedne za primjenu u bojom senzibiliziranim solarnim ćelijama (DSSC), a druge za primjenu u transparentnim luminiscentnim solarnim koncentradorima (TLSC). Glavni cilj je predviđanje fotovoltaičnih i fotokemijskih svojstava, kao što su efikasnost fotoelektrične pretvorbe i efikasnost svjetlosne emisije (QY). Teza se sastoji od dva smjera istraživanja. Prvi smjer istraživanja stavlja u fokus nove hibridne bio-nano senzibilizatore za primjenu u DSSC sustavima, posebice hibridne cijanidin-srebrne nanoklastere. Nadalje, prikazan je utjecaj na učinkovitost i stabilnost bio-nano hibrida kroz istraživanje parnog i neparnog broja elektrona te dopiranja zlatom ili bakrom. Drugi smjer istraživanja bavi se razvojem pravila za pouzdano teoretsko predviđanje efikasnosti svjetlosne emisije (fluorescentni QY) unutar harmonijske aproksimacije. Dodatno, uključuje teoretski dizajn J-agregata na bazi skvaraina kao prozirnih TLSC luminofora s visokim fluorescentnim QY. Izračuni strukturnih i optičkih svojstava temelje se na teoriji funkcionala gustoće (DFT) i njenoj vremenski ovisnoj varijanti (TDDFT). Teorijsko modeliranje fotovoltaičnih i fotokemijskih svojstava služi za potvrdu i stimulaciju eksperimentalnih istraživanja u području novih solarnih tehnologija.

(117 stranica, 39 slika, 2 sheme, 12 tablica, 181 referenci, 2 priloga, jezik izvornika: engleski)

Rad je pohranjen u:

Nacionalnoj sveučilišnoj knjižnici u Zagrebu

Sveučilišnoj knjižnici u Splitu

Knjižnici Prirodoslovno-matematičkog fakulteta Sveučilišta u Splitu

Ključne riječi: fluorescentne boje, bio-nano hibridi, DSSC, fluorescentni QY, TLSC, J-agregati, DFT, TDDFT

Mentorica: prof. dr. dr. h. c. Vlasta Bonačić-Koutecký

Komentor: prof. dr. sc. Mile Dželalija

Ocjenjivači:

1. izv. prof. dr. sc. Perica Bošković
2. dr. sc. Emmanuelle Bignon
3. doc. dr. sc. Ivana Anđelić

Rad prihvaćen:

ACKNOWLEDGMENTS

I would like to express my gratitude to my mentor, prof. dr. dr. h. c. Vlasta Bonačić-Koutecký for her guidance and support. Especially, for expertise and commitment that have been vital to the completion of this work.

I thank my co-mentor, prof. dr. Mile Dželalija, as well as the review committee for their valuable recommendations.

Furthermore, I want to thank all of my international collaborators for their time, hard work, educational contributions, and insightful comments.

I am truly grateful to my colleagues and collaborators, dr. Antonija Mravak, dr. Martina Perić Bakulić and dr. Željka Sanader Maršić, whose cooperation and knowledge have enriched my professional life beyond measure. I appreciate their teamwork and the stimulating discussions that have pushed the boundaries of our work. Thank you all for your extraordinary contributions and for being crucial part of this achievement.

I extend my thanks to colleagues from STIM-REI project and MedILS Institute.

To my family, my husband, and my daughter, I am deeply grateful for all the love they have shared with me on this journey. I also want to thank my brother and sister, mother and father, as well as grandmothers for their patience and support.

I dedicate this thesis to my grandfather, the late dr. Berislav Glunčić, whose work and contribution to science have served as my greatest source of inspiration.

PUBLICATIONS

The following list of publications constitutes the main part of the thesis:

1. Alexander Humeniuk, Margarita Bužančić, Joscha Hoche, Javier Cerezo, Roland Mitrić, Fabrizio Santoro and Vlasta Bonačić-Koutecký. Predicting fluorescence quantum yields for molecules in solution: A critical assessment of the harmonic approximation and the choice of the lineshape function. *The Journal of Chemical Physics*, 152 (5), 054107, 2020. doi:10.1063/1.5143212
2. Margarita Bužančić Milosavljević, Antonija Mravak, Martina Perić Bakulić and Vlasta Bonačić-Koutecký. Model systems for dye-sensitized solar cells: cyanidin-silver nanocluster hybrids at TiO₂ support. *RSC Advances*, 13 (9), 6010-6016, 2023. doi:10.1039/D3RA00165B
3. Margarita Bužančić Milosavljević and Vlasta Bonačić-Koutecký. Design of J-aggregates-like oligomers built from squaraine dyes exhibiting transparency in the visible regime and high fluorescence quantum yield in the NIR region. *Phys. Chem. Chem. Phys.*, 26, 1314-1321, 2024. doi:10.1039/D3CP05291E
4. Margarita Bužančić Milosavljević, Martina Perić Bakulić, Željka Sanader Maršić, Antonija Mravak and Vlasta Bonačić-Koutecký. Enhancing efficiency of dye sensitized solar cells by coinage metal doping of cyanidin-silver trimer hybrids at TiO₂ support based on theoretical study. *Nanomaterials*, 14, 1034, 2024. doi:10.3390/nano14121034

Contents

| | | |
|----------|--|------------|
| 1 | Introduction | 1 |
| 1.1 | General concept | 1 |
| 1.2 | Solar energy harvesting: A sustainable solution | 3 |
| 1.2.1 | Development and efficiency of solar cells | 3 |
| 1.2.2 | Transparent luminescent solar concentrators | 6 |
| 1.3 | Methodology | 10 |
| 1.3.1 | Density functional theory (DFT) | 11 |
| 1.3.2 | Time-dependent density functional theory (TDDFT) | 12 |
| 1.3.3 | Environment description | 12 |
| 1.3.4 | Limitations of computational approach | 14 |
| 1.4 | Research objectives | 16 |
| 1.4.1 | Modeling cyanidin-silver nanocluster hybrids at TiO ₂ support | 17 |
| 1.4.2 | Doping of cyanidin-silver trimer hybrids at TiO ₂ support | 18 |
| 1.4.3 | Theoretical prediction of fluorescence quantum yields | 19 |
| 1.4.4 | Design of J-aggregates squaraine dyes as TLSC materials | 20 |
| 2 | Design of sensitizers for dye-sensitized solar cells at TiO₂ support | 22 |
| 2.1 | Cyanidin-silver nanocluster hybrids | 22 |
| 2.2 | Coinage metal doping of cyanidin-silver trimer hybrids | 30 |
| 3 | Design of luminophores for transparent luminescent solar concentrators | 43 |
| 3.1 | Theoretical prediction of fluorescence quantum yields | 43 |
| 3.2 | Squaraine-based J-aggregates | 56 |
| 4 | Conclusion and outlook | 65 |
| | References | 67 |
| A | Appendix to Chapter 2 | 85 |
| B | Appendix to Chapter 3 | 103 |

Contents

| | |
|-------------------------|------------|
| Curriculum Vitae | 115 |
| Publications | 117 |

Introduction

1.1 General concept

The increasing energy consumption along with growing temperature and climate change, represent one of the greatest challenges in modern civilization. In this context, harvesting the energy of the Sun presents a sustainable solution. The Sun is a clean, inexhaustible, renewable energy source that can be continuously harnessed [1–3]. If we compare global energy consumption in a year, which is ~ 410 quintillion joules, with the energy provided by the Sun in an hour, ~ 430 quintillion joules, it becomes clear that the Sun hourly delivers more energy than mankind consumes in a year [4, 5]. Moreover, the amount of solar energy absorbed by Earth in three days corresponds to the overall energy supply originating from fossil fuels [6]. By replacing traditional fossil fuels, solar energy has the potential to reduce greenhouse gas emissions and the overall carbon footprint, with the ultimate goal of creating a cleaner environment [3, 7].

There is a great emphasis in the European Union on achieving the strategic goal of transforming Europe into a climate-neutral continent by 2050. This objective is a central issue of the European Green Deal, which sets a comprehensive plan for reducing greenhouse gas emissions to net-zero values [8]. In this context, implementing the green transition involves developing photovoltaic (PV) systems that can be integrated into buildings and architecture while maintaining high aesthetics and efficiency [3]. This has served as motivation for the present study, with the aim to theoretically design novel nanoscale materials for application in solar harvesting technologies.

Solar energy can be harvested directly by solar cells, or indirectly by solar concentrators [2]. The solar cell converts solar radiation into electric energy via the photovoltaic effect, while the solar concentrator uses internal reflection on its surface to redirect captured energy to the edges where solar cells are located [3]. There are different technologies of solar cells, among which dye-sensitized solar cells (DSSC) represent a sustainable option based on the natural photosynthesis effect [9]. On the other hand, the concept of transparent luminescent solar concentrators (TLSCs) was developed to maintain the original functionality and aesthetics of the building environment [10]. The present study is carried out within the framework of DSSC sensitizers and TLSC luminophores. In both cases, fluorescent dye is an active component

whose structural and optical properties can be modeled, in that way influencing the overall efficiency of the system. Altogether, the general concept of the thesis represents the theoretical design of fluorescent dyes as new materials for application in DSSC and TLSC technologies.

An efficient DSSC design involves a sensitizer that interacts with semiconductor film, promoting electron injection into the TiO_2 conducting band [11]. In this context, natural dyes, as representatives of green technology, are non-toxic [12], easily available [13], and have been extensively investigated for DSSC applications [14, 15]. However, they exhibit limitations in stability and efficiency [14]. For small nanoclusters (NCs) of noble metals, with discrete quantum states, the structural and optical properties depend on the number of metal atoms involved [16, 17]. Natural dyes in combination with small silver nanoclusters produce bio-nano hybrid systems with donor-acceptor character. This property is important for capturing, transferring, and injecting photons into the conduction band of a semiconductor, thus increasing the energy conversion efficiency [18]. Furthermore, coinage metal doping of silver NC within bio-nano hybrids enhances their stability at TiO_2 surface. Theoretical modeling of bio-nano hybrids offers a solution for improving the efficiency of natural-based DSSC sensitizers, which has to be further experimentally confirmed.

In the case of TLSC, efficient design requires bringing together two opposed properties; transparency through near-infrared (NIR) absorption and high fluorescence quantum yield (QY) [19–22]. This is challenging to achieve because a bathochromic shift often results in an enhancement of non-radiative transition rates, causing a decrease in QY values. Secondly, the QY prediction from first principles relies on the calculation of transition rates based on harmonic approximation [23, 24]. However, the description of the internal conversion (IC) rate depends on highly excited vibrational states which usually deviate from the harmonic oscillator model. The J-aggregates as oligomers of organic dyes, due to their excitonic properties [25] can act as selective collectors of electromagnetic radiation while maintaining a high fluorescence QY. The aim of this study is to determine the reliability of theoretical prediction for fluorescence QY by confirming available experimental results, as well as to design J-aggregate oligomers based on squaraine dyes as new luminophore materials for TLSC application.

The theoretical design of DSSC sensitizer as well as of TLSC luminophore, represents a scientific contribution to the field of novel materials for solar harvesting. In order to calculate the structural and optical properties of modeled systems, density functional theory (DFT) and its time-dependent variant (TDDFT) are used. The focus is on investigating photovoltaic and photochemical properties, including energy conversion efficiency and fluorescence QY.

The introduction is structured as follows: first, a summary of the most recent advancements in solar harvesting technologies is discussed, followed by the theoretical framework and methodology overview. Afterwards, a brief description of research objectives within the thesis is presented. The main body of the thesis consists of a collection of articles organized into two

sections. The first section (cf. Chapter 2) addresses the theoretical design of DSSC sensitizers anchored to TiO₂ support, specifically cyanidin-silver nanocluster hybrids. The second section focuses on the design of luminophores for TLSC, including the theoretical prediction of fluorescence quantum yields and the design of squaraine-based J-aggregates (cf. Chapter 3). The corresponding supporting materials for each article are included in Appendices A and B.

1.2 Solar energy harvesting: A sustainable solution

Harnessing the energy of the Sun originates from ancient civilisations. In old Greece and China, it was utilized for passive house heating, while the Romans used it for the thermal heating of public baths and greenhouses [26]. However, it wasn't until the 19th century that the photovoltaic effect was discovered [27–29], and not until the mid-20th century that the first solar cells were applied as an electrical power source [30]. Since then, technological development has led to two distinct types of solar energy harvesting [2]; direct harvesting by immediate conversion of solar energy to electric power and indirect harvesting by collecting solar radiation from a large surface and concentrating it into a small area. The former corresponds to the solar cell, while the latter to the solar concentrator [3]. Today, solar energy harvesting represents the fastest-growing technology for energy production in Europe [31]. More specifically, in 2023, solar energy accounted for 1.34% of total EU energy production, with an increase of 47.5% compared to 2020 [32]. From 2020 to 2023, the total installed PV capacity has an annual growth rate of $\geq 40\%$ [33], indicating substantial potential for the future development of solar harvesters.

1.2.1 Development and efficiency of solar cells

There are three generations of solar cells. The first-generation corresponds to crystalline silicon solar cells [34]. The manufacturing of silicon dioxide into crystalline silicon with high purity requires substantial energy [35, 36]. This makes these types of cells less cost-effective than conventional energy sources [37, 38] and limits their future advancement [36]. Nevertheless, due to their efficiency that can reach up to 25% in high performance, they remain the most commercially abundant [36]. In search of more cost-effective technology, the second-generation of solar cells, also known as thin-film solar cells, has been developed. They consist of amorphous silicon instead of crystalline silicon deposited in single or multiple layers, making them thin and flexible [9, 37]. In the meantime, they have expanded to include other thin-film semiconductor materials, such as cadmium telluride and copper indium gallium sulfide/selenide/diselenide [9]. Third-generation solar cells consist of several different PV technologies that have a shared goal of achieving high efficiency while maintaining low production costs. Some of the most common third-generation cells are perovskite [39], organic [40, 41], dye-sensitized solar cells [9],

quantum dots [42, 43], nanocrystal [44, 45], and tandem cells based on multi-junction design [46]. Among them, DSSCs stand out as cost-effective cells, easy to fabricate with potential for further improvements in efficiency and stability. To illustrate interest among research groups for their development; DSSCs have been the subject of extensive research over the last two decades, with more than 1,500 articles published annually according to the Web of Science [9].

Design of dye-sensitized solar cell

DSSC was first proposed by O'Regan i Grätzel [47–49] as a photochemical solar cell based on natural light absorption [50]. The working mechanism relies on the interaction between the dye sensitizer and the semiconductor film. When the dye absorbs sunlight, an electron is excited from the ground state to an excited state, allowing electron injection into the semiconductor's conduction band. Afterwards, the dye is regenerated through the electrolyte [11]. A dye sensitizer is a key component of DSSC that consists of charge-transfer molecules attached to the semiconductor surface. The charge-transfer character of dye sensitizer promotes its efficiency in absorbing and injecting electrons into the semiconductor conducting band [11]. Among different semiconductors, titanium dioxide (TiO_2) is the most frequently used one due to its suitable bandgap energies [51], stability, non-toxicity, and low-cost [52]. There are several natural crystalline structures of TiO_2 , including anatase, rutile, and brookite. However, since the anatase has the largest band gap and highest energy of conduction band edge, it is the most commonly utilized TiO_2 form [53, 54].

In order to obtain efficient performance of DSSC sensitizer, several design requirements have to be satisfied [11]:

- *Effective photo-induced electron transfer* from the dye to the semiconductor conduction band that depends on the alignment between energy levels of sensitizer, semiconductor, and electrolyte.

To ensure efficient electron injection into the semiconductor conduction band, the energy of the lowest unoccupied molecular orbital (LUMO) of the dye sensitizer must be higher than the energy of the conduction band edge of TiO_2 . ΔG^{inject} refers to the driving force behind the electron injection rate. Furthermore, the oxidation potential of the dye, which is related to the energy of the dye's highest occupied molecular orbital (-HOMO), needs to be above the energy of I^-/I_3^- redox potential to enable dye regeneration.

- *Efficient charge-transfer complex* which promotes fast electron injection. A charge-transfer complex is formed through intramolecular interaction, where the electron-rich part acts as the electron donor and the electron-poor part acts as the electron acceptor. The absorption of light triggers the photoinduced charge-transfer process in a dye sensitizer,

causing a charge-separated state. This process can be analyzed through calculations of the relevant molecular orbitals (MOs), where the HOMO corresponds to the donor and the LUMO corresponds to the acceptor.

- *Enhancement of absorption intensity* that directly increases the effectiveness of light absorption, such as the light-harvesting efficiency (LHE). Furthermore, with better light absorption, more excited electrons contribute to enhancing the photocurrent response.
- *High incident photon-to-current conversion efficiency (IPCE)* quantifies the ratio of the generated photocurrent to the number of incident photons. As a measure of the efficiency of converting light into electrical energy, IPCE represents the key parameter in assessing the performance of photovoltaic devices.
- *Anchoring to the semiconductor surface* that is determined through the binding interaction between the sensitizer dye and the TiO₂ surface. Appropriate binding of the dye to the oxide surface ensures enhancement of absorption stability and efficient electron injection [55].
- *High photostability* is a precondition of efficient light harvesting, as well as *the compatibility* with cell elements such as semiconductor and electrolyte [18].

The details for theoretical determination of photovoltaic parameters, such as incident photon conversion efficiency (IPCE), driving force for electron injection (ΔG^{inject}), and light harvesting efficiency (LHE), are given in Appendix A.

The dye sensitizers can be categorised as organic [56, 57], metal-free organic dyes [58], inorganic [59] materials, or transition metal complexes [60]. Among them, Ru-complexes show remarkable photovoltaic properties [49, 57]. The natural dyes [61, 62], on the other hand, have a low efficiency with a maximum of around 4% [62]. However, their non-toxic and environmentally friendly characteristics make them promising candidates for further enhancement. Anthocyanidins are characterized as salt derivatives of flavylum cation and belong to a group of common natural pigments [63]. Their investigation as dyes for DSSC sensitizers [15, 64, 65] demonstrates low stability [66] with efficiency reaching a maximum of around 1% [67]. Furthermore, their structure does not possess charge-transfer intramolecular formation. Some of the dyes belonging to the group of anthocyanidins are pelargonidin, delphinidin, peonidin, cyanidin, petunidin, and malvidin [68, 69] with cyanidin being the most investigated one. Different modifications of natural dyes in the form of hybrids have been investigated, with the aim of efficiency enhancement. [70–74].

The small silver nanoclusters in the non-scalable regime (with sizes < 2 nm) exhibit unique structural and optical properties. In combination with organic dyes, they form bio-nano hybrids

with increased photoabsorption and emission. This is because the interaction between excited states of silver cluster and π - π^* states of aromatic rings enhances the absorption of biomolecules [16, 17]. Furthermore, the bio-nano concept introduces the charge-transfer donor-acceptor interaction between the silver cluster and aromatic rings of natural dye. The silver cluster can serve as an electron acceptor and natural dye as the electron donor. The stability of the nanocluster is affected by the number of electrons, where the clusters with an even number of electrons are more stable than those with odd numbers [75]. Enhancement of optical properties together with introduction of charge-transfer features directly influence the photon to conversion efficiency. Additionally, further structural design of bio-nano hybrid properties is obtained through the concept of NCs doping with a single coinage metal atom. As small metal NCs belong to the size regime in which each atom counts, modifying a single atom affects their entire electronic structure and stability [76, 77]. Coinage metal atoms, specifically gold and copper are characterized by a smaller s-d energy gap compared to silver atoms [78, 79], which influences their participation in bond formation. Furthermore, due to relativistic effect in Au and Cu metal atoms, the d electrons are much closer to the s electrons and participate in bonding, while in Ag NCs mainly s electrons are involved. This results in a narrow spectrum with the large intensity of silver NCs, and a broader spectral range of gold and copper NCs [16].

The cyanidin-NC bio-nano hybrids meet all of the design requirements stated above. Specifically, in contrast to the pure anthocyanidin dyes, the bio-nano hybrids have HOMO and LUMO energies that align with the energy levels with TiO_2 semiconductor and I^-/I_3^- redox potential. All of them exhibit negative ΔG^{inject} driving force for electron injection, donor-acceptor charge-transfer character, and enhanced absorption efficiency. As a result, they have large LHE and better overall photocurrent efficiency. The use of bio-nano hybrids as DSSC sensitizers has not been previously investigated. Altogether, this makes them promising candidates for future experimental research in the context of DSSC applications.

1.2.2 Transparent luminescent solar concentrators

The concept of a luminescent solar concentrator (LSC) originated over 40 years ago [80–83]. An LSC represents a simple device that absorbs and re-emits light, directing it to photovoltaic cells for energy conversion. It is assembled from a transparent carrier embedded by luminescent emitters, such as luminophore dyes. When light is absorbed, photons are trapped inside the carrier and then re-emitted through internal reflection towards the outer edges, where solar cells are located [84]. However, in order to apply solar concentrators to large built-up areas, it is necessary to develop technology that would maintain both aesthetics and functionality [31]. Following this, in 2013, R. R. Lunt has proposed the transparent luminescent solar concentrator

(TLSC) [10]. The main difference between TLSC and conventional LSC is in the luminophore dye, which absorbs in the ultraviolet (UV) or NIR spectral region [85, 86] thus obtaining transparency of the LSC plate [19–22].

Requirements for efficient luminophore design for TLSC applications [22, 87]:

- *Wavelength selectivity* as a prerequisite for high aesthetic quality. This implies the development of luminophores that are visibly transparent and selectively absorb UV and/or NIR radiation. More precisely, their most intense absorption transitions should remain outside the VIS range, specifically outside the 435-675 nm wavelengths [20].
- *Optimal band-gap* that ensures capture and transmission of absorbed photons through the concentrator media as well as compatibility with applied solar cells. Thermalisation loss via non-radiative transition can be minimised and overall efficiency improved by optimising band-gap, all while preserving transparency [86].
- *Narrow emission and separated emission and absorption*, both properties minimise the energy loss due to photon reabsorption. In this way, efficiency increases towards Shockley–Queisser (SQ) limit [88]. The theoretical SQ limit represents the upper boundary of solar power conversion efficiency. Furthermore, a narrow emission band produces a better alignment of re-emitted photons with the absorption spectrum of the solar cells at the LSC edge. In this way, efficient light absorption is ensured and overall energy conversion is enhanced.
- *High fluorescence QY* serves as an efficiency measurement of the photoluminescence. The fluorescence QY indicates how efficiently absorbed photons are converted into emitted photons. The higher the QY value, the more of the absorbed photons are re-emitted through radiative processes, losing a smaller amount of photons through non-radiative channels.

Altogether, the photochemical modeling of luminophores with all the above-stated qualities represents a significant theoretical challenge. This is because obtaining absorption in the NIR region while simultaneously achieving high fluorescence QY contradicts the energy gap law [89]. According to this law, as the energy difference (ΔE) between the excited state and the ground states decreases with a shift to the NIR region, it promotes the non-radiative processes and as a result leads to a smaller QY. In addition, theoretical calculations of photo-induced processes, like fluorescence QY and transition rates are even more demanding. There are three theoretical approaches for QY prediction; non-adiabatic molecular dynamics [90, 91], machine learning [92, 93], and Fermi's golden rule that relies on an accurate description of potential energy surfaces (PES) within harmonic approximation. The prediction based on Fermi's golden

rule is the most widely used since it offers a balance between accuracy, computational efficiency, and applicability [94].

In luminescent dyes, photon absorption triggers the excitation of electrons from the ground to an excited state. Following excitation, electrons undergo a decay transition through radiative or non-radiative processes, where the two most common non-radiative transitions are internal conversion (IC) and intersystem crossing (ISC) [95]. Since the fluorescence QY is defined as a ratio between radiative (k_r) and the sum of all other transition rates, the competition between radiative and non-radiative transitions significantly influences the QY efficiency.

Prediction of QY based on Fermi's golden rule relies on the first-order perturbation theory where the type of transition between states is described through the applied perturbation operator. In that context, the transition dipole moment operator is used for the description of radiative rate, non-adiabatic coupling for IC, and spin-orbit coupling for ISC rates [94]. Additionally, for systems with numerous normal modes, a full description of PES cannot be done. As a result, initial and final state PES are approximated by harmonic oscillators in the form of quadratic parabolic functions. However, a simple anharmonic model may be obtained by substituting harmonic oscillators with the Morse potential [96].

Radiative transition primarily occurs between the vibrational minima of initial and final state PES. Meanwhile, the IC rate corresponds to the transition from the minimum of the excited state PES to highly excited vibrational states within the ground state PES. There are several different harmonic models within the vertical (V) or adiabatic (A) approach. They differ in the description of PES expansion of the final state. In vertical models it is expanded around the geometry of the excited-state minimum, while in adiabatic models expansion occurs around the geometry of the the ground-state minimum [97, 98]. In addition, depending on the complexity of the description, there are: adiabatic shift (AS) and vertical gradient (VG) models, adiabatic shift frequencies (ASF) and vertical gradient frequencies (VGF), and adiabatic Hessian (AH) and vertical Hessian (VH) models. The AS and VG represent the simplest models that only differ in equilibrium geometries, ASF and VGF include equilibrium geometry as well as different frequencies of initial and final states. AH and VH are the most complex as they also include different Hessian matrices [97, 98]. There are few computational codes [23, 24, 99–104] developed in the literature for calculating transition rates within Fermi's Golden rule. In the framework of this thesis, calculations of fluorescence QY and transition rates have been performed within FCclasses3 [105].

In addition, theoretical modeling of photochemical properties can be strongly influenced by the broadening description of spectral line. This is particularly important for IC prediction, where choice of the broadening can have a significant influence on the obtained result. There are several types of broadening, including homogeneous broadening (Lorentzian lineshape), inhomogeneous broadening (Gaussian lineshape), and Voigt broadening that corresponds to

the convolution of the Lorentzian and Gaussian profiles. Homogeneous broadening uniformly outlines the radiation of molecules or atoms and is primarily caused by the finite lifetime of excited states and is described by the Heisenberg uncertainty principle [106]. In contrast, the inhomogeneous broadening results from a response to different variation shifts in the environment [107]. The computation of transition rates and fluorescence QY with different harmonic models, and broadening functions involves theoretical constraints that must be carefully considered in the context of reliability. The reliable prediction of fluorescence QY is a prerequisite for the theoretical modeling of luminophore dyes.

In this context, molecular aggregates represent systems with required properties. However, despite some literature contributions [108, 109], they have not been extensively investigated for LSC luminophores. J-aggregates are discovered by Scheibe and Jelley as types of dyes with unique opto-electronic properties [110, 111]. They have a distinct narrow absorption band (J-band) that is bathochromically shifted compared to the monomer, coupled with increased absorption intensity and narrow-band fluorescence. These properties result from the phenomenon of supramolecular self-organization at the nanoscale, specifically their excitonic nature, where the excited states of J-aggregates create extended domains of coherently coupled molecular transition dipoles [25]. An increase in their delocalization length has several effects: it induces the superradiance phenomenon, which is characterized by a linear increase of radiative rate; it leads to an emission energy drop due to exciton splitting [112]; and it causes a decrease in the IC constant [113]. These characteristics result in a high fluorescence QY and absorption in the NIR, making them potential candidates for the TLSC design.

In addition, squaraine dyes are widely used due to their strong absorption and emission in the VIS and NIR regions, photochemical stability, and simple synthesis [114, 115]. Their absorption in NIR as well as their potential for achieving high QY has been experimentally studied [116–118]. The opto-electronic and exciton characteristics of squaraine dye J-aggregates, in the form of linear, covalently bound dimers, and trimers [119–121], as well as the effect of chain length, have been investigated [122–125]. Squaraine dyes have a characteristic central squaric acid ring with two oxygen atoms and two indoline groups attached on both sides forming symmetrical *trans* conformation with an inversion center (SQA). In *cis* squaraine (SQB) with C_{2v} symmetry, conformation change occurs because of the substitution of one oxygen by dicyanovinylene group [119]. In the scope of this thesis, squaraine J-aggregates such as SQA and SQB tetramers have been theoretically investigated. They have a characteristic structure of linear homoaggregates with head-to-tail orientation of localized transition dipole moments illustrating their exciton nature [126].

Although extensively investigated, J-aggregates of squaraine dyes have not been studied in the context of luminophores for TLSC design. Squaraine tetramers exhibit desirable features such as narrow emission, sharp absorption in NIR, and high fluorescence QY. Due to these

properties, as demonstrated in the thesis, they are promising luminophores for integration into TLSC devices.

1.3 Methodology

A brief description of the used methodology from the literature is presented. This includes density functional theory, time-dependent density functional theory, environmental description as well as limitations of computational approach (sections 1.3.1 - 1.3.4).

Computational modeling of photochemical properties relies on the mathematical description of energy levels and transitions between the states of interest. Photochemistry includes processes originating from the absorption of light (photons). It is possible to predict the energies, electronic structure, and properties of nanoscale materials using quantum mechanical approximations. A different software programs have been developed to calculate molecular ground and excited states, as well as to determine different energy mechanisms. They serve as tools for the design of novel materials. In addition, simulations of processes arising from the nature of light provide insights into the field of photophysics which is experimentally unavailable [127]. However, even though the mathematical aspects of quantum mechanics were established during the 1920s [128, 129], computational chemistry did not become widely accessible until the development of computers in the 1950s and the release of the first semiempirical and *ab initio* programs [130, 131]. Today, computational photochemistry together with experimental methods offers a comprehensive understanding of light induced phenomena.

On the molecular level, properties of the system can be described quantum mechanically using the time-independent Schrödinger equation:

$$H\psi = E\psi \quad (1.1)$$

where H is the Hamiltonian operator, E is the total energy and ψ is the wavefunction of the system. Furthermore, the Hamiltonian of an N-particle system is defined as the sum of the potential and kinetic energies:

$$H_{tot} = T_n + T_e + V_{nn} + V_{ee} + V_{ne} \quad (1.2)$$

where T_n corresponds to the kinetic operator of the nuclei and T_e of the electrons. V_{nn} is the potential energy operator for nuclear repulsion, V_{ee} for electron-electron repulsion, and V_{ne} for nuclei-electron interactions. Solving the time-independent Schrödinger equation involves the Born-Oppenheimer (BO) approximation, which is based on the assumption that nuclei, having larger mass than electrons, move slower, therefore their motion can be neglected and they can

be treated as stationary. The obtained expression can be solved for the electron wavefunction with the electronic Hamiltonian operator given by:

$$H_e = T_e + V_{nn} + V_{ee} + V_{ne} \quad (1.3)$$

Solving the electronic Schrödinger equation for many different nuclear configurations results in potential energy surface, where the PES represents the core concept in computational chemistry. It displays a static surface on which electronic energy acts as a function of the nuclear coordinates. These methods are known as “electronic structure calculations”. Furthermore, if there are no experimental parameters involved, they belong to so-called *ab initio* methods [132].

1.3.1 Density functional theory (DFT)

Density Functional Theory is used for determining the ground state electronic energy of the system. Initially described by Thomas and Fermi [133, 134], it was later proved by Hohenberg and Kohn [135]. In DFT, the ground state electronic energy of atoms is expressed as functional of electron density ρ . This implies a direct relationship between the electron density and the energy of a system. Additionally, since electron density corresponds to the square of the wavefunction, it is determined by three spatial variables (x, y, and z) and is independent of the number of electrons. Compared with the wavefunction where complexity increases with electron numbers, electron density remains constant. This results in the reduced computational time needed for the calculation of molecular properties. However, DFT has limitations in describing some important features such as weak dispersion interactions and loosely bound electrons. In addition, the approximation of correlation effects has the influence on the results. The computation of ground state electronic energy remained challenging until 1965, when Kohn and Sham introduced their theorem [136]. They proposed that total kinetic energy $T[\rho]$ can be divided into two parts: a larger contribution in the form of kinetic energy under the assumption of non-interacting electrons $T_s[\rho]$, and a smaller part in the form of exchange-correlation term $E_{ex}[\rho]$. In that way, the DFT energy of the ground state can be written as:

$$E_{DFT}[\rho] = T_s[\rho] + E_{ne}[\rho] + J[\rho] + E_{ex}[\rho] \quad (1.4)$$

where $J[\rho]$ is the Coulomb (electrostatic) interaction, and the nuclei-electron attraction $E_{ne}[\rho]$ corresponds to the external potential at ground state minimum $V_{ext}(r)$. The remaining exchange-correlation energy $E_{ex}[\rho]$ is unknown and must be further approximated by different functionals. Functional represents a mathematical form of "a function of a function". There are different functionals developed based on the properties of the system. In this context, the choice of the exchange-correlation functional can significantly influence the computational accuracy.

In addition, the Kohn-Sham method is self-consistent. This means that it requires an initial guess of the electron density. The process then iterates until the density and exchange-correlation energy converge and the orbital and energy level values are obtained [132, 137].

1.3.2 Time-dependent density functional theory (TDDFT)

Time-dependent density functional theory represents a time-dependent analogue of the Hohenberg-Kohn theorem, that is used for computing the electronically excited states. It is based on the Runge and Gross (RG) theorem stating that a unique mapping correlates time-dependent density and time-dependent external potential, $V_{ext}(\vec{r}, t)$. The external potential represents interactions or external fields. This map is obtained by solving the time-dependent Schrödinger equation for the system with the fixed initial state, and by calculating the resulting densities in response to the different external potentials. TDDFT is referred also as density response theory. The key principle of the RG theorem states that this map can be inverted, so if you know the exact density you can reconstruct the potential. Furthermore, this is proved by the uniqueness of potentials, where if two potentials are distinguished by more than only a time-dependent function $c(t)$:

$$V_{ext}(\vec{r}, t) - V'_{ext}(\vec{r}, t) \neq c(t) \quad (1.5)$$

they will result in different densities [138]. RG theorem enables the application of TDDFT to systems evolving in time under the influence of external fields.

However, the calculation of the time-dependent Schrödinger equation demands a great deal of computational time and memory. To overcome this problem, the molecular system is described through non-interacting electrons with corresponding time-dependent Kohn and Sham equations. Nevertheless, the complexities of interacting electrons are accounted for in the exchange-correlation functional. In order to use the described theory, the exchange-correlation functional needs to be further approximated [139]. These approximations have a great influence on TDDFT accuracy, limiting its application. The consequences of approximations are best illustrated by the fact that TDDFT is most reliable for low-energy excited states [140]. However, when the energy levels are very close together, as in non-adiabatic transitions, the Born-Oppenheimer approximation breaks down. These limitations should be considered carefully.

1.3.3 Environment description

Depending on the studied phenomena as well as on experimental measurements, environment description includes systems in vacuum, solvent, or on the surface. Computation in the gas phase usually corresponds to experiments in a vacuum, where only intramolecular forces are part of the model. Furthermore, gas phase simulations provide insight into intrinsic molecular

properties like electronic structure, energies, spectra, or chemical reactions without external interference [140].

However, in the cases of liquids where the environment has a significant influence on the system or its specific properties, the inclusion of the solvent is necessary. The solvent medium can be described implicitly as a homogeneous medium, or explicitly where the individual solvent molecules are included at the same level of simulation as the solute ones. The explicit approach gives a more physical description of the solvation process. Nevertheless, due to the large number of molecules needed for the description of the solvent around the solute, it is computationally very demanding. On the other hand, the implicit solvation model represents a quantum mechanical approximation of the solvent in the form of a homogeneous continuum defined by its dielectric constant and cavity shape.

There are few basic assumptions in the continuum model: the solvent is a dielectric continuum, the solute-solvent interactions are electrostatic, the solution is very dilute and isotropic, and the cavity around the solute acts as a carrier of the dielectric continuum inside and as a charge carrier on its surface. There are different cavity descriptions such as solvent-accessible surface (SAS), solvent-excluded surface (SES), and van der Waals (vdW) surface [141]. The first two are determined from the interaction of the molecule with the atomic probe. Usually, the probe represents a solvent molecule in form of a sphere corresponding to helium or argon atoms [142]. The SAS defines the boundary that the center of the probe can reach, representing the accessible surface area. In contrast, the SES boundary is defined as the line where the probe touches the molecule, thereby excluding solvent from the cavity [141]. The vdW surface, on the other hand, provides a more physical description. It is based on the idea that the cavity is assembled from the superposition of corresponding atomic van der Waals spheres [143], with Bondi [144] definition of vdW radii being the most commonly used.

The Schrödinger equation for the homogeneous continuum can be written as:

$$[H_{eff} + V_{int}]\psi = E\psi \quad (1.6)$$

with V_{int} representing solute-solvent interaction potential, and the Hamiltonian is simplified to focus on the solute and its interaction with the solvent as a continuous medium. In that way obtained effective Hamiltonian:

$$H_{eff}(f, r) = H(f) + H^{int}(f, r) \quad (1.7)$$

consists of the "focused" (f) solute part and solute-solvent interaction, while the "remained" (r) solvent part is neglected. One of the first and the most frequently used implicit type of continuum solvent distribution model is the Polarizable Continuum Model (PCM) [145, 146]. PCM describes the solute-solvent interaction using a self-consistent polarization interaction

potential and an effective Hamiltonian for the solute. This potential is between the charge distribution on the cavity surface, which represents the solute, and the dielectric polarizable continuum that represents the solvent [146]. Different PCM models have been proposed to define the cavity surface charges, among which the integral equation formalism (IEFPCM) represents the most generally used one [147–149]. Furthermore, the computation of excited state solvation requires a proper description of the interaction between electronic state relaxation and solvent dynamics. Depending on the solvent's response to changes in the solute, equilibrium, and nonequilibrium solvation regimes can be distinguished. The equilibrium solvation regime describes the processes where, upon solute excitation, the solvent has time to fully respond and reorient its molecules to the solute distribution. In the nonequilibrium solvation regime, processes are too rapid for the solvent to fully respond, representing the vertical approach [147].

The computation on the surface refers to the modeling of the interaction between the solid surface and the system of interest, adsorbed on the surface. On a quantum mechanical level, only a fragment of the surface interacting with the adsorbed molecule can be observed. Anything larger than the upper boundary of a few hundred atoms goes beyond the quantum mechanical theory level and may be addressed with the introduction of different approximations or with the use of lower theoretical levels. The solids in crystalline form can be modeled as an infinite crystal cut to a finite size, where the center consists of an active site and the edge is "closed" with the hydrogen atoms. This is because the hydrogen atoms have similar electronegativity to the carbon atoms that usually form the backbone of the studied surface and are computationally less demanding [150]. In such molecule-surface systems, surface anchoring plays an important role, since different anchoring can influence molecule-surface binding energy, electronic properties, and overall system stability.

1.3.4 Limitations of computational approach

Since DFT and TDDFT methods are relatively efficient under lower computational time they are widely used for calculations of ground and excited states, as well as of properties that arise from their interaction. However, they have some limitations that must be taken with caution.

- *Dependence on the exchange-correlation (xc) functional choice.* This is particularly significant for TDDFT accuracy and is considered a major method limitation. The xc functional incorporates spin-correlated effects, such as exchange and correlation energy [137], which cannot be calculated directly but are instead approximated using methods like local spin density approximation (LSDA) or generalized gradient approximation (GGA) [132]. Hybrid functionals like B3LYP [151] and PBE0 [152, 153] are generally used for the description of low-lying singlet excitations [154]. However, both standard and hybrid functional descriptions do not account for any long-range electron interactions, including

van der Waals forces and charge-transfer excitations. In photochemical reactions, charge-transfer that occurs between excited and ground states represents one of the fundamental properties. In such cases, the description of distant electron interaction plays an important role, and the long-range xc functionals need to be employed. The most commonly used long-range xc functionals for the description of charge-transfer states [154] are CAM-B3LYP [155] and ω B97XD [156].

- *Inadequate description of strong correlation effects.* This is related to DFT and TDDFT dependence on the choice of xc functional. Strong electron-electron correlation effects emerge when electrons are not equally delocalised over the molecular system but tend to localize in atomic orbitals. These effects are observed in transition-metal complexes, many open-shell states, systems with atypical bonding, and ground/excited state crossings [157]. Despite some contributions in the literature [158, 159], these limitations need to be further addressed.
- *Breaking of the Born-Oppenheimer approximation.* When excited, electrons can undergo non-adiabatic transitions between excited states, such as conical intersection or intersystem crossing. In such cases, electronic motion cannot be separated from nuclear motion, leading to a strong coupling between them. This coupling causes the excited state potential energy surfaces to become close in energy, resulting in the breakdown of the Born-Oppenheimer approximation [132]. As a result, these transitions cannot be fully described within the TDDFT level.
- *Description of excited-state relaxation.* In light emission effects, an excited electron has to reach the excited state minimum before decaying into the ground state. In order to describe properties emerging from electron emission, an adequate description of excited state relaxation is required. This is particularly important when solvent effects are included. Solvent response to electron excitation can be classified as equilibrium or nonequilibrium. The vertical energy transitions correspond to the nonequilibrium solvation, while excited state optimizations with fully relaxed solvent must be obtained within the equilibrium description [160]. Although the description of excited state relaxation is not a limitation per se, it must be addressed with caution.
- *Description of relativistic effects.* Relativistic effects introduce specific electron-nuclei and electron-electron behaviour that are not accounted for in general DFT and TDDFT formalism. While the relativistic R-DFT is developed [161], the inclusion of relativistic effects in TDDFT is the area of continuous theoretical effort [162, 163].

Nevertheless, computation of molecular properties based on DFT/TDDFT calculations is continuously developing, setting the TDDFT as the standard computational method in modeling of

excited states and photochemical effects.

1.4 Research objectives

The core issue in solar energy production is its lower efficiency compared to conventional fossil fuels. In order to address this, there is a strong focus on developing new photovoltaic materials that are both efficient and sustainable. Theoretical simulations with advanced computational tools serve for qualitative predictions of molecular material properties. They stimulate experimental investigations by predicting material behavior. Furthermore, computational photochemistry provides fundamental insights into light-matter interactions such as absorption, emission, and charge-transfer mechanisms. Understanding these processes guides the development of photovoltaic materials optimized for specific applications such as solar cells and solar concentrators. The aim of the thesis is to theoretically design fluorescent dyes as new photovoltaic materials with enhanced light-harvesting efficiency.

Fluorescent dye, whether utilised as a sensitizer in DSSC or as a luminophore in TLSC, is a component whose modification affects their overall efficiency. Its structural optimisation and design lead to new materials with enhanced solar energy harvesting potential and integration into the built environment.

The thesis consists of two parallel topics:

*1) Theoretical design of sensitizer for dye-sensitized solar cells (DSSC)
(Chapter II)*

The research emphasises a novel class of bio-nano hybrid sensitizers at TiO₂ support. The objective is to design natural-based sensitizers with optimal stability and efficiency for DSSC application. By combining metal nanoclusters with natural dyes, bio-nano hybrid systems induce a donor-acceptor character that enhances their opto-electronic and photovoltaic properties. More specifically, the influence of valence electron number (even or odd) of silver nanoclusters and their doping with coinage metal atoms (Au and Cu) have been theoretically investigated. The computations are carried out within the density functional theory and its time-dependent variant (cf.1.3 Methodology). Altogether, bio-nano hybrids demonstrate increased overall efficiency. Nanoclusters possessing an even number of valence electrons are identified as effective acceptors, whereas doping has a positive impact on optical and photovoltaic properties. The stability of these hybrids is shown in their strong coupling with the TiO₂ surface. As a result of theoretical study, bio-nano hybrids at TiO₂ surface have the potential for application in DSSC technology, while experimental confirmation is still needed.

II) Theoretical design of dye as luminophore for transparent luminescent solar concentrators (TLSC)

(Chapter III)

The research objective is to develop transparent materials with high fluorescence QY for application in TLSCs. Design of luminophores as novel TLSC materials requires reliable prediction of transition rates (k_r , k_{ic}) and fluorescence QY, in addition to computation of the structural and optical properties. The calculations are performed within a harmonic vibrational model at DFT and TDDFT theoretical levels (cf.1.3 Methodology). However, due to its limitations, a reliable framework within the harmonic approximation is needed. In particular, the comparison of different harmonic models and the broadening functions serves as a basis for the reliability rules in QY prediction.

J-aggregates due to the delocalisation of excitons can serve as selective collectors of electromagnetic radiation while preserving a high fluorescence QY. Theoretical modeling of squaraine J-aggregates has demonstrated high quantum yield (QY) while absorbing in the near-infrared (NIR) region, resulting in transparency within the visible (VIS) spectrum. These findings have been confirmed by available experimental data, making them suitable TLSC candidates.

Altogether, the theoretical design of new materials with improved properties stimulates experimental investigation and offers valuable insights into the photochemical nature of organic dyes and their hybrids. This comprehension is important for their application in photovoltaic solar technologies. Advances in this field promote the development and optimisation of materials for more efficient solar energy conversion.

1.4.1 Modeling cyanidin-silver nanocluster hybrids at TiO₂ support

Chapter 2.1 provides a simple yet effective concept of enhancing charge-transfer and efficiency in DSSCs through theoretical modeling of hybrid sensitizer. Present research [164] focusses on bio-nano donor-acceptor hybrids formed by combining cyanidin, a common natural dye, with small silver nanoclusters (NCs). Additionally, the objective is to theoretically investigate the opto-electronic properties and performance of hybrid photosensitizers within the context of DSSCs.

Bringing together biomolecules and small noble metal nanoclusters has several advantages. First, the combination of their excited states produces higher absorption intensity [16], resulting in improved light harvesting efficiency. Second, silver NCs induce donor-acceptor character in hybrids, with the NC acting as the acceptor and the cyanidin dye as the donor, promoting effective electron injection. In particular, the cyanidin-Ag_n (n = 3, 5, 9, 21) hybrids with an even

number of NCs valence electrons have better stability compared to those with an odd number. The findings are consistent with previous investigations [78]. As a result, they have a negative value of ΔG^{inject} , as well as HOMO and LUMO energy levels that match the TiO_2 conduction band and I^-/I_3^- redox potential. This indicates successful electron injection to the semiconductor conduction band and system regeneration. Furthermore, increasing the size of NCs in hybrids improve stability and reduce the HOMO–LUMO gap, leading to a bathochromic shift and enhanced efficiency. Larger NCs, such as Ag_9^+ and Ag_{21}^+ , are consequently more suitable for application.

Efficient charge-transfer from the sensitizer to the semiconductor is essential for increasing light-to-electricity conversion and enhancing the solar cell efficiency of DSSCs. The semiconductor surface is simulated by a two-layer anatase TiO_2 (100) model [165, 166]. The cyanidin- Ag_9 hybrid binds to the surface through two titanium-oxygen bonds, thereby forming an anchoring mechanism required for effective electron injection into the semiconductor. {Cyanidin- Ag_9 }- TiO_2 complex shows a shift to the red region and effective charge-separation, demonstrating the stabilisation of the sensitizer on the semiconductor surface.

Both experimental and theoretical investigations are required to develop new nanoscale materials with improved DSSC efficiency. In this context, theoretical design serves to stimulate experimental research by focusing on the optical and photovoltaic properties of bio-nano hybrids on TiO_2 substrates.

1.4.2 Doping of cyanidin-silver trimer hybrids at TiO_2 support

In Chapter 2.2 theoretical investigation of coinage metal doping of bio-nano hybrid sensitizers at the TiO_2 surface has been presented. The investigation involves doping of silver trimer with one Au or one Cu atom, and mixed Au-Cu atoms, to elucidate their influence on opto-electronic and photovoltaic properties of bio-nano hybrid sensitizer. The demonstrated doped cyanidin-(hetero-metal) trimer exhibits better photovoltaic properties and stability compared to the cyanidin-silver NCs hybrids. Furthermore, it showed enhanced linear and non-linear properties. Consequently, the cyanidin- Ag_2Au and cyanidin- AgAuCu hybrids have improved properties compared with cyanidin- Ag_n hybrids with larger NCs, such as Ag_9^+ and Ag_{21}^+ . Such behaviour arises from the relativistic effects of Au and Cu valence electrons, causing a smaller s-d energy gap [78, 79]. Specifically, the expansion of the d-orbitals promotes the participation of d-electrons in bond formation, resulting in a more stable structure [78]. Further support of this effect arises from binding energy calculations, which indicate higher values for the doped systems. Overall, findings presented in the thesis [167] indicate that doping by single Au or Cu atoms, as well as combined Au-Cu, produces a more stable hybrid structure.

In terms of photovoltaic properties, doped hybrids fulfill the requirements for an effective

sensitizer. Their HOMO-LUMO levels are well-aligned, their ΔG^{inject} value is negative, and they have LHE comparable to that of cyanidin-Ag₉⁺ and cyanidin-Ag₂₁⁺. This is in accordance with the results of the doped hybrids on the surface. As mentioned in previous work [164], the semiconductor model contains 30 TiO₂ subunits capped with 12 hydrogen atoms. Two Ti-O bonds ensure strong binding of the cyanidin-Ag₂Au hybrid to the TiO₂ surface. Effective electron induction is indicated by the formation of charge-transfer excited states between the hybrid and the semiconductor. Additionally, compared to the cyanidin-Ag₃ at TiO₂ support, the attached doped hybrid has a higher absorption intensity.

Since doping significantly improves the stability of silver NCs [76, 77], the substitution of larger silver NCs by smaller doped ones is favoured. This approach enables the development of affordable bio-nano hybrid sensitizers while maintaining enhanced stability and efficiency. As a result, doped hybrids enhance the performance of DSSC sensitizers. These findings should be further validated by experimental investigation.

1.4.3 Theoretical prediction of fluorescence quantum yields

Theoretical investigation of coumarin derivatives in solution is presented in Chapter 3.1, together with its comparison with available experimental data [168–173]. The objective is to reliably predict the radiative (k_r), and non-radiative decay rates, specifically internal conversion (k_{ic}), as well as the fluorescence quantum yield (QY). Internal conversion is considered to be the only significant non-radiative process, while the other decay processes are neglected. In particular, the focus is on investigating the impact of anharmonicity, the choice of harmonic model, and the broadening function. The Franck-Condon and harmonic approximations have been used to compute the emission spectra and transition rates [23, 24, 105, 174]. Within the scope of this thesis, several "Rules of thumb" for reliable prediction of QY from first principles are established [175]. The anharmonicity level can be determined by comparing different harmonic models [97, 98], since for harmonic potential the adiabatic and vertical models should provide the same result. The harmonic approximation accurately predicts the radiative decay rate k_r (Rule I), while k_{ic} depends on the accurate description of emission spectral tail. As a result, to obtain a reliable harmonic prediction of k_{ic} , frequency changes, and Duschinsky rotation need to be taken into account (Rule II). Furthermore, large k_{ic} values are associated with a broad emission spectrum (Rule III). For the narrow-spectra of coumarins labeled as 102, 343, and 522, the k_{ic} values are small and sensitive to broadening. In contrast, 3-chloro-7-methoxy-4-methylcoumarin CIMMC has a broad spectrum and a large k_{ic} . Inhomogeneous broadening does not significantly influence transition rates (Rule IV), while rates that depend on homogeneous broadening are not reliable (Rule V). Therefore, the k_{ic} rate is more affected by homogeneous broadening. This can be explained by the long tail of the Lorentzian profile which allows non-radiative transitions between vibrational states with significant energy difference, leading to an increase in k_{ic} .

Additionally, a high value of homogeneous broadening washes out the vibrational structure, and the rate depends solely on the broadening function. Therefore, adopting a large amount of homogeneous broadening to fit an experimental non-radiative rate will produce unreliable results.

Following the previous statement, harmonic adiabatic hessian (AH) and vertical hessian (VH) harmonic models must be equivalent (Rule VI). The anharmonic Adiabatic Shift (AS) model is examined by replacing each normal mode of the harmonic AS model with a Morse potential, therefore introducing a degree of anharmonicity. These calculations show that deviations from the energy gap law are caused by anharmonicities, and that as anharmonicity increases, the rate also increases. An analogous outcome can be obtained with a large value of Lorentzian broadening. For $k_{ic}(\Delta E)$ values $< 10^{-5}k_{ic}^{max}$, the homogeneous broadening and anharmonicity have a considerable influence (Rule VII). The fulfillment of the last rule relies on balancing two opposite requirements. Smaller ΔE results in a shift to NIR and an increase of k_{ic} , while larger vibronic overlap leads to a broader spectrum and lower k_{ic} value. Based on these requirements, the QY prediction for CIMMC coumarin in water and cyclohexane solvents is accurate. In summary, for a reliable prediction of fluorescence QY, harmonic models and broadening functions must be analysed and compared with experimental data.

1.4.4 Design of J-aggregates squaraine dyes as TLSC materials

Chapter 3.2 emphasises the theoretical design of luminophores for transparent luminescent solar concentrators (TLSCs) investigating their potential as selective UV and NIR light harvesters with high fluorescence QY. Transparency and high QY are two essential features of visually appealing and efficient TLSC. Enhancement of QY minimises photon reabsorption [176–179] which is one of the main causes of energy loss [180]. The aim is to identify J-aggregates formed from squaraine dyes that are suitable for TLSC applications. In this thesis, the optical properties as well as the QY prediction of SQA and SQB J-aggregates in toluene solvent are theoretically studied [181]. More specifically, the influence of the number of monomer subunits on their opto-electronic properties is investigated. Results are in agreement with experimental findings for dimers (dSQA, dSQB) and trimers (tSQA, tSQB) [119], while our prediction extends for tetramers (tetSQA, tetSQB).

It is particularly challenging to obtain a high QY in the NIR region. The reason for this is because the red shift produces a reduction in excitation energy. This significantly increases the non-radiative rate and, as a consequence, lowers the quantum yield. On the other hand, J-aggregates exhibit the superradiance effect as a result of the exciton delocalisation which is illustrated by the linear increase of radiative rate with the delocalisation length. Additionally, the internal conversion rate (k_{ic}) decreases simultaneously [112].

The investigated squaraine J-aggregates consist of linearly arranged SQA or SQB squaraine

dyes. According to Kasha's molecular exciton model [126], the exciton character of these homoaggregates (SQA and SQB) is demonstrated by the superposition of transition dipole moments, leading to an enhancement in dipole strength and a bathochromic shift with an increase in the number of subunits. The effect is more pronounced for SQA than for SQB J-aggregates. Additionally, the substitution of one oxygen by dicyanovinylene group results in a red shift of SQB J-aggregates compared to SQA. The absorption spectra of all systems exhibit characteristic J-aggregate splitting, while their fluorescence spectra show a narrow J-band in the near-infrared. Both tetramers have the highest absorption intensity in the NIR region. The tetSQA J-aggregate satisfies the requirements for transparency, whereas the tetSQB shows considerable intensity in VIS, indicating semitransparency. In SQA, the QY values match experimental findings, with minimal broadening impact on k_{ic} values. Both findings serve as reliability checks for QY prediction. Additionally, fluorescence QY increases with system size, and SQA has a higher computed QY than SQB, therefore fulfilling the high value for QY. In order to extend the QY predictions for larger systems, the k_{ic} rate is calculated using the Englman-Jortner energy gap law [89, 112]. This qualitative scaling model supports the aforementioned findings. Therefore, the tetSQA J-aggregates in toluene solvent or those with a larger number of subunits are promising candidates for TLSC applications. These new materials proposed within this thesis demonstrate the requirements for efficient light harvesting and conversion in TLSC devices.

Design of sensitizers for dye-sensitized solar cells at TiO₂ support




2.1 Cyanidin-silver nanocluster hybrids

Reprinted from:

Margarita Bužančić Milosavljević, Antonija Mravak, Martina Perić Bakulić and Vlasta Bonačić-Koutecký. Model systems for dye-sensitized solar cells: cyanidin-silver nanocluster hybrids at TiO₂ support. *RSC Advances*, 13 (9), 6010-6016, 2023. Reproduced with permission from the Royal Society of Chemistry.


 Cite this: *RSC Adv.*, 2023, **13**, 6010

Model systems for dye-sensitized solar cells: cyanidin-silver nanocluster hybrids at TiO₂ support†

 Margarita Bužančić Milosavljević, ^a Antonija Mravak, ^a Martina Perić Bakulić ^{*,a} and Vlasta Bonačić-Koutecký ^{*,abc}

Theoretical study of structural, optical, and photovoltaic properties of novel bio-nano hybrids (dye-nanocluster), as well as at TiO₂ surface model support is presented in the context of the application for dye-sensitized solar cells (DSSC). A group of anthocyanidin dyes (pelargonidin, cyanidin, delphinidin, peonidin, petunidin, and malvidin) represented by cyanidin covalently bound to silver nanoclusters (NCs) with even or odd number of valence electrons have been investigated using DFT and TDDFT approach. The key role of nanoclusters as acceptors in hybrids cyanidin-NC has been shown. The nanoclusters with an even number of valence electrons are suitable as acceptors in hybrids. The interaction of bio-nano (cyanidin-NC) hybrid with the TiO₂ surface model has been investigated in the context of absorption in near-infrared (NIR) and charge separation due to donor and acceptor subunits. Altogether, the theoretical concept serves to identify the key steps in the design of novel solar cells based on bio-nano hybrids at TiO₂ surface for DSSC application.

 Received 9th January 2023
Accepted 10th February 2023

DOI: 10.1039/d3ra00165b

rsc.li/rsc-advances

1 Introduction

In a search for a photovoltaic cell that would be commercially more attractive due to better energy conversion efficiency, Grätzel *et al.* proposed a dye-sensitized solar cell (DSSC),^{1–3} based on light harvesting dye that sensitizes the transparent TiO₂ semiconductor film. Since then, a significant experimental and theoretical effort has been invested into finding the optimal sensitizer.^{4–8} Transition metal compounds, specifically Ru-complexes, have emerged as highly efficient DSSC dye candidates with promising photovoltaic properties.^{3,9} However, the search for new materials has led to natural dyes,^{10–12} that are non-toxic for both humans and the environment,¹³ and easily available through plant extraction.¹⁴ The reported efficiency of these dyes is rather small (maximum value of over 4%¹²). Nevertheless, their modification by small silver nanoclusters (NCs) opens a route to design new systems with donor-acceptor properties. These properties have been previously studied

within sensitizers¹⁵ based on ruthenium,^{16,17} porphyrin¹⁸ complexes, and metal-free¹⁹ organic dyes.

Anthocyanidins, a subclass of flavonoids, have absorption maxima lying ~500 nm²⁰ and are extensively investigated in the context of the DSSC application.^{21–23} However, they have low stability²⁴ and low efficiency as solar cell sensitizers (maximum around 1%²⁵). Also, they do not satisfy the donor-acceptor condition.

Although several properties of the DSSC system can be tuned to improve efficiency, our approach is the modification of the sensitizer by introducing the donor-acceptor concept through bio-nano hybrid. A variety of modified natural dyes based on bio-nano hybrids have been investigated. Those include but are not limited to complexes of two or more natural dyes,^{25,26} natural and synthetic dyes²⁷ and multilayered natural dyes DSSC.²⁸ Also, the addition of metal atoms to natural dye (*e.g.* iron-cyanidin complex) has been reported to improve optical properties compared to pure pigments.²⁹

Furthermore, the silver nanoclusters (NCs) forming bio-nano hybrids substantially increase optical absorption of pure biomolecules due to the interaction between intense excitations within the cluster and $\pi-\pi^*$ excitations within aromatic rings of biomolecule.³⁰ This opens a route for enhancing the optical properties as well as improving the light-harvesting efficiency of natural dyes through interaction with silver NCs which introduces donor-acceptor subunits. Previous work has demonstrated that ligated noble metal NCs^{31,32} as well as noble metal nanoparticles (NPs)^{33,34} can contribute towards more efficient sensitizers.

^aCenter of Excellence for Science and Technology-Integration of Mediterranean Region (STIM), Faculty of Science, University of Split, Ruđera Boškovića 33, 21000 Split, Croatia. E-mail: margarita@stim.unist.hr; antonija@stim.unist.hr; martina@stim.unist.hr

^bInterdisciplinary Center for Advanced Science and Technology (ICAST) at University of Split, Meštrovićevo šetalište 45, 21000 Split, Croatia

^cDepartment of Chemistry, Humboldt Universität zu Berlin, Brook-Taylor-Strasse 2, 12489 Berlin, Germany. E-mail: vbk@cms.hu-berlin.de

† Electronic supplementary information (ESI) available. See DOI: <https://doi.org/10.1039/d3ra00165b>



The anchoring of the dye on the TiO₂ surface is critical for ensuring electron injection from the dye to the semiconductor, which is one of the important conditions for DSSC efficiency.³⁵ Therefore, anchoring the cyanidin-NC on the TiO₂ semiconductor has been investigated by modeling the complex {cyanidin-NC}-TiO₂. Such hybrids have not been investigated previously in the context of DSSC application.

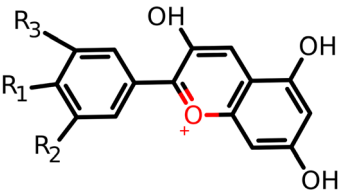
In the present paper, we focus on the theoretical study of the dye and silver NC (cyanidin-NC) hybrids by their opto-electronic and DSSC properties within the DFT and TDDFT methods. Results involve theoretical prediction of structural and linear optical properties (one-photon absorption, OPA) of bio-nano hybrids, in order to find out how the overall efficiency depends on selected NCs. Calculations of nonlinear optical properties (two-photon absorption, TPA) on chosen example have also been performed. Anchoring of the bio-nano hybrids on the semiconductor surface of TiO₂ model is addressed in the context of charge separation and shift in near-infrared (NIR) regime for a potential application.

2 Molecular models for dye-NC hybrids anchored on TiO₂ surface

The basic concept behind the proposed DSSC system is that light is captured by sensitizer dye-NC hybrid which is coupled to the semiconductor allowing electron injection into its conduction band after which dye is regenerated *via* electrolyte.³⁶ Photovoltaic parameters (light harvesting efficiency, LHE and driving force for electron injection, ΔG^{inject}), defined in the supplement, serve as an indication for the appropriate choice of hybrid sensitizer.

Anthocyanidins as salt derivatives of flavylium cation belong to the group of natural pigments.³⁷ The most common naturally produced anthocyanidins are pelargonidin, cyanidin, delphinidin, peonidin, petunidin, and malvidin^{38,39} (*cf.* Scheme 1). However, they do not contain acceptor-donor subunits. For this purpose, the silver nanoclusters serve to offer one of the needed subunits. Among structures from this family of natural pigments, we have chosen cyanidin to study the interaction with the NCs whose sizes have been selected according to their electronic properties. Structural and optical properties, as well as DSSC parameters of cyanidin-NCs with silver clusters containing 2, 4, 8, and 20 valence electrons, have been compared

| | R ₁ | R ₂ | R ₃ |
|-----------------|----------------|------------------|------------------|
| Pelargonidin | OH | H | H |
| Cyanidin | OH | OH | H |
| Delphinidin | OH | OH | OH |
| Peonidin | OH | OCH ₃ | H |
| Petunidin | OH | OH | OCH ₃ |
| Malvidin | OH | OCH ₃ | OCH ₃ |



Scheme 1 The molecular structure of the six most common anthocyanidin dyes.

with hybrids involving clusters with an odd number of valence electrons. All of them have discrete energy levels and belong to the size regime <2 nm in which each atom counts.³⁰ It is well known that the pure nanoclusters with an even number of electrons are more stable than those with an odd number of electrons.⁴⁰

A TiO₂ semiconductor was used as a surface model to investigate the anchoring of cyanidin-Ag₉ hybrid. Anatase is the most widely used crystal type of TiO₂ for DSSC application since it has a large band gap and conduction band edge energy.⁴⁴ Consequently, the 2-layer anatase model of TiO₂ (100) adapted from Koch *et al.* was selected.^{42,43} The anchoring on the surface was modeled by hydroxyl groups (-OH) through dissociative binding, which is more energetically favorable than the undissociative one.⁴⁴ The link between the cyanidin-Ag₉ hybrid and the surface is established by two titanium-oxygen bonds. In addition, binding over Ag₉ and over both Ag₉ and cyanidin has been also studied. However, the energies of all studied isomers are very close.

3 Computational

The structural and optical properties of cyanidin and cyanidin-NC hybrids have been determined using density functional theory (DFT) and its time-dependent version (TDDFT) in Gaussian 16 program.⁴⁵ The ground state geometries of all systems were optimized with the Perdew-Burke-Ernzerhof (PBE) functional.^{46,47} For cyanidin-NC hybrids, an extensive search for the lowest energy isomer has been carried out using simulated annealing as implemented in TURBOMOLE.⁴⁸ The Coulomb-attenuated version of Becke's three-parameter nonlocal exchange functional together with the Lee-Yang-Parr gradient-corrected correlation functional (CAM-B3LYP)⁴⁹ has been employed to calculate optical properties due to its accurate assessment of silver NCs excitation energies.^{50,51} For all atoms, split valence polarization atomic basis set (SVP) has been used.⁵² For the silver atoms, the 19-e⁻ relativistic effective core potential (19-e⁻ RECP) from the Stuttgart group taking into account scalar relativistic effects has been employed.⁵³ Nonlinear optical properties; TPA spectra and cross sections (σ)⁵⁴ were obtained using either single residue or double residue quadratic response procedure^{55,56} implemented in Dalton electronic structure program^{57,58}

The fragment representing semiconductor TiO₂ contains 30 TiO₂ units saturated with 12 hydrogen atoms forming (TiO₂)₃₀O₆H₁₂. Systems of similar sizes have been already used for such applications.⁵⁹ The considered surface model is {cyanidin-Ag₉}-TiO₂, where TiO₂ fragment is interacting with a cyanidin-Ag₉ hybrid. The complex was optimized within the Gaussian 16 program⁴⁵ using the PBE exchange-correlation functional. The SVP basis set was used for all atoms, with the addition of a 19-e⁻ RECP for Ag atoms.^{52,60} Due to the size of the complex, the density fitting Weigend-06 (W06) was employed with the GGA functional to speed up computations. The calculation of the absorption spectrum was performed at the same level of theory as for the hybrids.



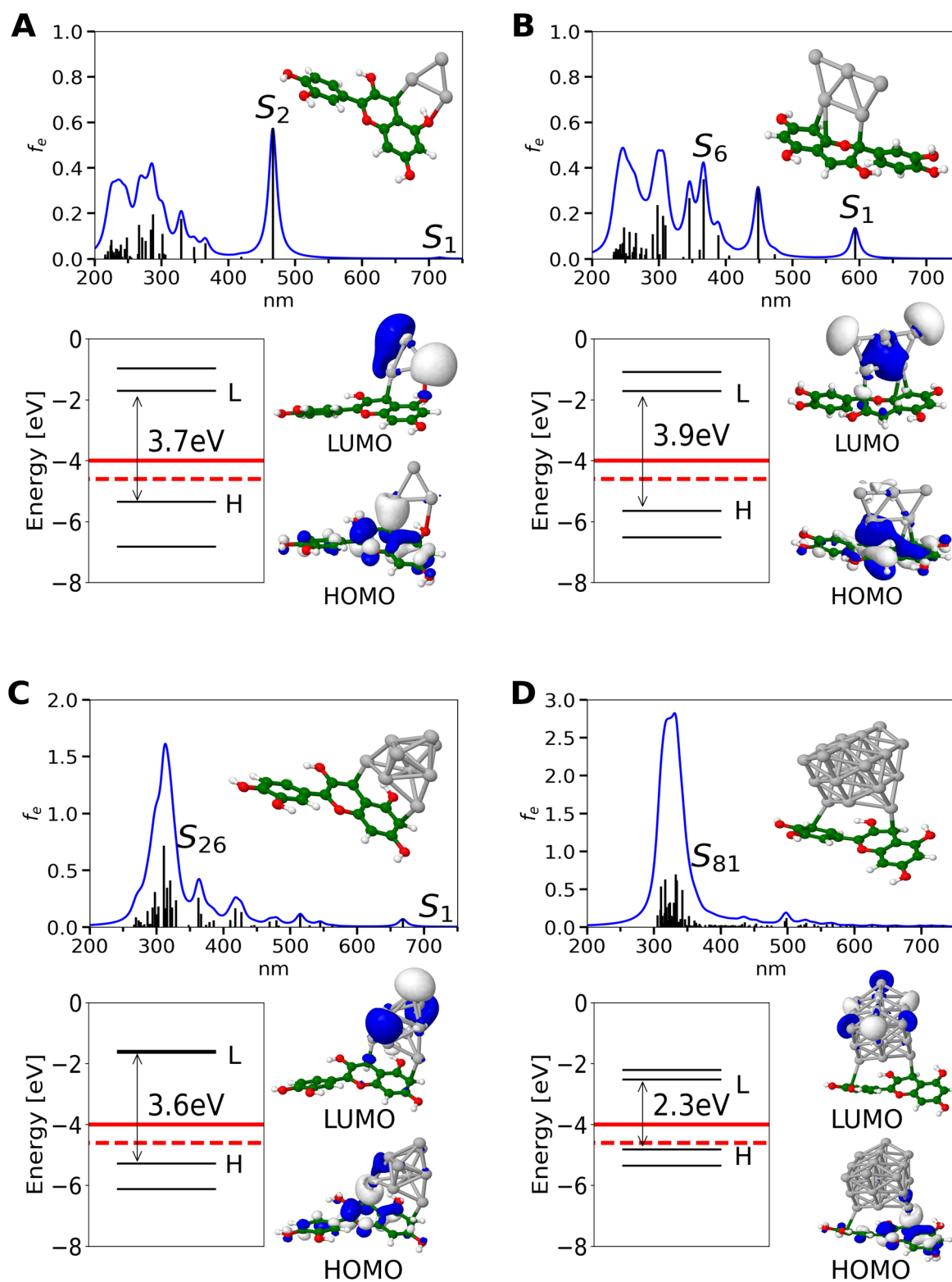
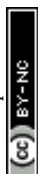


Fig. 1 TDDFT calculated absorption spectra for the: (A) cyanidin-Ag₃, (B) cyanidin-Ag₅, (C) cyanidin-Ag₉ and (D) cyanidin-Ag₂₁ employing CAM-B3LYP/def2-SVP method. For the cyanidin-Ag₂₁ (D), S₁ is located at 1794 nm with zero oscillator strength. Structures have been optimized at PBE/def2-SVP level of theory. DFT HOMO, LUMO, HOMO-1, and LUMO+1 energy gaps versus vacuum [eV] and HOMO-LUMO orbitals. Experimental TiO₂ conduction band edge (full red line) and I⁻/I₃⁻ redox level (dashed red line).



4 Results and discussion

None of the anthocyanidin dyes including selected cyanidin satisfy conditions for photovoltaic parameters needed for DSSC applications (*cf.* Fig. S1†). HOMO and LUMO orbitals of pure anthocyanidin dyes are delocalized over all three aromatic rings as presented by cyanidin creating characteristic bright π - π^* transition (*cf.* Fig. S2†). In order to form bio-nano hybrids as sensitizers for solar cells, adequate HOMO and LUMO energy levels are needed. The HOMO of the dye-NC should be lower than Γ^-/I_3^- redox potential allowing for system regeneration. In addition, to ensure conditions for charge generation the LUMO of the system should be higher than TiO_2 conduction band.³⁶ Both HOMO and LUMO energy levels of the anthocyanidin dyes lie below the electrolyte redox potential and semiconductor conduction band, thus requiring correction which is possible by silver NCs (*cf.* Fig. S1†).

The inclusion of silver NC of the given size and number of valence electrons shifts HOMO and LUMO energy levels to higher values allowing them to satisfy photovoltaic parameters. Absorption spectra for cyanidin- Ag_n ($n = 3, 5, 9, 21$ with 2, 4, 8, 20 valence electrons) together with MO energies as well as values for TiO_2 conduction band edge and Γ^-/I_3^- redox potential are shown in Fig. 1. Notice that the binding energy of NC's to dye is ~ -12 eV (*cf.* Table 1). In contrast, for cyanidin- Ag_n ($n = 6, 12$) with an odd number of valence electrons (5, 11) HOMO, LUMO energy levels lie above TiO_2 conduction band edge and Γ^-/I_3^- redox potential, due to their lower stability (*cf.* Fig. S3† and Table 1).

For dye- Ag_n hybrids containing silver cluster with an even number of valence electrons, the HOMO, LUMO energy levels are shifted in the right direction where HOMO level is lower than electrolyte redox potential and LUMO is higher than the TiO_2 conduction band, making them capable for electron injection and system regeneration (*cf.* Fig. 1). The decrease of the HOMO-LUMO gap with increasing cluster size shifts the absorption band towards the red regime which is suitable for efficiency.⁶¹ Dye- Ag_n ($n = 3, 5, 9, 21$) hybrids containing an even number of valence electrons have much smaller HOMO-LUMO energy gaps (3.9 eV–2.3 eV) in comparison with cyanidin dye (4.8 eV, *cf.* Fig. 1 and Fig. S2†). Furthermore, the HOMO energy level of cyanidin- Ag_9 hybrids remains similar to the cyanidin-

Ag_3 systems, but the HOMO-LUMO gap of the cyanidin- Ag_{21} hybrid is further reduced due to considerably larger cluster size. Overall, the silver NC interacting with the dye sensitizer influences the energy gap in the following manner: cyanidin > cyanidin- Ag_3, Ag_5, Ag_9 , > cyanidin- Ag_{21} . This suggests that the cyanidin- Ag_9 and the cyanidin- Ag_{21} are preferable in the context of DSSC application. From the experimental point of view, in the gas phase, only the charged species (cyanidin- Ag_n)^{+/-} can be identified.

A slight difference in the steric configuration (dihedral angle (θ) and the bond length) of dye-NC hybrids with even and odd numbers of electrons is shown in Fig. S4.† HOMO orbitals of hybrids are delocalized mainly within cyanidin, whereas LUMO orbitals are delocalized within nanoclusters, as shown in Fig. 1. Absorption spectra of hybrids are characterized by two groups of transitions. The first one is ~ 600 nm and below with low intensities and the second one is ~ 300 nm with higher intensities. For the latter one with a higher intensity, clusters with

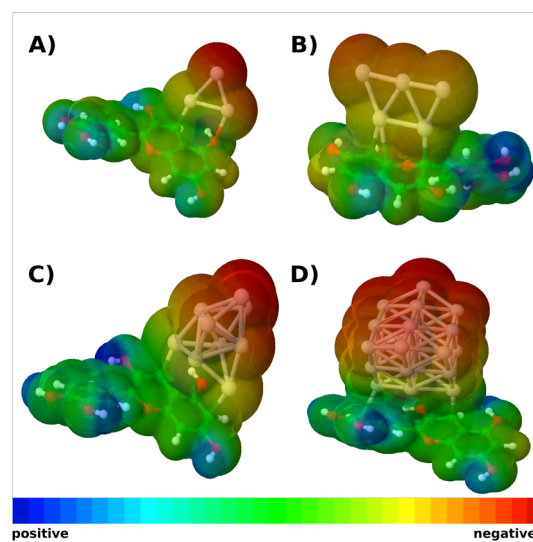


Fig. 2 Molecular electrostatic potential surface for (A) cyanidin- Ag_3 , (B) cyanidin- Ag_5 , (C) cyanidin- Ag_9 and (D) cyanidin- Ag_{21} . The red region represents the electron-rich area centered around the acceptor (NC) and the blue represents the electron-poor area corresponding to the donor (cyanidin).

Table 1 Calculated wavelengths (λ) and oscillator strengths (f_o) of maximum absorption, -HOMO, LHE, ΔG^{inject} and binding energies E_b (defined in the supplement) for cyanidin dye and cyanidin-NCs at CAM-B3LYP/def2-SVP level of theory. Cyanidin- Ag_n ($n = 3, 5, 9, 21$) hybrids with an even number of valence electrons are listed in part I of the table, and cyanidin- Ag_n ($n = 6, 12$) with an odd number of valence electrons are listed in part II. Plus and minus signs represent cations and anions, respectively

| | | S_{max} | λ_{max} [nm] | $f_{e_{\text{max}}}$ | -HOMO [eV] | LHE | ΔG^{inject} [eV] | E_b [eV] |
|----|-------------------------------------|------------------|--------------------------------|----------------------|------------|------|---------------------------------|------------|
| I | Cyanidin ⁺ | S ₁ | 459 | 0.60 | 10.52 | 0.75 | 3.815 | |
| | Cyanidin- Ag_3 | S ₂ | 467 | 0.57 | 5.35 | 0.73 | -1.304 | -12.45 |
| | Cyanidin- Ag_5 | S ₆ | 367 | 0.34 | 5.65 | 0.55 | -1.730 | -12.56 |
| | Cyanidin- Ag_9 | S ₂₆ | 311 | 0.71 | 5.28 | 0.80 | -2.706 | -11.73 |
| | Cyanidin- Ag_{21} | S ₈₁ | 332 | 0.68 | 4.82 | 0.79 | -2.908 | -11.07 |
| II | (Cyanidin- Ag_6) ⁻ | S ₁₀ | 393 | 0.49 | 2.47 | 0.68 | -4.683 | -8.26 |
| | (Cyanidin- Ag_{12}) ⁻ | S ₃₀ | 360 | 0.68 | 2.69 | 0.79 | -4.750 | -8.97 |



a given number of valence electrons are responsible. This is illustrated in Fig. S5† in which absorption spectra obtained for pure cationic clusters with an even number of electrons are shown. Cluster structures have been taken from optimized hybrids. In fact, donor–acceptor properties of cyanidin-NCs are illustrated in molecular electrostatic potential surfaces (*cf.* Fig. 2), where clusters correspond to acceptors and cyanidin to donors.

In this contribution, two photon absorption (TPA) of cyanidin and cyanidin-Ag₉ is also presented (*cf.* Fig. S6†). The addition of Ag₉ cluster to cyanidin dye produces a large cross section only in near-infrared due to the resonance of OPA S₁ and TPA S₃₄ state. MOs presented for the S₃₄ state demonstrate the donor–acceptor nature of the cyanidin-Ag₉ system indicating charge transfer between cyanidin and Ag₉ NC. This increases transition dipole moments causing the enhancement of TPA cross sections. The enlarged NIR region of calculated TPA spectra is shown also in Fig. S6†. For cyanidin-Ag₉ cross sections are several orders of magnitude larger compared to cyanidin dye which extends the TPA spectrum in the near-infrared range (notice the σ values for 600–1100 nm). Investigation of the nonlinear optical properties is needed for the evaluation of the solar cells since their enhancement is connected with better photovoltaic performance.^{62,63}

A design of novel materials with desirable linear and nonlinear optical properties can induce in solar cells a better harvesting of photons in the visible and near-infrared region.

Photovoltaic parameters such as LHE and ΔG^{inject} are important for influencing incident photon to the conversion efficiency (IPCE) of the solar cell. LHE of the sensitizer is directly connected with the oscillator strength of absorption maximum.

The increasing size of the NC enhances the intensity of the absorption spectra of the hybrids in a region ~ 300 nm consisting of multiple transitions with similar intensities. In contrast, the maximum absorption of cyanidin dye is characterized by a single transition. For this reason, regardless of hybrids having larger absorption intensity, LHE values of both cyanidin dye and hybrids remain similar (*cf.* Table 1). Cyanidin dye has the LUMO below the TiO₂ conduction band which is

reflected in the positive value of the ΔG^{inject} , and the low possibility of the electron injection. In contrast, the interaction with the small silver NC containing an even number of electrons shifts the HOMO and LUMO energy levels matching the TiO₂ conduction band and I⁻/I₃⁻ redox potential. This produces negative values of the ΔG^{inject} favoring spontaneous electron injection from the excited state of the sensitizer to the semiconductor conduction band. The trend for the lowering ΔG^{inject} is further supported by the increased size of the nanocluster.

Anchoring of cyanidin-Ag₉ on TiO₂ semiconductor has been investigated due to the importance of the efficient charge transfer from the sensitizer to the semiconductor. The details of the model system are described in the Sections 2 and 3.

The isomers bound to surface over silver cluster have very low oscillator strengths (*cf.* Fig. S7A and B†). Therefore, we have selected the isomer bound over cyanidin which exhibits stronger interaction (*cf.* Fig. 3A). The structure of selected cyanidin-Ag₉ forms two covalent bonds with the TiO₂ model, which results in the adsorption energy (E_{ads} , defined in the supplement) of the hybrid by -2.1 eV. The calculation of the binding energy of cyanidin to TiO₂ has a similar value (-2.13 eV). This ensures the formation of the complex necessary for the electron injection from the hybrid cyanidin-Ag₉ to the semiconductor.

The calculated absorption spectrum of the cyanidin-Ag₉ anchored on TiO₂ reveals a bathochromic shift (*cf.* Fig. 3A) compared to the spectrum of the cyanidin-Ag₉. It also reveals two distinct regions, one ~ 500 nm and the other one ~ 700 nm. Both regions consist of transitions with low intensities. The HOMO of the anchored hybrid is delocalized on the cyanidin and two silver atoms. Also, it is energetically close to the HOMO of the hybrid without support. In contrast, the LUMO is entirely delocalized on the TiO₂ model, as reported previously.⁶⁴ The HOMO and LUMO orbitals (*cf.* Fig. 3B) along with the analysis of transitions corresponding to the largest absorption peaks (*cf.* Table S1 and Fig. S8†) demonstrate charge separation between the hybrid and TiO₂ semiconductor which is a prerequisite for efficient DSSC performance. Altogether, the hybrid cyanidin-Ag₉ anchored on the TiO₂ surface serves as a model for stabilization of the bio-nano hybrid at the semiconductor surface.

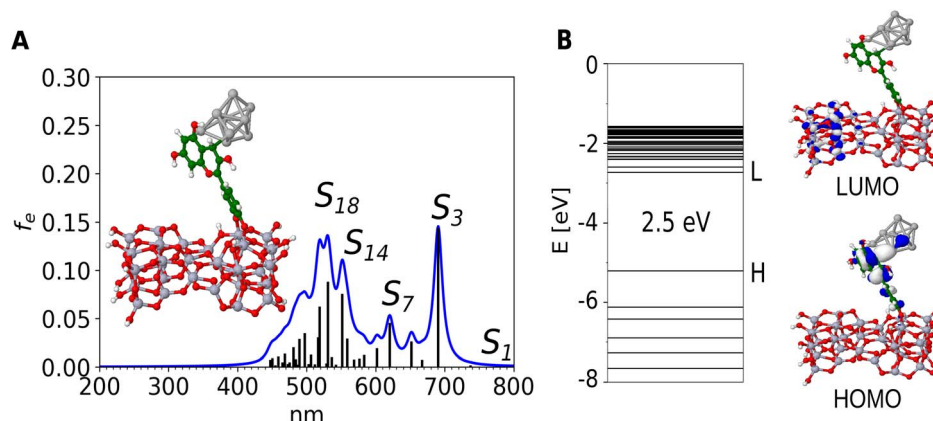
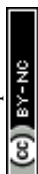


Fig. 3 (A) TDDFT calculated absorption spectrum at CAM-B3LYP/def2-SVP level of theory for {cyanidin-Ag₉}-TiO₂ with a structure optimized with PBE/def2-SVP/W06, (B) HOMO is delocalized at bio-nano hybrid, while LUMO at the surface model.



5 Conclusion

Theoretical investigation of optical properties of model systems including the direct estimate of photovoltaic parameters is an important step in the context of improvement of DSSC performance. In the present paper, we have proposed bio-nano donor-acceptor hybrids as photosensitizers for DSSC application. These systems are formed by the interaction of silver NCs with the most common anthocyanidin dyes represented by cyanidin. The proposed strategy is based on a simple concept of bringing together natural dye and silver metal nanoclusters to form a donor-acceptor hybrid. The hybrids containing NC with an even number of valence electrons are more stable than those with an odd number of valence electrons. Therefore, NCs of selected sizes (with 2, 4, 8, 20 valence electrons) play a key role for the optical properties of cyanidin-NC hybrids as well as for determining photovoltaic parameters. In contrast to pure anthocyanidin dyes, bio-nano hybrids reveal the improvement of the overall efficiency (cf. LHE and ΔG^{inject}). The interaction of the hybrid with TiO₂ semiconductor model confirms the stability of the bio-nano system.

We have demonstrated that silver NCs due to their unique electronic and optical properties introduce acceptor subunits interacting with natural pigments as donors. In summary, these findings serve to stimulate experimental investigation of optical and photovoltaic properties of bio-nano hybrids at TiO₂ support, in order to realize novel materials at the nanoscale to improve DSSC's efficiency.

Conflicts of interest

There are no conflicts to declare.

Acknowledgements

This research was supported by the project STIM – REI, Contract Number: KK.01.1.1.01.0003, funded by the European Union through the European Regional Development Fund – the Operational Programme Competitiveness and Cohesion 2014–2020 (KK.01.1.1.01). M. B. M., A. M. and M. P. B. acknowledge computational facilities of the HPC computer within the STIM-REI project, Doctoral study of Biophysics at the University of Split, as well as thank Professor Miroslav Radman at MedILS and Split-Dalmatia County. Also, the authors would like to thank Dr Rodolphe Antoine for his helpful comments.

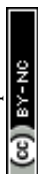
Notes and references

- 1 B. O'Regan and M. Grätzel, *Nature*, 1991, **353**, 737–740.
- 2 M. Grätzel, *Nature*, 2001, **414**, 338–344.
- 3 M. Grätzel, *J. Photochem. Photobiol., C*, 2003, **4**, 145–153.
- 4 A. Hagfeldt, G. Boschloo, L. Sun, L. Kloo and H. Pettersson, *Chem. Rev.*, 2010, **110**, 6595–6663.
- 5 V. Sugathan, E. John and K. Sudhakar, *Renewable Sustainable Energy Rev.*, 2015, **52**, 54–64.
- 6 K. Sharma, V. Sharma and S. Sharma, *Nanoscale Res. Lett.*, 2018, **13**, 1–46.

- 7 F. De Angelis, S. Fantacci and A. Sgamellotti, *Theor. Chem. Acc.*, 2007, **117**, 1093–1104.
- 8 M. Pastore, E. Mosconi, S. Fantacci and F. De Angelis, *Curr. Org. Synth.*, 2012, **9**, 215–232.
- 9 N. Tomar, A. Agrawal, V. S. Dhaka and P. K. Surolia, *Sol. Energy*, 2020, **207**, 59–76.
- 10 A. Kay and M. Grätzel, *J. Phys. Chem.*, 1993, **97**, 6272–6277.
- 11 H. Hug, M. Bader, P. Mair and T. Glatzel, *Appl. Energy*, 2014, **115**, 216–225.
- 12 N. Mariotti, M. Bonomo, L. Fagioliari, N. Barbero, C. Gerbaldi, F. Bella and C. Barolo, *Green Chem.*, 2020, **22**, 7168–7218.
- 13 S. Ito, *Solar Cells-Dye-Sensitized Devices*, 2011, pp. 19–48.
- 14 G. Richhariya, A. Kumar, P. Tekasakul and B. Gupta, *Renewable Sustainable Energy Rev.*, 2017, **69**, 705–718.
- 15 A. Carella, F. Borbone and R. Centore, *Front. Chem.*, 2018, **6**, 2296–2646.
- 16 J.-H. Yum, I. Jung, C. Baik, J. Ko, M. K. Nazeeruddin and M. Grätzel, *Energy Environ. Sci.*, 2009, **2**, 100–102.
- 17 I. M. Abdellah, A. I. Koraiem and A. El-Shafei, *Sol. Energy*, 2019, **177**, 642–651.
- 18 J. Lu, S. Liu and M. Wang, *Front. Chem.*, 2018, **6**, 541.
- 19 Z. Yao, M. Zhang, H. Wu, L. Yang, R. Li and P. Wang, *J. Am. Chem. Soc.*, 2015, **137**, 3799–3802.
- 20 J. Harborne, *Biochem.*, 1958, **70**, 22.
- 21 K. Tennakone, A. Kumarasinghe, G. Kumara, K. Wijayantha and P. Sirimanne, *J. Photochem. Photobiol., A*, 1997, **108**, 193–195.
- 22 S. Hao, J. Wu, Y. Huang and J. Lin, *Sol. Energy*, 2006, **80**, 209–214.
- 23 I. C. Maurya, A. K. Gupta, P. Srivastava and L. Bahadur, *J. Sol. Energy Eng.*, 2016, **138**, 051006.
- 24 J. Fleschhut, F. Kratzer, G. Rechkemmer and S. Kulling, *Eur. J. Nutr.*, 2006, **51**, 1461–1471.
- 25 R. Ramamoorthy, N. Radha, G. Maheswari, S. Anandan, S. Manoharan and R. V. Williams, *J. Appl. Electrochem.*, 2016, **46**, 929–941.
- 26 E. C. Prima, A. Nuruddin, B. Yulianto, G. Kawamura and A. Matsuda, *New J. Chem.*, 2018, **42**, 11616–11628.
- 27 D. D. Pratiwi, F. Nurosyid, A. Supriyanto and R. Suryana, *IOP Conf. Ser.: Mater. Sci. Eng.*, 2017, **176**, 012012.
- 28 N. Kumara, P. Ekanayake, A. Lim, L. Y. C. Liew, M. Iskandar, L. C. Ming and G. Senadeera, *J. Alloys Compd.*, 2013, **581**, 186–191.
- 29 A. Purwoko, V. Setiawati and S. Hadisaputra, *IOP Conf. Ser.: Mater. Sci. Eng.*, 2019, **509**, 012130.
- 30 V. Bonačić-Koutecký, A. Kulesza, L. Gell, R. Mitrić, R. Antoine, F. Bertorelle, R. Hamouda, D. Rayane, M. Broyer, T. Tabarin and P. Dugourd, *Phys. Chem. Chem. Phys.*, 2012, **14**, 9282–9290.
- 31 M. S. Kim, M. A. Abbas and J. H. Bang, *Bull. Korean Chem. Soc.*, 2016, **37**, 791–792.
- 32 M. A. Abbas, T.-Y. Kim, S. U. Lee, Y. S. Kang and J. H. Bang, *J. Am. Chem. Soc.*, 2016, **138**, 390–401.
- 33 S. Sreeja and B. Pesala, *Sci. Rep.*, 2020, **10**, 1–17.
- 34 N. Bakr, A. Ali and S. Jassim, *J. Adv. Phys.*, 2017, **6**, 370–374.



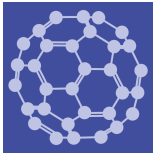
- 35 W.-C. Chen, S. Nachimuthu and J.-C. Jiang, *Sci. Rep.*, 2017, **7**, 1–13.
- 36 W. Fan, D. Tan and W.-Q. Deng, *ChemPhysChem*, 2012, **13**, 2051–2060.
- 37 S. C. Moldoveanu, *Pyrolysis of Organic Molecules*, Elsevier, 2nd edn, 2019, pp. 715–762.
- 38 F. J. Francis, *Crit. Rev. Food. Sci. Nutr.*, 1989, **28**, 273–314.
- 39 J.-M. Kong, L.-S. Chia, N.-K. Goh, T.-F. Chia and R. Brouillard, *Phytochemistry*, 2003, **64**, 923–933.
- 40 V. Bonačić-Koutecky, L. Češpiva, P. Fantucci and J. Koutecky, *J. Chem. Phys.*, 1993, **98**, 7981–7994.
- 41 N. Martsinovich, D. R. Jones and A. Troisi, *J. Phys. Chem. C*, 2010, **114**, 22659–22670.
- 42 R. Koch, A. S. Lipton, S. Filipek and V. Renugopalakrishnan, *J. Mol. Model.*, 2011, **17**, 1467–1472.
- 43 E. Marcano, *Energy Harvest. Syst.*, 2018, **5**, 29–38.
- 44 F. De Angelis, S. Fantacci, A. Selloni, M. Grätzel and M. K. Nazeeruddin, *Nano Lett.*, 2007, **7**, 3189–3195.
- 45 M. J. Frisch, G. W. Trucks, H. B. Schlegel, G. E. Scuseria, M. A. Robb, J. R. Cheeseman, G. Scalmani, V. Barone, G. A. Petersson, H. Nakatsuji, X. Li, M. Caricato, A. V. Marenich, J. Bloino, B. G. Janesko, R. Gomperts, B. Mennucci, H. P. Hratchian, J. V. Ortiz, A. F. Izmaylov, J. L. Sonnenberg, D. Williams-Young, F. Ding, F. Lipparini, F. Egidi, J. Goings, B. Peng, A. Petrone, T. Henderson, D. Ranasinghe, V. G. Zakrzewski, J. Gao, N. Rega, G. Zheng, W. Liang, M. Hada, M. Ehara, K. Toyota, R. Fukuda, J. Hasegawa, M. Ishida, T. Nakajima, Y. Honda, O. Kitao, H. Nakai, T. Vreven, K. Throssell, J. A. Montgomery Jr., J. E. Peralta, F. Ogliaro, M. J. Bearpark, J. J. Heyd, E. N. Brothers, K. N. Kudin, V. N. Staroverov, T. A. Keith, R. Kobayashi, J. Normand, K. Raghavachari, A. P. Rendell, J. C. Burant, S. S. Iyengar, J. Tomasi, M. Cossi, J. M. Millam, M. Klene, C. Adamo, R. Cammi, J. W. Ochterski, R. L. Martin, K. Morokuma, O. Farkas, J. B. Foresman and D. J. Fox, *Gaussian 16 Revision A.03*, Gaussian Inc, Wallingford CT, 2016.
- 46 J. P. Perdew, K. Burke and M. Ernzerhof, *Phys. Rev. Lett.*, 1996, **77**, 3865–3868.
- 47 J. P. Perdew, K. Burke and M. Ernzerhof, *Phys. Rev. Lett.*, 1997, **78**, 1396.
- 48 *TURBOMOLE V7.5 2020, A Development of University of Karlsruhe and Forschungszentrum Karlsruhe GmbH, 1989–2007, TURBOMOLE GmbH, since 2007, available from <http://www.turbomole.com>.*
- 49 T. Yanai, D. Tew and N. Handy, *Chem. Phys. Lett.*, 2004, **393**, 51–57.
- 50 F. Rabilloud, *J. Phys. Chem. A*, 2013, **117**, 4267–4278.
- 51 B. Anak, M. Bencharif and F. Rabilloud, *RSC Adv.*, 2014, **4**, 13001–13011.
- 52 F. Weigend, *Phys. Chem. Chem. Phys.*, 2006, **8**, 1057–1065.
- 53 D. Andrae, U. Häußermann, M. Dolg, H. Stoll and H. Preuß, *Theor. Chim. Acta*, 1990, **77**, 123–141.
- 54 L. Frediani, Z. Rinkevicius and H. Ågren, *J. Chem. Phys.*, 2005, **122**, 244104.
- 55 N. H. List, R. Zalesny, N. A. Murugan, J. Kongsted, W. Bartkowiak and H. Ågren, *J. Chem. Theory Comput.*, 2015, **11**, 4182–4188.
- 56 P. Norman, *Phys. Chem. Chem. Phys.*, 2011, **13**, 20519–20535.
- 57 *Dalton, A Molecular Electronic Structure Program, Release Dalton2020.alpha*, 2020, <http://daltonprogram.org>.
- 58 K. Aidas, C. Angeli, K. L. Bak, V. Bakken, R. Bast, L. Boman, O. Christiansen, R. Cimiraglia, S. Coriani, P. Dahle, E. K. Dalskov, U. Ekström, T. Enevoldsen, J. J. Eriksen, P. Ettenhuber, B. Fernández, L. Ferrighi, H. Fliegl, L. Frediani, K. Hald, A. Halkier, C. Hättig, H. Heiberg, T. Helgaker, A. C. Hennum, H. Hettema, E. Hjertenæs, S. Høst, I.-M. Høyvik, M. F. Iozzi, B. Jansík, H. J. A. Jensen, D. Jonsson, P. Jørgensen, J. Kauczor, S. Kirpekar, T. Kjærgaard, W. Klopper, S. Knecht, R. Kobayashi, H. Koch, J. Kongsted, A. Krapp, K. Kristensen, A. Ligabue, O. B. Lutnæs, J. I. Melo, K. V. Mikkelsen, R. H. Myhre, C. Neiss, C. B. Nielsen, P. Norman, J. Olsen, J. M. H. Olsen, A. Osted, M. J. Packer, F. Pawłowski, T. B. Pedersen, P. F. Provasi, S. Reine, Z. Rinkevicius, T. A. Ruden, K. Ruud, V. V. Rybkin, P. Sałek, C. C. M. Samson, A. S. de Merás, T. Saue, S. P. A. Sauer, B. Schimmelpfennig, K. Snegov, A. H. Steindal, K. O. Sylvester-Hvid, P. R. Taylor, A. M. Teale, E. I. Tellgren, D. P. Tew, A. J. Thorvaldsen, L. Thøgersen, O. Vahtras, M. A. Watson, D. J. D. Wilson, M. Ziolkowski and H. Ågren, *WIREs Comput. Mol. Sci.*, 2014, **4**, 269–284.
- 59 M. J. Lundqvist, M. Nilsing, P. Persson and S. Lunell, *Int. J. Quantum Chem.*, 2006, **106**, 3214–3234.
- 60 F. Weigend and R. Ahlrichs, *Phys. Chem. Chem. Phys.*, 2005, **7**, 3297–3305.
- 61 R. Ma, P. Guo, H. Cui, X. Zhang, M. K. Nazeeruddin and M. Grätzel, *J. Phys. Chem. A*, 2009, **113**, 10119–10124.
- 62 A. Guillén-López, C. Delesma, C. Amador-Bedolla, M. Robles and J. Muñiz, *Theor. Chem. Acc.*, 2018, **137**, 1–15.
- 63 Z. Hu, V. Khadka, W. Wang, D. Galipeau and X. Yan, *J. Mol. Model.*, 2012, **18**, 3657–3667.
- 64 J. K. Roy, S. Kar and J. Leszczynski, *J. Phys. Chem. C*, 2019, **123**, 3309–3320.



2.2 Coinage metal doping of cyanidin-silver trimer hybrids

Reprinted from:

Margarita Bužančić Milosavljević, Martina Perić Bakulić, Željka Sanader Maršić, Antonija Mravak and Vlasta Bonačić-Koutecký. Enhancing efficiency of dye sensitized solar cells by coinage metal doping of cyanidin-silver trimer hybrids at TiO₂ support based on theoretical study. *Nanomaterials*, 14, 1034, 2024. Reproduced with permission from the Multidisciplinary Digital Publishing Institute.



Article

Enhancing Efficiency of Dye Sensitized Solar Cells by Coinage Metal Doping of Cyanidin-Silver Trimer Hybrids at TiO₂ Support Based on Theoretical Study

Margarita Bužančić Milosavljević, Martina Perić Bakulić, Željka Sanader Maršić, Antonija Mravak and Vlasta Bonačić-Koutecký

Special Issue




Advanced Studies in Bionanomaterials

Edited by
Prof. Dr. Marta Marmiroli



Article

Enhancing Efficiency of Dye Sensitized Solar Cells by Coinage Metal Doping of Cyanidin-Silver Trimer Hybrids at TiO₂ Support Based on Theoretical Study

Margarita Bužančić Milosavljević ¹, Martina Perić Bakulić ², Željka Sanader Maršić ³, Antonija Mravak ^{3,*}
and Vlasta Bonačić-Koutecký ^{1,4,5,*}

¹ Center of Excellence for Science and Technology-Integration of Mediterranean Region (STIM), Faculty of Science, University of Split, Ruđera Boškovića 33, 21000 Split, Croatia; margarita@stim.unist.hr

² Faculty of Chemistry and Technology, University of Split, Ruđera Boškovića 35, 21000 Split, Croatia; martina.peric-bakulic@ktf-split.hr

³ Faculty of Science, University of Split, Ruđera Boškovića 33, 21000 Split, Croatia; zsm@pmfst.hr

⁴ Interdisciplinary Center for Advanced Science and Technology (ICAST), University of Split, Meštrovićevo Šetalište 45, 21000 Split, Croatia

⁵ Department of Chemistry, Humboldt Universität zu Berlin, Brook-Taylor-Strasse 2, 12489 Berlin, Germany

* Correspondence: amravak@pmfst.hr (A.M.); vbk@cms.hu-berlin.de (V.B.-K.)

Abstract: Identification of a natural-based sensitizer with optimal stability and efficiency for dye-sensitized solar cell (DSSC) application remains a challenging task. Previously, we proposed a new class of sensitizers based on bio-nano hybrids. These systems composed of natural cyanidin dyes interacting with silver nanoclusters (NCs) have demonstrated enhanced opto-electronic and photovoltaic properties. In this study, we explore the doping of silver nanocluster within a cyanidin-Ag₃ hybrid employing Density Functional Theory (DFT) and its time-dependent counterpart (TDDFT). Specifically, we investigate the influence of coinage metal atoms (Au and Cu) on the properties of the cyanidin-Ag₃ system. Our findings suggest that cyanidin-Ag₂Au and cyanidin-AgAuCu emerge as the most promising candidates for improved light harvesting efficiency, increased two-photon absorption, and strong coupling to the TiO₂ surface. These theoretical predictions suggest the viability of replacing larger silver NCs with heterometallic trimers such as Ag₂Au or AgAuCu, presenting new avenues for utilizing bio-nano hybrids at the surface for DSSC application.

Keywords: bio-nano sensitizer; cyanidin-NC hybrid; DFT; TDDFT; light harvesting efficiency; coinage metal atoms



Citation: Bužančić Milosavljević, M.; Perić Bakulić, M.; Sanader Maršić, Ž.; Mravak, A.; Bonačić-Koutecký, V. Enhancing Efficiency of Dye Sensitized Solar Cells by Coinage Metal Doping of Cyanidin-Silver Trimer Hybrids at TiO₂ Support Based on Theoretical Study. *Nanomaterials* **2024**, *14*, 1034. <https://doi.org/10.3390/nano14121034>

Academic Editor: Marta Marmiroli

Received: 24 May 2024

Revised: 10 June 2024

Accepted: 14 June 2024

Published: 15 June 2024



Copyright: © 2024 by the authors. Licensee MDPI, Basel, Switzerland. This article is an open access article distributed under the terms and conditions of the Creative Commons Attribution (CC BY) license (<https://creativecommons.org/licenses/by/4.0/>).

1. Introduction

The energy demand rises with increasing the global population and technological advancement [1,2]. The sun, an easily attainable, clean, renewable, and free energy resource, emerges as the optimal choice for generating sustainable energy. Consequently, solar harvesting technology holds the potential to supplant conventional energy sources [2,3]. According to the EU Market Outlook (2023), photovoltaic (PV) technology represents the fastest-growing energy production in European Union, with installed PV capacity increasing by more than 40% annually in recent years [4]. Additionally, there is an emphasis on advancing architecture-integrated photovoltaics to maximize solar harvesting efficiency. This involves integrating PV into smart buildings and surroundings to improve efficiency and achieve net-zero energy consumption [2,5]. Dye-sensitized solar cells (DSSCs) play an important role in the field of renewable energy by offering a promising solution, as a thin layered, flexible, and cost-effective technology. DSSCs were first proposed by O'Regan and Grätzel [6–8] as photochemical solar cells that imitate natural light absorption [9]. The fundamental idea behind DSSC lies in the interaction between dye and semiconductor, where dye absorbs light and sensitizes the transparent TiO₂ semiconductor film. This

allows electrons to be injected into the semiconductor's conduction band, followed by regeneration of the dye through the electrolyte [10]. One of their key components is the dye sensitizer, which requires specific properties for efficient performance in DSSC. This includes high light harvesting efficiency (*LHE*) and suitable energy levels of the highest occupied (HOMO) and the lowest unoccupied (LUMO) molecular orbitals for effective charge transfer processes. Furthermore, it requires photostability and compatibility with other solar cell components, particularly anchoring to the semiconductor film [11]. In general, dye sensitizers can be classified [12] as organic [13,14], inorganic [15], metal-free organic dyes [16], and transition metal complexes [17]. Due to their non-toxicity, availability, and cost-effectiveness, natural dyes such as anthocyanidins [18] are an environmentally acceptable alternative to predominantly used Ru-based dyes [14,19–21]. However, the low efficiency of natural dyes limits their effectiveness [22], thus reducing overall DSSC performance. In response, various hybrid modifications of natural dyes have been researched so far [23–27].

In that context, we have previously computationally explored a new class of bio-nano sensitizers based on noble metal nanoclusters (NCs) interacting with natural (anthocyanidin) dyes [28]. In these bio-nano hybrid systems, nanoclusters introduce donor-acceptor properties shifting the HOMO and LUMO molecular orbitals in the desired direction, thus satisfying preconditions for successful electron injection and system regeneration [29]. The interaction between the excited states of nanoclusters and the excited π - π^* states of aromatic rings in biomolecules enhances the absorption intensity within the bio-nano hybrid [30]. Consequently, combined DFT/TDDFT study has demonstrated improvements in photovoltaic properties, such as light harvesting efficiency (*LHE*) and driving force of electron injection (ΔG^{inject}), together with strong coupling to the TiO₂ surface [28]. Among the examined bio-nano hybrids, those including Ag NCs with an even number of electrons ($n = 2, 4, 8, 20$) have demonstrated better stability, with cyanidin-(Ag₉⁺) and cyanidin-(Ag₂₁⁺) emerging as the most preferable model sensitizers.

Previously, DSSC efficiency has been enhanced through doping of nanostructured TiO₂ by metal ions which induced electrical surface-state modifications [31]. In the present study, we theoretically explore the modification of the electronic and photophysical properties of bio-nano hybrid model sensitizers by hetero-metal atom doping. The justification for this strategy arises from the known potential of doping to tune the geometric and electronic properties of NCs while also improving their stability [32,33]. Specifically, we investigate the effects of substituting a single Ag atom in cyanidin-Ag₃ with a coinage metal atom, such as gold or copper. In addition, to examine trimetallic hybrids, we also study the influence of mixed gold-copper doping. The selection of coinage metal atoms (Au, Cu) is motivated by their electronic configurations similar to that of Ag, leading to a closed shell for all doped systems. While silver atoms have a large s-d energy gap, gold and copper atoms possess significantly smaller s-d energy gaps [34,35]. Consequently, s electrons are crucial for bond formation in Ag clusters in contrast to d electrons in Au and Cu clusters [34]. Moreover, copper is a highly abundant, inexpensive metal and has familiar coordination chemistry [36]. Although gold is more expensive, it is nontoxic and shows promising linear and nonlinear optical properties when used as a dopant in ligated silver NCs [37].

Altogether, first, we elucidate how coinage metal doping influences the properties of hybrid systems. Second, we examine if systems with small doped NCs are viable alternatives to hybrids with larger silver clusters. For the computation of opto-electronic and photovoltaic properties, we adopt Density Functional Theory (DFT) and Time-Dependent Density Functional Theory (TDDFT) approaches. In addition to examining linear optical properties like one-photon absorption (OPA), the nonlinear optical properties, particularly two-photon absorption (TPA) are also investigated. Subsequently, we compare the obtained findings with those obtained from the reference monometallic hybrid system, cyanidin-Ag₃. After the investigation of the doping effect in bio-Ag₃ system, the role of TiO₂ surface has been studied.

2. Computational Methods

The optimized geometry of the cyanidin-Ag₃ was taken from our previous work as a reference model since this is the smallest investigated hybrid system with decent photovoltaic properties [28]. All cyanidin-Ag₂Au and cyanidin-AgAuCu hybrids were optimized with the Perdew–Burke–Ernzerhof (PBE) [38] functional using the Gaussian 16 program [39]. The split valence polarization atomic basis set (SVP) [40] has been used for all atoms. Relativistic effective core potential (19-e⁻ RECP) [41] for silver and gold atoms has been employed. Previous studies on nanocluster-biomolecule hybrids [35] have demonstrated that this method accurately describes bio-nano hybrid systems containing silver, gold, and copper. To determine optical properties, the Coulomb-attenuated version of Becke’s three-parameter nonlocal exchange functional together with the Lee–Yang–Parr gradient-corrected correlation functional (CAM-B3LYP) [42] has been employed together with the same AO basis set. Nonlinear optical properties were obtained using the Dalton program [43,44]. TPA spectra and cross-sections (σ) [45] were calculated applying single residue or double residue quadratic response procedure [46,47].

The binding energy E_b of the doped NC to the cyanidin dye is given by:

$$E_b = E_{\text{cyanidin-NC}_{\text{doped}}} - (E_{\text{cyanidin}} + E_{\text{NC}_{\text{doped}}}) \quad (1)$$

with $E_{\text{cyanidin-NC}_{\text{doped}}}$ representing energy of the optimized doped hybrid, E_{cyanidin} energy of cyanidin, and $E_{\text{NC}_{\text{doped}}}$ energy of the doped trimer.

The photovoltaic properties, such as light harvesting efficiency (LHE) is calculated according to Equation (2):

$$LHE = 1 - 10^{-f} \quad (2)$$

where f represents the oscillator strength of the maximum absorption. In addition, the driving force of electron injection (ΔG^{inject}) is calculated according to Equation (3):

$$\Delta G^{\text{inject}} = (-HOMO - \lambda_{\text{max}}) - ECB \quad (3)$$

where λ_{max} is the maximum absorption energy and ECB experimental conduction band energy of TiO₂ (−4 eV [7,48,49]).

The TiO₂ surface model consisting of 30 TiO₂ units capped with 12 hydrogens has been adopted from our earlier work [28]. The calculation of the structural and optical properties of the TiO₂ model was performed at the same level of theory as for the hybrids, with the addition of W06 density fitting [40,50]. Different adsorption features strongly affect the binding of the hybrid to the surface and as a result, influence the efficacy of charge separation [12,51,52]. For that reason, we have previously modeled different positions of the hybrid relative to the surface and analyzed the electronic and optical properties of those structures [28]. The bio-nano hybrids are strongly anchored to the semiconductor model over cyanidin, showing significantly greater absorption intensities compared to other adsorption characteristics. Consequently, the modeling of the doped bio-nano hybrids’ anchoring to the semiconductor was carried out using the cyanidin dye. Adsorption energy E_{ads} to TiO₂ is given by:

$$E_{\text{ads}} = E_{\text{complex}} - (E_{\text{TiO}_2} + E_{\text{cyanidin-NC}_{\text{doped}}}) \quad (4)$$

where E_{complex} is the energy of the DFT optimized adsorbed hybrid and E_{TiO_2} energy of the TiO₂ model.

3. Results and Discussion

3.1. Structural and Electronic Properties of Cyanidin-Trimer Hybrids

The single Au-doped structures were obtained by substituting one Ag atom at various positions in Ag₃⁺ with a single Au atom, resulting in three different cyanidin-Ag₂Au isomers. Similarly, the single Cu-doped structures were obtained by exchanging one Ag

by one Cu. Additionally, to investigate the effects of mixed Au-Cu doping, cyanidin-AgAuCu systems were examined. Here, the two Ag atoms were simultaneously replaced by one Au and one Cu atom, yielding six possible combinations. During optimization, the two structures reached the same minimum and were consequently considered as one, resulting in five Au-Cu-doped isomers. Figure 1 illustrates the obtained isomers and their corresponding relative energies. Note that Ag_3^+ has a closed shell, so the replacement of one or two Ag atoms by the coinage metal atom (which is in the same periodic group) results in a closed shell system.

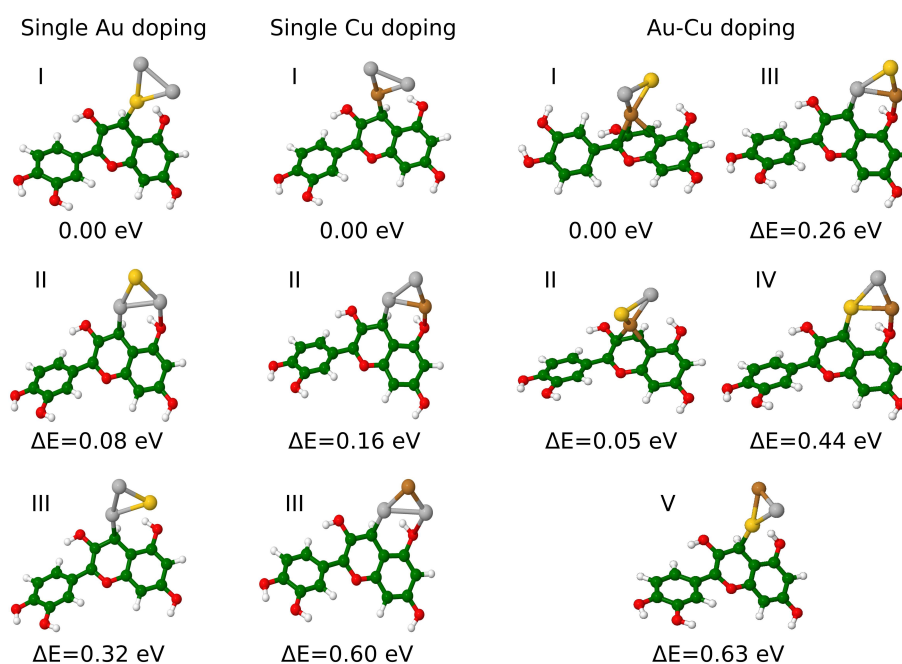


Figure 1. Isomers of cyanidin- Ag_2Au , cyanidin- Ag_2Cu and cyanidin- AgAuCu optimized at PBE/def2-SVP level of theory. Numbers I–V indicate the order of isomers. Ag, Au, Cu, C, O, and H atoms are depicted in grey, yellow, brown, green, red, and white.

An illustration of bonding between the cluster and the cyanidin, as well as the bond length analysis within each doped trimer isomer, is presented in Figure 1 and Table S1, respectively. The lowest energy isomer of cyanidin- Ag_2Au forms a single Au–C bond between the trimer and the dye. By comparison, the lowest energy isomer of Cu-doped systems forms a single Cu–C bond. In contrast, in cyanidin- AgAuCu isomer I, the cluster is bound to the dye through three Cu–C bonds.

This diverse bonding between the trimer and the dye significantly changes the stability of the systems as evident by the energy difference between isomers. Since the doping of Ag_3 generally affects their stability [32], the binding energies (E_b) of the doped trimer bound to the cyanidin dye have also been calculated (Table 1) and compared to E_b of cyanidin- Ag_3 (−12.45 eV) [28]. Overall, the binding energies of the doped systems are increased by ~0.2 up to ~1.1 eV, suggesting that the doping with single Au or Cu and mixed Au–Cu significantly enhances the stability of the hybrids. Considering that Ag NCs often suffer from lower stability [32], doping could be an important strategy for the future applicability of bio-nano hybrid systems.

Furthermore, the charge transfer between different atoms within doped trimers plays a key role in their structural and electronic properties [34]. For this purpose, Mulliken charge analysis has been performed, revealing variation in NC/dye charge transfers between different isomers of the same doping group. The sum of the charges on the single Au-doped trimers ranges from −0.19 to 0.07, for Cu-doped trimers from 0.11 to 0.2, and mixed Au–Cu-doped from −0.24 to 0.08 (cf. Table 1). Notably, Au atoms exhibit negative charges

in all Au-doped and mixed Au-Cu-doped systems, consistent with previous findings that Au withdraws electrons from Ag in Au-Ag NCs [34].

Table 1. Binding energies of the doped NCs to the dye and the analysis of Mulliken charges on the doped-NCs within bio-nano hybrid systems. The order of silver atoms (Ag_1 , Ag_2) is chosen starting from Au atoms clockwise.

| Au Doping | | | | | |
|--------------|------------|-------------------|-----------|---------------|---------------|
| | E_b [eV] | Net Trimer Charge | Au Charge | Ag_1 Charge | Ag_2 Charge |
| Isomer I | −12.95 | 0.02 | −0.20 | 0.09 | 0.13 |
| Isomer II | −12.87 | 0.07 | −0.07 | 0.15 | −0.01 |
| Isomer III | −12.63 | −0.19 | −0.28 | 0.05 | 0.04 |
| Cu Doping | | | | | |
| | E_b [eV] | Net Trimer Charge | Cu Charge | Ag_1 Charge | Ag_2 Charge |
| Isomer I | −12.77 | 0.20 | 0.17 | 0.01 | 0.02 |
| Isomer II | −12.61 | 0.11 | 0.20 | −0.03 | −0.06 |
| Isomer III | −12.17 | 0.12 | 0.09 | 0.09 | −0.06 |
| Au-Cu Doping | | | | | |
| | E_b [eV] | Net Trimer Charge | Au Charge | Cu Charge | Ag Charge |
| Isomer I | −13.56 | −0.24 | −0.22 | −0.07 | 0.05 |
| Isomer II | −13.50 | −0.06 | −0.21 | 0.15 | −0.001 |
| Isomer III | −13.29 | 0.08 | −0.13 | 0.22 | −0.01 |
| Isomer IV | −13.12 | 0.02 | −0.10 | 0.20 | −0.08 |
| Isomer V | −12.92 | 0.02 | −0.17 | 0.21 | −0.02 |

3.2. Linear Optical and Photovoltaic Properties of Cyanidin-Trimer Hybrids

Appropriate positioning of the HOMO and LUMO levels is crucial to meet the prerequisites for successful electron injection and system regeneration [10]. Our previous study on bio-nano hybrids has demonstrated that the addition of Ag NCs to anthocyanidin dyes effectively shifts the HOMO and LUMO levels in the desired direction [28]. Accordingly, analysis of HOMO and LUMO levels shows that all of the doped isomers have favorably positioned HOMO and LUMO levels. HOMO is lying below I^-/I_3^- redox potential (−4.6 eV [53] vs. vacuum) and LUMO above TiO_2 conduction band, thus satisfying the requirement for an efficient sensitizer. The HOMO, LUMO values, maximum absorptions, and the key photovoltaic properties are listed in Table 2.

Due to a connection between the strong and broad sensitizer absorption in visible and near-infrared (NIR) and the photocurrent generation [10], we have examined the UV-VIS spectra for all modeled systems. Figures S1–S3 provide orbital analysis and comparison of the absorption spectrum of cyanidin- Ag_3 with those of isomers within the Au, Cu, and Au-Cu doping groups, respectively.

Generally, absorption spectra of the doped hybrids exhibit characteristic features similar to the hybrid with monometallic Ag NC. Specifically, two distinct transition regions can be observed, one around 300 and the second around 500 nm. For all systems, the first peak characterized by very low intensity corresponds to the HOMO \rightarrow LUMO transition. Orbital analysis of the doped model systems reveals that the HOMO is predominantly delocalized over cyanidin and one trimer atom directly connected to the carbon atom of the dye (cf. Figures S1 and S2). By comparison, the doped systems containing Au bound to the dye through a single bond exhibit delocalization over the entire structure, including both the trimer and the dye (cf. Figure 2a,c). In contrast, the LUMO is delocalized only on the trimer. The strongest transition is S_2 for most of the isomers, representing the HOMO \rightarrow LUMO + 1 transition. The latter orbital is delocalized over the trimer and the area around its connection with the dye.

Table 2. Calculated HOMO, LUMO levels, wavelengths (λ_{max}) and oscillator strengths (f_e) of maximum absorption, LHE , ΔG^{inject} and HOMO-LUMO gaps at CAM-B3LYP/def2-SVP level of theory.

| | HOMO [eV] | LUMO [eV] | λ_{max} [nm] | f_e | LHE | ΔG^{inject} [eV] | HOMO-LUMO |
|---------------------------------|-----------|-----------|----------------------|-------|-------|--------------------------|-----------|
| cyanidin-Ag ₃ * | −5.35 | −1.65 | 467 | 0.57 | 0.73 | −1.30 | 3.70 |
| cyanidin-Ag ₉ * | −5.28 | −1.68 | 311 | 0.71 | 0.80 | −2.71 | 3.60 |
| cyanidin-Ag ₂₁ * | −4.82 | −2.52 | 332 | 0.68 | 0.79 | −2.91 | 2.30 |
| cyanidin-Ag ₂ Au I | −5.58 | −2.08 | 463 | 0.81 | 0.85 | −1.10 | 3.50 |
| cyanidin-Ag ₂ Au II | −5.52 | −1.71 | 435 | 0.52 | 0.70 | −1.33 | 3.81 |
| cyanidin-Ag ₂ Au III | −5.29 | −2.53 | 518 | 0.46 | 0.65 | −1.10 | 2.77 |
| cyanidin-Ag ₂ Cu I | −5.51 | −1.84 | 440 | 0.37 | 0.57 | −1.31 | 3.67 |
| cyanidin-Ag ₂ Cu II | −5.30 | −0.98 | 444 | 0.52 | 0.70 | −1.49 | 4.33 |
| cyanidin-Ag ₂ Cu III | −5.29 | −1.72 | 457 | 0.51 | 0.69 | −1.42 | 3.57 |
| cyanidin-AgAuCu I | −5.68 | −1.96 | 449 | 0.23 | 0.41 | −0.26 | 3.72 |
| cyanidin-AgAuCu II | −5.42 | −2.12 | 228 | 0.27 | 0.46 | −4.01 | 3.29 |
| cyanidin-AgAuCu III | −5.51 | −0.86 | 425 | 0.45 | 0.65 | −1.41 | 4.65 |
| cyanidin-AgAuCu IV | −5.53 | −1.06 | 419 | 0.62 | 0.76 | −1.43 | 4.47 |
| cyanidin-AgAuCu V | −5.54 | −1.89 | 468 | 0.72 | 0.81 | −1.11 | 3.65 |

* Ref [28].

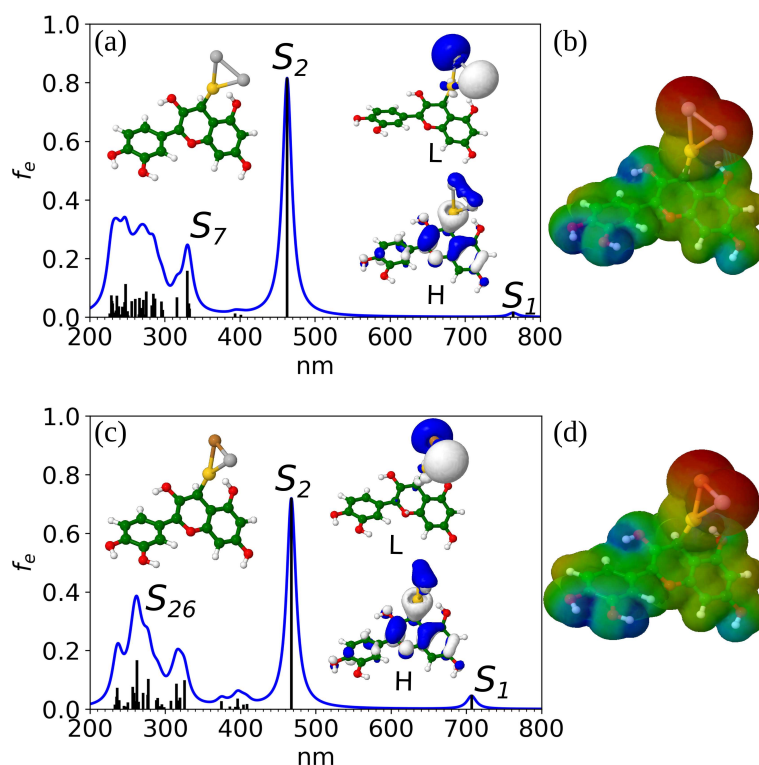


Figure 2. One-photon absorption spectra of (a) cyanidin-Ag₂Au (isomer I) and (c) cyanidin-AgAuCu (isomer V) at CAM-B3LYP/def2-SVP level of theory. The inset figures represent HOMO and LUMO orbitals. (b,d) Molecular electrostatic potential (MEP) surfaces of corresponding doped systems with red color representing electron-rich and blue color electron-poor area. For atom color legend please refer to the caption of Figure 1.

As shown in Figures S1 and S3, and Table 2, the overall largest maximum absorption is present in the spectra of cyanidin-Ag₂Au I and cyanidin-AgAuCu V. Their maximum absorption is almost at the same wavelength as in the case of the cyanidin-Ag₃ (~460 nm, cf. Table 2, Figure 2a,c), but the oscillator strength is increased from 0.57 to 0.81 and 0.72, respectively. This has direct consequences on the calculation of the LHE which is the

highest for the Au-doped isomer I (0.85) while the second best *LHE* corresponds to isomer V of Au-Cu-doped systems (0.81). These values are approximately the same as those of cyanidin-(Ag₉⁺) and cyanidin-(Ag₂₁⁺) which were identified as optimal sensitizers in our previous study [28]. This shows the potential of replacing larger Ag NCs in bio-nano hybrid systems with smaller doped trimers, opening new possibilities for designing cost-effective bio-nano-based sensitizers with improved stability and light harvesting efficiency.

The two systems with the largest *LHE* have trimer bound to cyanidin via a single Au-C bond. Overlapping these two structures shows that dihedral angles between the Au-C bond and the indoline plane (118° for the Au-doped and 113° for the Au-Cu-doped hybrid) are nearly the same. Interestingly, in both cases the sum of Mulliken charges on the doped trimer is 0.02, demonstrating the importance of the charge and its redistribution within the different metal atoms on the *LHE*. The type of the dopant atom(s), as well as its position, affects the *LHE* improvement.

Following earlier studies, we have also examined the electronic distribution of the cyanidin-Ag₂Au I and cyanidin-AgAuCu V by visualizing their molecular electrostatic potential (MEP) surfaces, presented in Figure 2b,d. In agreement with the previous findings, two distinct regions are present; the electron-rich area on the trimer (the donor) and the electron-poor area on the cyanidin dye (the acceptor).

Further analysis of isomers II and III in the Au-doped group reveals *LHE* values similar to the reference ones. The Cu-doping isomers generally exhibit comparable but slightly lower *LHE*, with isomer II demonstrating the highest value within the group (0.7). The mixed Au-Cu doping group exhibits diverse *LHE* values, ranging from 0.41 to 0.81.

In addition to the *LHE*, ΔG^{inject} also indicates if the selected models are suitable for DSSC application. The negative ΔG^{inject} , observed in all doped systems, suggesting that the electron injection process is spontaneous for all examined systems.

3.3. Nonlinear Optical Properties of Cyanidin-Trimers Hybrids

While conventional photovoltaic materials primarily rely on OPA to generate electron-hole pairs per absorbed photon, TPA enables the creation of such pairs through the simultaneous absorption of two photons. This mechanism substantially enhances the absorption cross-section of materials in DSSCs, allowing for the capture of a greater number of light photons across a wider spectrum of wavelengths. Consequently, it has the potential to increase light harvesting efficiency under low intensity light and improve the overall efficiency of the photovoltaic device [54–56]. TPA spectra for the monometallic cyanidin-Ag₃ model, as well as the dopant models cyanidin-Ag₂Au (isomer I) and cyanidin-AgAuCu (isomer V), are illustrated (cf. Figure S4). For the cyanidin-Ag₃ model, a substantial cross-section is already observed in the visible part of the spectra, around 460 nm (cf. Figure S4a). Doping with gold significantly enhances the intensity of the cross-section, highlighting the donor-acceptor nature and charge transfer between cyanidin and the heterometallic cluster in the gold-doped bio-nano hybrid (cf. Figure S4b). Additionally, when copper is added to the gold-doped bio-nano hybrid, a prominent peak emerges, surpassing the others in intensity (cf. Figure S4c). Analysis of the molecular orbitals for the last model demonstrates that the HOMO and LUMO for S₃₉ excited state are concentrated solely on the Ag-Au-Cu nanocluster. Doping with Au and Cu induces enhanced values of cross-sections around 460 nm, due to resonance between one-photon and two-photon excited states (cf. Figure S5). The optical properties of Au, Ag, and Cu atoms differ because of variations in their electronic configurations, particularly the occupancy of their s and d orbitals [57–60]. These electronic configurations determine how the atoms interact with light. Previous studies have established that gold with the smaller s-d energy gap [34], has a more pronounced relativistic effect compared to silver, allowing the d electrons to participate in bonding.

3.4. Cyanidin-Trimer Sensitizer Anchored on a TiO₂ Model Surface

We have selected cyanidin-Ag₂Au (isomer I) with the largest *LHE* and anchored it to a semiconductor model in order to create a realistic system of the doped dye adsorbed on a TiO₂ surface. The bonding between the TiO₂ model over two Ti-O bonds ensures a strong binding energy of -1.9 eV. Even though the region of maximum absorption is at the approximately same wavelength (~ 480 nm), the absorption spectrum of the supported doped hybrid reveals much stronger intensities compared to anchored cyanidin-Ag₃ (Figure 3a). The HOMO is localized over the whole cyanidin-Ag₂Au I and it is energetically at the same position as the free doped hybrid, while the LUMO is completely delocalized on the TiO₂ surface model (Figure 3b). Also, the energy level of the LUMO is close to the LUMO of the dye. The spatial distribution of the HOMO, LUMO orbitals illustrates the charge transfer between the dye and the semiconductor model. The main contributions to the strongest peak include transitions from the bio-nano hybrid to the trimer and semiconductor model (LUMO + 43) and entirely to the semiconductor (LUMO + 6, LUMO + 18) (cf. Table S2 and Figure S6).

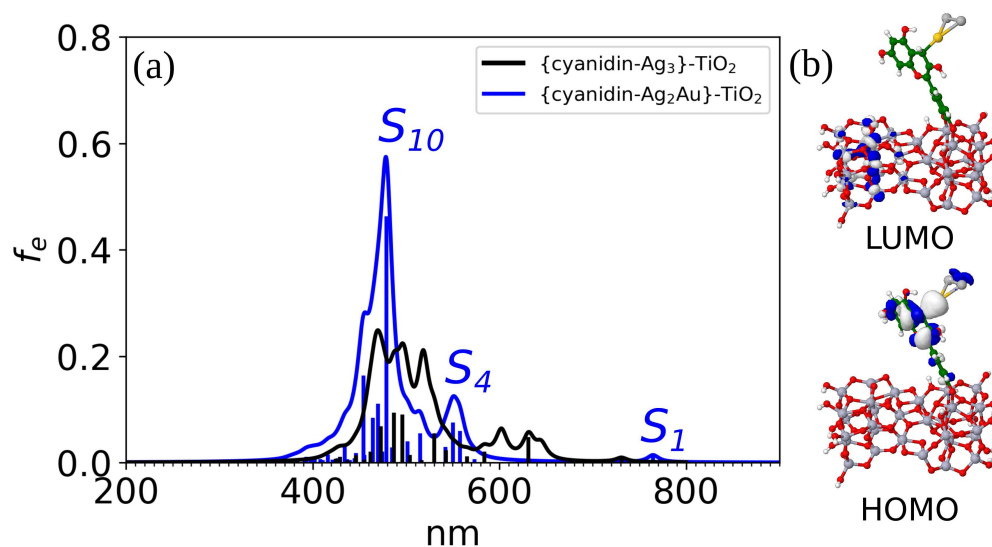


Figure 3. (a) Absorption spectrum of {cyanidin-Ag₂Au}-TiO₂ at CAM-B3LYP/def2-SVP level of theory. (b) Visualization of HOMO and LUMO orbitals; HOMO orbital is delocalized entirely at the bio-nano hybrid and LUMO at the TiO₂ model. Ti atoms are depicted in lilac color.

4. Conclusions

In this contribution, we have theoretically investigated the doping strategy for tuning the opto-electronic and photovoltaic properties of bio-nano hybrid systems at TiO₂ surface. Extensive analysis of single Au, single Cu, and mixed Au-Cu doping of Ag NC within the hybrid revealed that the isomers cyanidin-Ag₂Au I and cyanidin-AgAuCu V exhibit the best *LHE* value while also satisfying other preconditions for efficient DSSC sensitizer. Overall, these systems share similar structural properties and the same net trimer charge. This is the result of charge redistribution between the dopant atom(s) and the Ag which plays a key role in the structural properties of heterometallic trimer. Furthermore, the origin of their superior opto-electronic and photovoltaic properties is most likely due to the influence of the different s-d energy gaps for Ag and Au/Cu. Remarkably, TPA calculations on isomers I and V exhibit substantially higher intensities compared to the monometallic cyanidin-trimer hybrid, with cyanidin-AgAuCu having the largest cross-section. In addition, a successful electron injection is ensured through strong binding to the TiO₂ semiconductor with the anchored system revealing significantly enhanced calculated absorption compared to our previous studies. Thus, such systems could substitute previously predicted bio-nano hybrids based on larger Ag₉⁺ and Ag₂₁⁺ clusters. Our preliminary studies on single Au-doped cyanidin-Ag₈Au have shown no improvements in photovoltaic properties. Hence,

an effect of single Au and mixed Au/Cu doping is pronounced only on smaller cyanidin-trimer hybrids. The open question is whether doping with two or more atoms would produce the same effect on larger NCs.

Since low stability in silver nanoclusters (Ag NCs) is present, strategies such as coinage metal doping emerge as an important way for enhancing the stability of bio-nano hybrid systems at surfaces. The cost-effective way to design new bio-nano-based sensitizers with improved stability and light harvesting efficiency is the replacement of larger Ag NCs in bio-nano hybrid systems by smaller doped trimers. Future experimental preparation of such bio-nano sensitizers should connect the theory and application, with the ultimate goal of designing energy harvesting systems with superior properties.

Supplementary Materials: The following supporting information can be downloaded at: <https://www.mdpi.com/article/10.3390/nano14121034/s1>, Figure S1: Comparison of absorption spectra of cyanidin-Ag₂Au isomers and cyanidin-Ag₃ at CAM-B3LYP/def2-SVP level of theory; Figure S2: Comparison of OPA spectra of cyanidin-Ag₂Cu isomers and cyanidin-Ag₃ at CAM-B3LYP/def2-SVP level of theory; Figure S3: Comparison of OPA spectra of cyanidin-AgAuCu isomers and cyanidin-Ag₃ at CAM-B3LYP/def2-SVP level of theory; Figure S4: TPA spectra obtained by TDDFT at CAM-B3LYP/def2-SVP level of theory for cyanidin-Ag₃, cyanidin-Ag₂Au isomer I, and cyanidin-AgAuCu isomer V; Figure S5: Energies of one-photon OPA and two-photon TPA illustrating the resonance in cyanidin-Ag₃, cyanidin-Ag₂Au isomer I, and cyanidin-AgAuCu isomer V; Figure S6: Absorption spectrum of {cyanidin-Ag₂Au}-TiO₂ at CAM-B3LYP/def2-SVP level of theory with the main transitions; Table S1: Analysis of bond lengths of the doped NCs within bio-nano hybrid systems; Table S2: Analysis of the key excited states of {cyanidin-Ag₂Au}-TiO₂ at CAM-B3LYP/def2-SVP level of theory.

Author Contributions: Conceptualization, M.B.M. and A.M.; methodology, M.B.M., M.P.B. and A.M.; software, M.B.M., M.P.B. and A.M.; validation, M.B.M., M.P.B. and A.M.; formal analysis, M.B.M., M.P.B. and A.M.; investigation, M.B.M., M.P.B. and A.M.; resources, Ž.S.M. and V.B.-K.; data curation, M.B.M., M.P.B. and A.M.; writing—original draft preparation, M.B.M., M.P.B. and A.M.; writing—review and editing, M.B.M., M.P.B., Ž.S.M., A.M. and V.B.-K.; visualization, M.B.M., M.P.B. and A.M.; supervision, Ž.S.M. and V.B.-K.; project administration, Ž.S.M. and V.B.-K.; funding acquisition, Ž.S.M. and V.B.-K. All authors have read and agreed to the published version of the manuscript.

Funding: This research was partially supported by the project STIM—REI, Contract Number: KK.01.1.1.01.0003, funded by the European Union through the European Regional Development Fund—the Operational Programme Competitiveness and Cohesion 2014–2020 (KK.01.1.1.01).

Data Availability Statement: The original contributions presented in the study are included in the article and Supplementary Materials, further inquiries can be directed to the corresponding author.

Acknowledgments: Authors acknowledge computational facilities of the HPC computer within the STIM-REI project and University Computing Center in Zagreb, M.B.M. acknowledge Doctoral study of Biophysics at the University of Split.

Conflicts of Interest: The authors declare no conflicts of interest.

References

1. Kılış, S.; Krajačić, G.; Duić, N.; Montorsi, L.; Wang, Q.; Rosen, M.A.; Ahmad Al-Nimr, M. Research frontiers in sustainable development of energy, water and environment systems in a time of climate crisis. *Energy Convers. Manag.* **2019**, *199*, 111938. [[CrossRef](#)]
2. Pulli, E.; Rozzi, E.; Bella, F. Transparent photovoltaic technologies: Current trends towards upscaling. *Energy Convers. Manag.* **2020**, *219*, 112982. [[CrossRef](#)]
3. Rennuit-Mortensen, A.W.; Dalgas Rasmussen, K.; Grahn, M. How replacing fossil fuels with electrofuels could influence the demand for renewable energy and land area. *Smart Energy* **2023**, *10*, 100107. [[CrossRef](#)]
4. SolarPower Europe. *EU Market Outlook for Solar Power 2023–2027*; SolarPower Europe: Brussels, Belgium, 2023.
5. Traverse, C.; Pandey, R.; Barr, M.; Lunt, R. Emergence of highly transparent photovoltaics for distributed applications. *Nat. Energy* **2017**, *2*, 849–860. [[CrossRef](#)]
6. O'Regan, B.; Grätzel, M. A low-cost, high-efficiency solar cell based on dye-sensitized colloidal TiO₂ films. *Nature* **1991**, *353*, 737–740. [[CrossRef](#)]

7. Grätzel, M. Photoelectrochemical cells. *Nature* **2001**, *414*, 338–344. [[CrossRef](#)] [[PubMed](#)]
8. Grätzel, M. Dye-sensitized solar cells. *J. Photochem. Photobiol. C Photochem. Rev.* **2003**, *4*, 145–153. [[CrossRef](#)]
9. Bagher, A.M.; Vahid, M.M.A.; Mohsen, M. Types of Solar Cells and Application. *Am. J. Opt. Photonics* **2015**, *3*, 94–113. [[CrossRef](#)]
10. Fan, W.; Tan, D.; Deng, W.Q. Acene-modified triphenylamine dyes for dye-sensitized solar cells: A computational study. *ChemPhysChem* **2012**, *13*, 2051–2060. [[CrossRef](#)]
11. Carella, A.; Borbone, F.; Centore, R. Research Progress on Photosensitizers for DSSC. *Front. Chem.* **2018**, *6*, 481. [[CrossRef](#)]
12. Chauke, N.M.; Mohlala, R.L.; Ngqoloda, S.; Raphulu, M.C. Harnessing visible light: Enhancing TiO₂ photocatalysis with photosensitizers for sustainable and efficient environmental solutions. *Front. Chem. Eng.* **2024**, *6*, 1356021. [[CrossRef](#)]
13. Birel, Ö.; Nadeem, S.; Duman, H. Porphyrin-Based Dye-Sensitized Solar Cells (DSSCs). *J. Fluoresc.* **2017**, *27*, 1075–1085. [[CrossRef](#)] [[PubMed](#)]
14. Tomar, N.; Agrawal, A.; Dhaka, V.S.; Surolia, P.K. Ruthenium complexes based dye sensitized solar cells: Fundamentals and research trends. *Sol. Energy* **2020**, *207*, 59–76. [[CrossRef](#)]
15. Alizadeh, A.; Roudgar-Amoli, M.; Bonyad-Shekalgourabi, S.M.; Shariatnia, Z.; Mahmoudi, M.; Saadat, F. Dye sensitized solar cells go beyond using perovskite and spinel inorganic materials: A review. *Renew. Sustain. Energy Rev.* **2022**, *157*, 112047. [[CrossRef](#)]
16. Badawy, S.A.; Salem, K.E.; Fadda, A.A.; Abdel-Latif, E.; Elmorsy, M.R. Advancements in metal-free organic dyes: Achieving over 10% efficiency in DSSCs. *Dyes Pigment.* **2024**, *225*, 112096. [[CrossRef](#)]
17. Muniz, C.N.; Archer, C.A.; Applebaum, J.S.; Alagaratnam, A.; Schaab, J.; Djurovich, P.I.; Thompson, M.E. Two-Coordinate Coinage Metal Complexes as Solar Photosensitizers. *J. Am. Chem. Soc.* **2023**, *145*, 13846–13857. [[CrossRef](#)] [[PubMed](#)]
18. Yazie, A.N.; Worku, A.D.; Tsigie, Y.A. Recent advances in anthocyanin dyes extracted from plants for dye sensitized solar cell. *Mater. Renew. Sustain. Energy* **2020**, *9*, 23. [[CrossRef](#)]
19. Nazeeruddin, M.K.; Klein, C.; Liska, P.; Grätzel, M. Synthesis of novel ruthenium sensitizers and their application in dye-sensitized solar cells. *Coord. Chem. Rev.* **2005**, *249*, 1460–1467. [[CrossRef](#)]
20. Yin, J.F.; Velayudham, M.; Bhattacharya, D.; Lin, H.C.; Lu, K.L. Structure optimization of ruthenium photosensitizers for efficient dye-sensitized solar cells—A goal toward a “bright” future. *Coord. Chem. Rev.* **2012**, *256*, 3008–3035. [[CrossRef](#)]
21. Alenazi, N.A.; Abualnaja, M.M.; El-Metwaly, N.M. Development of organic co-sensitizers based on piperonal for over 10% efficient ruthenium complex dye-sensitized solar cells. *J. Mol. Liq.* **2024**, *398*, 124337. [[CrossRef](#)]
22. Hug, H.; Bader, M.; Mair, P.; Glatzel, T. Biophotovoltaics: Natural pigments in dye-sensitized solar cells. *Appl. Energy* **2014**, *115*, 216–225. [[CrossRef](#)]
23. Pratiwi, D.D.; Nurosyid, F.; Supriyanto, A.; Suryana, R. Efficiency enhancement of dye-sensitized solar cells (DSSC) by addition of synthetic dye into natural dye (anthocyanin). *IOP Conf. Ser. Mater. Sci. Eng.* **2017**, *176*, 012012. [[CrossRef](#)]
24. Prima, E.C.; Nuruddin, A.; Yulianto, B.; Kawamura, G.; Matsuda, A. Combined spectroscopic and TDDFT study of single-double anthocyanins for application in dye-sensitized solar cells. *New J. Chem.* **2018**, *42*, 11616–11628. [[CrossRef](#)]
25. Purwoko, A.; Setiawati, V.; Hadisaputra, S. Metal-pigment complex derived from natural dye of anthocyanin: A potential candidate for DSSC photosensitizer. *IOP Conf. Ser. Mater. Sci. Eng.* **2019**, *509*, 012130. [[CrossRef](#)]
26. Shah, W.; Faraz, S.M.; Awan, Z.H. Photovoltaic properties and impedance spectroscopy of dye sensitized solar cells co-sensitized by natural dyes. *Phys. B Condens. Matter* **2023**, *654*, 414716. [[CrossRef](#)]
27. Pramananda, V.; Fityay, T.A.H.; Misran, E. Anthocyanin as natural dye in DSSC fabrication: A review. *IOP Conf. Ser. Mater. Sci. Eng.* **2021**, *1122*, 012104. [[CrossRef](#)]
28. Bužančić Milosavljević, M.; Mravak, A.; Perić Bakulić, M.; Bonačić-Koutecký, V. Model systems for dye-sensitized solar cells: Cyanidin-silver nanocluster hybrids at TiO₂ support. *RSC Adv.* **2023**, *13*, 6010–6016. [[CrossRef](#)]
29. Sharma, K.; Sharma, V.; Sharma, S. Dye-sensitized solar cells: Fundamentals and current status. *Nanoscale Res. Lett.* **2018**, *13*, 381. [[CrossRef](#)]
30. Bonačić-Koutecký, V.; Kulesza, A.; Gell, L.; Mitrić, R.; Antoine, R.; Bertorelle, F.; Hamouda, R.; Rayane, D.; Broyer, M.; Tabarin, T.; et al. Silver cluster-biomolecule hybrids: From basics towards sensors. *Phys. Chem. Chem. Phys.* **2012**, *14*, 9282–9290. [[CrossRef](#)]
31. Ko, K.H.; Lee, Y.C.; Jung, Y.J. Enhanced efficiency of dye-sensitized TiO₂ solar cells (DSSC) by doping of metal ions. *J. Colloid Interface Sci.* **2005**, *283*, 482–487. [[CrossRef](#)]
32. Yang, J.; Pang, R.; Song, D.; Li, M.B. Tailoring silver nanoclusters via doping: Advances and opportunities. *Nanoscale Adv.* **2021**, *3*, 2411–2422. [[CrossRef](#)] [[PubMed](#)]
33. Sahoo, K.; Gazi, T.R.; Roy, S.; Chakraborty, I. Nanohybrids of atomically precise metal nanoclusters. *Commun. Chem.* **2023**, *6*, 157. [[CrossRef](#)] [[PubMed](#)]
34. Bonačić-Koutecký, V.; Burda, J.; Mitrić, R.; Ge, M.; Zampella, G.; Fantucci, P. Density functional study of structural and electronic properties of bimetallic silver-gold clusters: Comparison with pure gold and silver clusters. *J. Chem. Phys.* **2002**, *117*, 3120–3131. [[CrossRef](#)]
35. Kulesza, A.; Mitrić, R.; Bonačić-Koutecký, V. Unique optical properties of silver cluster-biochromophore hybrids: Comparison with copper and gold. *Chem. Phys. Lett.* **2011**, *501*, 211–214. [[CrossRef](#)]
36. Colombo, A.; Dragonetti, C.; Roberto, D.; Fagnani, F. Copper complexes as alternative redox mediators in dye-sensitized solar cells. *Molecules* **2021**, *26*, 194. [[CrossRef](#)]

37. Pniakowska, A.; Kumaranchira Ramankutty, K.; Obstarczyk, P.; Perić Bakulić, M.; Sanader Maršić, Ž.; Bonačić-Koutecký, V.; Bürgi, T.; Olesiak-Bañska, J. Gold-Doping Effect on Two-Photon Absorption and Luminescence of Atomically Precise Silver Ligated Nanoclusters. *Angew. Chem. Int. Ed.* **2022**, *61*, e202209645. [[CrossRef](#)] [[PubMed](#)]
38. Perdew, J.P.; Burke, K.; Ernzerhof, M. Generalized Gradient Approximation Made Simple. *Phys. Rev. Lett.* **1996**, *77*, 3865–3868. Erratum in *Phys. Rev. Lett.* **1997**, *78*, 1396. [[CrossRef](#)] [[PubMed](#)]
39. Frisch, M.J.; Trucks, G.W.; Schlegel, H.B.; Scuseria, G.E.; Robb, M.A.; Cheeseman, J.R.; Scalmani, G.; Barone, V.; Petersson, G.A.; Nakatsuji, H.; et al. *Gaussian 16 Revision A.03*; Gaussian Inc.: Wallingford, CT, USA, 2016.
40. Weigend, F. Accurate Coulomb-fitting basis sets for H to Rn. *Phys. Chem. Chem. Phys.* **2006**, *8*, 1057–1065. [[CrossRef](#)] [[PubMed](#)]
41. Andrae, D.; Haeussermann, U.; Dolg, M.; Stoll, H.; Preuss, H. Energy-adjusted ab initio pseudopotentials for the second and third row transition elements. *Theor. Chim. Acta* **1990**, *77*, 123–141. [[CrossRef](#)]
42. Yanai, T.; Tew, D.; Handy, N. A new hybrid exchange-correlation functional using the Coulomb-attenuating method (CAM-B3LYP). *Chem. Phys. Lett.* **2004**, *393*, 51–57. [[CrossRef](#)]
43. Aidas, K.; Angeli, C.; Bak, K.L.; Bakken, V.; Bast, R.; Boman, L.; Christiansen, O.; Cimiraglia, R.; Coriani, S.; Dahle, P.; et al. The Dalton quantum chemistry program system. *WIREs Comput. Mol. Sci.* **2014**, *4*, 269–284. [[CrossRef](#)] [[PubMed](#)]
44. Dalton, a Molecular Electronic Structure Program, Release Dalton2020.alpha. 2020. Available online: <http://daltonprogram.org> (accessed on 14 May 2024).
45. Frediani, L.; Rinkevicius, Z.; Ågren, H. Two-photon absorption in solution by means of time-dependent density-functional theory and the polarizable continuum model. *J. Chem. Phys.* **2005**, *122*, 244104. [[CrossRef](#)] [[PubMed](#)]
46. Norman, P. A perspective on nonresonant and resonant electronic response theory for time-dependent molecular properties. *Phys. Chem. Chem. Phys.* **2011**, *13*, 20519–20535. [[CrossRef](#)] [[PubMed](#)]
47. List, N.H.; Zalesny, R.; Murugan, N.A.; Kongsted, J.; Bartkowiak, W.; Ågren, H. Relation between nonlinear optical properties of push–pull molecules and metric of charge transfer excitations. *J. Chem. Theory Comput.* **2015**, *11*, 4182–4188. [[CrossRef](#)] [[PubMed](#)]
48. Kim, H.S.; Lee, C.R.; Im, J.H.; Lee, K.B.; Moehl, T.; Marchioro, A.; Moon, S.J.; Humphry-Baker, R.; Yum, J.H.; Moser, J.E.; et al. Lead Iodide Perovskite Sensitized All-Solid-State Submicron Thin Film Mesoscopic Solar Cell with Efficiency Exceeding 9%. *Sci. Rep.* **2012**, *2*, 591. [[CrossRef](#)] [[PubMed](#)]
49. Fujisawa, J.; Eda, T.; Hanaya, M. Comparative study of conduction-band and valence-band edges of TiO₂, SrTiO₃, and BaTiO₃ by ionization potential measurements. *Chem. Phys. Lett.* **2017**, *685*, 23–26. [[CrossRef](#)]
50. Weigend, F.; Ahlrichs, R. Balanced basis sets of split valence, triple zeta valence and quadruple zeta valence quality for H to Rn: Design and assessment of accuracy. *Phys. Chem. Chem. Phys.* **2005**, *7*, 3297–3305. [[CrossRef](#)] [[PubMed](#)]
51. Anselmi, C.; Mosconi, E.; Pastore, M.; Ronca, E.; De Angelis, F. Adsorption of organic dyes on TiO₂ surfaces in dye-sensitized solar cells: Interplay of theory and experiment. *Phys. Chem. Chem. Phys.* **2012**, *14*, 15963–15974. [[CrossRef](#)]
52. Adhikari, S.G.; Gascooke, J.R.; Alotabi, A.S.; Andersson, G.G. Anchoring Modes of Ru-Based N719 Dye onto Titania Substrates. *J. Phys. Chem. C* **2024**, *128*, 3136–3147. [[CrossRef](#)]
53. Zhang, G.; Bai, Y.; Li, R.; Shi, D.; Wenger, S.; Zakeeruddin, S.M.; Grätzel, M.; Wang, P. Employ a bisthienothiophene linker to construct an organic chromophore for efficient and stable dye-sensitized solar cells. *Energy Environ. Sci.* **2009**, *2*, 92–95. [[CrossRef](#)]
54. Ørnsø, K.B.; Garcia-Lastra, J.M.; De La Torre, G.; Himpel, F.J.; Rubio, A.; Thygesen, K.S. Design of two-photon molecular tandem architectures for solar cells by ab initio theory. *Chem. Sci.* **2015**, *6*, 3018–3025. [[CrossRef](#)] [[PubMed](#)]
55. Guillén-López, A.; Delesma, C.; Amador-Bedolla, C.; Robles, M.; Muñoz, J. Electronic structure and nonlinear optical properties of organic photovoltaic systems with potential applications on solar cell devices: A DFT approach. *Theor. Chem. Acc.* **2018**, *137*, 85. [[CrossRef](#)]
56. Hu, Z.; Khadka, V.; Wang, W.; Galipeau, D.; Yan, X. Theoretical study of two-photon absorption properties and up-conversion efficiency of new symmetric organic π -conjugated molecules for photovoltaic devices. *J. Mol. Model.* **2012**, *18*, 3657–3667. [[CrossRef](#)] [[PubMed](#)]
57. Jain, P.K.; Lee, K.S.; El-Sayed, I.H.; El-Sayed, M.A. Calculated Absorption and Scattering Properties of Gold Nanoparticles of Different Size, Shape, and Composition: Applications in Biological Imaging and Biomedicine. *J. Phys. Chem. B* **2006**, *110*, 7238–7248. [[CrossRef](#)] [[PubMed](#)]
58. Suemoto, T.; Yamanaka, K.; Sugimoto, N.; Kobayashi, Y.; Otsu, T.; Tani, S.; Koyama, T. Relaxation dynamics of hot electrons in the transition metals Au, Ag, Cu, Pt, Pd, and Ni studied by ultrafast luminescence spectroscopy. *J. Appl. Phys.* **2021**, *130*, 025101. [[CrossRef](#)]
59. Jain, P.K.; Huang, X.; El-Sayed, I.H.; El-Sayed, M.A. Noble Metals on the Nanoscale: Optical and Photothermal Properties and Some Applications in Imaging, Sensing, Biology, and Medicine. *Acc. Chem. Res.* **2008**, *41*, 1578–1586. [[CrossRef](#)]
60. Wang, Z.; Chen, B.; Rogach, A.L. Synthesis, optical properties and applications of light-emitting copper nanoclusters. *Nanoscale Horiz.* **2017**, *2*, 135–146. [[CrossRef](#)]

Disclaimer/Publisher’s Note: The statements, opinions and data contained in all publications are solely those of the individual author(s) and contributor(s) and not of MDPI and/or the editor(s). MDPI and/or the editor(s) disclaim responsibility for any injury to people or property resulting from any ideas, methods, instructions or products referred to in the content.

Design of luminophores for transparent luminescent solar concentrators

3.1 Theoretical prediction of fluorescence quantum yields

Reprinted from:

Alexander Humeniuk, Margarita Bužančić, Joscha Hoche, Javier Cerezo, Roland Mitrić, Fabrizio Santoro and Vlasta Bonačić-Koutecký. Predicting fluorescence quantum yields for molecules in solution: A critical assessment of the harmonic approximation and the choice of the lineshape function. *The Journal of Chemical Physics*, 152 (5), 054107, 2020. Reproduced with the permission of AIP Publishing.

Predicting fluorescence quantum yields for molecules in solution: A critical assessment of the harmonic approximation and the choice of the lineshape function

Cite as: J. Chem. Phys. **152**, 054107 (2020); <https://doi.org/10.1063/1.5143212>

Submitted: 20 December 2019 . Accepted: 19 January 2020 . Published Online: 05 February 2020

Alexander Humeniuk, Margarita Bužančić , Joscha Hoche , Javier Cerezo, Roland Mitrić ,
Fabrizio Santoro, and Vlasta Bonačić-Koutecký 



View Online



Export Citation



CrossMark

Lock-in Amplifiers

Find out more today



 Zurich
Instruments

AIP
Publishing

Predicting fluorescence quantum yields for molecules in solution: A critical assessment of the harmonic approximation and the choice of the lineshape function

Cite as: J. Chem. Phys. 152, 054107 (2020); doi: 10.1063/1.5143212

Submitted: 20 December 2019 • Accepted: 19 January 2020 •

Published Online: 5 February 2020



View Online



Export Citation



CrossMark

Alexander Humeniuk,¹ Margarita Bužančić,²  Joscha Hoche,¹  Javier Cerezo,³ Roland Mitrić,^{1,a)} 
Fabrizio Santoro,^{4,b)} and Vlasta Bonačić-Koutecký^{2,5,c)} 

AFFILIATIONS

¹Institut für Physikalische und Theoretische Chemie, Universität Würzburg, Am Hubland, 97074 Würzburg, Germany

²Center of Excellence for Science and Technology-Integration of Mediterranean Region (STIM), Faculty of Science, University of Split, Poljička cesta 35, 2100 Split, Croatia

³Departamento de Química, Facultad de Ciencias, Universidad Autónoma de Madrid, 28049 Madrid, Spain

⁴Istituto di Chimica dei Composti Organometallici (ICCOM-CNR), Area della Ricerca del CNR, Via Moruzzi 1, I-56124 Pisa, Italy

⁵Department of Chemistry, Humboldt Universität zu Berlin, Brook-Taylor-Strasse 2, 12489 Berlin, Germany

^{a)}Electronic mail: roland.mitric@uni-wuerzburg.de

^{b)}Electronic mail: fabrizio.santoro@pi.iccom.cnr.it

^{c)}Author to whom correspondence should be addressed: vbk@chemie.hu-berlin.de

ABSTRACT

For the rational design of new fluorophores, reliable predictions of fluorescence quantum yields from first principles would be of great help. However, efficient computational approaches for predicting transition rates usually assume that the vibrational structure is harmonic. While the harmonic approximation has been used successfully to predict vibrationally resolved spectra and radiative rates, its reliability for non-radiative rates is much more questionable. Since non-adiabatic transitions convert large amounts of electronic energy into vibrational energy, the highly excited final vibrational states deviate greatly from harmonic oscillator eigenfunctions. We employ a time-dependent formalism to compute radiative and non-radiative rates for transitions and study the dependence on model parameters. For several coumarin dyes, we compare different adiabatic and vertical harmonic models (AS, ASF, AH, VG, VGF, and VH), in order to dissect the importance of displacements, frequency changes, and Duschinsky rotations. In addition, we analyze the effect of different broadening functions (Gaussian, Lorentzian, or Voigt). Moreover, to assess the qualitative influence of anharmonicity on the internal conversion rate, we develop a simplified anharmonic model. We address the reliability of these models considering the potential errors introduced by the harmonic approximation and the phenomenological width of the broadening function.

Published under license by AIP Publishing. <https://doi.org/10.1063/1.5143212>

I. INTRODUCTION

Luminescence has many technological applications, such as organic light-emitting diodes, luminescent solar concentrators,¹ and *in vivo* fluorescence imaging.² The high cost for synthesizing and characterizing new molecules has revived the interest in reliable

prediction of fluorescence and phosphorescence quantum yields (QYs) from first principles. To identify the candidate molecules for synthesis, virtual screenings could be performed for identifying the most promising novel compounds with high quantum yields and other desirable properties, such as low emission energy in the infrared part of the spectrum.

Recently, several programs^{3,4} were developed for predicting rates for radiative and non-radiative (internal conversion, IC,^{5,6} and intersystem crossing, ISC^{7,8}) decays using Fermi's golden rule. They are based on the idea that the decay processes are slower than thermalization and that the couplings are small. In addition, all of these approaches make use of the harmonic approximation for the ground- and excited-state potential energy surfaces (PESs) since this is at the moment the only way how to deal with systems of interest having dozens or hundreds of normal modes. Some of the methods can account for mixing of modes (Duschinsky rotation), the Herzberg–Teller correction, and temperature dependence. The scope of this article is to investigate the range of validity of these state of the art methodologies. Despite some contributions in the literature,⁹ this question is not yet well assessed.

Differences between simulated IC rates based on Fermi's golden rule and experimental non-radiative rates can have many origins: additional decay channels (ISC or conical intersections, dark trap states), additional effects that were not considered (Duschinsky or Herzberg–Teller effect), or simply a questionable description of the electronic structure. These issues can be treated by more advanced harmonic models that take all relevant vibronic effects into account or by including additional rate constants for pronounced non-harmonic processes, such as thermally activated decay through a conical intersection.^{10,11} However, what about the harmonic approximation itself, on which the whole theory rests?

The harmonic approximation is the central issue for calculations of radiative and internal conversion rates, in particular, if one is interested in large systems. All kinds of transitions (radiative, IC, ISC, and charge transfer) can be formulated in terms of Fermi's golden rule making use of the harmonic approximation.^{3,12} However, the approximation is not equally applicable to all transitions. Radiative rates are usually determined by transitions between vibrational ground states or states with few vibrational quanta. Intersystem crossing is most effective if the singlet and triplet states are almost degenerate so that the ISC rate is also dominated by transitions between vibrational ground states. On the other hand, internal conversion involves transitions to highly excited vibrational final states (see Fig. 1). Electronic energy of a few electron volts is converted into vibrational energy, which is enough to overcome the barriers that separate different isomers on the ground-state PES. These considerations should be taken as warnings regarding the use of the harmonic approximation. However, it is the only practical approach because of the convenient form of multidimensional Gaussian integrals and it is very difficult to go beyond it.

To test how well the harmonic approximation is suited for predicting fluorescence quantum yields, we study a series of coumarin dyes for which experimental non-radiative rates and quantum yields are available. We use a quite general time-dependent formalism¹³ to compute rates as Fourier transforms of correlation functions. Density functional theory in combination with a polarizable continuum model (PCM) for solvation provides the vibrational structure of the initial and final electronic states. Since only a few standard electronic structure calculations are required and the time-dependent formalism is very efficient, this approach for *ab initio* prediction of fluorescence quantum yields seems attractive.

However, the question remains whether the harmonic approximation is valid and how we can test its validity without knowing

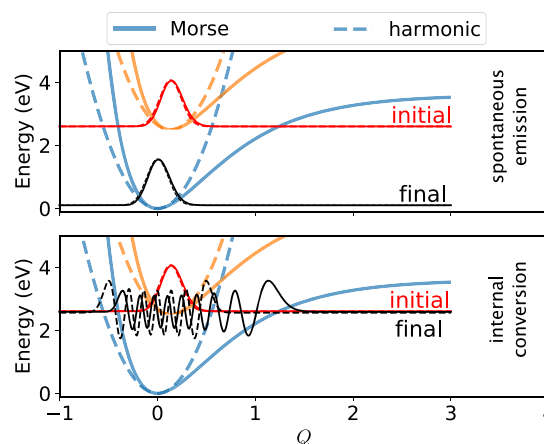


FIG. 1. Morse potential for a C=C stretching mode. The initial and final states for radiative (top) and non-radiative (bottom) transitions are also shown both for the Morse potential (anharmonicity $\chi = 0.014$, solid lines) and the harmonic approximation ($\chi = 0.0$, dashed lines). The radiative rate is dominated by the transition between two vibrational ground states, for which the harmonic approximation is valid. With perfect energy conservation, the non-radiative rate is determined by the transition between a vibrational ground state on the excited-state PES and a highly excited vibrational state on the ground-state PES. The wavefunction of the final vibrational state differs considerably from a harmonic oscillator wavefunction. However, the overlap between the initial and the final state is very low due to the narrow oscillations in both the Morse and the harmonic oscillator wavefunction.

the exact solution. For 1D and 2D systems, the exact solution can be obtained, but such low-dimensional systems are not relevant models for typical chromophores, which contain dozens to a 100 vibrational modes, whose frequencies span the range from $<50 \text{ cm}^{-1}$ to $>3500 \text{ cm}^{-1}$.

Since in principle molecular PESs are not harmonic, one has to choose a point at which the quadratic approximation is made. This choice defines different harmonic models.¹⁴ The models can be separated into two classes, depending on around which point the potential energy surface of the electronic ground state is expanded to second order. In adiabatic models (AS/ASF/AH), the potential is expanded around the geometry of the ground-state minimum, while in vertical models (VG/VGF/VH), the surface is expanded around the excited-state minimum. The models can be further distinguished depending on whether the initial and final states have different equilibrium geometries, but the same normal modes [adiabatic shift (AS) and vertical gradient (VG)] differ in equilibrium geometry and frequencies [adiabatic shift frequencies (ASF) and vertical gradient frequencies (VGF)] or differ in equilibrium geometry and the Hessian matrix [adiabatic Hessian (AH) and vertical Hessian (VH)].

In this contribution, we compare the performance of these models. There is a clear hierarchy with those higher up being in principle more accurate: $AS < ASF < AH$ and $VG < VGF < VH$. Although AH and VH are the best models, retaining inferior ones has the advantage that we can decompose the non-radiative rate into contributions from different effects. Moreover, since AH and VH models should deliver identical results if harmonic approximation is

exact, we will inquire to what extent an analysis of their difference is a trustworthy reporter of the importance of anharmonic effects.

As a second step of our analysis, in this contribution, we explicitly tackle the study of possible anharmonic effects on the internal conversion rate by considering simple models. More specifically, for this purpose, we formulate a model that interpolates smoothly between the harmonic approximation and a fictitious anharmonic system.¹⁵ Realistic harmonic frequencies, displacements, and electronic non-adiabatic coupling vectors are taken from a TD-DFT+PCM calculation. These are the same quantities needed for the adiabatic shift (AS) model, where ground- and excited-state PESs differ only by a vertical shift in energy and a horizontal shift of the equilibrium geometries. To incorporate anharmonicity, each normal mode is replaced by a Morse potential that is characterized by an anharmonicity χ . For $\chi = 0$, the Morse potential turns into a harmonic potential with the same frequency and equilibrium position as the corresponding harmonic potential. χ is a global parameter and it is the same for all modes. For $\chi > 0$, the modes acquire some anharmonicity. Since the dissociation energy D of a Morse potential with frequency ω is related to the anharmonicity via $D = \frac{\hbar\omega}{4\chi}$, modes with low frequencies are more affected.

It is important to note that the anharmonic model is not a realistic representation of any molecule for a number of reasons: low-lying modes, such as rotations, do not have the form of a Morse potential; the modes are assumed to be independent of each other and all other approximations made in the AS model, except for the harmonicity of the potential, still apply. With these caveats in mind, we investigate how the rate of internal conversion in 3-chloro-7-methoxy-4-methylcoumarin, CIMMC, changes with the anharmonicity χ .

This paper is structured in the following way: in Sec. II, we sketch the time-dependent formalism for obtaining transition rates in the harmonic approximation and derive the anharmonic AS model. Section III gives the computational details. In Sec. IV, we present vibrationally resolved emission spectra, non-radiative rates, and quantum yields for a selection of coumarin dyes, focusing on the influence of anharmonicity, choice of the harmonic model, and broadening function.

II. THEORY

A. Harmonic models—Transition rates in the time-dependent formalism

Non-radiative transitions are treated with first-order perturbation theory. We invoke the Born–Oppenheimer approximation so that the initial (excited) and the final (ground) state can be expressed as products of an electronic (Ψ) and a vibrational (Θ) wavefunction. The non-adiabatic transition is mediated by the nuclear kinetic energy operator $\hat{V} = \hat{T}_{\text{nuc}}$,

$$|\Psi_{\text{es}}, \Theta_{\text{es},i}\rangle \xrightarrow{\hat{V}} |\Psi_{\text{gs}}, \Theta_{\text{gs},f}\rangle. \quad (1)$$

We further assume that the probability to be initially in state i is given by the Boltzmann distribution with partition function $Z = \sum_i e^{-\beta E_i^{(\text{es})}}$ with $\beta = 1/(k_B T)$. The internal conversion rate is then given by Fermi's golden rule,

$$k_{\text{ic}}(\Delta E) = \frac{2\pi}{\hbar} \sum_{i,f} \frac{e^{-\beta E_i^{(\text{es})}}}{Z} |\langle \Psi_{\text{es}}, \Theta_{\text{es},i} | \hat{V} | \Psi_{\text{gs}}, \Theta_{\text{gs},f} \rangle|^2 \times \delta(\Delta E + E_i^{(\text{es})} - E_f^{(\text{gs})}). \quad (2)$$

For the definition of the vibrational energies $E_i^{(\text{es})}$ and $E_f^{(\text{gs})}$ and the adiabatic excitation energy ΔE , see Fig. 2. Enumerating and summing over all relevant vibrational states in even a medium-sized molecule is very difficult. In the time-dependent formalism, this problem is solved by replacing the summation by a propagation in time. The lineshape function $\delta(\dots)$, which enforces energy conservation, is replaced by its Fourier decomposition,

$$\delta(\Delta E + E_i^{(\text{es})} - E_f^{(\text{gs})}) = \frac{1}{2\pi} \int_{-\infty}^{\infty} e^{i(\Delta E + E_i^{(\text{es})} - E_f^{(\text{gs})})t} \tilde{f}(t) dt. \quad (3)$$

Here, $\tilde{f}(t)$ is the Fourier transform of the lineshape function and accounts for homogeneous and inhomogeneous broadening. In this way, the Fourier transform of the rate is expressed formally as a time correlation function,

$$\tilde{k}_{\text{ic}}(t) = \frac{2\pi}{\hbar} \frac{1}{Z} \text{Tr} \left(e^{(it-\beta)\hat{H}^{(\text{es})}} \hat{V}_{\text{e,g}} e^{-it\hat{H}^{(\text{gs})}} \hat{V}_{\text{e,g}}^\dagger \right). \quad (4)$$

$\hat{H}^{(\text{es})}$ and $\hat{H}^{(\text{gs})}$ are the vibrational Hamiltonians of the excited and ground states, respectively, and $\hat{V}_{\text{e,g}} = \langle \Psi_{\text{es}} | \hat{V} | \Psi_{\text{gs}} \rangle$ is the matrix element of the coupling operator between the electronic parts of the wavefunctions. The rate is obtained by the inverse Fourier transform,

$$k_{\text{ic}}(\Delta E) = \frac{1}{2\pi} \int_{-\infty}^{\infty} dt e^{i\Delta E t} \tilde{f}(t) \tilde{k}_{\text{ic}}(t). \quad (5)$$

The same formalism can also be applied to the radiative rate. Evaluating the correlation function in Eq. (4) is still a formidable task, unless the vibrational Hamiltonians $\hat{H}^{(\text{es})}$ and $\hat{H}^{(\text{gs})}$ are approximated by harmonic oscillators. For the general case of two harmonic potential energy surfaces, the working equations for computing radiative and non-radiative rates have been derived in Refs. 3,

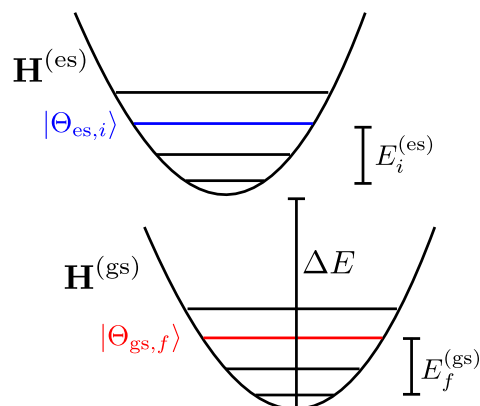


FIG. 2. Harmonic potential energy surfaces, adiabatic excitation energy ΔE , and vibrational energies of an initial and a final state.

13, 16, and 17. The reader is referred to these publications for more details. The formalism can deal with the changes in frequencies and mixing of normal modes (Duschinsky effect) and only requires standard electronic structure calculations. Geometry optimizations and frequency calculations can be routinely applied to the excited states of medium-sized molecules. Two of us, Santoro and Cerezo, have implemented the time-dependent formalism into a development version of the code *FCclasses3*.⁴

To study the effect of anharmonicity, we modify the simplest of the harmonic models, the AS model, by replacing the quadratic potentials with Morse potentials. We now describe the anharmonic AS model and derive the corresponding expressions for the non-radiative rate.

B. The anharmonic adiabatic shift model—internal conversion rates

An adiabatic shift (AS) model for internal conversion is fully characterized by the adiabatic excitation energy ΔE , the vibrational frequencies ω_i , the displacements ΔQ_i , and the electronic non-adiabatic couplings between the ground and excited electronic states, $C_i = \langle \Psi_{\text{es}} | \frac{\partial \Psi_{\text{gs}}}{\partial Q_i} \rangle$, for each of the independent vibrational modes Q_i ($i = 1, \dots, N$). Using these quantities, we construct potential energy surfaces for the electronic ground and excited states, where the harmonic oscillators for both the ground and excited states of a mode i are replaced by Morse potentials,^{18,19}

$$V_{\text{gs}}^{(i)}(Q_i) = D_i(1 - e^{-\alpha_i Q_i})^2, \quad (6)$$

$$V_{\text{es}}^{(i)}(Q_i) = D_i(1 - e^{-\alpha_i(Q_i - \Delta Q_i)})^2 + \Delta E. \quad (7)$$

The ground- and excited-state minima lie at $Q_i = 0$ and $Q_i = \Delta Q_i$, respectively. Around them, the potential energy surfaces can be approximated by a harmonic oscillator potential with frequency ω_i ,

$$V_{\text{gs}}^{(i)}(Q_i) \approx \frac{1}{2} \omega_i^2 Q_i^2, \quad (8)$$

$$V_{\text{es}}^{(i)}(Q_i) \approx \frac{1}{2} \omega_i^2 (Q_i - \Delta Q_i)^2 + \Delta E. \quad (9)$$

The parameters D_i and α_i in the definition of the Morse potential can be expressed in terms of the frequency ω_i and an anharmonicity parameter χ ,

$$D_i = \frac{\omega_i}{4\chi}, \quad (10)$$

$$\alpha_i = \sqrt{2\omega_i\chi}. \quad (11)$$

For $\chi \rightarrow 0$, the Morse potentials turn into the harmonic oscillator potentials of Eqs. (8) and (9). The time-independent Schrödinger equation,

$$-\frac{\hbar^2}{2} \frac{\partial^2 \phi^{(i)}}{\partial Q^2} + V^{(i)}(Q) \phi_n^{(i)}(Q) = \epsilon \phi_n^{(i)}(Q), \quad (12)$$

is exactly solvable for the Morse potential, leading to bound states with the eigenenergies

$$\epsilon_n^{(i)} = \hbar\omega_i \left(\left(n + \frac{1}{2} \right) - \chi \left(n + \frac{1}{2} \right)^2 \right) \quad n = 0, 1, \dots, n_{\text{max}}. \quad (13)$$

The index of the highest vibrational state n_{max} , which is still bound, can be determined by the requirement that the energy increases monotonically with the index n ; therefore,

$$\left. \frac{\partial \epsilon}{\partial n} \right|_{n=n_{\text{max}}} = 0 \Rightarrow n_{\text{max}} = \left\lfloor \frac{1}{2} \left(\frac{1}{\chi} - 1 \right) \right\rfloor. \quad (14)$$

The main difference between the harmonic and the Morse potential is that in the latter most states are unbound so that the density of the final states is increased if the adiabatic excitation energy exceeds the dissociation energy.

We solve the Schrödinger equation for the ground- and excited-state Morse potential numerically for each mode on an equidistant grid by diagonalizing a finite difference Hamiltonian. The overlap integrals between eigenfunctions on the excited state (n_i) and the ground state (m_i), $\langle n'_i | m_i \rangle = \int dQ_i \phi_n^{(i)}(Q_i - \Delta Q_i)^* \phi_m^{(i)}(Q_i)$, as well as the nuclear non-adiabatic coupling vectors, $\langle n'_i | \nabla m_i \rangle = \int dQ_i \phi_n^{(i)}(Q_i - \Delta Q_i)^* \frac{\partial \phi_m^{(i)}(Q_i)}{\partial Q_i}$, are evaluated numerically and tabulated. The fact that the eigenenergies are known exactly and that the Franck–Condon factors should sum to $\sum_{m_i=0} |\langle n'_i | m_i \rangle|^2 = 1$ serves as a check.

A multidimensional potential energy surface (for the ground or excited state) is constructed as a sum of the N Morse potentials,

$$V(Q_1, Q_2, \dots, Q_N) = \sum_{i=1}^N V^{(i)}(Q_i). \quad (15)$$

A vibrational wavefunction is specified by the number of phonons m_i in each mode

$$|\vec{m}\rangle = |m_1, m_2, \dots, m_N\rangle, \quad (16)$$

with eigenenergies

$$E_{\vec{m}} = \sum_{i=1}^N \epsilon_{m_i}^{(i)}. \quad (17)$$

Vibrational relaxation in the excited state is taken to be very fast as compared to electronic relaxation. Therefore, the probability of being in the initial vibrational state \vec{n} is given by the Boltzmann distribution $P_{\vec{n}} = \frac{e^{-\beta E_{\vec{n}}}}{Z}$.

The total rate of internal conversion is the sum over all transitions between the initial states $\Psi_{\text{es}\Theta_{\text{es},\vec{n}}}$ and the final states $\Psi_{\text{gs}\Theta_{\text{gs},\vec{m}}}$ weighted by the probability $P_{\vec{n}}$,

$$k_{\text{ic}}(\Delta E) = 2\pi \sum_{\vec{n}, \vec{m}} P_{\vec{n}} \left| \sum_i \langle \Psi_{\text{gs}} | \frac{\partial \Psi_{\text{es}}}{\partial Q_i} \rangle \langle \Theta_{\text{gs},\vec{m}} | \frac{\partial \Theta_{\text{es},\vec{n}}}{\partial Q_i} \rangle \right|^2 \times \delta(\Delta E + E_{\vec{n}} - E_{\vec{m}}). \quad (18)$$

$\delta(\dots)$ enforces (approximate) energy conservation between the initial and final states, $\Delta E + E_{\vec{n}} \approx E_{\vec{m}}$. In the time-dependent formalism, the non-radiative rate is expressed as

$$k_{\text{ic}}(\Delta E) = \frac{1}{2\pi} \int_{-\infty}^{+\infty} e^{i\Delta E t} \tilde{f}(t) \tilde{k}_{\text{ic}}(t) dt, \quad (19)$$

where $\tilde{f}(t)$ is the Fourier transform of the lineshape function [Gaussian $\tilde{f}_{\text{G}}(t) = 1/(2\pi) \exp(-1/2\sigma^2 t^2)$, Lorentzian

$\tilde{f}_L(t) = 1/(2\pi)[\exp(\gamma t)\theta(-t) + \exp(-\gamma t)\theta(t)]$ with $\theta(t)$ the Heaviside step function, or a Voigt profile $\tilde{f}_V(t) = \tilde{f}_G(t)\tilde{f}_L(t)$ and $\tilde{k}_{ic}(t)$ is a correlation function,

$$\tilde{k}_{ic}(t) = u_{ic}Z^{-1} \sum_{\bar{n}} e^{-\beta E_{\bar{n}}} \sum_{\bar{m}} F_{\bar{n},\bar{m}} N_{\bar{n},\bar{m}}^2 e^{-\nu(E_{\bar{m}} - E_{\bar{n}})t}. \quad (20)$$

The factor $u_{ic} = 2.598 \times 10^{17} \text{ s}^{-1}$ converts the rate to s^{-1} if all other quantities are given in atomic units. The sum extends over all vibrational initial and final states with occupation numbers \bar{n} and \bar{m} , respectively. $F_{\bar{n},\bar{m}}$ is the product of Franck–Condon factors $\text{FCF}_{n_i,m_i,i} = |\langle n'_i | m_i \rangle|^2$,

$$F_{\bar{n},\bar{m}} = |\langle \bar{n} | \bar{m} \rangle|^2 = \prod_{i=1}^N \text{FCF}_{n_i,m_i,i}, \quad (21)$$

and $N_{\bar{n},\bar{m}}$ is the scalar product of the electronic with the nuclear non-adiabatic coupling vector (divided by the overlap),

$$N_{\bar{n},\bar{m}} = \sum_{i=1}^N \left\langle \Psi_{es} \left| \frac{\partial \Psi_{gs}}{\partial Q_i} \right. \right\rangle \cdot \frac{\langle n'_i | \frac{\partial}{\partial Q_i} | m_i \rangle}{\langle n'_i | m_i \rangle} = \sum_i C_i \cdot K_{n_i,m_i,i}. \quad (22)$$

To bring Eq. (20) into a manageable form, we define

$$G_{n,m,i}(\beta, t) = e^{-\beta \epsilon_n^{(i)}} F_{n,m,i} e^{-\nu(\epsilon_m^{(i)} - \epsilon_n^{(i)})t} \quad (23)$$

and sums over products $G_{n,m,i}$ with the non-adiabatic couplings $K_{n,m,i}$,

$$g_i^{(0)}(\beta, t) = \sum_m \sum_n G_{m,n,i}(\beta, t), \quad (24)$$

$$g_i^{(1)}(\beta, t) = \sum_m \sum_n G_{m,n,i}(\beta, t) K_{n,m,i}, \quad (25)$$

$$g_i^{(2)}(\beta, t) = \sum_m \sum_n G_{m,n,i}(\beta, t) K_{n,m,i}^2. \quad (26)$$

For a harmonic oscillator, these sums can be obtained analytically, in the case of the Morse potentials, the sum runs over all eigenstates, whose number is limited by the size of the grid that was used to calculate them.

It can be shown that with these abbreviations, the correlation function becomes

$$\tilde{k}_{ic}(t) = u_{ic}Z^{-1} \left\{ \sum_{i=1}^N \sum_{j=1}^N g_i^{(1)}(\beta, t) g_j^{(1)}(\beta, t) \prod_{\substack{k \neq i \\ k \neq j}}^k g_k^{(0)}(\beta, t) + \sum_{i=1}^N g_i^{(2)}(\beta, t) \prod_{k \neq i} g_k^{(0)}(\beta, t) \right\}. \quad (27)$$

III. COMPUTATIONAL DETAILS

For the simulation of vibrationally resolved fluorescence spectra of the studied systems, the molecular structure has been first optimized in the framework of density functional theory (DFT), using the PBE0 hybrid functional (25% HF exchange)^{20,21} and the B3LYP

hybrid functional^{22,45} in combination with the def2-SVP²³ basis set as implemented in the Gaussian16²⁴ software package. The PBE0²⁰ functional was employed for the main part of the analysis, because it has been found to give reasonably accurate spectral lineshapes in the previous studies of coumarin dyes.^{25,26} The excited-state properties have been calculated using time-dependent density functional theory (TD-DFT) with the same functional and basis set. The solvent effects are treated in an implicit way via the polarizable continuum model (PCM).²⁷ For the calculation of excited-state properties, the reaction field of the solvent is adjusted to the electronic density of the first excited state (equilibrium solvation). The vibrationally resolved emission spectra together with radiative and non-radiative rates from the lowest electronic excited state were simulated within the harmonic and Franck–Condon approximations employing the *FCclasses3*⁴ program.

The internal conversion rates based on the anharmonic AS model are calculated for a range of anharmonicity parameters, $\chi = \{0.0, 0.01, 0.02, 0.03, 0.04, 0.05, 0.06, 0.07\}$. The correlation function $\tilde{k}_{ic}(t)$ of Eq. (27) is evaluated on an equidistant time grid covering the interval $[-T, T]$ for $T = 1000 \text{ fs}$ with $N_t = 2^{14} + 1$ samples. $\tilde{k}_{ic}(t)$ is Fourier transformed followed by interpolation on the discrete energy grid to obtain the rate $k_{ic}(\Delta E)$ at the emission energy ΔE .

IV. RESULTS

To test whether we can predict fluorescence quantum yields using harmonic models, we selected a sample of coumarin derivatives, for which experimental quantum yields in solution are available in the literature.^{28–33} Coumarin derivatives are versatile laser dyes³⁴ and photosensitizers in solar cells and have been studied before by some of us.³⁵ Interestingly, coumarin itself does not fluoresce presumably because of a conical intersection that opens an ultrafast decay channel to the ground state through ring cleavage.³⁶ In other coumarin derivatives, fluorescence is diminished by the presence of a dark $\pi\pi^*$ state below the photoexcited $\pi\pi^*$ state, whose relative position depends on the polarity of the solvent.³⁶ Since we want to study the validity of the harmonic approximation separately from other problems that might occur, we selected coumarins **102**, **343**, **522**, and **CIMMC**, which are well-behaved from the theoretical point of view: they do not have low-lying accessible conical intersections. Their S_1 state is bright and of $\pi\pi^*$ character and is separated by a large energy gap from higher states so that no mixing of states and breakdown of the Born–Oppenheimer approximation has to be considered. In coumarins **102** and **343**, the amine group is rigidized by six-membered rings,³⁴ which impedes pyramidalization and rotation.

A. Harmonic models and broadening functions

First, we compare different harmonic models. In Fig. 3 (and Figs. 1 and 2 in the [supplementary material](#)), we present emission spectra and radiative and internal conversion rates for all coumarins. Comparing vertical (V^*) and adiabatic (A^*) models gives us the opportunity to assess the degree of anharmonicity, because corresponding adiabatic and vertical models should give the same results for a strictly harmonic potential. In this case, the point around which the potential is expanded to second order becomes irrelevant. The

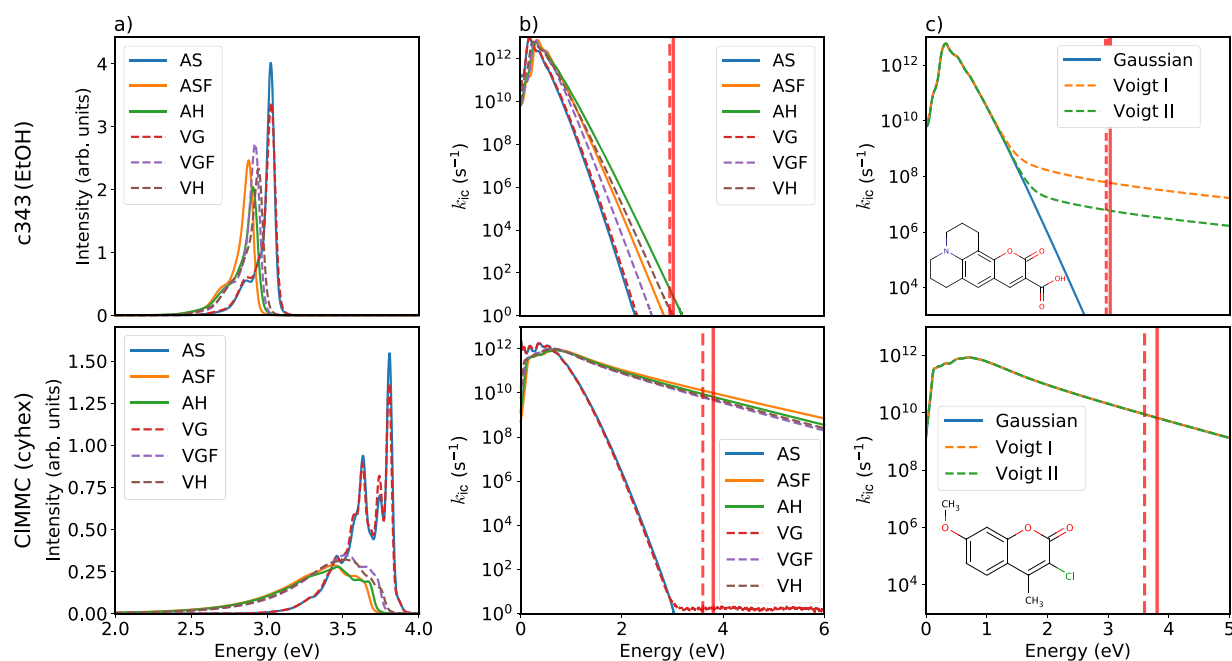


FIG. 3. **c343** in EtOH (top) and **CIMMC** in cyhex (bottom) (at $T = 300$ K). (a) Vibrationally resolved emission spectrum for different harmonic models (with Gaussian broadening of $\text{HWHM}_G = 0.02$ eV). (b) IC rate vs emission energy for different models and the same Gaussian broadening. (c) IC rate with the AH model for different broadening functions: Gaussian ($\text{HWHM}_G = 0.02$ eV), Voigt I ($\text{HWHM}_G = 0.02$ eV and $\text{HWHM}_L = 0.001$ eV), and Voigt II ($\text{HWHM}_G = 0.02$ eV and $\text{HWHM}_L = 0.0001$ eV). The solid (dashed) red line marks the adiabatic (vertical) emission energy.

agreement between vertical and adiabatic models, however, is only a necessary but not sufficient condition for the validity of the harmonic approximation, since the models become identical if the shift between the initial and final state minima is very small.

The accuracy of the harmonic approximation for the radiative decay rate k_r is remarkable (see Table I). For all cases, in which experimental data are available, our computations agree within a factor of 2, except the AH value for **CIMMC** in cyhex, which is 37% of the experimental value. The VH value for coumarin **102** in MeCN is only 7% smaller than what is measured in experiment. The emission spectra are narrow and structured for AS and VG models and are broadened and shifted to lower energies for VH and AH models. Therefore, the radiative rate, k_r , is also larger for AS and VG models, since the rate scales as ΔE^3 . Differences in the predictions of AH and VH models are almost in all cases very minor, except for **CIMMC** in cyhex where a factor of 1.7 is observed. This is not unexpected since k_r mainly depends on the overlap between the thermally populated vibrational states of the excited states (few quanta) and the low-energy vibrational states of the ground electronic state (due to the ΔE^3 dependence). These states should be well described in the harmonic approximation for rigid molecules as the coumarins considered here.

Moving to the predictions for the internal conversion rate, for all coumarins, they increase if frequency changes and Duschinsky mixings are taken into account. The rates of all harmonic models follow the exponential energy gap law, $k_{ic}(\Delta E) \propto e^{-\alpha\Delta E}$, yet the exponent depends on the model. Interestingly, also for k_{ic} AH and VH predictions are always similar, even in those cases in which

k_{ic} is very small, order of magnitudes less than what is necessary for a reliable prediction of the fluorescence quantum yield (see below). This means that if, in those cases, the underestimation of k_{ic} is due to anharmonic effects, a comparison between AH and VH does not seem to be able to highlight it. Interestingly, broad emission spectra correlate positively with high non-radiative rates.

The choice of the broadening function has only a moderate effect on the radiative rate but, on the contrary, it can have a profound influence on the non-radiative rate. It determines how tightly energy conservation between the initial and final states is enforced. The physical origin of the broadening is twofold: Inhomogeneous broadening (with a Gaussian lineshape) occurs because different molecules in the solution experience slightly different environments leading to small shifts in their energy levels. The energy shifts in an ensemble of molecules follow a Gaussian distribution. These random fluctuations increase with temperature so that the Gaussian broadening can be related to the thermal energy and the solvent reorganization energy.^{37,38} The inhomogeneous broadening can actually be estimated from first principle (using state-specific solvation models³⁸ or from molecular dynamics simulations⁵⁹) but all these estimates may introduce a computational error. Therefore, due to the scopes of this paper, we prefer to treat it as a phenomenological parameter to better understand its impact on k_r and k_{ic} . In Fig. 4, the vibrational resolved emission spectra from the AH model are compared to the experimental spectra. An inhomogeneous broadening of $\text{HWHM}_G = 0.125$ eV reproduces the spectral width and shape well. However, since the vibrational structure is

TABLE I. Fluorescence quantum yields $QY = k_r(k_r + k_{ic})^{-1}$ of coumarins predicted by harmonic models. The broadening functions are a Gaussian with $HWHM_G = 0.02$ eV and a Voigtian with $HWHM_G = 0.02$ eV and $HWHM_L = 0.001$ eV. k_{nr} is the experimental non-radiative rate. For caveats about using the Voigt profile, see Sec. IV A.

| Coumarin (solvent) | Broad. funct. | $k_r/10^8 \text{ s}^{-1}$ | | | $k_{ic} (\text{s}^{-1})$ | | $k_{nr} (\text{s}^{-1})$ Expt. | QY | | | References |
|-------------------------|------------------|---------------------------|-----|-------|--------------------------|----------------------|-----------------------------------|------|------|------------|------------|
| | | AH | VH | Expt. | AH | VH | | AH | VH | Expt. | |
| 102 (MeCN) | Gauss | 2.4 | 2.6 | 2.8 | 2.1×10^1 | 5.4×10^{-1} | 2.7×10^7 | 1.00 | 1.00 | 0.91 | 29 |
| | Voigt | 2.3 | 2.6 | | 4.6×10^7 | 4.6×10^7 | | 0.83 | 0.85 | | |
| 102 (cyhex) | Gauss | 1.9 | 2.1 | ... | 1.4×10^1 | 2.6×10^{-1} | ... | 1.00 | 1.00 | 1.05 | 29 |
| | Voigt | 1.9 | 2.1 | | 3.2×10^7 | 3.1×10^7 | | 0.85 | 0.87 | | |
| 102 (EtOH) | Gauss | 2.3 | 2.6 | 1.3 | 2.0×10^1 | 5.3×10^{-1} | 8.6×10^7 | 1.00 | 1.00 | 0.60, 0.77 | 30 and 31 |
| | Voigt | 2.3 | 2.6 | | 4.6×10^7 | 4.6×10^7 | | 0.84 | 0.85 | | |
| 343 (EtOH) | Gauss | 3.0 | 3.4 | ... | 7.9×10^0 | 9.6×10^{-1} | ... | 1.00 | 1.00 | 0.81, 0.63 | 32 and 34 |
| | Voigt | 2.9 | 3.4 | | 5.8×10^7 | 6.1×10^7 | | 0.83 | 0.85 | | |
| 522 (MeCN) | Gauss | 1.7 | 2.0 | 1.5 | 4.3×10^3 | 6.9×10^2 | 2.3×10^7 | 1.00 | 1.00 | 0.87 | 29 |
| | Voigt | 1.7 | 1.9 | | 6.4×10^7 | 6.3×10^7 | | 0.73 | 0.75 | | |
| 522 (cyhex) | Gauss | 1.4 | 1.6 | 2.3 | 4.0×10^4 | 1.3×10^4 | 5.0×10^6 | 1.00 | 1.00 | 0.98 | 29 |
| | Voigt | 1.4 | 1.6 | | 4.3×10^7 | 4.3×10^7 | | 0.76 | 0.79 | | |
| CIMMC (cyhex) | Gauss | 0.7 | 1.2 | 1.9 | 6.6×10^9 | 5.1×10^9 | 1.4×10^9 | 0.01 | 0.02 | 0.12 | 33 |
| | Voigt | 0.7 | 1.2 | | 6.7×10^9 | 5.2×10^9 | | 0.01 | 0.02 | | |
| CIMMC (water) | Gauss | 2.6 | 2.9 | 2.1 | 4.0×10^7 | 1.4×10^7 | 6.0×10^7 | 0.87 | 0.95 | 0.83 | 33 |
| | Voigt | 2.6 | 2.9 | | 7.9×10^7 | 5.2×10^7 | | 0.76 | 0.85 | | |

completely washed out, we use a smaller inhomogeneous broadening of $HWHM_G = 0.02$ eV for presenting the emission spectra in Fig. 3. The effect of the inhomogeneous broadening on the radiative and non-radiative rates is only minor.

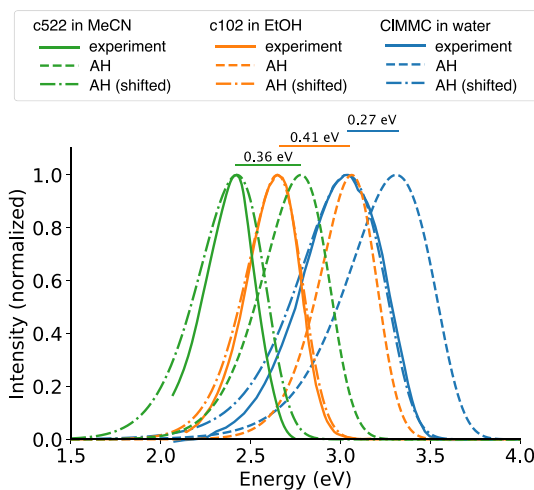


FIG. 4. Comparison between experimental and theoretical emission spectra. The theoretical spectra were obtained with the AH model ($HWHM_G = 0.125$ eV and $HWHM_L = 0$ eV) at $T = 300$ K. To make comparison of the spectral width and shape easier, the theoretical spectra were shifted so that the maxima of the experimental and theoretical curves coincide. Experimental spectra were digitized from the following sources: **c522** in MeCN,⁴⁴ **c102** in EtOH,³⁰ and **CIMMC** in water.³³

The homogeneous broadening (Lorentzian lineshape) in turn is due to the finite lifetime τ of vibrational states, with $HWHM_L = \gamma = \frac{1}{\tau}$. This type of broadening can be understood as a consequence of the Heisenberg uncertainty principle. Both types of broadening are combined in the Voigt profile, which is the convolution of a Gaussian with a Lorentzian function. Data in Table I show that the effect of the adopted Lorentzian broadening on k_r is negligible. In contrast, while results for the non-radiative rate are not very sensitive to the Gaussian broadening, they can be dramatically affected by the Lorentzian broadening. A Lorentzian profile has a long tail and, thus, allows transitions between vibrational states with large energy mismatch, where the Franck-Condon factors are large. Consequently, the internal conversion rate increases with γ , as demonstrated in Fig. 4 of the supplementary material. For large γ , the rate in fact becomes independent of the vibrational structure and is completely dominated by the broadening function. It is very difficult to estimate γ without knowledge of the experimental emission spectrum. If a spectrum is available with some luck a Voigt profile can be fitted to a shoulder of the lowest vibrational peak. However, separating the inhomogeneous from the homogeneous broadening is a tricky task, in particular since both types of broadening affect the spectral width and, thus, the radiative rate, while it is mostly the homogeneous broadening which affects the internal conversion rate. Also, this approach defeats the purpose of predicting decay rates from first principles. Actually, we compute the contribution to the lifetime due to spontaneous emission as k_r^{-1} (data in Table I). So we can say that k_r^{-1} represents an upper bound for the lifetime. It is usually so long that it does not alter k_{ic} .

The choice of the broadening function affects the non-radiative rates strongly, unless the rate is very large already. The Voigt profile

gives a high non-radiative rate at energies where the rate is zero with a Gaussian profile. In this regime, the non-radiative rate depends solely on the width of the Lorentzian and not on the vibrational structure. For instance, for coumarin **343** the Gaussian profile predicts $k_{ic} \approx 0.0 \text{ s}^{-1}$ at an adiabatic emission energy of 3 eV, while the Voigt profile predicts $k_{ic} = 10^7$ to 10^9 s^{-1} depending on the width of the Lorentzian (see the top of Fig. 3).

In the case of CIMMC (see the bottom of Fig. 3), accounting for frequency changes (ASF and VGF) increases the rate dramatically by several orders of magnitude relative to the displaced oscillator models. The Duschinsky effect, which in the case of CIMMC is small, increases the rates further. Here, adiabatic and vertical models give similar results pointing to the validity of the harmonic approximation. Unlike all other coumarins, the non-radiative rate does not depend on the broadening function, and Gaussian and Voigt profiles give the same results over the entire energy range.

We proceed to compare the predicted fluorescence quantum yields, $QY = k_r(k_r + k_{ic})^{-1}$, with experiment in Table I. The large difference between AS/VG and the other models shows that the assumption of independent modes is usually not valid. In Table I, we, therefore, only list rates and quantum yields for the AH and VH models. With the exception of CIMMC, the Gaussian profile yields non-radiative rates, which are orders of magnitude too low so that the fluorescence quantum yield is always 1. With a Voigt profile, the non-radiative rates increase to a reasonable level; however, they depend on the arbitrary choice of the width of the Lorentzian. The apparent agreement between the experimental and theoretical rates when using the Voigt profile with $\gamma = 0.001 \text{ eV}$ can be misleading. If we interpret the homogeneous broadening as the result of a finite lifetime of the excited state, this γ corresponds to a lifetime of 658 fs, i.e., to the existence of another non-radiative decay process (e.g., ISC and CI) that has $k'_{nr} = 1.5 \times 10^{12} \text{ s}^{-1}$. If this process exists, it completely dominates the other ones and brings QY to 0 since $QY = k_r(k_r + k_{ic} + k'_{nr})^{-1}$. In other terms, the fact that the internal conversion rate increases from 10^1 to 10^7 s^{-1} is of little interest. No excited-state population decays via internal conversion since the other process is much faster. Before internal conversion can set in, all population has already decayed via the additional channel. Thus, if a large γ is needed to reproduce experimental rates, this means that either the most important decay channel is missing in the model or that anharmonicities are not negligible. Therefore, fitting γ to reproduce experimental non-radiative rates⁴⁰ is not advisable.

A possible way to determine a unique γ is to use a self-consistent procedure: we start with an arbitrary γ and compute the radiative and IC rates. In the following iterations, we set $\gamma = k_r + k_{ic}$ and repeat the calculation of the rates with the new Lorentzian broadening. γ converges typically after a few iterations to a unique value that does not depend on the initial starting value. The self-consistent broadenings are close to 0: $\gamma_{SC} = 4.4 \times 10^{-6} \text{ eV}$ for CIMMC in cyhex and $\gamma_{SC} = 1.0 \times 10^{-7} \text{ eV}$ for **343** in ethanol. Although substituting the results of first-order perturbation theory back into a first-order theory is somewhat questionable, this procedure shows that if we require γ to be uniquely defined, its value is much smaller than what would be necessary to reproduce experimental non-radiative rates.

Only for CIMMC in water and cyclohexane (cyhex), the quantum yield is predicted reliably.

We can identify two conditions that should be met if the results are to be trusted: (1) AH and VH models should agree and (2) Gaussian and Voigt profiles should not differ greatly at the adiabatic emission energy. There is also an apparent connection between the width of the emission spectrum and the robustness of the predicted rates to the choice of the broadening function.

For systems with short vibronic progressions (narrow spectra), such as coumarins **102**, **343**, and **522**, the rate is small and very sensitive to the broadening, while for those with long vibronic progressions (broad spectra), such as CIMMC in cyhex and to a lesser degree in water, all broadening functions give the same result.

One of the decay processes we have neglected so far is inter-system crossing from S_1 to the energetically close T_2 state (see Table 1 in the supplementary material). Although the spin-orbit couplings are very small, we cannot exclude that this decay channel contributes significantly to the non-radiative rate. We leave this question to a future study. In a relativistic treatment, where spin is not a good quantum number anymore, singlet and triplet states would be mixed so that the distinction between IC and ISC becomes blurred. Therefore, all of the above considerations would also apply to ISC. However, we expect the harmonic approximation to be better justified in the case of ISC since the energy gap is usually smaller.

B. Anharmonic AS model—Anharmonicity and broadening function

Finally, we consider the effects of anharmonicity and the choice of the broadening function on the internal conversion rate in the adiabatic shift model. We use coumarin CIMMC in cyhex as an example.

Figure 5 depicts $k_{ic}(\Delta E)$ for increasing anharmonicity. At intermediate energies ($0.5 < \Delta E < 3.0 \text{ eV}$), the anharmonic rates are higher than the harmonic one, but $\log(k_{ic})$ still decreases linearly with ΔE , while at higher energies ($3.0 < \Delta E$) the rates start to deviate from the exponential energy gap law.⁴¹ High internal conversion

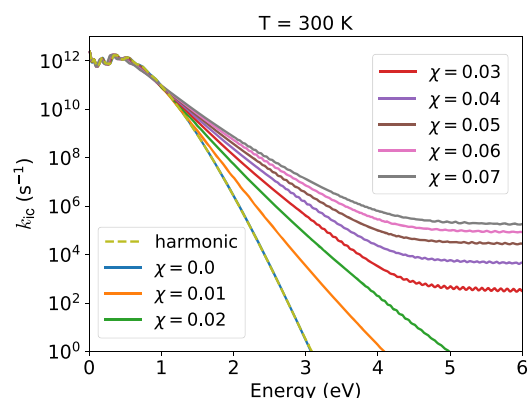


FIG. 5. CIMMC in cyhex. Internal conversion rates from an anharmonic AS model for different degrees of anharmonicity χ . The dashed line shows the rate obtained with *FCclasses3* for the AS model, which should be identical to the $\chi = 0.0$ case.

rates require energy conservation and large Franck–Condon factors, but these two conditions cannot be fulfilled at the same time: if the final states are low-lying vibrational states, the Franck–Condon factors are high but energy conservation is poorly fulfilled. On the other hand, if the final states are highly excited vibrational states such that the sum of the vibrational energies equals the optical gap ΔE , the Franck–Condon factors are very low, due to the oscillatory nature of high-lying vibrational states. In the harmonic approximation, the Franck–Condon factors $|\langle n'|m\rangle|^2$ vanish quickly as $m \rightarrow \infty$. The effect of including anharmonicity is that the Franck–Condon factors decrease slower with increasing m (see Fig. 3 in the [supplementary material](#)). Therefore, more final states are available, which have relatively high overlaps with the initial states in the anharmonic case than in the harmonic case.

What value should one take for the anharmonicity χ ? A possible qualitative argument for selecting a plausible value for χ is the following: in infrared spectroscopy, it is rather customary to multiply the computed harmonic frequencies by a factor, usually 0.96 for B3LYP/6-31G(d),⁴² since this improves the comparison of the harmonic vibrational frequencies with the experimental fundamentals. Of course, this is just a phenomenological parameter and it corrects also for other errors, but it is considered that one of the most important effects is anharmonicity.⁴² According to Eq. (13), the ratio of the first transition energy and the harmonic frequency is

$$\frac{\epsilon_1 - \epsilon_0}{\hbar\omega} = 1 - 2\chi. \quad (28)$$

Therefore, if we impose that this fraction is 0.96, we get $\chi = 0.02$. This suggests that the values $\chi = 0.03, \dots, 0.07$, where the deviations of k_{ic} from the harmonic approximation are sizable, might be too large. On the other hand, the anharmonic AS model just includes diagonal anharmonicities, while for the harmonic models, we have seen that quadratic couplings (frequency changes and Duschinsky effect) play an important role. Therefore, it is conceivable that the off-diagonal anharmonicities would be even more important than the diagonal ones.

These simple calculations with the AS model show that deviations from the energy gap law are attributable to anharmonicities. Choosing a large Lorentzian broadening γ has a similar effect (cf. Fig. 4 in the [supplementary material](#)). However, a large γ actually implies the existence of a non-radiative process we have not considered, which reduces the lifetime of the excited states. In both cases (large χ or large γ), the rates are higher and the function $\log(k_{ic}(\Delta E))$ exhibits a kink, where the slope of the curve suddenly becomes less steep.

Furthermore, it should be noted that the choice of the method to describe the electronic structure adds another uncertainty to the computed rates. Even within density functional theory, the choice of the functional type (GGA, hybrid, range-corrected hybrid) and the solvation model can lead to differences in the vibrational structure and, above all, to deviations in the vertical/adiabatic energies in the order of 0.5 eV. The differences in the resulting emission energies and IC rates between the PBE0 and the B3LYP functional are shown in Table II. Since the slope of the curve k_{ic} vs ΔE is very steep, the choice of the functional can change the internal conversion rates by several orders of magnitude.

TABLE II. Emission energies and internal conversion rates for the functionals PBE0 and B3LYP. E_{em} is the energy at the maximum of the emission spectrum. The theoretical spectra were obtained with the AH model ($HWHM_G = 0.125$ eV and $HWHM_L = 0$ eV) at $T = 300$ K. Sources for experimental spectra are the same as in Fig. 4, except for coumarin **343**⁴³ (PhotochemCAD online database).

| Coumarin (solvent) | E_{em} (eV) | | | k_{ic} (s ⁻¹) | |
|-----------------------|---------------|-------|-------|-----------------------------|----------------------|
| | PBE0 | B3LYP | Expt. | PBE0 | B3LYP |
| 102 (MeCN) | 3.06 | 2.63 | ... | 2.1×10^1 | 4.1×10^3 |
| 102 (cyhex) | 3.26 | 2.99 | ... | 1.4×10^1 | 9.0×10^2 |
| 102 (EtOH) | 3.06 | 2.64 | 2.65 | 2.0×10^1 | 3.9×10^3 |
| 343 (EtOH) | 2.88 | 2.77 | 2.65 | 7.9×10^0 | 1.5×10^2 |
| 522 (MeCN) | 2.78 | 2.39 | 2.42 | 4.3×10^3 | 4.6×10^5 |
| 522 (cyhex) | 2.99 | 2.70 | ... | 4.0×10^4 | 3.8×10^5 |
| CIMMC (cyhex) | 3.43 | 3.40 | ... | 6.6×10^9 | 1.2×10^{10} |
| CIMMC (water) | 3.31 | 3.32 | 3.04 | 4.0×10^7 | 3.0×10^7 |

V. CONCLUSION

In this work, we investigated the reliability of the harmonic approximation for the prediction of the radiative and non-radiative decay rates and, therefore, of the fluorescence quantum yield of a number of coumarin dyes. We first examined the performance of a hierarchy of vertical and adiabatic harmonic models, and afterward, we developed and applied a simple AS anharmonic model in order to qualitatively analyze the possible effect of anharmonicity. Therefore, we can try to enunciate a number of “rules of thumb” that can help judging whether the results predicted from harmonic models are reliable:

(Rule I) Harmonic predictions for k_r are in good agreement with experiment for the few cases where experimental data are available. Frequency changes and Duschinsky mixings have only a moderate effect and tend to slightly decrease k_r . *(Rule II) As far as the prediction of k_{ic} is concerned, it is fundamental to account for frequency changes and Duschinsky rotation since they increase k_{ic} strongly.* In the examples considered, the Duschinsky effect is more moderate, but this is a peculiarity of coumarins, and there are many other systems where mode mixing can be significant. Therefore, we advise against using the AS and VG models, as they neglect the effects that contribute most to the non-radiative rate. k_{ic} shows a much larger dependence on the specificity of the molecule and the adopted methodology than k_r . Therefore, it is much more difficult to compute. This is an expected result since k_{ic} mainly depends on a reliable description of strongly excited vibrational states, i.e., the same states that are responsible for the very far tail of the emission spectrum. *(Rule III) As a matter of fact, a broad emission spectrum correlates with large k_{ic} .* These observations suggest that a further check of the reliability of computational estimates might be: do the calculations allow for a realistic reproduction of the low-energy tail of the emission spectrum?

Broadening functions insert phenomenologically those effects that attenuate the energy conservation rule. They account for important facts like the effect of energy fluctuations, lifetimes, and other effects that matter. *(Rule IV) The inhomogeneous broadening has*

a weak impact on k_r and practically no impact on k_{ic} . The homogeneous broadening is connected with the lifetime of the excited state, which is equal to or shorter than the fluorescence lifetime k_r^{-1} . Of course, other processes can decrease the lifetime so that we also treated γ as a parameter. However, since, in general, we are not able to compute a realistic number for the lifetime, we use this analysis only to set a limit on the reliability of our results. (*Rule V*) *If our results strongly depend on γ , they are not reliable.* In fact, in those cases, k_{ic} is not dominated by the vibronic profile (which carries information on the target molecule) but by the phenomenological width of the Lorentzian γ . This happens when, with our level of theory, we predict a very small k_{ic} . It may be that in reality, the non-radiative decay is much faster than what we predict, but this depends on other processes—conical intersections, intersystem crossing, and internal conversions due to interactions with the environment (a kind of pressure broadening)—that have not been considered in our calculations. They would strongly modify the prediction of the fluorescence quantum yield and, clearly, their effect cannot be reproduced by a phenomenological increase in γ in the computation of the non-radiative process we have considered. In summary, when they are important, they should be identified and properly taken into account. This clearly makes a reliable computational prediction of QY for these systems much more complicated.

The effect of anharmonicity (beyond the AS model) is the most delicate and elusive point since anharmonicities can be many. In principle, conical intersections and multiple conformations all fall into the category of extreme anharmonicities. Assuming Morse potentials for all modes, we find that for a typical value of $\chi = 0.02$, anharmonic effects are not drastic. One should bear in mind, however, that a Morse potential does not describe low-energy modes, such as rotations around single bonds correctly, and that the coupling between different modes is also neglected in the AS model. Including anharmonic corrections for a realistic model of coupled modes is not feasible so far.

(*Rule VI*) *An obvious condition is that results from AH and VH models must be similar*, as this is necessary for the validity of the harmonic approximation. Since we should expect that the error is at least equal to the difference of AH and VH predictions, this sets a lower bound for the accuracy. Our results, however, clarify that it is only a necessary and not a sufficient condition. A second condition is that small values of the Lorentzian broadening should not strongly modify our estimate of the QY.

(*Rule VII*) *Interestingly, our results suggest that the width of the Lorentzian function and anharmonic effects start ruling k_{ic} for values of ΔE , for which $k_{ic}(\Delta E) < 10^{-5}k_{ic}^{\max}$.* In summary, we can conclude that our methodology can be considered reliable only for molecules with adiabatic excitation energies such that $k_{ic}(\Delta E) > 10^{-5}k_{ic}^{\max}$. Since k_{ic}^{\max} is typically 10^{12} to 10^{13} s^{-1} , the critical values for which our computed non-radiative rates start not being robust anymore are 10^7 to 10^8 s^{-1} , i.e., the typical values for k_r . This limits our predictability to the extreme case $\text{QY} = 0$: if $k_{ic} \gg k_r$ already in the harmonic approximation, the prediction $\text{QY} = 0$ is very robust since anharmonicity and homogeneous broadening only increase the internal conversion rate. However, values of $\text{QY} > 0$ are likely those more challenging for our theory and in those cases our prediction will always be a little bit questionable.

The fulfillment of the condition $k_{ic}(\Delta E) > 10^{-5}k_{ic}^{\max}$ depends on two factors working in different directions: the value of ΔE and

the extension of the vibronic progressions. The smaller ΔE and the longer the vibronic progressions, the easier it is that the condition is true. Small ΔE means emission in the red region of the visible spectrum or in the near infrared. Long vibronic progression means molecules with broad emission spectra and, therefore, characterized by significant displacements of the excited- and ground-state equilibrium geometries and, according to our analysis, also significant changes in the normal mode frequencies. It is worthwhile to reiterate the hypotheses underlying these considerations: we assume that direct internal conversion from a thermalized bright state to the ground state, triggered by non-adiabatic couplings, is the only relevant non-radiative process. In other words, sequential decay, possible ISC, photoisomerizations, and decay at conical intersections are neglected.

The chosen examples illustrate that in order to make theoretical predictions for fluorescence quantum yields, it is not sufficient to compare only simulated quantum yields with the experimental ones, but it is recommendable to compare and analyze the radiative and non-radiative rates and the influence of varying the harmonic model and broadening parameterization. If there is a drastic difference in the obtained values for k_{ic} , one should not consider these results accurate enough for the description of fluorescence quantum yields. In conclusion, a “black-box” method for predicting fluorescence quantum yields from first principles does not seem within reach, yet.

SUPPLEMENTARY MATERIAL

See the [supplementary material](#) for additional figures mentioned in the text.

ACKNOWLEDGMENTS

R.M. and A.H. acknowledge financial support within the ERC Consolidator Grant “DYNAMO” (Grant No. 646737). R.M. and J.H. thank the Deutsche Forschungsgemeinschaft for support of this work within the Research Group FOR 1809. This research was partially supported by the project STIM-REI, Contract Number: KK.01.1.1.01.0003, funded by the European Union through the European Regional Development Fund—the Operational Programme Competitiveness and Cohesion 2014-2020 (KK.01.1.1.01). V.B.K. and M.B. acknowledge computational facilities of the super-computer SRCE at the University of Zagreb as well as doctoral study of Biophysics at the University of Split.

REFERENCES

- 1 J. Batchelder, A. Zewai, and T. Cole, *Appl. Opt.* **18**, 3090 (1979).
- 2 J. V. Frangioni, *Curr. Opin. Chem. Biol.* **7**, 626 (2003).
- 3 Y. Niu, W. Li, Q. Peng, H. Geng, Y. Yi, L. Wang, G. Nan, D. Wang, and Z. Shuai, *Mol. Phys.* **116**, 1078 (2018).
- 4 F. Santoro and J. Cerezo, FCclasses3, a code to simulate electronic spectra, version FCclasses3-0.1, 2019, see <http://www.pi.iccom.cnr.it/fcclasses>.
- 5 S. Banerjee, A. Baiardi, J. Bloino, and V. Barone, *J. Chem. Theory Comput.* **12**, 774 (2016).
- 6 R. R. Valiev, V. N. Cherepanov, R. T. Nasibullin, D. Sundholm, and T. Kurten, *Phys. Chem. Chem. Phys.* **21**, 18495 (2019).

- ⁷B. de Souza, G. Farias, F. Neese, and R. Izsák, *J. Chem. Theory Comput.* **15**, 1896 (2019).
- ⁸R. R. Valiev, V. N. Cherepanov, G. V. Baryshnikov, and D. Sundholm, *Phys. Chem. Chem. Phys.* **20**, 6121 (2018).
- ⁹Q. Peng, Y. Yi, Z. Shuai, and J. Shao, *J. Am. Chem. Soc.* **129**, 9333 (2007).
- ¹⁰A. W. Kohn, Z. Lin, and T. Van Voorhis, *J. Phys. Chem. C* **123**, 15394 (2019).
- ¹¹J. Hoche, A. Schulz, L. M. Dietrich, A. Humeniuk, M. Stolte, D. Schmidt, T. Brixner, F. Würthner, and R. Mitrić, *Chem. Sci.* **10**, 11013 (2019).
- ¹²S. Lin, C. Chang, K. Liang, R. Chang, J. Zhang, T. Yang, M. Hayashi, Y. Shiu, and F. Hsu, *Adv. Chem. Phys.* **121**, 1 (2002).
- ¹³Q. Peng, Y. Niu, C. Deng, and Z. Shuai, *Chem. Phys.* **370**, 215 (2010).
- ¹⁴F. J. Avila Ferrer and F. Santoro, *Phys. Chem. Chem. Phys.* **14**, 13549 (2012).
- ¹⁵The effect of anharmonicity on the absorption and fluorescence spectra has been studied in C. Zhu *et al.*, *Chem. Phys.* **358**, 137 (2009) also employing the displaced oscillator model (AS) and the Morse potential.
- ¹⁶Y. Niu, Q. Peng, and Z. Shuai, *Sci. China, Ser. B: Chem.* **51**, 1153 (2008).
- ¹⁷Q. Peng, Y. Niu, Q. Shi, X. Gao, and Z. Shuai, *J. Chem. Theory Comput.* **9**, 1132 (2013).
- ¹⁸P. M. Morse, *Phys. Rev.* **34**, 57 (1929).
- ¹⁹J. P. Dahl and M. Springborg, *J. Chem. Phys.* **88**, 4535 (1988).
- ²⁰C. Adamo and V. Barone, *J. Chem. Phys.* **110**, 6158 (1999).
- ²¹M. Ernzerhof and G. E. Scuseria, *J. Chem. Phys.* **110**, 5029 (1999).
- ²²A. D. Becke, *J. Chem. Phys.* **98**, 1372 (1993).
- ²³F. Weigend, *Phys. Chem. Chem. Phys.* **8**, 1057 (2006).
- ²⁴M. J. Frisch, G. W. Trucks, H. B. Schlegel, G. E. Scuseria, M. A. Robb, J. R. Cheeseman, G. Scalmani, V. Barone, G. A. Petersson, H. Nakatsuji, X. Li, M. Caricato, A. V. Marenich, J. Bloino, B. G. Janesko, R. Gomperts, B. Mennucci, H. P. Hratchian, J. V. Ortiz, A. F. Izmaylov, J. L. Sonnenberg, D. Williams-Young, F. Ding, F. Lipparini, F. Egidi, J. Goings, B. Peng, A. Petrone, T. Henderson, D. Ranasinghe, V. G. Zakrzewski, J. Gao, N. Rega, G. Zheng, W. Liang, M. Hada, M. Ehara, K. Toyota, R. Fukuda, J. Hasegawa, M. Ishida, T. Nakajima, Y. Honda, O. Kitao, H. Nakai, T. Vreven, K. Throssell, J. A. Montgomery, Jr., J. E. Peralta, F. Ogliaro, M. J. Bearpark, J. J. Heyd, E. N. Brothers, K. N. Kudin, V. N. Staroverov, T. A. Keith, R. Kobayashi, J. Normand, K. Raghavachari, A. P. Rendell, J. C. Burant, S. S. Iyengar, J. Tomasi, M. Cossi, J. M. Millam, M. Klene, C. Adamo, R. Cammi, J. W. Ochterski, R. L. Martin, K. Morokuma, O. Farkas, J. B. Foresman, and D. J. Fox, Gaussian 16 Revision A.03, Gaussian, Inc., Wallingford, CT, 2016.
- ²⁵F. J. A. Ferrer, J. Cerezo, J. Soto, R. Improta, and F. Santoro, *Comput. Theor. Chem.* **1040-1041**, 328 (2014).
- ²⁶V. Barone, M. Biczysko, J. Bloino, L. Carta, and A. Pedone, *Comput. Theor. Chem.* **1040-1041**, 144 (2014).
- ²⁷J. Tomasi, B. Mennucci, and R. Cammi, *Chem. Rev.* **105**, 2999 (2005).
- ²⁸M. Taniguchi and J. S. Lindsey, *Photochem. Photobiol.* **94**, 290 (2018).
- ²⁹G. Jones II, W. R. Jackson, C. Y. Choi, and W. R. Bergmark, *J. Phys. Chem.* **89**, 294 (1985).
- ³⁰S. Mondal, R. Halder, B. Biswas, B. Jana, and P. C. Singh, *J. Chem. Phys.* **144**, 184504 (2016).
- ³¹K. Rurack and M. Spieles, *Anal. Chem.* **83**, 1232 (2011).
- ³²V. A. Lapina, T. A. Pavich, P. P. Pershukovich, A. V. Trofimov, N. N. Trofimova, Y. B. Tsaplev, and P. P. Zak, *J. Phys. Org. Chem.* **30**, e3731 (2017).
- ³³J. S. Seixas de Melo, R. S. Becker, and A. L. Maqanita, *J. Phys. Chem.* **98**, 6054 (1994).
- ³⁴G. Reynolds and K. H. Drexhage, *Opt. Commun.* **13**, 222 (1975).
- ³⁵J. Cerezo, F. J. A. Ferrer, and F. Santoro, *Phys. Chem. Chem. Phys.* **17**, 11401 (2015).
- ³⁶C. M. Krauter, J. Möhring, T. Buckup, M. Pernpointner, and M. Motzkus, *Phys. Chem. Chem. Phys.* **15**, 17846 (2013).
- ³⁷R. Marcus, *J. Chem. Phys.* **43**, 1261 (1965).
- ³⁸F. J. A. Ferrer, R. Improta, F. Santoro, and V. Barone, *Phys. Chem. Chem. Phys.* **13**, 17007 (2011).
- ³⁹J. Cerezo, F. J. A. Ferrer, G. Prampolini, and F. Santoro, *J. Chem. Theory Comput.* **11**, 5810 (2015).
- ⁴⁰I. Kim, W.-J. Son, Y.-S. Choi, A. Osipov, D. Lee, H. Lee, Y. Jung, J. Son, H. Choi, W. Sotoyama *et al.*, *J. Chem. Phys. C* **123**, 11140 (2019).
- ⁴¹R. Englman and J. Jortner, *Mol. Phys.* **18**, 145 (1970).
- ⁴²A. P. Scott and L. Radom, *J. Phys. Chem.* **100**, 16502 (1996).
- ⁴³H. Du, R.-C. A. Fuh, J. Li, L. A. Corkan, and J. S. Lindsey, *Photochem. Photobiol.* **68**, 141 (1998).
- ⁴⁴S. Nad and H. Pal, *J. Photochem. Photobiol., A* **134**, 9 (2000).
- ⁴⁵P. J. Stephens, F. J. Devlin, C. F. Chabalowski, and M. J. Frisch, *J. Phys. Chem.* **98**, 11623 (1994).

3.2 Squaraine-based J-aggregates

Reprinted from:

Margarita Bužančić Milosavljević and Vlasta Bonačić-Koutecký. Design of J-aggregates-like oligomers built from squaraine dyes exhibiting transparency in the visible regime and high fluorescence quantum yield in the NIR region. *Phys. Chem. Chem. Phys.*, 26, 1314-1321, 2024. Reproduced with permission from the Royal Society of Chemistry.


 Cite this: *Phys. Chem. Chem. Phys.*,
2024, 26, 1314

Design of J-aggregates-like oligomers built from squaraine dyes exhibiting transparency in the visible regime and high fluorescence quantum yield in the NIR region†

 Margarita Bužančić Milosavljević ^a and Vlasta Bonačić-Koutecký ^{*abc}

New materials for transparent luminescent solar concentrators (TLSCs) are of large interest. Therefore, we investigated the optical properties of J-aggregates-like oligomers (hereinafter referred to as J-aggregates) based on covalently bound squaraine dyes in toluene solvent using DFT and TD-DFT methods. In addition, the rate constants needed for the prediction of fluorescence quantum yield (QY) have been calculated using Fermi's Golden rule and vertical harmonic approximation (VH) for ground and excited states. In the context of QY prediction, different broadening of the lineshape has also been employed. We found that J-aggregates based on squaraine dyes exhibit near-infrared (NIR) selective absorption and emission as well as high fluorescence QY. Comparison of the properties obtained for dimers, trimers and tetramers belonging to two classes (SQA and SQB) of J-aggregates allows us to select the tetramer of SQA J-aggregates as suitable for application. The scaling model for $N \geq 4$ monomer subunits supports quantitative findings. Therefore, we propose J-aggregates containing $N \geq 4$ subunits of SQA with a central squaric acid ring with two oxygen atoms in toluene solvent as a suitable candidate for TLSC application.

 Received 31st October 2023,
Accepted 4th December 2023

DOI: 10.1039/d3cp05291e

rsc.li/pccp

1 Introduction

The design of materials with properties suitable for transparent luminescent solar concentrators (TLSCs) is a challenging task. TLSCs contain a harvesting surface with luminophores that should absorb and emit mainly outside the visible (VIS) region.^{1–4} Adequate materials for such devices require high aesthetic quality and high power conversion efficiency,⁵ which can be realized through transparency and by tuning optical efficiency. For this purpose, luminophores that harvest the ultraviolet (UV) and near-infrared (NIR) parts of the solar spectrum^{6,7} and at the same time have high fluorescence quantum yield (QY)^{5,8} are needed. For TLSC applications, the photophysical properties of luminophores, such as energy losses, have to be also considered. Among different luminophore energy losses, the reabsorption of photons seems to be

the important issue.⁹ The minimization of the reabsorption loss can be achieved with lowering of the non-radiative decay processes and consequently enhancing the QY.^{10–13} In the context of transparency and QY, some aggregates^{14,15} have been studied.

In this contribution, we investigate J-aggregates based on covalently bound squaraine dyes as candidates fulfilling both conditions of transparency and high QY. Numerous applications of squaraine dyes have been accomplished, including their use in photovoltaic devices.^{16,17} They have also been studied in the context of both high QY and NIR optical properties.^{18–20} Experimental and theoretical work has been performed on J-aggregates built from squaraine dimers and trimers^{21–23} to gain insight into their structural, optical, and exciton properties. In addition, the influence of oligomer chain length on optical characteristics has been investigated.^{24–27} Recently, a review on luminescent solar concentrators (LSCs) gave a critical view of the field and its potential for the future.²⁸

Squaraine based J-aggregates with a given number N of subunits producing a high QY can serve as UV and NIR selective harvesting materials. Therefore, they might be good candidates for integration into greenhouses, mobile electronics, and electric automobiles.

Fluorescence QY is determined by the ratio of the radiative rate k_r to the sum of the radiative rate k_r and all other non-

^a Center of Excellence for Science and Technology-Integration of Mediterranean region (STIM), Faculty of Science, University of Split, Ruđera Boškovića 33, 21000 Split, Croatia. E-mail: margarita@stim.unist.hr

^b Interdisciplinary Center for Advanced Science and Technology (ICAST) at University of Split, Meštrovićevo šetalište 45, 21000 Split, Croatia

^c Department of Chemistry, Humboldt Universität zu Berlin, Brook-Taylor-Strasse 2, 12489 Berlin, Germany. E-mail: vbk@cms.hu-berlin.de

† Electronic supplementary information (ESI) available. See DOI: <https://doi.org/10.1039/d3cp05291e>



radiative decay rates $k_{\text{nr}} = k_{\text{ic}} + k_{\text{isc}}$ including internal conversion (IC) and intersystem crossing (ISC). A high value of QY can be obtained by increasing k_{r} and decreasing k_{nr} rates. This is particularly difficult to achieve in NIR since k_{ic} increases strongly with the reduction of the excitation energy. Since the optimization of a single chromophore in order to reach a high QY depends on many parameters, J-aggregates might be a simple alternative. The enhancement of the fluorescence QY in some J-aggregates has been assigned to superradiance due to the linear growth of the radiative rate with the delocalization length. Furthermore, the internal conversion rate k_{ic} simultaneously decreases with delocalization length. Both effects depend on the delocalization of excitons.²⁹

In this contribution, in addition to optical properties, we present theoretical results for the QY prediction of SQA and SQB indolenine squaraine dyes in toluene solvent packed in J-aggregates. SQA contains a central squaric acid ring with two oxygen atoms as subunits and SQB squaraine dyes are formed by the dicyanovinylene group substitution at the central squaraine ring (*cf.* Scheme 1). For both J-aggregates built from SQA and SQB in toluene solvent, we investigated the optical properties in the VIS, UV, and NIR regimes in the context of application as materials for TLSC. Comparison of the theoretical and experimental optical properties of J-aggregates built from squaraine dimers and trimers serves to estimate the reliability of theoretical predictions. The results on the optical properties for tetramers of J-aggregates built from SQA and SQB squaraine dyes in toluene solvent, as well as QY values, serve to initiate additional experiments.

In order to determine the general trend of the internal conversion rate k_{ic} with the size N of the SQA and SQB J-aggregates, we use the scaling relation²⁹ based on the Englman and Jortner energy gap law.³⁰ This qualitative approach predicts lower k_{ic} and consequently higher QY values for SQA than for SQB J-aggregates. Although the SQB J-aggregates for $N \leq 4$ have QY values above 50%, higher QY values are preferable in the context of applications. In addition, minimized reabsorption loss can be achieved. We define the theoretical limit for intensity above $1.0 f_{\text{e}}$ as semitransparency in the VIS region of the absorption spectrum.

Altogether, both conditions, such as transparency in the visible regime as well as absorption and emission in NIR with

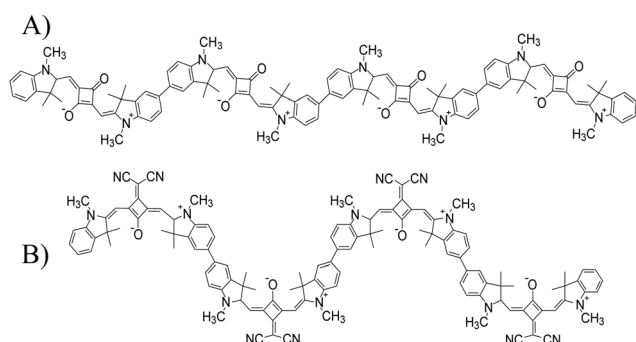
high fluorescence QY can be satisfied for SQA J-aggregates with $N \geq 4$. Therefore, we propose J-aggregates formed by SQA tetramers or by a larger number of subunits as new materials suitable for TLSC application.

2 Computational

Calculations of structural and optical properties, including the absorption and emission of J-aggregates in a solvent are necessary before determining radiative k_{r} and internal conversion rate k_{ic} constants needed for the calculation of fluorescence QY. For this purpose, we use density functional theory (DFT) for the optimization of molecular structures and time-dependent density functional theory (TD-DFT) to determine excited state properties using the Gaussian16³¹ program. In both cases, the PBE0 hybrid functional^{32,33} and def2-SVP³⁴ basis set are employed since they provide acceptable agreement with available experimental data. A comparison of the absorption spectra obtained by larger basis sets shows that the def2-SVP with 1230 AOs is adequate since the absorption spectra are not dependent on the choice of the tested basis sets (cc-pVTZ with 2628 AOs and def2-TZVP with 3050 AOs). The influence of different functionals on the absorption spectra has also been investigated. Comparison between experimental data for the most intense transition of the absorption spectrum for the trimer SQA J-aggregate shows the largest difference for CAM-B3LYP and wB97XD (~100 nm) and a smaller difference for B3LYP (30 nm) and PBE0 (63 nm) functionals. This supports the choice of either PBE0 or B3LYP functionals. The solvent effect has been included implicitly *via* the polarizable continuum model (PCM),³⁵ where excited state properties are calculated with equilibrium solvation (*cf.* ref. 36). For J-aggregates we use toluene solvent. Notice that optimization of structures for J-aggregates in toluene solvent has been carried out without symmetry constraints. If structural symmetry is present it has been introduced for the calculation of spectral properties.

Computational programs have been developed for the prediction of radiative k_{r} and non-radiative k_{nr} rates based on Fermi's Golden rule and harmonic approximation for ground and excited states.^{37,38} In this contribution, we employ the FCclasses3 code to simulate vibrationally resolved fluorescence spectra and to determine the rate constants needed for the calculation of QY values (version FCclasses3-0.1, 2019.³⁸). Prediction of fluorescence quantum yields for molecules in solution remains a challenging task due to the harmonic approximation and the choice of line shape function. The used approximations have been previously critically addressed in the context of reliable rate prediction.³⁶

Molecular potential energy surfaces (PES) are in principle not harmonic and therefore, the choice of the point at which the quadratic approximation is made defines different harmonic models. The models can be separated into two classes depending on around which point the PES of the electronic ground state is expanded to the second order. In the adiabatic hessian (AH) model the potential is expanded around the



Scheme 1 Structures of J-aggregates forming tetramers: (A) tetSQA and (B) tetSQB.



geometry of the ground state minimum and excited state minimum, respectively. In the vertical hessian (VH) model the expansion occurs around the excited state minimum for both states. AH and VH models differ in equilibrium geometry and Hessian matrix.^{39,40} They are the best models and should provide equal results if the harmonic approximation is valid. However, the AH model where two electronic states are described around different minimum energy structures (ground and excited) is not appropriate in the presence of large structural displacements. In this case, the VH model is recommended. Notice that for the VH model, the internal curvilinear coordinates better describe low-frequency modes than Cartesian coordinates, which can be responsible for the appearance of imaginary frequencies.⁴¹ For calculations of semi-rigid molecules as J-aggregates, we use the VH model with internal curvilinear coordinates, as implemented in the FCclasses3 code and compare the results with experimental data. We have chosen temperature $T = 300$ K for the calculation of QY.

The broadening of the lineshape is also an important issue because of its different origins. The inhomogeneous broadening (Gaussian lineshape) is due to the fact that the environment acts differently on different molecules in solution. Therefore, it causes small shifts in energy levels, which in the ensemble of molecules form a Gaussian distribution that can be related to the thermal energy and the solvent reorganization energy.^{42,43} The effect of inhomogeneous broadening on k_r and k_{ic} is usually small. Homogeneous broadening corresponding to the Lorentzian lineshape is a consequence of Heisenberg's uncertainty principle. Both types of broadening are combined in the Voigt profile. We use Voigt I and Voigt II, where the contribution of Lorentzian lineshape is an order of magnitude higher in Voigt I. The effect of Lorentzian broadening is negligible for k_r . In contrast, it influences substantially k_{ic} . The reliability of the predictions based on the first principle approach is not easy to judge. Therefore comparison with experimental results is useful. Nevertheless, due to the superradiant properties of J-aggregates, the trend of QY prediction is of interest in the context of applications and should be considered qualitatively. The influence of different broadening has been extensively investigated in ref. 36 and we consider the choice of broadening as a phenomenological parameter. For Gaussian broadening the choice of $\text{HWHM}_G = 0.02$ eV reproduces well the experimental lineshape (cf. Fig. 1). Even if Lorentzian broadening can be estimated from the lifetime of the state $1/\tau$, it yields 4×10^{-5} eV (for dSQA) which in combination with Gaussian broadening (0.02 eV) within Voigt, does not influence the rates. Therefore, we use Lorentzian broadening as a parameter for checking reliability; if the k_{ic} dependence on broadening is large, the prediction is not reliable.³⁶

Concerning charge transfer and transition dipole moments of studied J-aggregates, Fig. S1 and S2 (ESI[†]) confirm previous findings.^{21–23,25–27} In addition, Fig. S1 (ESI[†]) also shows that the choice of functional, PBE0 versus CAM-B3LYP, does not influence the electron density difference (EDD) between the first excited state (S_1) and ground (S_0) states. The investigated

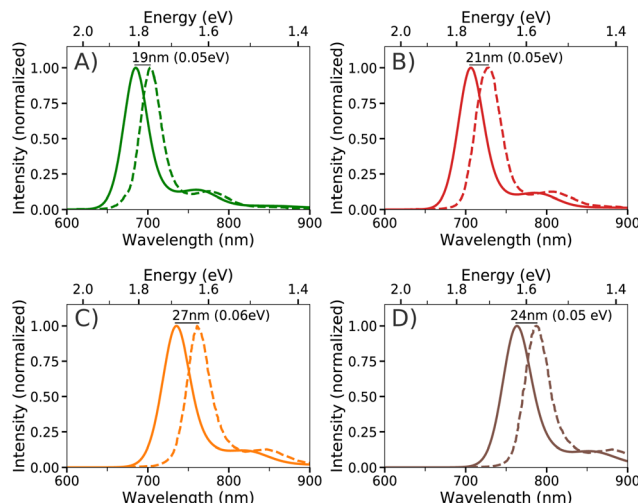


Fig. 1 Comparison between experimental (dashed line) and theoretical (full line) emission spectra for (A) dSQA, (B) tSQA, (C) dSQB, and (D) tSQB in toluene solvent. Theoretical emission spectra are obtained within the vertical hessian (VH) model using Gaussian broadening ($\text{HWHM}_G = 0.02$), at 300 K. Experimental spectra were digitized from ref. 21.

squaraine J-aggregates exhibit linear structures (cf. Fig. 2) with localized transition dipole moments, which are arranged head-to-tail having out-of-phase orientation. The calculated electron density difference (cf. Fig. S1, ESI[†]) illustrates exciton nature according to Kasha's molecular exciton model.⁴⁴ Fig. S2 (ESI[†]) shows the enlargement of the dipole strength (μ^2) as the number of subunits increases, with higher values for SQA than SQB J-aggregates. With an increasing number of subunits in the J-aggregates, a superposition of the transition dipole moments causes a bathochromic shift and an increase in the intensity of the first excited state. These results agree with characteristics of absorption spectra of dimers, trimers and tetramers as shown in the Results and discussion (cf. Fig. 2, Fig. S3 and S4, ESI[†]).

In order to determine the qualitative trend of k_{ic} values as a function of the number of subunits N of the J-aggregate, we use the scaling relation (cf. Table S2 and eqn (S1) and (S2), ESI[†]) for SQA and SQB. For this purpose, the required parameters are taken from Table S2 (ESI[†]). These parameters are determined from DFT and TD-DFT calculations of SQA and SQB monomers in toluene solvent, while exciton coupling is calculated from Davydov splitting. The same functional and AO basis set have been used as for the calculation of structural and optical properties. For J-aggregates with weak exciton coupling,²⁹ the scaling relation yields a decrease of k_{ic} rate with the length N . This result together with the superradiative effect of J-aggregates is responsible for the high QY.

3 Results and discussion

The aim is to find J-aggregates built from squaraine dyes suitable for TLSC application. Therefore, we first address theoretically obtained optical properties of SQA and SQB dimers and trimers forming J-aggregates in toluene solvent



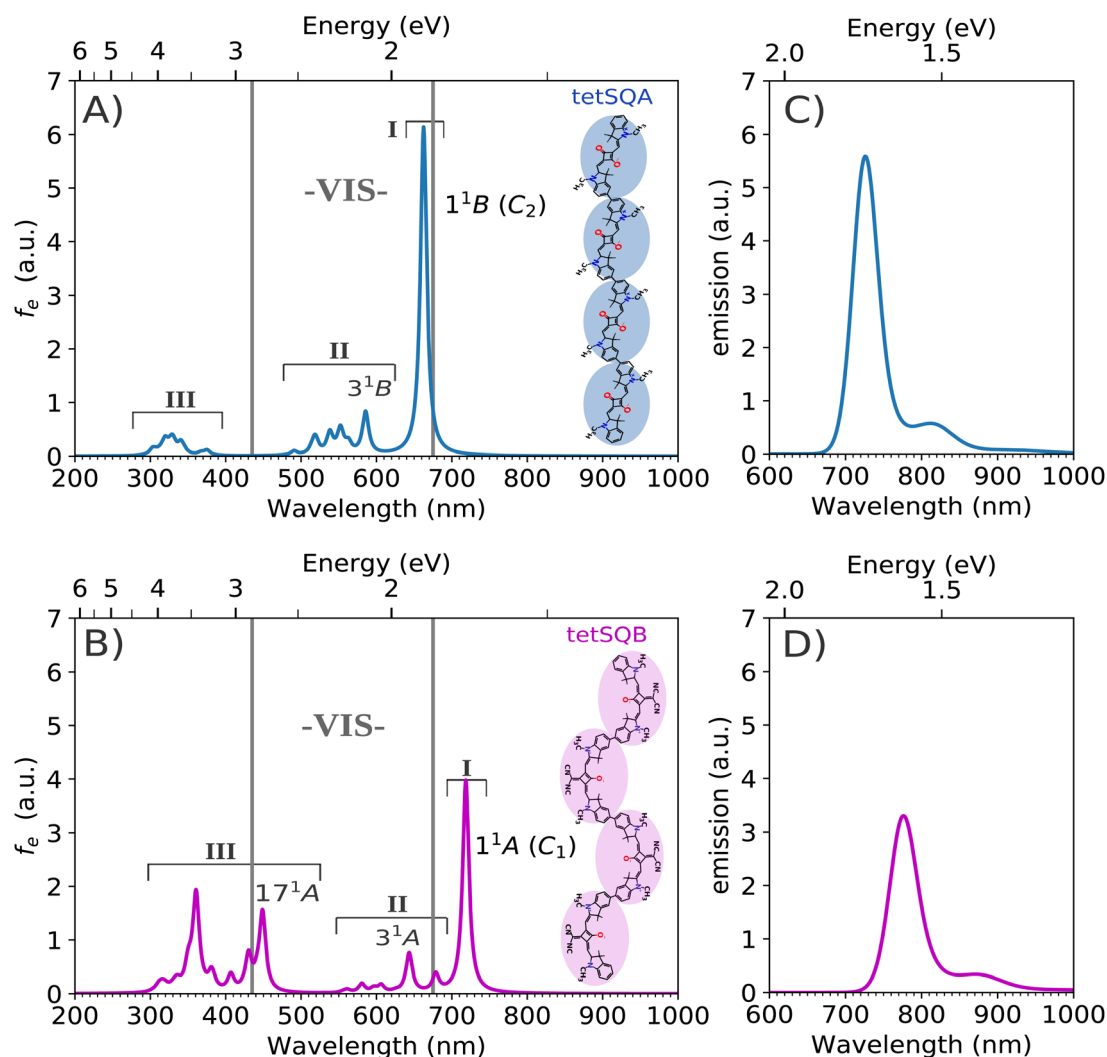


Fig. 2 TD-DFT absorption spectra of J-aggregates forming tetramers in toluene solvent: (A) tetSQA (blue) built from squaraine dyes with the central squaric acid ring and oxygen atoms, and (B) tetSQB (violet) built from squaraine dyes with the central squaric acid ring substituted with the dicyanovinylene group. The transitions are divided into groups I, II, and III. The most intense transitions (I) are labeled according to symmetry point groups. f_e labels oscillator strengths. The visible regime (VIS) is shown within gray lines. HOMO–LUMO gaps are 2.26 eV for tetSQA and 2.12 eV for tetSQB J-aggregates. Comparison between emission spectra of (C) tetSQA and (D) tetSQB J-aggregates in toluene solvent (*cf.* Computational). Notice that monomer subunits forming J-aggregates are covalently bound (1.5 Å).

for which experimental data²¹ are available. They have been already investigated in different contexts.^{22,23} Our calculated absorption and emission spectra for dimers (dSQA; dSQB) and trimers (tSQA; tSQB) are shown in Fig. S3 and S4 (ESI†). There are three groups of excited states (I, II, and III) present in the absorption spectra. Transitions due to HOMO–LUMO excitation with dominant intensities belong to group I, while groups II and III contain transitions with almost negligible intensities within the VIS and UV regimes, respectively. In order to obtain transparency for luminophores, the most intense transitions should be outside the VIS regime (435–675 nm²).

In the case of the dSQA, the calculated absorption spectrum in toluene solvent consists of two transitions characteristic of the J-aggregate peak splitting. The state 1^1B with the highest intensity is located at 625 nm (1.98 eV, group I), and the 4^1B state with very low intensity at 525 nm (2.36 eV, group II). They

correspond to the experimental ones measured at 690 nm (1.80 eV) and 621 nm (2.00 eV). States within the UV region (group III) have almost zero intensities (*cf.* Fig. S3A, ESI†). The dSQB spectrum is red shifted with respect to dSQA by 56 nm (*cf.* Table S1, ESI†). The most intense transition within group I lies outside the VIS regime and the transition 5^1A with very low intensity (group III) enters the VIS region (*cf.* Fig. S3B, ESI†). The difference between experimental and theoretical results is acceptable (*cf.* Computational).

The structure of the trimer tSQA has an inversion center and the absorption spectrum is characterized by two groups I and II belonging to J-aggregate features, which are also found experimentally (at 714 nm (1.74 eV) and 621 nm (2.00 eV)). They correspond to theoretically predicted 1^1A_u (at 652 nm (1.90 eV)) and 4^1A_u (at 563 nm (2.20 eV)) states as shown in Fig. S4A (ESI†). Group III does not contain any intense transitions. All



three groups of transitions for the tSQB J-aggregate are shifted to lower energies with respect to those of tSQA. Therefore, the 10^1A peak of tSQB (group III) is entering the VIS regime and the most intense transition (group I) is in the NIR (*cf.* Fig. S4B, ESI[†]). Comparison between absorption spectra of dimers and trimers confirms the characteristic bathochromic shift that J-aggregates exhibit with an increasing number of monomers. The calculated properties of SQA and SQB monomers including absorption and emission spectra as well as k_{ic} rates, shown in Fig. S5 and S6 (ESI[†]), are in qualitative agreement with the measured ones.²¹

The fluorescence spectra obtained from the calculations of dimers and trimers demonstrate analog features as their equivalent absorption spectra. Their characteristic is a narrow emission J-band whose maximum is located in the NIR region. The difference between normalized theoretical emission spectra calculated within the vertical hessian model (VH) and experimental ones for dimers and trimers of J-aggregates in toluene solvent is not larger than 27 nm (*cf.* Fig. 1). In addition, the lineshapes of the theoretical and experimental emission spectra are very similar (*cf.* Fig. 1) justifying the use of the VH model. Notice that in comparison with measured spectra the calculated absorption and emission spectra for dimers and trimers of J-aggregates are always blue shifted by 62–66 nm (*cf.* Table S1, ESI[†]) and by 19–27 nm (*cf.* Fig. 1), respectively. For these J-aggregates, the experimental data²¹ are in qualitative agreement with calculated properties.

Altogether, the described examples show the difference in absorption spectra between SQA and SQB of J-aggregates built from squaraine dyes. The increase in the number of subunits from dimers to trimers causes a red shift of absorption and emission. In addition, the qualitative agreement between theory and experiment for dimers and trimers motivated us to investigate J-aggregates containing tetramers as materials with suitable properties for applications.

Therefore, we present a comparison between theoretical absorption and emission spectra of tetramers tetSQA and tetSQB forming J-aggregates in toluene shown in Fig. 2. These results illustrate the influence of substitution at the central squaric acid ring by the dicyanovinylene group (tetSQB), but also show the red shift of the absorption due to increased size. Both tetSQA and tetSQB exhibit peak splitting within groups I and II following the J-aggregate features. Due to system elongation by one subunit, with respect to the SQA and SQB trimers, the calculated absorption spectra of the investigated tetramers are red shifted by 10 to 12 nm (*cf.* Table S1, ESI[†]). In addition to finding that the tetSQB state 1^1A is at 719 nm (1.72 eV), the location of the 1^1B state at 662 nm (1.87 eV) for the tetSQA J-aggregate is reaching the NIR region. In spite of the blue shift emerging from theoretical calculations due to the choice of DFT functional, the state with the largest intensity in the NIR region is present for both tetramers. The transparent visible regime of tetSQA contains low intensity states belonging to groups II and III located at 491–586 nm (2.53–2.12 eV) and 303–375 nm (4.09–3.31 eV), respectively. This is also valid for tetSQB transitions at 555–679 nm (2.23–1.83 eV) within group II.

In contrast, due to the state 17^1A in the VIS regime (at 449 nm (2.76 eV)) the transition intensities of tetSQB within group III are not negligible, therefore representing semitransparency. According to the above spectral analysis, the tetSQA J-aggregate fulfills the transparency requirements. The tetSQB NIR shift is in agreement with the smaller HOMO–LUMO gap in comparison with the tetSQA (*cf.* caption of Fig. 2). The emission spectra of both tetramers are in the red regime but tetSQA has a larger intensity for emission and absorption spectra than tetSQB. In addition, the shape of the absorption and emission spectra is important in the context of reabsorption loss. Notice that there is no significant overlap between absorption and emission spectra since the absorption spectral tail is characterized by the sharp edge and the emission spectra have a narrow shape. This is convenient because the small overlap can minimize the reabsorption loss by lowering the non-radiative rate and enhancing the QY value.

The calculated radiative k_r and internal conversion rate k_{ic} in toluene solvent for dimers, trimers and tetramers of J-aggregates together with the fluorescence QY, obtained using the FCclasses code, are presented in Table 1. The most challenging aspect of k_{ic} rate prediction is the choice of the broadening function. The predicted values strongly depend on details of the simulated emission spectrum (*cf.* Fig. 1). As described in ref. 36 the predicted value of k_{ic} has to be critically considered. Since k_{ic} depends on the description of highly excited vibronic states which are responsible for the very far tail of the emission spectra, they are only approximately described by different

Table 1 Fluorescence quantum yields QY = $k_r/(k_r + k_{ic})$ of J-aggregates calculated within the vertical hessian model (VH) in toluene solvent (at 300 K) using the FCclasses3 program (version FCclasses3-0.1,2019.³⁶). The broadening functions are Gaussian (HWHM_G = 0.02 eV), Voigt I (HWHM_G = 0.02 eV, HWHM_L = 0.001 eV) and Voigt II (HWHM_G = 0.02 eV, HWHM_L = 0.0001 eV). k_{nr} labels the experimental non-radiative rate

| Squaraine | Broad. f. | k_r (10^8 s ⁻¹) | | k_{ic} (s ⁻¹) | | k_{nr} (s ⁻¹) | | QY | |
|-----------|-----------|----------------------------------|------|-----------------------------|-------------------|-----------------------------|--------------------|----|--|
| | | VH | Exp. | VH | Exp. | VH | Exp. ²¹ | | |
| dsQA | Voigt I | 4.1 | 4.9 | 3.2×10^8 | 1.1×10^8 | 0.56 | 0.82 | | |
| | Voigt II | 4.2 | | 1.2×10^8 | | 0.77 | | | |
| | Gauss | 4.2 | | 1.0×10^8 | | 0.80 | | | |
| dsQB | Voigt I | 2.6 | 2.7 | 2.7×10^8 | 1.2×10^8 | 0.49 | 0.69 | | |
| | Voigt II | 2.6 | | 4.6×10^7 | | 0.85 | | | |
| | Gauss | 2.6 | | 2.2×10^7 | | 0.92 | | | |
| tSQA | Voigt I | 5.4 | 5.4 | 2.3×10^8 | 9.6×10^7 | 0.70 | 0.85 | | |
| | Voigt II | 5.6 | | 2.4×10^7 | | 0.96 | | | |
| | Gauss | 5.6 | | 1.7×10^6 | | 1.00 | | | |
| tSQB | Voigt I | 3.0 | 2.8 | 2.7×10^8 | 2.1×10^8 | 0.53 | 0.58 | | |
| | Voigt II | 3.1 | | 2.9×10^7 | | 0.92 | | | |
| | Gauss | 3.2 | | 1.8×10^6 | | 0.99 | | | |
| tetSQA | Voigt I | 6.5 | | 2.6×10^8 | | 0.71 | | | |
| | Voigt II | 6.7 | | 3.5×10^7 | | 0.95 | | | |
| | Gauss | 6.7 | | 9.2×10^6 | | 0.99 | | | |
| tetSQB | Voigt I | 3.7 | | 3.6×10^8 | | 0.51 | | | |
| | Voigt II | 3.9 | | 9.1×10^7 | | 0.81 | | | |
| | Gauss | 3.9 | | 6.1×10^7 | | 0.87 | | | |



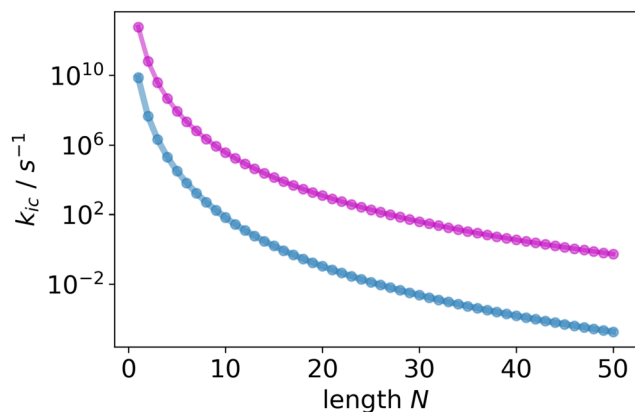


Fig. 3 Scaling of k_{ic} rate with length N of SQA (blue) and SQB (violet) J-aggregates. Parameters for scaling are determined from TD-DFT calculations of SQA and SQB (cf. Scaling relations and Table S2 in the ESI†). Comparison of k_{ic} values for SQA/SQB as a function of N subunits: $7.9 \times 10^9/6.1 \times 10^{12}$ for $N = 1$; $4.6 \times 10^7/6.5 \times 10^{10}$ for $N = 2$; $2.1 \times 10^6/3.9 \times 10^9$ for $N = 3$; $2.0 \times 10^5/4.8 \times 10^8$ for $N = 4$; and $3.1 \times 10^4/8.8 \times 10^7$ for $N = 5$.

broadenings. For example, a broad emission spectrum is connected with large k_{ic} . The influence of broadening on k_{ic} values has been illustrated in Table 1 on examples of Voigt I, Voigt II and Gaussian lineshapes (cf. Computational). Voigt I provides the closest results of k_{ic} to the available experimental one. The k_r values are independent from broadening and correlate very well with measurements for investigated dimers and trimers (cf. Table 1). In both cases, experimentally and theoretically, there is a clear superradiance effect observed, with enlargement of the k_r rate with the system size including the tetramers. This increase of radiative rate is experimentally much less pronounced for dSQB and tSQB with respect to the dSQA and tSQA.

The experimental k_{ic} rates for dimers and trimers decrease for SQA and increase for SQB. The calculated k_{ic} rates for SQA J-aggregates decrease also from dimer to trimer and in the case of tetSQA, the k_{ic} value is smaller than for dSQA. This produces an increase of QY (0.56–0.71, Voigt I) with system size. The QY values for the SQA dimer and trimer in toluene are in acceptable agreement with experimentally measured values, which are larger than 80%. In the case of SQB J-aggregates the theoretically predicted k_{ic} follows the experimental trend: the dimer and trimer have the same value for k_{ic} which increases for the tetramer. However, together with the enlargement of k_r , similar values for theoretically predicted QY for SQB J-aggregates have been obtained, including a very small decrease from trimer to tetramer (0.53–0.51, Voigt I).

The dSQB and tSQB have lower QY values in toluene solvent than dSQA and tSQA. Notice that the polarity of the solvent can strongly influence the values of QY. Therefore lower QY values for J-aggregates built from SQB in a polar solvent²⁶ (trichloromethane) than in non-polar solvent²¹ (toluene) are to be expected. In addition, dSQB and tSQB are more dependent on broadening. In the case of Voigt I, the values of broadening are in agreement with the measured ones, which are lower than for SQA dimers and trimers. Furthermore, the theoretical value of quantum yield for tetSQA is larger than 70% and for tetSQB is

larger than 50%, as shown in Table 1. The influence of broadening on all calculated k_{ic} rates for SQA and SQB is shown in Fig. S7 (ESI†). In the case of tetSQA and tetSQB, the broadening does not influence substantially the k_{ic} values allowing us to accept the prediction that QY is lower for tetSQB than for tetSQA. Therefore, the SQA tetramer satisfies both conditions, transparency and high QY. In order to extend the QY predictions for systems with subunits $N \geq 4$, we present a comparison of k_{ic} rate constants for the SQA and SQB J-aggregates using the scaling factor relation²⁹ in Fig. 3 (for very approximate qualitative scaling relation cf. ESI†). Both k_{ic} rates decrease with N , but k_{ic} for SQA J-aggregates is considerably lower than k_{ic} for SQB J-aggregates under the assumption of weak exciton coupling J_{ge} for SQA and SQB (-881 cm^{-1} and -645 cm^{-1}) defined in ref. 29. The qualitative approach supports our computational results also for tetramers. This means that the values of QY are larger for SQA than for SQB J-aggregates. In summary, according to the described findings and in order to initiate new experiments, we propose SQA J-aggregates with subunits ≥ 4 as suitable materials for TLSC applications.

4 Conclusions

Our theoretical study of optical properties as well as prediction of QY for SQA and SQB squaraine-based J-aggregates in toluene solvent provided us with the following results:

- (i) Increasing number of subunits in J-aggregates is responsible for the red shift and intensity enhancement of the absorption and emission spectra.
- (ii) Characteristics of J-aggregate's spectral properties containing one dominantly intense state and several states with very low intensities are present for all investigated cases.
- (iii) The main findings in the context of TLSC application are the difference between SQA and SQB J-aggregates for the given number of subunits. This includes both the presence of absorption and emission states with large intensities outside the VIS regime and high fluorescence QY.
- (iv) In the case of SQA dimers and trimers, the estimated computational error for the most intense transition is 62–66 nm. Therefore, the most intense transition is within the NIR regime.
- (v) The SQA tetramer shows the dominant state in the NIR regime based on theoretical predictions including estimated computational error (cf. iv).
- (vi) The calculated QY for SQA is larger than for SQB. These findings are also supported by a qualitative approach based on the scaling model.

Altogether tetSQA squaraine J-aggregate in toluene solvent or SQA J-aggregates with a larger numbers of subunits seem to be appropriate materials for TLSC application.

Conflicts of interest

There are no conflicts to declare.



Acknowledgements

This research was supported by the project STIM – REI, Contract Number: KK.01.1.1.01.0003, funded by the European Union through the European Regional Development Fund – the Operational Programme Competitiveness and Cohesion 2014–2020 (KK.01.1.1.01). M. B. M. acknowledges computational facilities of the HPC computer within the STIM-REI project, a Doctoral study of Biophysics at the University of Split. M. B. M. and V. B. K. thank Professor Miroslav Radman at MedILS and Split-Dalmatia County.

References

- 1 M. Currie, T. Heide, S. Goffri and M. Baldo, *Science*, 2008, **321**, 226–228.
- 2 R. R. Lunt, *Appl. Phys. Lett.*, 2012, **101**, 043902.
- 3 Y. Zhao, G. A. Meek, B. G. Levine and R. R. Lunt, *Adv. Opt. Mater.*, 2014, **2**, 606–611.
- 4 C. Yang and R. R. Lunt, *Adv. Opt. Mater.*, 2017, **5**, 1600851.
- 5 C. Yang, D. Liu and R. R. Lunt, *Joule*, 2019, **3**, 2871–2876.
- 6 K. Zhang, C. Qin, X. Yang, A. Islam, S. Zhang, H. Chen and L. Han, *Adv. Energy Mater.*, 2014, **4**, 1301966.
- 7 C. Yang, W. Sheng, M. Moemeni, M. Bates, C. K. Herrera, B. Borhan and R. R. Lunt, *Adv. Energy Mater.*, 2021, **11**, 2003581.
- 8 Y. Zhao and R. R. Lunt, *Adv. Energy Mater.*, 2013, **3**, 1143–1148.
- 9 C. Yang, J. Zhang, W.-T. Peng, W. Sheng, D. Liu, P. Kuttipillai, M. Young, M. Donahue, B. Levine, B. Borhan and R. R. Lunt, *Sci. Rep.*, 2018, **8**, 16359.
- 10 M. G. Debije and P. P. C. Verbunt, *Adv. Energy Mater.*, 2012, **2**, 12–35.
- 11 J. L. Banal, B. Zhang, D. J. Jones, K. P. Ghiggino and W. W. H. Wong, *Acc. Chem. Res.*, 2017, **50**, 49–57.
- 12 F. Proise, A.-L. Joudrier, J.-L. Pelouard and J.-F. Guillemoles, *EPJ Photovoltaics*, 2018, **9**, 12.
- 13 B. Zhang, C. Gao, N. Neto and W. Wong, *Principles and Applications of Aggregation-Induced Emission*, 2019, pp. 479–504.
- 14 A. Eisfeld and J. S. Briggs, *Phys. Status Solidi A*, 2018, **215**, 1700634.
- 15 J. L. Banal, J. M. White, T. W. Lam, A. W. Blakers, K. P. Ghiggino and W. W. H. Wong, *Adv. Energy Mater.*, 2015, **5**, 1500818.
- 16 K. Iliina, W. M. MacCuaig, M. Laramie, J. N. Jeouty, L. R. McNally and M. Henary, *Bioconjugate Chem.*, 2020, **31**, 194–213.
- 17 J. He, Y. J. Jo, X. Sun, W. Qiao, J. Ok, T.-I. Kim and Z. Li, *Adv. Funct. Mater.*, 2020, **31**, 2008201.
- 18 L. E. McNamara, T. A. Rill, A. J. Huckaba, V. Ganeshraj, J. Gayton, R. A. Nelson, E. A. Sharpe, A. Dass, N. I. Hammer and J. H. Delcamp, *Chemistry*, 2017, **23**, 12494–12501.
- 19 A. Zampetti, A. Minotto and F. Cacialli, *Adv. Funct. Mater.*, 2019, **29**, 1807623.
- 20 K. Strassel, A. Kaiser, S. Jenatsch, A. C. Véron, S. B. Anantharaman, E. Hack, M. Diethelm, F. Nüesch, R. Aderne, C. Legnani, S. Yakunin, M. Cremona and R. Hany, *ACS Appl. Mater. Interfaces*, 2018, **10**, 11063–11069.
- 21 H. Ceymann, A. Rosspeintner, M. H. Schreck, C. Mützel, A. Stoy, E. Vauthey and C. Lambert, *Phys. Chem. Chem. Phys.*, 2016, **18**, 16404–16413.
- 22 M. I. S. Röhr, H. Marciniak, J. Hoche, M. H. Schreck, H. Ceymann, R. Mitric and C. Lambert, *J. Phys. Chem. C*, 2018, **122**, 8082–8093.
- 23 C. Heshmatpour, P. Malevich, F. Plasser, M. Menger, C. Lambert, F. Šanda and J. Hauer, *J. Phys. Chem. Lett.*, 2020, **11**, 7776–7781.
- 24 S. F. Völker, S. Uemura, M. Limpinsel, M. Mingeback, C. Deibel, V. Dyakonov and C. Lambert, *Macromol. Chem. Phys.*, 2010, **211**, 1098–1108.
- 25 C. Lambert, F. Koch, S. F. Völker, A. Schmiedel, M. Holzapfel, A. Humeniuk, M. I. S. Röhr, R. Mitric and T. Brixner, *J. Am. Chem. Soc.*, 2015, **137**, 7851–7861.
- 26 A. Turkin, P. Malý and C. Lambert, *Phys. Chem. Chem. Phys.*, 2021, **23**, 18393–18403.
- 27 J. Selby, M. Holzapfel, K. Radacki, A. K. Swain, H. Braunschweig and C. Lambert, *Macromolecules*, 2022, **55**, 421–436.
- 28 M. Cao, X. Zhao and X. Gong, *JACS Au*, 2023, **3**, 25–35.
- 29 A. Humeniuk, R. Mitrić and V. Bonačić-Koutecký, *J. Phys. Chem. A*, 2020, **124**, 10143–10151.
- 30 R. Englman and J. Jortner, *Mol. Phys.*, 1970, **18**, 145–164.
- 31 M. J. Frisch, G. W. Trucks, H. B. Schlegel, G. E. Scuseria, M. A. Robb, J. R. Cheeseman, G. Scalmani, V. Barone, G. A. Petersson, H. Nakatsuji, X. Li, M. Caricato, A. V. Marenich, J. Bloino, B. G. Janesko, R. Gomperts, B. Mennucci, H. P. Hratchian, J. V. Ortiz, A. F. Izmaylov, J. L. Sonnenberg, D. Williams-Young, F. Ding, F. Lipparini, F. Egidi, J. Goings, B. Peng, A. Petrone, T. Henderson, D. Ranasinghe, V. G. Zakrzewski, J. Gao, N. Rega, G. Zheng, W. Liang, M. Hada, M. Ehara, K. Toyota, R. Fukuda, J. Hasegawa, M. Ishida, T. Nakajima, Y. Honda, O. Kitao, H. Nakai, T. Vreven, K. Throssell, J. A. Montgomery, Jr., J. E. Peralta, F. Ogliaro, M. J. Bearpark, J. J. Heyd, E. N. Brothers, K. N. Kudin, V. N. Staroverov, T. A. Keith, R. Kobayashi, J. Normand, K. Raghavachari, A. P. Rendell, J. C. Burant, S. S. Iyengar, J. Tomasi, M. Cossi, J. M. Millam, M. Klene, C. Adamo, R. Cammi, J. W. Ochterski, R. L. Martin, K. Morokuma, O. Farkas, J. B. Foresman and D. J. Fox, *Gaussian 16 Revision A.03*, Gaussian Inc, Wallingford CT, 2016.
- 32 C. Adamo and V. Barone, *J. Chem. Phys.*, 1999, **110**, 6158–6170.
- 33 M. Ernzerhof and G. E. Scuseria, *J. Chem. Phys.*, 1999, **110**, 5029–5036.
- 34 F. Weigend, *Phys. Chem. Chem. Phys.*, 2006, **8**, 1057–1065.
- 35 J. Tomasi, B. Mennucci and R. Cammi, *Chem. Rev.*, 2005, **105**, 2999–3094.
- 36 A. Humeniuk, M. Bužančić, J. Hoche, J. Cerezo, R. Mitrić, F. Santoro and V. Bonačić-Koutecký, *J. Chem. Phys.*, 2020, **152**, 054107.



Paper

- 37 Y. Niu, W. Li, Q. Peng, H. Geng, Y. Yi, L. Wang, G. Nan, D. Wang and Z. Shuai, *Mol. Phys.*, 2018, **116**, 1078–1090.
- 38 F. Santoro and J. Cerezo, FCclasses3, a code to simulate electronic spectra. Version FCclasses3-0.1, 2019. Visit <https://www.pi.iccom.cnr.it/fcclasses>.
- 39 F. J. Avila Ferrer and F. Santoro, *Phys. Chem. Chem. Phys.*, 2012, **14**, 13549–13563.
- 40 F. Santoro and D. Jacquemin, *Wiley Interdiscip. Rev.: Comput. Mol. Sci.*, 2016, **6**, 460–486.
- 41 J. Cerezo and F. Santoro, *J. Chem. Theory Comput.*, 2016, **12**, 4970–4985.
- 42 R. Marcus, *J. Chem. Phys.*, 1965, **43**, 1261–1274.
- 43 F. J. A. Ferrer, R. Improta, F. Santoro and V. Barone, *Phys. Chem. Chem. Phys.*, 2011, **13**, 17007–17012.
- 44 M. Kasha, *Radiat. Res.*, 1963, **20**, 55–71.



Conclusion and outlook

The present study, motivated by the global energy and climate crisis, proposes novel harvesting solutions in the field of material science. The aim was to theoretically design new materials for solar energy harvesting, by investigating the properties of bio-nano hybrid sensitizers for DSSC and J-aggregate luminophores for TLSC applications.

Theoretical predictions of optical and photovoltaic properties enable the design of materials with improved performance. In this context, the concept of bio-nano donor–acceptor systems for hybrid DSSC photosensitizers has not been previously investigated. The idea is based on merging specific properties of silver-NCs with anthocyanidin dyes to create novel bio-nano hybrids with donor-acceptor characteristics. Theoretical characterization of bio-nano hybrids reveals a favourable alignment of the hybrid sensitizer energies with those of the TiO₂ semiconductor band edge and I⁻/I₃⁻ redox potential. It also shows enhanced spectral intensity, improved photovoltaic properties, charge-transfer character, and stability on the TiO₂ surface. This applies to bio-nano hybrids with an even number of NC valence electrons. Altogether, bio-nano hybrid sensitizers exhibit desirable properties, such as high light-harvesting and photocurrent efficiency.

In addition, the doping of NCs in bio-nano hybrids by coinage metal (Au and Cu) atoms on the TiO₂ surface was investigated. It has been shown that single-gold atom and mixed gold-copper doping enhance the photovoltaic properties of silver trimer NCs in hybrids. Both cyanidin-Ag₂Au and cyanidin-AgAuCu demonstrate better LHE efficiency and stability in comparison with larger Ag NCs. This improvement can be attributed to their unique opto-electronic properties due to the s-d band gap. However, these results refer specifically to trimer NCs, while the influence of doping on the larger NCs needs to be investigated. Overall, the findings show the potential of bio-nano hybrids for DSSC applications, encouraging experimental research with a focus on enhancement of efficiency and designing improved energy-harvesting systems.

The theoretical design of new materials for TLSC requires reliable prediction of excited state properties such as decay rate transitions and fluorescence QY. They rely on the harmonic approximation models and the choice of broadening function. The reliability of the harmonic approximation for radiative and internal conversion rates was investigated on coumarin dyes. Additionally, several "Rules of thumb" were determined based on comparisons between different harmonic models and the influence of broadening on QY predictions. These rules are valid

primarily for IC rate, since the radiative rate is less sensitive to prediction. In comparison with other harmonic models the AH and VH yield better results, while a large influence of broadening can produce unreliable results. Furthermore, similar values obtained from vertical and adiabatic approaches confirm the harmonicity of the potential energy surface. These conclusions show the need for harmonic approximation analysis and its comparison with experimental findings. The theoretical design of J-aggregate luminophores for TLSC applications was performed within the reliability of fluorescence QY prediction as a measure of light emission efficiency. More specifically, the structural, optical, and excitonic properties of squaraine-based tetramers in toluene solvent were proposed. It has been shown that increasing the number of subunits results in enhanced absorption, narrow emission, shift to the NIR region, and high QY. Both SQA and SQB tetramers exhibit characteristic exciton features. In the context of TLSC, SQA shows to be more efficient compared to SQB. In addition, the results are further supported by a qualitative scaling model. These properties correlate with the J-aggregate excitonic nature and the superradiance effect, demonstrating that the SQA J-aggregates with a larger number of subunits present a novel, transparent, and highly efficient material as TLSC luminophore.

In summary, the thesis provides valuable insights into the design and optimization of bio-nano hybrids and J-aggregates as novel materials for DSSC and TLSC harvesting technologies. It encourages future research which should include experimental validation of predicted properties.

References

- [1] D. Hao, L. Qi, A. M. Tairab, A. Ahmed, A. Azam, D. Luo, Y. Pan, Z. Zhang, and J. Yan. “Solar energy harvesting technologies for PV self-powered applications: A comprehensive review”. In: *Renewable Energy* 188 (2022), pp. 678–697. DOI: 10.1016/j.renene.2022.02.066.
- [2] A. K. Pandey, R. K. Rajamony, and M. Samykano. “Chapter 1 - Solar energy: direct and indirect methods to harvest usable energy”. In: *Dye-Sensitized Solar Cells*. Ed. by A. K. Pandey, S. Shahabuddin, and M. S. Ahmad. Academic Press, 2022, pp. 1–24. ISBN: 978-0-12-818206-2. DOI: 10.1016/B978-0-12-818206-2.00007-4.
- [3] E. Pulli, E. Rozzi, and F. Bella. “Transparent photovoltaic technologies: Current trends towards upscaling”. In: *Energy Conversion and Management* 219 (2020), p. 112982. DOI: 10.1016/j.enconman.2020.112982.
- [4] E. Hossain. “The Sun and the Earth”. In: *The Sun, Energy, and Climate Change*. Cham: Springer Nature Switzerland, 2023, pp. 1–67. ISBN: 978-3-031-22196-5. DOI: 10.1007/978-3-031-22196-5_1.
- [5] M. G. Norton. “Here comes the Sun”. In: *A modern history of materials: From stability to sustainability*. Cham: Springer International Publishing, 2023, pp. 127–146. ISBN: 978-3-031-23990-8. DOI: 10.1007/978-3-031-23990-8_7.
- [6] N. S. Lewis. “Toward cost-effective solar energy use”. In: *Science* 315.5813 (2007), pp. 798–801. DOI: 10.1126/science.1137014.
- [7] A. W. Rennuit-Mortensen, K. Dalgas Rasmussen, and M. Grahn. “How replacing fossil fuels with electrofuels could influence the demand for renewable energy and land area”. In: *Smart Energy* 10 (2023), p. 100107. DOI: 10.1016/j.segy.2023.100107.
- [8] European-Commission. *Communication from the Commission to the European Parliament, the European Council, the Council, the European Economic and Social Committee and the Committee of the Regions, the European Green Deal*. Brussels, COM(2019) 640 final.

- [9] R. Sasikumar, S. Thirumalaisamy, B. Kim, and B. Hwang. “Dye-sensitized solar cells: Insights and research divergence towards alternatives”. In: *Renewable and Sustainable Energy Reviews* 199 (2024), p. 114549. DOI: 10.1016/j.rser.2024.114549.
- [10] Y. Zhao and R. R. Lunt. “Transparent luminescent solar concentrators for large-area solar windows enabled by massive Stokes-shift nanocluster phosphors”. In: *Advanced Energy Materials* 3.9 (2013), pp. 1143–1148. DOI: 10.1002/aenm.201300173.
- [11] W. Fan, D. Tan, and W.-Q. Deng. “Acene-modified triphenylamine dyes for dye-sensitized solar cells: A computational study”. In: *ChemPhysChem* 13.8 (2012), pp. 2051–2060. DOI: 10.1002/cphc.201200064.
- [12] S. Ito. “Investigation of dyes for dye-sensitized solar cells: Ruthenium-complex dyes, metal-free dyes, metal-complex porphyrin dyes and natural dyes”. In: *Solar Cells-Dye-Sensitized Devices* (2011), pp. 19–48. DOI: 10.5772/19960.
- [13] G. Richhariya, A. Kumar, P. Tekasakul, and B. Gupta. “Natural dyes for dye sensitized solar cell: A review”. In: *Renewable and Sustainable Energy Reviews* 69 (2017), pp. 705–718. DOI: 10.1016/j.rser.2016.11.198.
- [14] H. Hug, M. Bader, P. Mair, and T. Glatzel. “Biophotovoltaics: Natural pigments in dye-sensitized solar cells”. In: *Applied Energy* 115 (2014), pp. 216–225. DOI: 10.1016/j.apenergy.2013.10.055.
- [15] S. Hao, J. Wu, Y. Huang, and J. Lin. “Natural dyes as photosensitizers for dye-sensitized solar cell”. In: *Solar energy* 80.2 (2006), pp. 209–214. DOI: 10.1016/j.solener.2005.05.009.
- [16] V. Bonačić-Koutecký, A. Kulesza, L. Gell, R. Mitrić, R. Antoine, F. Bertorelle, R. Hamouda, D. Rayane, M. Broyer, T. Tabarin, et al. “Silver cluster–biomolecule hybrids: From basics towards sensors”. In: *Physical Chemistry Chemical Physics* 14 (2012), pp. 9282–9290. DOI: 10.1039/C2CP00050D.
- [17] V. Bonačić-Koutecký. “Theoretical design of new class of optical materials based on small noble metal nanocluster-biomolecule hybrids and its potential for medical applications”. In: *Advances in Physics: X* 2.3 (2017), pp. 695–716. DOI: 10.1080/23746149.2017.1352458.
- [18] A. Carella, F. Borbone, and R. Centore. “Research progress on photosensitizers for DSSC”. In: *Frontiers in Chemistry* 6 (2018), pp. 2296–2646. DOI: 10.3389/fchem.2018.00481.
- [19] M. Currie, T. Heidel, S. Goffri, and M. Baldo. “High-efficiency organic solar concentrators for photovoltaics”. In: *Science* 321.5886 (2008), pp. 226–228. DOI: 10.1126/science.1158342.

- [20] R. R. Lunt. “Theoretical limits for visibly transparent photovoltaics”. In: *Applied Physics Letters* 101.4 (2012), p. 043902. DOI: 10.1063/1.4738896.
- [21] Y. Zhao, G. A. Meek, B. G. Levine, and R. R. Lunt. “Near-infrared harvesting transparent luminescent solar concentrators”. In: *Advanced Optical Materials* 2.7 (2014), pp. 606–611. DOI: 10.1002/adom.201400103.
- [22] C. Yang and R. R. Lunt. “Limits of visibly transparent luminescent solar concentrators”. In: *Advanced Optical Materials* 5.8 (2017), p. 1600851. DOI: 10.1002/adom.201600851.
- [23] Y. Niu, W. Li, Q. Peng, H. Geng, Y. Yi, L. Wang, G. Nan, D. Wang, and Z. Shuai. “MOlecular MAterials Property Prediction Package (MOMAP) 1.0: a software package for predicting the luminescent properties and mobility of organic functional materials”. In: *Molecular Physics* 116.7-8 (2018), pp. 1078–1090. DOI: 10.1080/00268976.2017.1402966.
- [24] J. Cerezo and F. Santoro. “FCclasses3: Vibrationally-resolved spectra simulated at the edge of the harmonic approximation”. In: *Journal of Computational Chemistry* 44.4 (2023), pp. 626–643. DOI: 10.1002/jcc.27027.
- [25] F. Würthner, T. E. Kaiser, and C. R. Saha-Möller. “J-Aggregates: From serendipitous discovery to supramolecular engineering of functional dye materials”. In: *Angewandte Chemie International Edition* 50.15 (2011), pp. 3376–3410. DOI: 10.1002/anie.201002307.
- [26] K. Butti and J. Perlin. *A golden thread: 2500 years of solar architecture and technology*. Vol. 514. Cheshire Books, Palo Alto, 1980. ISBN: 978-0442240059.
- [27] B. M. Edmond. “Memoire sur les effets d’electricques produits sous l’influence des rayons solaires”. In: *Comptes Rendus Hebdomadaires des Seances de L’Academie des Sciences* 9 (1839), pp. 561–567.
- [28] S. Willoughby. *Selenium: Its electrical qualities and the effect of light thereon*. Hayman Bros. and Lilly Printers: London, UK, 1877, pp. 1–21.
- [29] C. E. Fritts. “On the Fritts selenium cells and batteries”. In: *Journal of the Franklin Institute* 119.3 (1885), pp. 221–232. DOI: 10.1016/0016-0032(85)90426-0.
- [30] R. A. Marques Lameirinhas, J. P. N. Torres, and J. P. de Melo Cunha. “A photovoltaic technology review: History, fundamentals and applications”. In: *Energies* 15.5 (2022). DOI: 10.3390/en15051823.
- [31] C. Traverse, R. Pandey, M. Barr, and R. Lunt. “Emergence of highly transparent photovoltaics for distributed applications”. In: *Nature Energy* 2 (2017), pp. 849–860. DOI: 10.1038/s41560-017-0016-9.

- [32] Eurostat(2020-2022). *European Commission — energy balances sheet*, https://ec.europa.eu/eurostat/cache/infographs/energy_balances/enbal.html. Accessed on 16/3/2024.
- [33] SolarPower-Europe. *EU Market Outlook for Solar Power 2023–2027*. SolarPower Europe: Brussels, Belgium, 2023.
- [34] A. Goetzberger, J. Knobloch, and B. Voß. *Crystalline silicon solar cell*. John Wiley Sons, England, 1998. ISBN: 9780471971443. DOI: 10.1002/9781119033769.ch9.
- [35] R. M. Swanson. “A vision for crystalline silicon photovoltaics”. In: *Progress in Photovoltaics: Research and Applications* 14.5 (2006), pp. 443–453. DOI: 10.1002/pip.709.
- [36] N. Noorasid, F. Arith, A. Mustafa, M. Azam, S. Mahalingam, P. Chelvanathan, and N. Amin. “Current advancement of flexible dye sensitized solar cell: A review”. In: *Optik* 254 (2022), p. 168089. DOI: 10.1016/j.ijleo.2021.168089.
- [37] D. Javiya, M. Vyas, M. Mashru, P. Josely Jose, U. Rathod, S. Jethva, C. Savaliya, Y. Jani, M. Keshvani, and A. Ravalia. “Studies and comparison of natural dye-sensitized solar cells and thin-film solar cells”. In: *Materials Today: Proceedings* 73 (2023), pp. 545–549. DOI: 10.1016/j.matpr.2022.10.222.
- [38] H. S. Min, A. Supriyanto, and M. S. Hardani. “Thin film-based solar cell and dye-sensitized solar cells: review”. In: *International Journal of Advanced Science and Technology* 29 (2020), pp. 2413–2426.
- [39] R. A. Afre and D. Pugliese. “Perovskite solar cells: A review of the latest advances in materials, Fabrication Techniques, and Stability Enhancement Strategies”. In: *Micromachines* 15.2 (2024). DOI: 10.3390/mi15020192.
- [40] Y. Li, W. Huang, D. Zhao, L. Wang, Z. Jiao, Q. Huang, P. Wang, M. Sun, and G. Yuan. “Recent progress in organic solar cells: A review on materials from acceptor to donor”. In: *Molecules* 27.6 (2022). DOI: 10.3390/molecules27061800.
- [41] E. K. Solak and E. Irmak. “Advances in organic photovoltaic cells: A comprehensive review of materials, technologies, and performance”. In: *RSC Advances* 13.18 (2023), pp. 12244–12269. DOI: 10.1039/D3RA01454A.
- [42] J. Markna and P. K. Rathod. “Review on the efficiency of quantum dot sensitized solar cell: Insights into photoanodes and QD sensitizers”. In: *Dyes and Pigments* 199 (2022), p. 110094. DOI: 10.1016/j.dyepig.2022.110094.
- [43] “Recent advances in the development of high efficiency quantum dot sensitized solar cells (QDSSCs): A review”. In: *Materials Science for Energy Technologies* 6 (2023), pp. 533–546. DOI: 10.1016/j.mset.2023.05.001.

- [44] J. Wang, J. Liu, H. Yin, S. Li, V. Kuvondikov, and L. Ye. “Eco-friendly and ultrathin solar cells featuring nanocrystals: Advances and perspectives”. In: *Materials Chemistry Frontiers* 7.20 (2023), pp. 4693–4706. DOI: 10.1039/D3QM00334E.
- [45] B. Yang, J. Cang, Z. Li, and J. Chen. “Nanocrystals as performance-boosting materials for solar cells”. In: *Nanoscale Advances* 6 (2024), pp. 1331–1360. DOI: 10.1039/D3NA01063E.
- [46] O. Saif, A. Zekry, M. Abouelatta-Ebrahim, and A. Shaker. “A comprehensive review of tandem solar cells integrated on silicon substrate: III/V vs perovskite”. In: *Silicon* 15 (2023), pp. 1–19. DOI: 10.1007/s12633-023-02466-8.
- [47] B. O’Regan and M. Grätzel. “A low-cost, high-efficiency solar cell based on dye-sensitized colloidal TiO₂ films”. In: *Nature* 353 (1991), pp. 737–740. DOI: 10.1038/353737a0.
- [48] M. Grätzel. “Photoelectrochemical cells”. In: *Nature* 414 (2001), pp. 338–344. DOI: 10.1038/35104607.
- [49] M. Grätzel. “Dye-sensitized solar cells”. In: *Journal of Photochemistry and Photobiology C: Photochemistry Reviews* 4.2 (2003), pp. 145–153. DOI: 10.1016/S1389-5567(03)00026-1.
- [50] A. M. Bagher, M. M. A. Vahid, and M. Mohsen. “Types of solar cells and application”. In: *American Journal of Optics and Photonics* 3.5 (2015), pp. 94–113. DOI: 10.11648/j.ajop.20150305.17.
- [51] J. Nowotny. “*Oxide semiconductors for solar energy conversion—titanium dioxide*”. CRC Press, Taylor Francis Group, 2012. ISBN: 9780429104671. DOI: 10.1201/b11109.
- [52] S. Sankaranarayanan, M. Hariram, S. Vivekanandhan, and C. Ngamcharussrivichai. “Chapter 15 - Biosynthesized transition metal oxide nanostructures for photocatalytic degradation of organic dyes”. In: *Green Functionalized Nanomaterials for Environmental Applications*. Ed. by U. Shanker, C. M. Hussain, and M. Rani. Micro and Nano Technologies. Elsevier, 2022, pp. 417–460. ISBN: 978-0-12-823137-1. DOI: 10.1016/B978-0-12-823137-1.00016-6.
- [53] N. Martsinovich, D. R. Jones, and A. Troisi. “Electronic structure of TiO₂ surfaces and effect of molecular adsorbates using different DFT implementations”. In: *Journal of Physical Chemistry C* 114.51 (2010), pp. 22659–22670. DOI: 10.1021/jp109756g.
- [54] A. Hagfeldt, G. Boschloo, L. Sun, L. Kloo, and H. Pettersson. “Dye-sensitized solar cells”. In: *Chemical Reviews* 110.11 (2010), pp. 6595–6663. DOI: 10.1021/cr900356p.

- [55] W.-C. Chen, S. Nachimuthu, and J.-C. Jiang. “Revealing the influence of cyano in anchoring groups of organic dyes on adsorption stability and photovoltaic properties for dye-sensitized solar cells”. In: *Scientific Reports* 7.1 (2017), pp. 1–13. DOI: 10.1038/s41598-017-05408-8.
- [56] Ö. Birel, S. Nadeem, and H. Duman. “Porphyrin-based dye-sensitized solar cells (DSSCs): A review”. In: *Journal of Fluorescence* 27 (2017), pp. 1075–1085. DOI: 10.1007/s10895-017-2041-2.
- [57] N. Tomar, A. Agrawal, V. S. Dhaka, and P. K. Surolia. “Ruthenium complexes based dye sensitized solar cells: Fundamentals and research trends”. In: *Solar Energy* 207 (2020), pp. 59–76. DOI: 10.1016/j.solener.2020.06.060.
- [58] S. A. Badawy, K. E. Salem, A. A. Fadda, E. Abdel-Latif, and M. R. Elmorsy. “Advancements in metal-free organic dyes: Achieving over 10% efficiency in DSSCs”. In: *Dyes and Pigments* 225 (2024), p. 112096. DOI: 10.1016/j.dyepig.2024.112096.
- [59] A. Alizadeh, M. Roudgar-Amoli, S.-M. Bonyad-Shekalgourabi, Z. Shariatinia, M. Mahmoudi, and F. Saadat. “Dye sensitized solar cells go beyond using perovskite and spinel inorganic materials: A review”. In: *Renewable and Sustainable Energy Reviews* 157 (2022), p. 112047. DOI: 10.1016/j.rser.2021.112047.
- [60] C. N. Muniz, C. A. Archer, J. S. Applebaum, A. Alagaratnam, J. Schaab, P. I. Djurovich, and M. E. Thompson. “Two-coordinate coinage metal complexes as solar photosensitizers”. In: *Journal of the American Chemical Society* 145.25 (2023), pp. 13846–13857. DOI: 10.1021/jacs.3c02825.
- [61] A. Kay and M. Grätzel. “Artificial photosynthesis. 1. Photosensitization of titania solar cells with chlorophyll derivatives and related natural porphyrins”. In: *Journal of Physical Chemistry* 97.23 (1993), pp. 6272–6277. DOI: 10.1021/j100125a029.
- [62] N. Mariotti, M. Bonomo, L. Fagiolari, N. Barbero, C. Gerbaldi, F. Bella, and C. Barolo. “Recent advances in eco-friendly and cost-effective materials towards sustainable dye-sensitized solar cells”. In: *Green Chemistry* 22.21 (2020), pp. 7168–7218. DOI: 10.1039/D0GC01148G.
- [63] S. C. Moldoveanu. “Chapter 16 - Pyrolysis of aromatic heterocyclic compounds”. In: *Pyrolysis of organic molecules*. Ed. by S. C. Moldoveanu. Second Edition. Elsevier, 2019, pp. 715–762. ISBN: 978-0-444-64000-0. DOI: 10.1016/B978-0-444-64000-0.00016-0.
- [64] K. Tennakone, A. Kumarasinghe, G. Kumara, K. Wijayantha, and P. Sirimanne. “Nanoporous TiO₂ photoanode sensitized with the flower pigment cyanidin”. In: *Journal of Photochemistry and Photobiology A: Chemistry* 108.2 (1997), pp. 193–195. DOI: 10.1016/S1010-6030(97)00090-7.

- [65] I. C. Maurya, A. K. Gupta, P. Srivastava, and L. Bahadur. “Natural dye extracted from *Saraca asoca* flowers as sensitizer for TiO₂-based dye-sensitized solar cell”. In: *Journal of Solar Energy Engineering* 138.5 (2016), p. 051006. DOI: 10.1115/1.4034028.
- [66] J. Fleschhut, F. Kratzer, G. Rechkemmer, and S. Kulling. “Stability and biotransformation of various dietary anthocyanins *in vitro*”. In: *European Journal of Nutrition* 51 (2006), pp. 1461–1471. DOI: 10.1007/s00394-005-0557-8.
- [67] R. Ramamoorthy, N. Radha, G. Maheswari, S. Anandan, S. Manoharan, and R. V. Williams. “Betalain and anthocyanin dye-sensitized solar cells”. In: *Journal of Applied Electrochemistry* 46.9 (2016), pp. 929–941. DOI: 10.1007/s10800-016-0974-9.
- [68] F. J. Francis. “Food colorants: Anthocyanins.” In: *Critical Reviews in Food Science and Nutrition* 28.4 (1989), pp. 273–314. DOI: 10.1080/10408398909527503.
- [69] J.-M. Kong, L.-S. Chia, N.-K. Goh, T.-F. Chia, and R. Brouillard. “Analysis and biological activities of anthocyanins”. In: *Phytochemistry* 64.5 (2003), pp. 923–933. DOI: 10.1016/S0031-9422(03)00438-2.
- [70] D. D. Pratiwi, F. Nurosyid, A. Supriyanto, and R. Suryana. “Efficiency enhancement of dye-sensitized solar cells (DSSC) by addition of synthetic dye into natural dye (anthocyanin)”. In: *IOP Conference Series: Materials Science and Engineering* 176 (2017), p. 012012. DOI: 10.1088/1757-899x/176/1/012012.
- [71] E. C. Prima, A. Nuruddin, B. Yulianto, G. Kawamura, and A. Matsuda. “Combined spectroscopic and TDDFT study of single-double anthocyanins for application in dye-sensitized solar cells”. In: *New Journal of Chemistry* 42.14 (2018), pp. 11616–11628. DOI: 10.1039/C8NJ01202D.
- [72] A. Purwoko, V. Setiawati, and S. Hadisaputra. “Metal-pigment complex derived from natural dye of anthocyanin: A potential candidate for DSSC photosensitizer”. In: *IOP Conference Series: Materials Science and Engineering* 509 (2019), p. 012130. DOI: 10.1088/1757-899X/509/1/012130.
- [73] W. Shah, S. M. Faraz, and Z. H. Awan. “Photovoltaic properties and impedance spectroscopy of dye sensitized solar cells co-sensitized by natural dyes”. In: *Physica B: Condensed Matter* 654 (2023), p. 414716. DOI: 10.1016/j.physb.2023.414716.
- [74] V. Pramananda, T. A. H. Fityay, and E. Misran. “Anthocyanin as natural dye in DSSC fabrication: A review”. In: *IOP Conference Series: Materials Science and Engineering* 1122.1 (2021), p. 012104. DOI: 10.1088/1757-899X/1122/1/012104.

- [75] V. Bonačić-Koutecký, L. Češpiva, P. Fantucci, and J. Koutecký. “Effective core potential-configuration interaction study of electronic structure and geometry of small neutral and cationic Ag_n clusters: Predictions and interpretation of measured properties”. In: *The Journal of Chemical Physics* 98.10 (1993), pp. 7981–7994. DOI: 10.1063/1.464552.
- [76] J. Yang, R. Pang, D. Song, and M.-B. Li. “Tailoring silver nanoclusters *via* doping: Advances and opportunities”. In: *Nanoscale Advances* 3.9 (2021), pp. 2411–2422. DOI: 10.1039/D1NA00077B.
- [77] K. Sahoo, T. R. Gazi, S. Roy, and I. Chakraborty. “Nanohybrids of atomically precise metal nanoclusters”. In: *Communications Chemistry* 6.1 (2023), p. 157. DOI: 10.1038/s42004-023-00958-7.
- [78] V. Bonačić-Koutecký, J. Burda, R. Mitrić, M. Ge, G. Zampella, and P. Fantucci. “Density functional study of structural and electronic properties of bimetallic silver–gold clusters: Comparison with pure gold and silver clusters”. In: *The Journal of Chemical Physics* 117.7 (2002), pp. 3120–3131. DOI: 10.1063/1.1492800.
- [79] A. Kulesza, R. Mitrić, and V. Bonačić-Koutecký. “Unique optical properties of silver cluster-biochromophore hybrids: Comparison with copper and gold”. In: *Chemical Physics Letters* 501.4-6 (2011), pp. 211–214. DOI: 10.1016/j.cplett.2010.11.026.
- [80] W. H. Weber and J. Lambe. “Luminescent greenhouse collector for solar radiation”. In: *Applied Optics* 15 (1976), pp. 2299–2300. DOI: 10.1364/AO.15.002299.
- [81] A. Goetzberger and W. Greube. “Solar energy conversion with fluorescent collectors”. In: *Journal of Applied Physics* 48 (1977), pp. 123–139. DOI: 10.1007/BF00883080.
- [82] J. S. Batchelder, A. H. Zewai, and T. Cole. “Luminescent solar concentrators. 1: Theory of operation and techniques for performance evaluation”. In: *Applied Optics* 18.18 (1979), pp. 3090–3110. DOI: 10.1364/AO.18.003090.
- [83] A. Hermann. “Luminescent solar concentrators - A review”. In: *Solar Energy* 29.4 (1982), pp. 323–329. DOI: 10.1016/0038-092X(82)90247-X.
- [84] S. Castelletto and A. Boretti. “Luminescence solar concentrators: A technology update”. In: *Nano Energy* 109 (2023), p. 108269. DOI: 10.1016/j.nanoen.2023.108269.
- [85] K. Zhang, C. Qin, X. Yang, A. Islam, S. Zhang, H. Chen, and L. Han. “High-performance, transparent, dye-sensitized solar cells for see-through photovoltaic windows”. In: *Advanced Energy Materials* 4.11 (2014), p. 1301966. DOI: 10.1002/aenm.201301966.
- [86] C. Yang, W. Sheng, M. Moemeni, M. Bates, C. K. Herrera, B. Borhan, and R. R. Lunt. “Ultraviolet and near-infrared dual-band selective-harvesting transparent luminescent solar concentrators”. In: *Advanced Energy Materials* 11.12 (2021), p. 2003581. DOI: 10.1002/aenm.202003581.

- [87] C. Yang, D. Liu, and R. R. Lunt. “How to accurately report transparent luminescent solar concentrators”. In: *Joule* 3.12 (2019), pp. 2871–2876. DOI: 10.1016/j.joule.2019.10.009.
- [88] W. Shockley and H. J. Queisser. “Detailed balance limit of efficiency of p- junction solar cells”. In: *Journal of Applied Physics* 32.3 (1961), pp. 510–519. DOI: 10.1063/1.1736034.
- [89] R. Englman and J. Jortner. “The energy gap law for radiationless transitions in large molecules”. In: *Molecular Physics* 18.2 (1970), pp. 145–164. DOI: 10.1080/00268977000100171.
- [90] B. F. E. Curchod and T. J. Martínez. “Ab initio nonadiabatic quantum molecular dynamics”. In: *Chemical Reviews* 118.7 (2018), pp. 3305–3336. DOI: 10.1021/acs.chemrev.7b00423.
- [91] T. R. Nelson, A. J. White, J. A. Bjorgaard, A. E. Sifain, Y. Zhang, B. Nebgen, S. Fernandez-Alberti, D. Mozysky, A. E. Roitberg, and S. Tretiak. “Non-adiabatic excited-state molecular dynamics: Theory and applications for modeling photophysics in extended molecular materials”. In: *Chemical Reviews* 120.4 (2020), pp. 2215–2287. DOI: 10.1021/acs.chemrev.9b00447.
- [92] C.-W. Ju, H. Bai, B. Li, and R. Liu. “Machine learning enables highly accurate predictions of photophysical properties of organic fluorescent materials: Emission wavelengths and quantum yields”. In: *Journal of Chemical Information and Modeling* 61.3 (2021), pp. 1053–1065. DOI: 10.1021/acs.jcim.0c01203.
- [93] J. Li, M. Vacher, P. O. Dral, and S. A. Lopez. “Chapter 6 - Machine learning methods in photochemistry and photophysics”. In: *Theoretical and Computational Photochemistry*. Ed. by C. García-Iriepa and M. Marazzi. Elsevier, 2023, pp. 163–189. ISBN: 978-0-323-91738-4. DOI: 10.1016/B978-0-323-91738-4.00002-6.
- [94] M. T. do Casal, K. Veys, M. H. E. Bousquet, D. Escudero, and D. Jacquemin. “First-principles calculations of excited-state decay rate constants in organic fluorophores”. In: *The Journal of Physical Chemistry A* 127.48 (2023), pp. 10033–10053. DOI: 10.1021/acs.jpca.3c06191.
- [95] Y. Jestin, S. Chandra, B. Cass, H. Ahmed, and S. McCormack. “1.25 - Down-shifting of the incident light for photovoltaic applications”. In: *Comprehensive Renewable Energy*. Ed. by T. M. Letcher. Second Edition. Oxford: Elsevier, 2022, pp. 534–560. ISBN: 978-0-12-819734-9. DOI: 10.1016/B978-0-12-819727-1.00126-6.
- [96] C. Zhu, K. K. Liang, M. Hayashi, and S. H. Lin. “Theoretical treatment of anharmonic effect on molecular absorption, fluorescence spectra, and electron transfer”. In: *Chemical Physics* 358.1-2 (2009), pp. 137–146. DOI: 10.1016/j.chemphys.2009.01.006.

- [97] F. J. Avila Ferrer and F. Santoro. “Comparison of vertical and adiabatic harmonic approaches for the calculation of the vibrational structure of electronic spectra”. In: *Physical Chemistry Chemical Physics* 14.39 (2012), pp. 13549–13563. DOI: 10.1039/C2CP41169E.
- [98] F. Santoro and D. Jacquemin. “Going beyond the vertical approximation with time-dependent density functional theory”. In: *WIREs Computational Molecular Science* 6.5 (2016), pp. 460–486. DOI: 10.1002/wcms.1260.
- [99] S. Banerjee, A. Baiardi, J. Bloino, and V. Barone. “Temperature dependence of radiative and nonradiative rates from time-dependent correlation function methods”. In: *Journal of Chemical Theory and Computation* 12.2 (2016), pp. 774–786. DOI: 10.1021/acs.jctc.5b01017.
- [100] R. R. Valiev, V. N. Cherepanov, R. T. Nasibullin, D. Sundholm, and T. Kurtén. “Calculating rate constants for intersystem crossing and internal conversion in the Franck–Condon and Herzberg–Teller approximations”. In: *Physical Chemistry Chemical Physics* 21.34 (2019), pp. 18495–18500. DOI: 10.1039/C9CP03183A.
- [101] B. de Souza, G. Farias, F. Neese, and R. Izsák. “Predicting phosphorescence rates of light organic molecules using time-dependent density functional theory and the path integral approach to dynamics”. In: *Journal of Chemical Theory and Computation* 15.3 (2019), pp. 1896–1904. DOI: 10.1021/acs.jctc.8b00841.
- [102] R. R. Valiev, V. N. Cherepanov, G. V. Baryshnikov, and D. Sundholm. “First-principles method for calculating the rate constants of internal-conversion and intersystem-crossing transitions”. In: *Physical Chemistry Chemical Physics* 20.9 (2018), pp. 6121–6133. DOI: 10.1039/C7CP08703A.
- [103] R. R. Valiev, B. S. Merzlikin, R. T. Nasibullin, A. Kurtzevitch, V. N. Cherepanov, R. R. Ramazanov, D. Sundholm, and T. Kurtén. “Internal conversion rate constant calculations considering Duschinsky, anharmonic and Herzberg–Teller effects”. In: *Physical Chemistry Chemical Physics* 25.8 (2023), pp. 6406–6415. DOI: 10.1039/D2CP05275J.
- [104] R. Nasibullin, B. Merzlikin, R. Valiev, and V. Cherepanov. “Fast calculation of internal conversion rate constant using the time-dependent formalism”. In: *Chemical Physics Letters* 840 (2024), p. 141147. DOI: 10.1016/j.cplett.2024.141147.
- [105] F. Santoro and J. Cerezo. *FCclasses3*, a code to simulate electronic spectra. Version FCclasses3-0.1, 2019. Visit "<http://www.pi.iccom.cnr.it/fcclasses>".

- [106] M. Bass, C. DeCusatis, J. Enoch, V. Lakshminarayanan, G. Li, C. MacDonald, V. Mahajan, and E. Van Stryland. *Handbook of optics, Third edition volume II: Design, fabrication and testing, sources and detectors, radiometry and photometry*. Handbook of Optics v. 2. McGraw Hill LLC, 2009. ISBN: 9780071629270.
- [107] F. J. A. Ferrer, R. Improta, F. Santoro, and V. Barone. “Computing the inhomogeneous broadening of electronic transitions in solution: a first-principle quantum mechanical approach”. In: *Physical Chemistry Chemical Physics* 13.38 (2011), pp. 17007–17012. DOI: 10.1039/C1CP22115A.
- [108] A. Eisfeld and J. S. Briggs. “Dye aggregates in luminescent solar concentrators”. In: *Physica Status Solidi (A)* 215.2 (2018), p. 1700634. DOI: 10.1002/pssa.201700634.
- [109] J. L. Banal, J. M. White, T. W. Lam, A. W. Blakers, K. P. Ghiggino, and W. W. H. Wong. “A transparent planar concentrator using aggregates of gem-pyrene ethenes”. In: *Advanced Energy Materials* 5.19 (2015), p. 1500818. DOI: 10.1002/aenm.201500818.
- [110] G. Scheibe. “Über die Veränderlichkeit der Absorptionsspektren in Lösungen und die Nebenvalenzen als ihre Ursache”. In: *Angewandte Chemie* 50 (1937), pp. 212–219. DOI: 10.1002/ange.19370501103.
- [111] E. E. Jelley. “Spectral absorption and fluorescence of dyes in the molecular state”. In: *Nature* 138.3502 (1936), pp. 1009–1010. DOI: 10.1038/1381009a0.
- [112] A. Humeniuk, R. Mitrić, and V. Bonačić-Koutecký. “Size dependence of non-radiative decay rates in J-aggregates”. In: *The Journal of Physical Chemistry A* 124.49 (2020), pp. 10143–10151. DOI: 10.1021/acs.jpca.0c09074.
- [113] B. Scharf and U. Dinur. “Striking dependence of the rate of electronic radiationless transitions on the size of the molecular system”. In: *Chemical Physics Letters* 105.1 (1984), pp. 78–82. DOI: 10.1016/0009-2614(84)80417-0.
- [114] J. He, Y. J. Jo, X. Sun, W. Qiao, J. Ok, T.-i. Kim, and Z. Li. “Squaraine dyes for photovoltaic and biomedical applications”. In: *Advanced Functional Materials* 31.12 (2020), p. 2008201. DOI: 10.1002/adfm.202008201.
- [115] K. Ilina, W. M. MacCuaig, M. Laramie, J. N. Jeouty, L. R. McNally, and M. Henary. “Squaraine dyes: Molecular design for different applications and remaining challenges”. In: *Bioconjugate Chemistry* 31.2 (2020), pp. 194–213. DOI: 10.1021/acs.bioconjchem.9b00482.
- [116] L. E. McNamara, T. A. Rill, A. J. Huckaba, V. Ganeshraj, J. Gayton, R. A. Nelson, E. A. Sharpe, A. Dass, N. I. Hammer, and J. H. Delcamp. “Indolizine–squaraines: NIR fluorescent materials with molecularly engineered Stokes shifts”. In: *Chemistry* 23.51 (2017), pp. 12494–12501. DOI: 10.1002/chem.201702209.

- [117] A. Zampetti, A. Minotto, and F. Cacialli. “Near-infrared (NIR) organic light-emitting diodes (OLEDs): Challenges and opportunities”. In: *Advanced Functional Materials* 29.21 (2019), p. 1807623. DOI: 10.1002/adfm.201807623.
- [118] K. Strassel, A. Kaiser, S. Jenatsch, A. C. Véron, S. B. Anantharaman, E. Hack, M. Diethelm, F. Nüesch, R. Aderne, C. Legnani, et al. “Squaraine dye for a visibly transparent all-organic optical upconversion device with sensitivity at 1000 nm”. In: *ACS Applied Materials Interfaces* 10.13 (2018), pp. 11063–11069. DOI: 10.1021/acsami.8b00047.
- [119] H. Ceymann, A. Rosspeintner, M. H. Schreck, C. Mützel, A. Stoy, E. Vauthey, and C. Lambert. “Cooperative enhancement *versus* additivity of two-photon-absorption cross sections in linear and branched squaraine superchromophores”. In: *Physical Chemistry Chemical Physics* 18.24 (2016), pp. 16404–16413. DOI: 10.1039/C6CP02312F.
- [120] M. I. S. Röhr, H. Marciniak, J. Hoche, M. H. Schreck, H. Ceymann, R. Mitric, and C. Lambert. “Exciton dynamics from strong to weak coupling limit illustrated on a series of squaraine dimers”. In: *The Journal of Physical Chemistry C* 122.15 (2018), pp. 8082–8093. DOI: 10.1021/acs.jpcc.8b00847.
- [121] C. Heshmatpour, P. Malevich, F. Plasser, M. Menger, C. Lambert, F. Šanda, and J. Hauer. “Annihilation dynamics of molecular excitons measured at a single perturbative excitation energy”. In: *The Journal of Physical Chemistry Letters* 11.18 (2020), pp. 7776–7781. DOI: 10.1021/acs.jpcllett.0c02141.
- [122] S. F. Völker, S. Uemura, M. Limpinsel, M. Mingeback, C. Deibel, V. Dyakonov, and C. Lambert. “Polymeric squaraine dyes as electron donors in bulk heterojunction solar cells”. In: *Macromolecular Chemistry and Physics* 211.10 (2010), pp. 1098–1108. DOI: 10.1002/macp.200900670.
- [123] C. Lambert, F. Koch, S. F. Völker, A. Schmiedel, M. Holzapfel, A. Humeniuk, M. I. S. Röhr, R. Mitric, and T. Brixner. “Energy transfer between squaraine polymer sections: From helix to zigzag and all the way back”. In: *Journal of the American Chemical Society* 137.24 (2015), pp. 7851–7861. DOI: 10.1021/jacs.5b03644.
- [124] A. Turkin, P. Malý, and C. Lambert. “Fluorescence band exchange narrowing in a series of squaraine oligomers: energetic *vs.* structural disorder”. In: *Physical Chemistry Chemical Physics* 23.34 (2021), pp. 18393–18403. DOI: 10.1039/D1CP02136B.
- [125] J. Selby, M. Holzapfel, K. Radacki, A. K. Swain, H. Braunschweig, and C. Lambert. “Polymeric indolenine–squaraine foldamers with a preferred helix twist sense and their chiroptical absorption and emission properties”. In: *Macromolecules* 55.2 (2022), pp. 421–436. DOI: 10.1021/acs.macromol.1c02155.

- [126] M. Kasha. “Energy transfer mechanisms and the molecular exciton model for molecular aggregates”. In: *Radiation Research* 20 (1963), pp. 55–71. DOI: 10.1667/rrav03.1.
- [127] M. Olivucci and A. Sinicropi. “I - Computational photochemistry”. In: *Computational photochemistry*. Ed. by M. Olivucci. Vol. 16. Theoretical and Computational Chemistry. Elsevier, 2005, pp. 1–33. DOI: 10.1016/S1380-7323(05)80018-4.
- [128] E. Schrödinger. “An undulatory theory of the mechanics of atoms and molecules”. In: *Physical Review* 28.6 (1926), pp. 1049–1070. DOI: 10.1103/PhysRev.28.1049.
- [129] W. Heisenberg. “Zur Theorie des Ferromagnetismus”. In: *Zeitschrift für Physik* 49.9-10 (1928), pp. 619–636. DOI: 10.1007/BF01328601.
- [130] W. J. Hehre, R. F. Stewart, and J. A. Pople. “Self-consistent molecular-orbital methods. I. Use of gaussian expansions of slater-type atomic orbitals”. In: *The Journal of Chemical Physics* 51.6 (1969), pp. 2657–2664. DOI: 10.1063/1.1672392.
- [131] J. A. Pople. “Quantum chemical models (Nobel lecture)”. In: *Angewandte Chemie International Edition* 38.13-14 (1999), pp. 1894–1902. DOI: 10.1103/RevModPhys.71.1267.
- [132] F. Jensen. *Introduction to computational chemistry*. Wiley, 2013. ISBN: 978-0470011874.
- [133] L. H. Thomas. “The calculation of atomic fields”. In: *Mathematical Proceedings of the Cambridge Philosophical Society* 23.5 (1927), pp. 542–548. DOI: 10.1017/S0305004100011683.
- [134] E. Fermi. “Eine statistische Methode zur Bestimmung einiger Eigenschaften des Atoms und ihre Anwendung auf die Theorie des periodischen Systems der Elemente”. In: *Zeitschrift für Physik* 48.73 (1928), pp. 542–548. DOI: 10.1007/BF01351576.
- [135] P. Hohenberg and W. Kohn. “Inhomogeneous electron gas”. In: *Physical Review* 136.3B (1964), B864–B871. DOI: 10.1103/PhysRev.136.B864.
- [136] W. Kohn and L. J. Sham. “Self - consistent equations including exchange and correlation effects”. In: *Physical Review* 140.4A (1965), A1133–A1138. DOI: 10.1103/PhysRev.140.A1133.
- [137] P. Atkins and J. De Paula. *Atkins’ physical chemistry*. Oxford University Press, 2002. ISBN: 9780198847816.
- [138] E. Runge and E. K. U. Gross. “Density - functional theory for time - dependent systems”. In: *Physical Review Letters* 52.12 (1984), pp. 997–1000. DOI: 10.1103/PhysRevLett.52.997.

References

- [139] M. A. L. Marques and E. K. U. Gross. “Time-dependent density functional theory.” In: *Annual review of physical chemistry* 55 (2004), pp. 427–55. DOI: 10.1146/annurev.physchem.55.091602.094449.
- [140] C. J. Cramer. *Essentials of computational chemistry, theories and models*. Wiley, 2002. ISBN: 9780470091838. DOI: 10.1021/ci010445m.
- [141] J. Tomasi, B. Mennucci, and R. Cammi. “Quantum mechanical continuum solvation models”. In: *Chemical Reviews* 105.8 (2005), pp. 2999–3094. DOI: 10.1021/cr9904009.
- [142] J. Bentley. “Exclusion surfaces for molecules in argon and helium”. In: *The Journal of Chemical Physics* 119.11 (2003), pp. 5449–5456. DOI: 10.1063/1.1600435.
- [143] L. Onsager. “Electric moments of molecules in liquids”. In: *Journal of the American Chemical Society* 58.8 (1936), pp. 1486–1493. DOI: 10.1021/ja01299a050.
- [144] A. Bondi. “van der Waals volumes and radii”. In: *The Journal of Physical Chemistry* 68.3 (1964), pp. 441–451. DOI: 10.1021/j100785a001.
- [145] S. Miertuš, E. Scrocco, and J. Tomasi. “Electrostatic interaction of a solute with a continuum. A direct utilization of AB initio molecular potentials for the prevision of solvent effects”. In: *Chemical Physics* 55.1 (1981), pp. 117–129. DOI: 10.1016/0301-0104(81)85090-2.
- [146] C. Amovilli, V. Barone, R. Cammi, E. Cancès, M. Cossi, B. Mennucci, C. S. Pomelli, and J. Tomasi. “Recent advances in the description of solvent effects with the polarizable continuum model”. In: *Advances in Quantum Chemistry* 32 (1998), pp. 227–261. DOI: 10.1016/S0065-3276(08)60416-5.
- [147] B. Mennucci, C. Cappelli, C. A. Guido, R. Cammi, and J. Tomasi. “Structures and properties of electronically excited chromophores in solution from the polarizable continuum model coupled to the time-dependent density functional theory”. In: *The Journal of Physical Chemistry A* 113.13 (2009), pp. 3009–3020. DOI: 10.1021/jp8094853.
- [148] E. Cancès and B. Mennucci. “New applications of integral equations methods for solvation continuum models: ionic solutions and liquid crystals”. In: *Journal of Mathematical Chemistry* 23.3-4 (1998), pp. 309–326. DOI: 10.1023/A:1019133611148.
- [149] E. Cancès, B. Mennucci, and J. Tomasi. “A new integral equation formalism for the polarizable continuum model: Theoretical background and applications to isotropic and anisotropic dielectrics”. In: *The Journal of Chemical Physics* 107.8 (1997), pp. 3032–3041. DOI: 10.1063/1.474659.
- [150] D. Young. *Computational chemistry: A practical guide for applying techniques to real world problems*. John Wiley Sons, Inc., 2001, pp. 32–41. ISBN: 9780471220657. DOI: 10.1002/0471220655.ch4.

- [151] A. D. Becke. “A new mixing of Hartree–Fock and local density–functional theories”. In: *The Journal of Chemical Physics* 98.2 (1993), pp. 1372–1377. DOI: 10.1063/1.464304.
- [152] C. Adamo and V. Barone. “Toward reliable density functional methods without adjustable parameters: The PBE0 model”. In: *The Journal of Chemical Physics* 110.13 (1999), pp. 6158–6170. DOI: 10.1063/1.478522.
- [153] M. Ernzerhof and G. E. Scuseria. “Assessment of the Perdew–Burke–Ernzerhof exchange–correlation functional”. In: *The Journal of Chemical Physics* 110.11 (1999), pp. 5029–5036. DOI: 10.1063/1.478401.
- [154] D. Jacquemin, B. Mennucci, and C. Adamo. “Excited-state calculations with TD-DFT: from benchmarks to simulations in complex environments”. In: *Physical Chemistry Chemical Physics* 13.38 (2011), pp. 16987–16998. DOI: 10.1039/C1CP22144B.
- [155] T. Yanai, D. P. Tew, and N. C. Handy. “A new hybrid exchange–correlation functional using the Coulomb–attenuating method (CAM-B3LYP)”. In: *Chemical Physics Letters* 393.1-3 (2004), pp. 51–57. DOI: 10.1016/j.cplett.2004.06.011.
- [156] J.-D. Chai and M. Head-Gordon. “Long-range corrected hybrid density functionals with damped atom–atom dispersion corrections”. In: *Physical Chemistry Chemical Physics* 10.44 (2008), pp. 6615–6620. DOI: 10.1039/B810189B.
- [157] S. Mai and L. González. “Molecular photochemistry: Recent developments in theory”. In: *Angewandte Chemie International Edition* 59.39 (2020), pp. 16832–16846. DOI: 10.1002/anie.201916381.
- [158] A. Wodyński, A. V. Arbuznikov, and M. Kaupp. “Strong-correlation density functionals made simple”. In: *The Journal of Chemical Physics* 158.24 (2023), p. 244117. DOI: 10.1063/5.0153463.
- [159] M. Kaupp, A. Wodyński, A. V. Arbuznikov, S. Fürst, and C. J. Schattenberg. “Toward the next generation of density functionals: Escaping the zero-sum game by using the exact-exchange energy density”. In: *Accounts of Chemical Research* 57.13 (2024), pp. 1815–1826. DOI: 10.1021/acs.accounts.4c00209.
- [160] N. S. Hill and M. L. Coote. “Chapter seven - A comparison of methods for theoretical photochemistry: Applications, successes and challenges”. In: *Annual Reports in Computational Chemistry*. Ed. by D. A. Dixon. Vol. 15. Elsevier, 2019, pp. 203–285. DOI: <https://doi.org/10.1016/bs.arcc.2019.08.008>.
- [161] E. Engel. “Chapter 10 - Relativistic density functional theory: foundations and basic formalism”. In: *Relativistic Electronic Structure Theory*. Ed. by P. Schwerdtfeger. Vol. 11. Theoretical and Computational Chemistry. Elsevier, 2002, pp. 523–621. DOI: 10.1016/S1380-7323(02)80036-X.

- [162] T. Moitra, L. Konecny, M. Kadek, A. Rubio, and M. Repisky. “Accurate relativistic real-time time-dependent density functional theory for valence and core attosecond transient absorption spectroscopy”. In: *The Journal of Physical Chemistry Letters* 14.7 (2023), pp. 1714–1724. DOI: 10.1021/acs.jpcclett.2c03599.
- [163] W. Liu and Y. Xiao. “Relativistic time-dependent density functional theories”. In: *Chemical Society Reviews* 47.12 (2018), pp. 4481–4509. DOI: 10.1039/C8CS00175H.
- [164] M. Bužančić Milosavljević, A. Mravak, M. Perić Bakulić, and V. Bonačić-Koutecký. “Model systems for dye-sensitized solar cells: Cyanidin-silver nanocluster hybrids at TiO₂ support”. In: *RSC Advances* 13.9 (2023), pp. 6010–6016. DOI: 10.1039/D3RA00165B.
- [165] R. Koch, A. S. Lipton, S. Filipek, and V. Renugopalakrishnan. “Arginine interactions with anatase TiO₂ (100) surface and the perturbation of 49 Ti NMR chemical shifts—a DFT investigation: relevance to Renu-Seeram bio solar cell”. In: *Journal of Molecular Modeling* 17.6 (2011), pp. 1467–1472. DOI: 10.1007/s00894-010-0853-y.
- [166] E. Marcano. “DFT study of anthocyanidin and anthocyanin pigments for dye sensitized solar cells: Electron injecting from the excited states and adsorption onto TiO₂ (anatase) surface”. In: *Energy Harvesting and Systems* 5.1-2 (2018), pp. 29–38. DOI: 10.1515/ehs-2018-0008.
- [167] M. Bužančić Milosavljević, M. Perić Bakulić, Ž. Sanader Maršić, A. Mravak, and V. Bonačić-Koutecký. “Enhancing efficiency of dye sensitized solar cells by coinage metal doping of cyanidin-silver trimer hybrids at TiO₂ support based on theoretical study”. In: *Nanomaterials* 14.12 (2024). DOI: 10.3390/nano14121034.
- [168] M. Taniguchi and J. S. Lindsey. “Database of absorption and fluorescence spectra of >300 common compounds for use in photochemCAD”. In: *Photochemistry and Photobiology* 94.2 (2018), pp. 290–327. DOI: 10.1111/php.12860.
- [169] G. Jones II, W. R. Jackson, C. Y. Choi, and W. R. Bergmark. “Solvent effects on emission yield and lifetime for coumarin laser dyes. Requirements for a rotatory decay mechanism”. In: *Journal of Physical Chemistry* 89.2 (1985), pp. 294–300. DOI: 10.1021/j100248a024.
- [170] S. Mondal, R. Halder, B. Biswas, B. Jana, and P. C. Singh. “Solvent organization around the perfluoro group of coumarin 153 governs its photophysical properties: An experimental and simulation study of coumarin dyes in ethanol as well as fluorinated ethanol solvents”. In: *The Journal of Chemical Physics* 144.18 (2016), p. 184504. DOI: 10.1063/1.4948704.

- [171] K. Rurack and M. Spieles. “Fluorescence quantum yields of a series of red and near-infrared dyes emitting at 600-1000 nm”. In: *Analytical Chemistry* 83.4 (2011), pp. 1232–1242. DOI: 10.1021/ac101329h.
- [172] V. A. Lapina, T. A. Pavich, P. P. Pershukevich, A. V. Trofimov, N. N. Trofimova, Y. B. Tsaplev, and P. P. Zak. “Exploring the utility of coumarins-based luminescent spectra converters”. In: *Journal of Physical Organic Chemistry* 30.9 (2017), e3731. DOI: 10.1002/poc.3731.
- [173] J. S. Seixas de Melo, R. S. Becker, and A. L. Maqanita. “Photophysical behavior of coumarins as a function of substitution and solvent: Experimental evidence for the existence of a lowest lying $1(n,\pi^*)$ state”. In: *Journal of Physical Chemistry* 98.24 (1994), pp. 6054–6058. DOI: 10.1021/j100075a002.
- [174] F. Santoro, R. Improta, A. Lami, J. Bloino, and V. Barone. “Effective method to compute Franck-Condon integrals for optical spectra of large molecules in solution”. In: *The Journal of Chemical Physics* 126.8 (2007), p. 084509. DOI: 10.1063/1.2437197.
- [175] A. Humeniuk, M. Bužančić, J. Hoche, J. Cerezo, R. Mitrić, F. Santoro, and V. Bonačić-Koutecký. “Predicting fluorescence quantum yields for molecules in solution: A critical assessment of the harmonic approximation and the choice of the lineshape function”. In: *The Journal of Chemical Physics* 152.5 (2020), p. 054107. DOI: 10.1063/1.5143212.
- [176] M. G. Debije and P. P. C. Verbunt. “Thirty years of luminescent solar concentrator research: Solar energy for the built environment”. In: *Advanced Energy Materials* 2.1 (2012), pp. 12–35. DOI: 10.1002/aenm.201100554.
- [177] J. L. Banal, B. Zhang, D. J. Jones, K. P. Ghiggino, and W. W. H. Wong. “Emissive molecular aggregates and energy migration in luminescent solar concentrators”. In: *Accounts of Chemical Research* 50.1 (2017), pp. 49–57. DOI: 10.1021/acs.accounts.6b00432.
- [178] F. Proise, A.-L. Joudrier, J.-L. Pelouard, and J.-F. Guillemoles. “Loss analysis in luminescent sheet concentrators: From ideal to real system”. In: *EPJ Photovoltaics* 9 (2018), p. 12. DOI: 10.1051/epjpv/2018010.
- [179] B. Zhang, C. Gao, N. Neto, and W. Wong. *Principles and applications of aggregation-induced emission*. Springer Cham, 2019, pp. 479–504. ISBN: 978-3-319-99036-1. DOI: 10.1007/978-3-319-99037-8_20.
- [180] C. Yang, J. Zhang, W.-T. Peng, W. Sheng, D. Liu, P. Kuttipillai, M. Young, M. Donahue, B. Levine, B. Borhan, et al. “Impact of Stokes shift on the performance of near-infrared harvesting transparent luminescent solar concentrators”. In: *Scientific Reports* 8 (2018), p. 16359. DOI: 10.1038/s41598-018-34442-3.

- [181] M. Bužančić Milosavljević and V. Bonačić-Koutecký. “Design of J-aggregates-like oligomers built from squaraine dyes exhibiting transparency in the visible regime and high fluorescence quantum yield in the NIR region”. In: *Physical Chemistry Chemical Physics* 26.2 (2024), pp. 1314–1321. doi: 10.1039/d3cp05291e.

Appendix to Chapter 2

Supplementary information:
Model systems for dye-sensitized solar cells: cyanidin-silver
nanocluster hybrids at TiO₂ support

Margarita Bužančić Milosavljević¹, Antonija Mravak¹, Martina Perić Bakulić^{1,*}, and
Vlasta Bonačić-Koutecký^{1,2,3,*}

¹Center of Excellence for Science and Technology-Integration of Mediterranean
region (STIM), Faculty of Science, University of Split, Ruđera Boškovića 33, 21000
Split, Croatia.

²Interdisciplinary Center for Advanced Science and Technology (ICAST) at
University of Split, Meštrovićevo šetalište 45, 21000 Split, Croatia

³Department of Chemistry, Humboldt Universität zu Berlin, Brook-Taylor-Strasse 2,
12489 Berlin, Germany.

Photovoltaic parameters

Incident photon to conversion efficiency (IPCE) of dye-sensitized solar cells (DSSC):

$$IPCE = LHE \cdot \Phi_{inj} \cdot \eta_c \quad (1)$$

can be evaluated as a product of light harvesting efficiency (LHE), electron injection efficiency (Φ_{inj}) and charge collection efficiency (η_c).

Light harvesting efficiency is approximated using the equation:

$$LHE = 1 - 10^{-f} \quad (2)$$

where f is the oscillator strength of maximum absorption. High performance of DSSCs is related to the large value of the LHE.

Electron injection efficiency (Φ_{inj}), is proportional to the driving force (ΔG^{inject}), which corresponds to the difference between oxidation potential energy of the excited state (E_{ox}^{dye*}), and reduction potential energy of conduction band (ECB).¹

$$E_{ox}^{dye*} = E_{ox}^{dye} - \lambda_{max} \quad (3)$$

where redox E_{ox}^{dye} is potential of the ground state, and λ_{max} is maximum absorption energy of the sensitizer. Finally, ΔG^{inject} can be written as:

$$\Delta G^{inject} = (E_{ox}^{dye} - \lambda_{max}) - ECB \quad (4)$$

$$E_{ox}^{dye} = -HOMO \quad (5)$$

Experimental ECB of TiO_2 has a value of -4 eV^{2-4} vs. vacuum.

To obtain effective photo-induced electron transfer from the dye sensitizer to the semiconductor, energy levels of the highest occupied (HOMO) and lowest unoccupied (LUMO) molecular orbitals of the dye are required to match the redox potential of the electrolyte, I^-/I_3^- (-4.6 eV^5 vs. vacuum) and the conduction band edge of the semiconductor.¹

Binding energy

The binding energy of the hybrid system E_b corresponds to the:

$$E_b = E_{hybrid} - (E_{cyanidin} + E_{NC}) \quad (6)$$

where E_{hybrid} , $E_{cyanidin}$ and E_{NC} are energies of optimized cyanidin-NC hybrid, cyanidin dye, and NC systems, respectively.

The binding (adsorption) energy E_{ads} of the cyanidin- Ag_9 at TiO_2 surface model is defined as:

$$E_{ads} = E_{complex} - (E_{TiO_2} + E_{cyanidin-Ag_9}) \quad (7)$$

$E_{complex}$ is the energy of adsorbed cyanidin- Ag_9 , E_{TiO_2} is the energy of the optimized TiO_2 model and $E_{cyanidin-Ag_9}$ energy of the optimized cyanidin- Ag_9 .

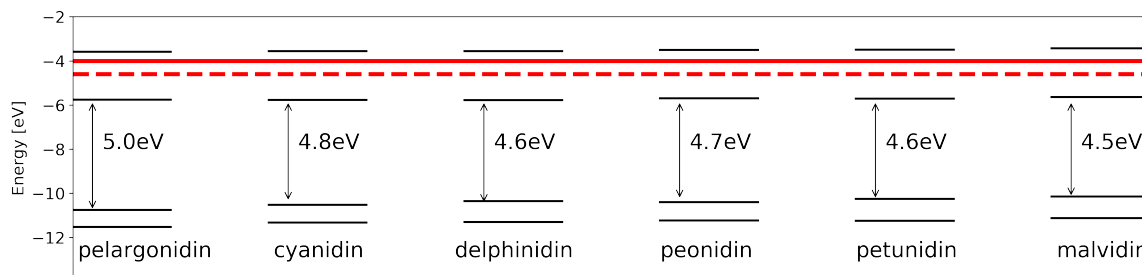


Figure S1: DFT calculated HOMO–LUMO (and HOMO-1, LUMO+1) energy gaps versus vacuum[eV] for the anthocyanidin dyes in comparison with the experimental TiO_2 conduction band edge (red line) and I^-/I_3^- redox level (dashed red line).

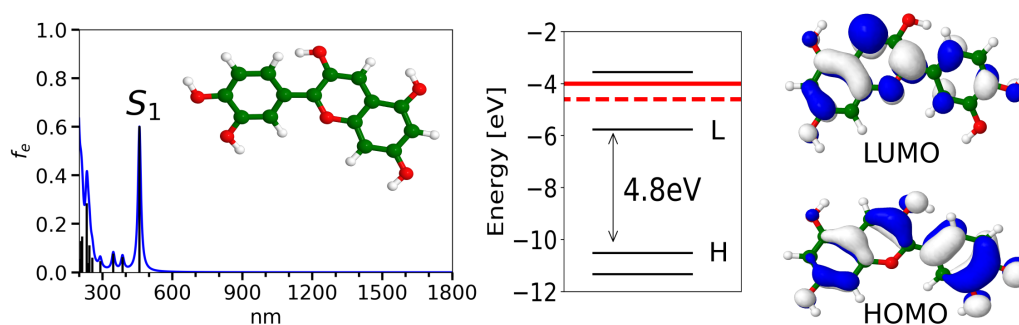


Figure S2: TDDFT calculated absorption spectrum for cyanidin dye employing CAM-B3LYP/def2-SVP method. The structure has been optimized at PBE/def2-SVP level of theory. DFT HOMO, LUMO orbitals, and HOMO, LUMO, HOMO-1 and LUMO+1 energy gaps versus vacuum. Experimental TiO_2 conduction band edge (full red line) and I^-/I_3^- redox level (dashed red line).

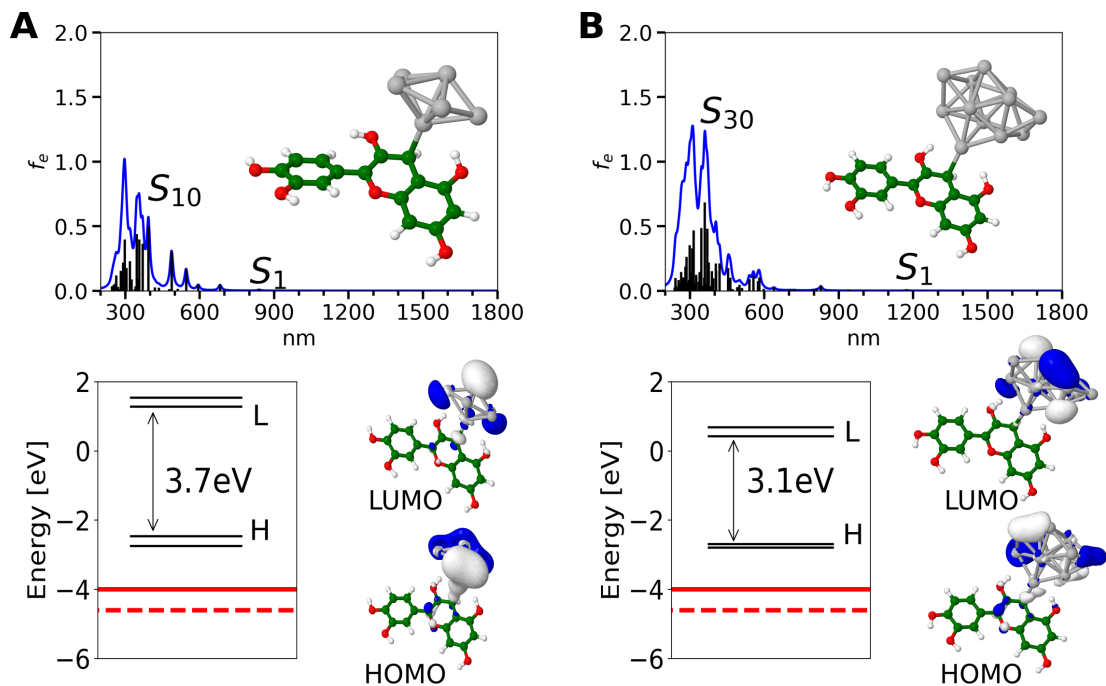


Figure S3: TDDFT calculated absorption spectra for the: A) (cyanidin-Ag₆)⁻, B) (cyanidin-Ag₁₂)⁻ employing CAM-B3LYP/def2-SVP method. Structures have been optimized at PBE/def2-SVP level of theory.

DFT HOMO, LUMO, HOMO-1, and LUMO+1 energy gaps versus vacuum[eV] and HOMO-LUMO orbitals. Experimental TiO₂ conduction band edge (full red line) and I⁻/I₃⁻ redox level (dashed red line)

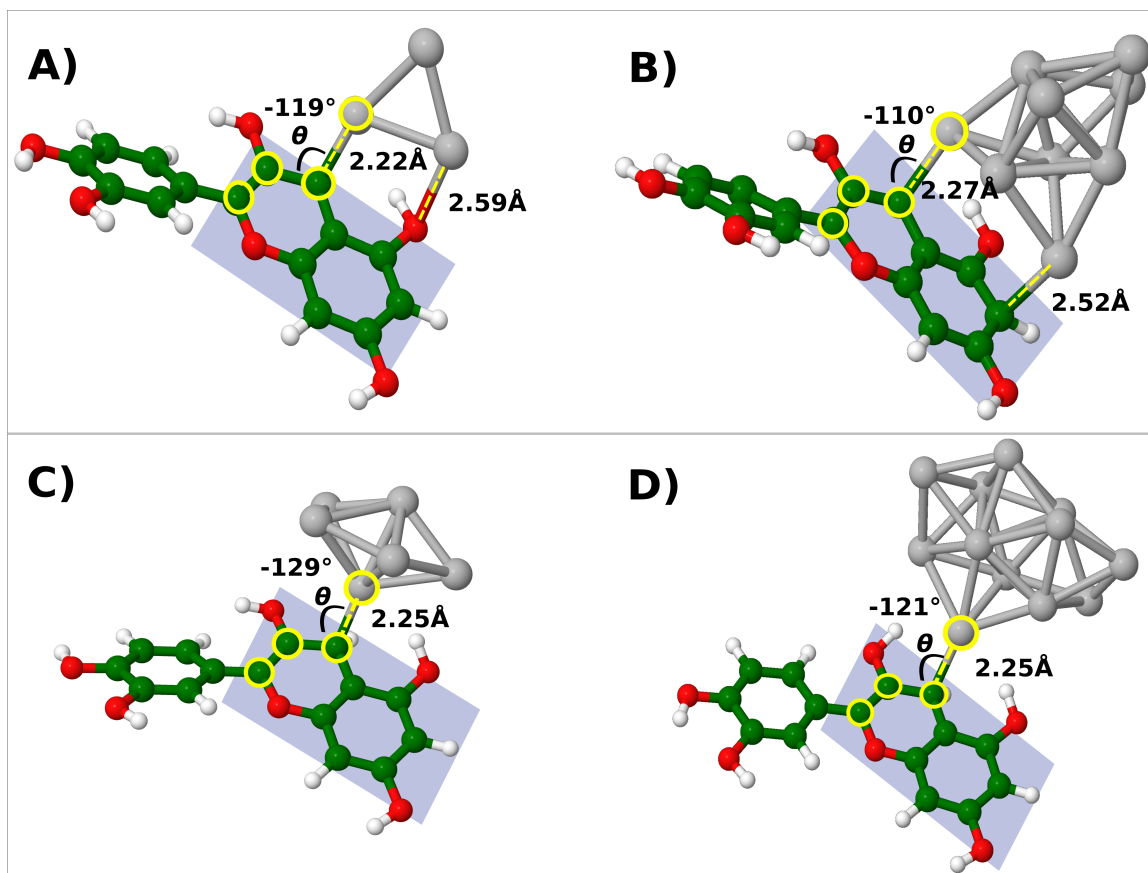


Figure S4: The bond lengths and dihedral angles between cyanidin and silver NC of hybrid systems are shown for A) cyanidin-Ag₃, B) cyanidin-Ag₉ with an even number of electrons, and C) (cyanidin-Ag₆)⁻, D) (cyanidin-Ag₁₂)⁻ with an odd number of electrons. The blue rectangle represents the plane of the indoline group of the cyanidin dye, θ is the dihedral angle between the plane and silver NC.

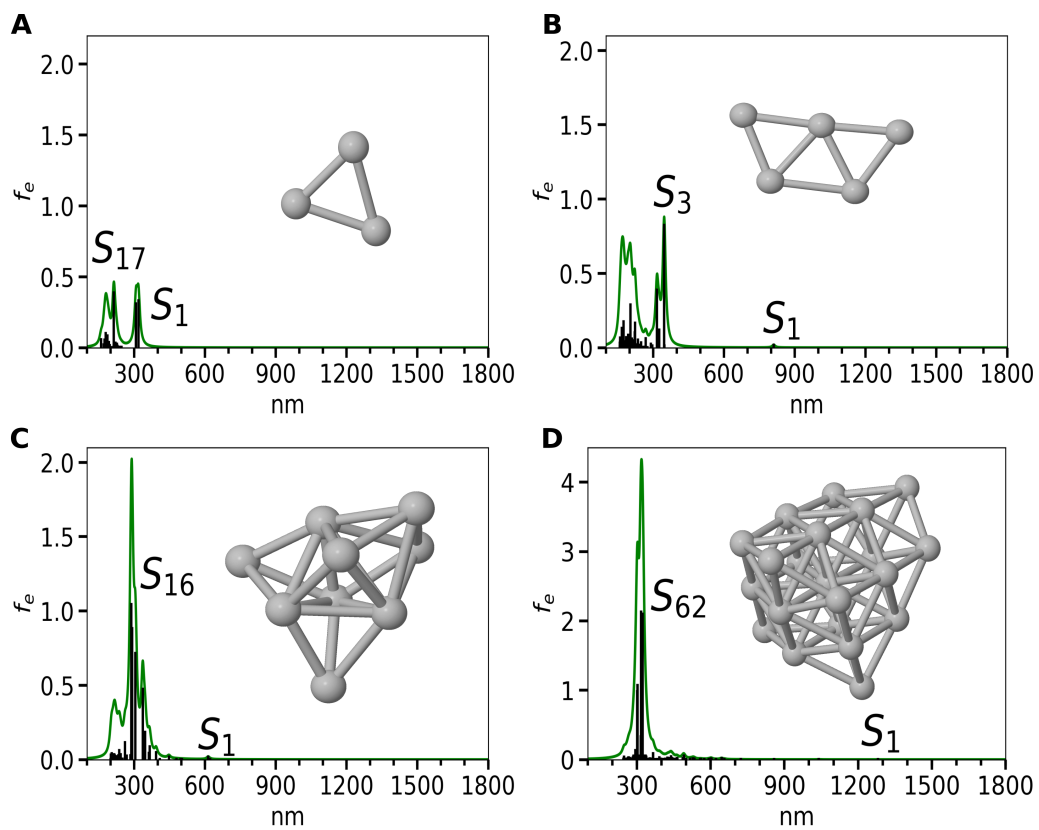


Figure S5: TDDFT calculated absorption spectra for the: A) Ag_3^+ , B) Ag_5^+ , C) Ag_9^+ and D) Ag_{21}^+ clusters with structures from cyanidin-NC hybrids at CAM-B3LYP/def2-SVP level of theory.

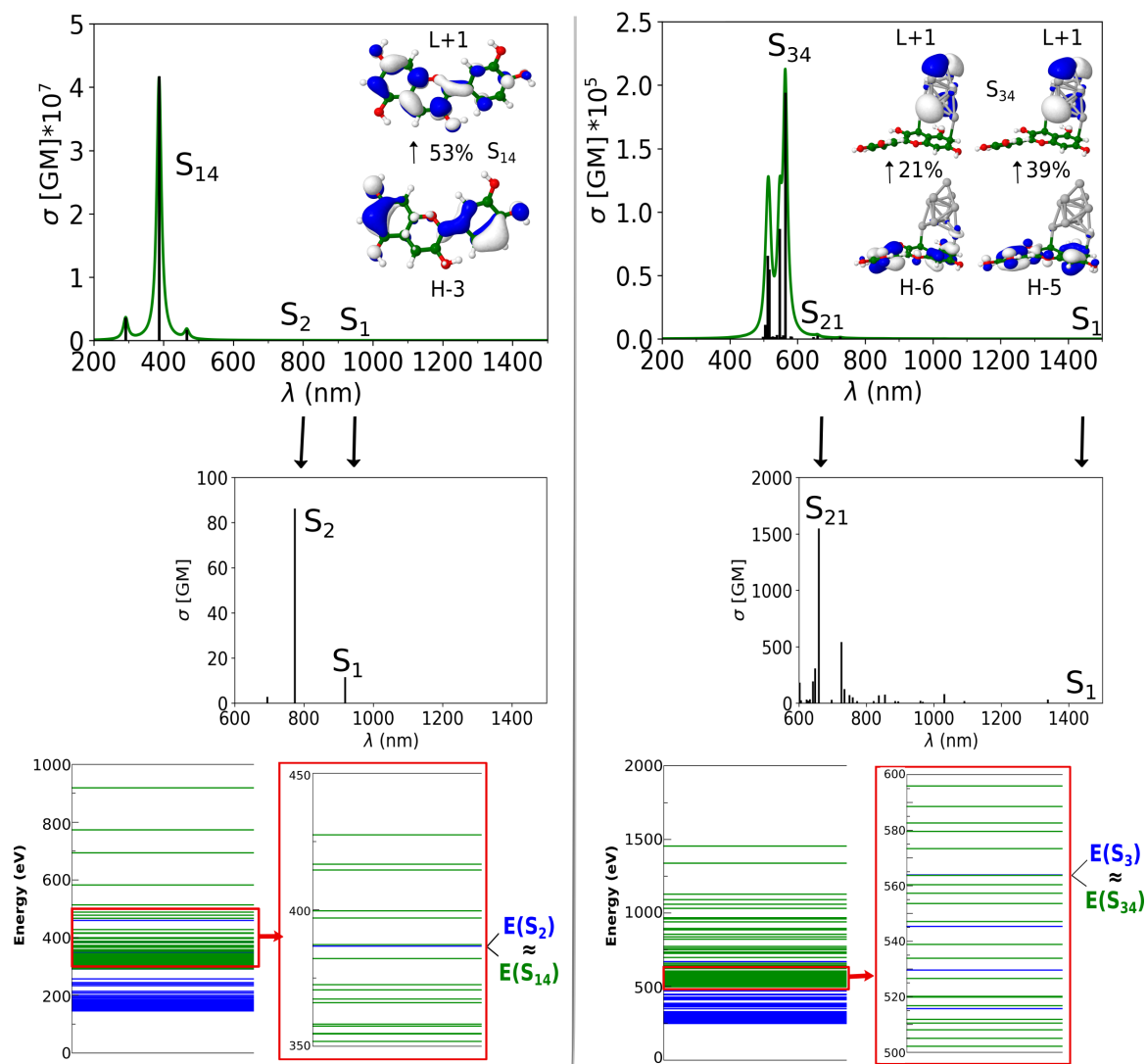


Figure S6: TPA spectra obtained by TDDFT for cyanidin (left) and cyanidin-Ag₉ (right). MO analysis is shown. TPA cross sections for states in NIR regime are also presented (middle). The resonance between OPA (blue) and TPA (green) states is included (bottom).

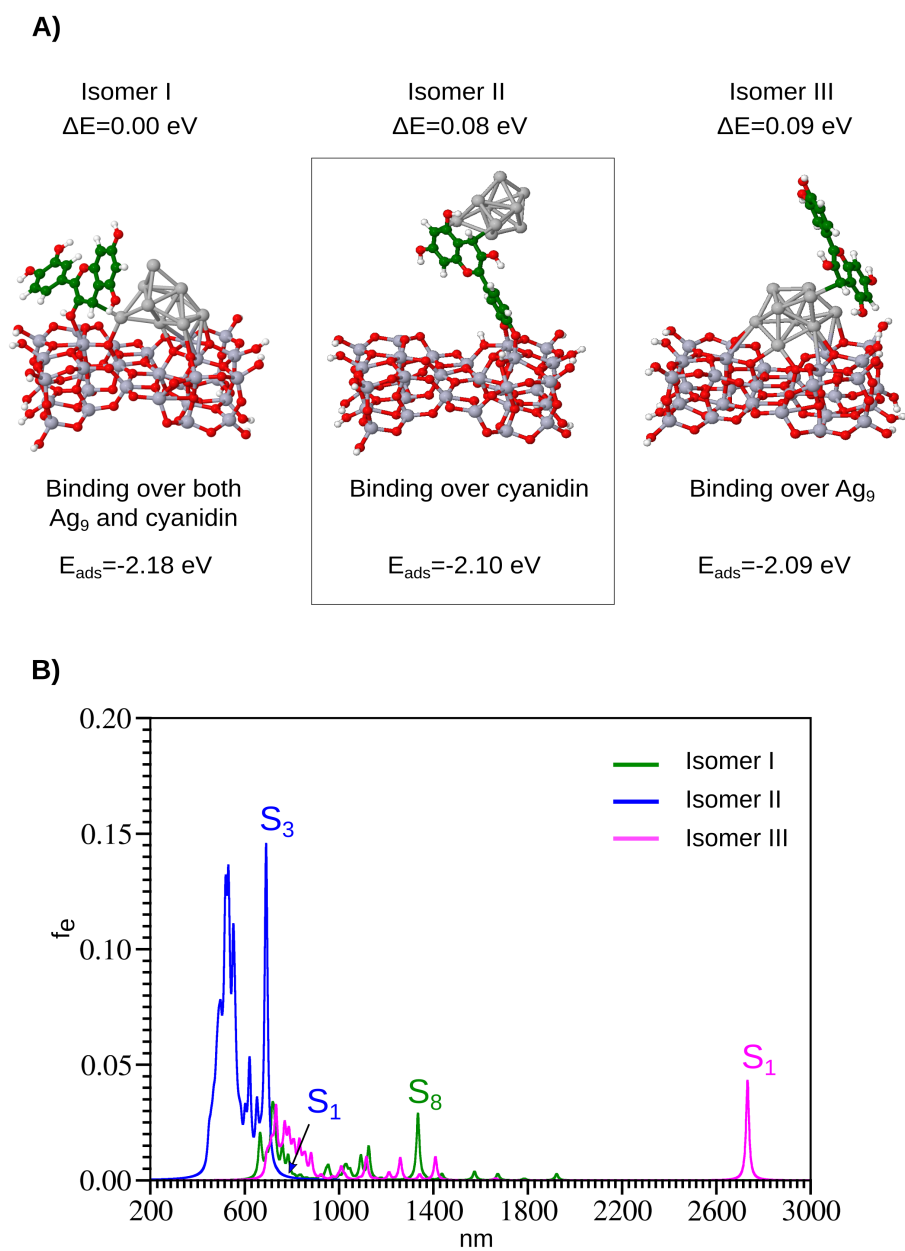


Figure S7: A) Isomers of {cyanidin-Ag₉}-TiO₂ with different adsorption modes. B) TDDFT calculated absorption spectra for isomers I, II and III of {cyanidin-Ag₉}-TiO₂ at CAM-B3LYP/def2-SVP level of theory. S₁ state of isomer I is located at 6090 nm ($f_e=0.027$).

Table S1: Excited states corresponding to the largest calculated absorptions for {cyanidin-Ag₉}-TiO₂ at CAM-B3LYP/def2-SVP level of theory with calculated wavelengths λ , oscillator strengths f_e and predominant transitions

| Excited state | $\lambda[nm]$ | f_e | Transitions |
|-----------------|---------------|--------|--|
| S ₃ | 691 | 0.1425 | H → L+25 (39%) H → L+26 (26%) H → L+29 (11%) |
| S ₇ | 620 | 0.0440 | H → L+2 (38%) H → L+14 (13%) H → L+12 (12%) |
| S ₁₄ | 551 | 0.0742 | H → L+49 (20%) H → L+51 (16%) H → L+52 (10%) |
| S ₁₈ | 531 | 0.0868 | H → L+19 (19%) H-1 → L+25 (15%) |

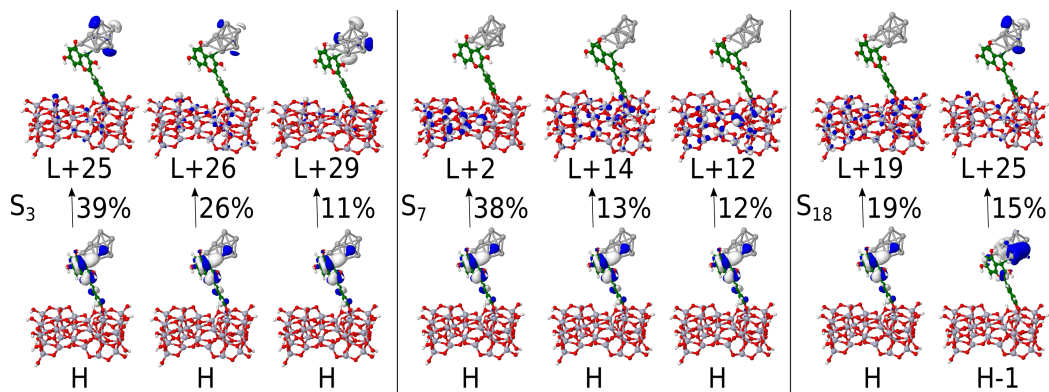


Figure S8: Transitions representing S₃, S₇ and S₁₈ states are shown. S₃ state corresponds to transitions from HOMO orbital delocalized on the hybrid to higher LUMO orbitals delocalized partly at support and partly at Ag₉. The transitions associated with the excited states higher in energy (S₇, S₁₈) demonstrate clear charge transfer from HOMO (HOMO-1) to higher LUMO orbitals delocalized entirely at TiO₂ model.

References

- ¹ W. Fan, D. Tan, W.-Q. Deng, Acene-modified triphenylamine dyes for dye-sensitized solar cells: A computational study, *ChemPhysChem* 13 (8) (2012) 2051–2060. doi:<https://doi.org/10.1002/cphc.201200064>.
- ² M. Grätzel, Photoelectrochemical cells, *Nature* 414 (2001) 338–344. doi:[10.1038/35104607](https://doi.org/10.1038/35104607).
- ³ H.-S. Kim, C.-R. Lee, J.-H. Im, K.-B. Lee, T. Moehl, A. Marchioro, S.-J. Moon, R. Humphry-Baker, J.-H. Yum, J.-E. Moser, M. Grätzel, N.-G. Park, Lead iodide perovskite sensitized all-solid-state submicron thin film mesoscopic solar cell with efficiency exceeding 9%, *Scientific reports* 2 (2012) 591. doi:[10.1038/srep00591](https://doi.org/10.1038/srep00591).
- ⁴ J. ichi Fujisawa, T. Eda, M. Hanaya, Comparative study of conduction-band and valence-band edges of tio2, sr tio3, and batio3 by ionization potential measurements, *Chemical Physics Letters* 685 (2017) 23–26. doi:<https://doi.org/10.1016/j.cplett.2017.07.031>.
- ⁵ G. Zhang, Y. Bai, R. Li, D. Shi, S. Wenger, S. M. Zakeeruddin, M. Grätzel, P. Wang, Employ a bithienothiophene linker to construct an organic chromophore for efficient and stable dye-sensitized solar cells, *Energy Environ. Sci.* 2 (2009) 92–95. doi:[10.1039/B817990E](https://doi.org/10.1039/B817990E).

Supplementary Materials: Enhancing Efficiency of Dye Sensitized Solar Cells by Coinage Metal Doping of Cyanidin-Silver Trimer Hybrids at TiO₂ Support Based on Theoretical Study






Margarita Bužančić Milosavljević ¹, Martina Perić Bakulić ², Željka Sanader Maršić ³, Antonija Mravak ^{3,*} and Vlasta Bonačić-Koutecký ^{1,4,5,*}

Table S1. Analysis of bond lengths of the doped NCs within bio-nano hybrid systems. The order of silver atoms (Ag₁, Ag₂) is chosen starting from Au atoms clockwise.

| Au doping | | | |
|---------------------|------------------------------|------------------------------|--|
| | Au-Ag₁ [Å] | Au-Ag₂ [Å] | Ag₁-Ag₂ [Å] |
| Isomer I | 2.79 | 2.78 | 2.61 |
| Isomer II | 2.64 | 2.77 | 2.72 |
| Isomer III | 2.73 | 2.60 | 2.87 |
| Cu doping | | | |
| | Cu-Ag₁ [Å] | Cu-Ag₂ [Å] | Ag₁-Ag₂ [Å] |
| Isomer I | 2.64 | 2.52 | 2.64 |
| Isomer II | 2.52 | 2.45 | 2.81 |
| Isomer III | 2.43 | 2.57 | 2.76 |
| Au-Cu doping | | | |
| | Au-Ag [Å] | Au-Cu [Å] | Ag-Cu [Å] |
| Isomer I | 2.82 | 2.47 | 2.27 |
| Isomer II | 2.83 | 2.48 | 2.47 |
| Isomer III | 2.77 | 2.44 | 2.53 |
| Isomer IV | 2.79 | 2.52 | 2.46 |
| Isomer V | 2.90 | 2.48 | 2.42 |

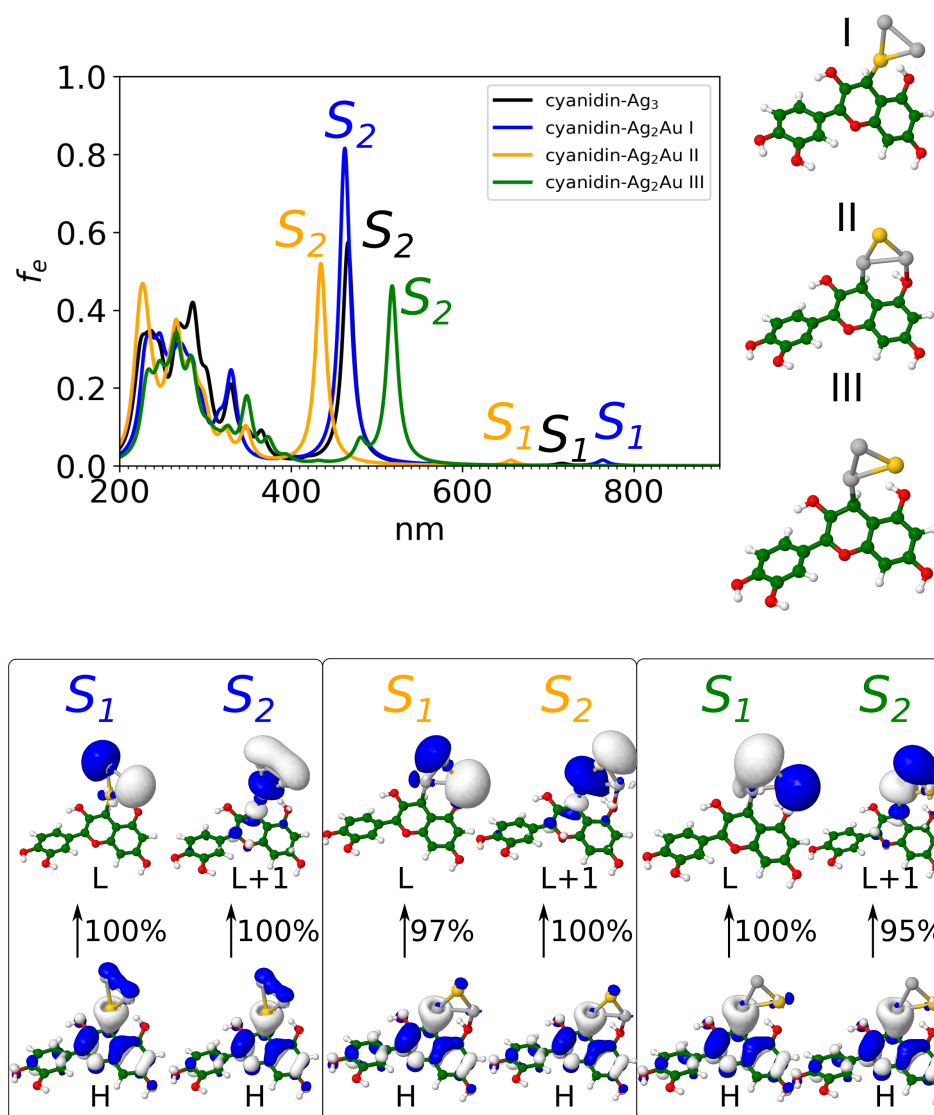


Figure S1. Comparison of absorption spectra of cyanidin- Ag_2Au isomers and cyanidin- Ag_3 at CAM-B3LYP/def2-SVP level of theory. The structures of Au-doped isomers optimized at the PBE/def2-SVP level of theory are shown on the right. The transitions with orbitals analysis corresponding to S_1 and S_2 states are shown below.

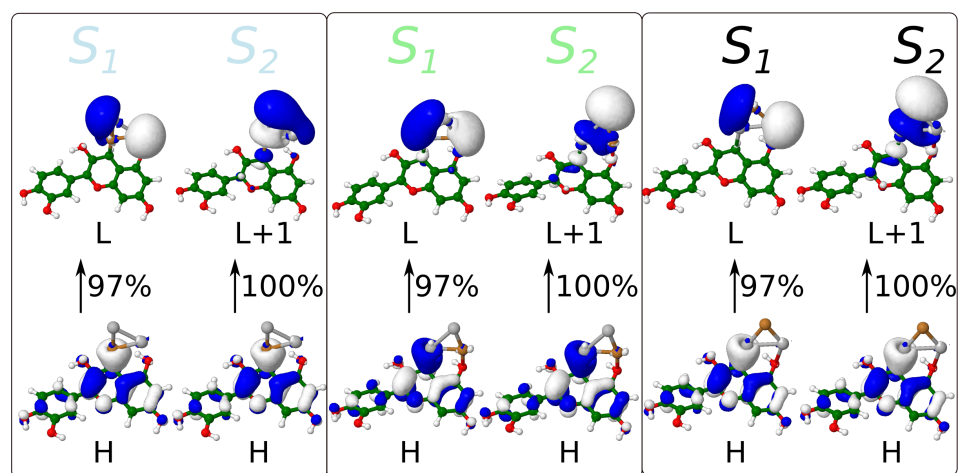
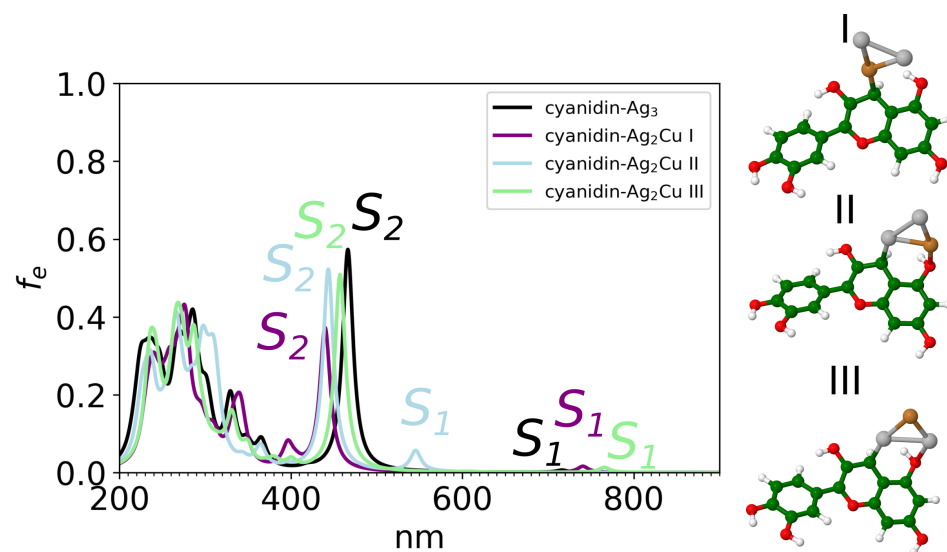


Figure S2. Comparison of OPA spectra of cyanidin- Ag_2Cu isomers and cyanidin- Ag_3 at CAM-B3LYP/def2-SVP level of theory. The structures of Cu-doped isomers optimized at the PBE/def2-SVP level of theory are shown on the right. The transitions with orbitals analysis corresponding to S_1 and S_2 states are shown below.

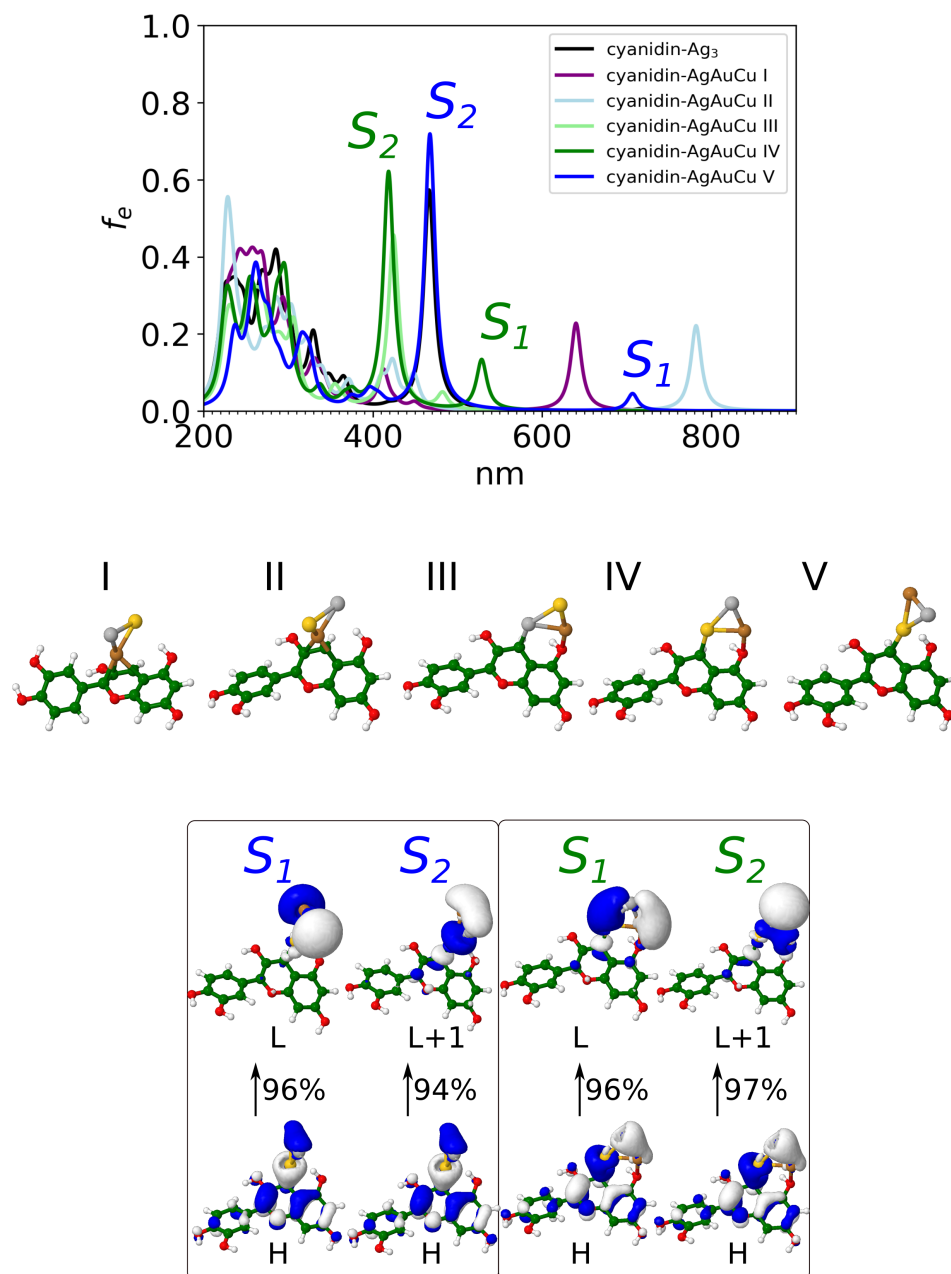


Figure S3. Comparison of OPA spectra of cyanidin-AgAuCu isomers and cyanidin-Ag₃ at CAM-B3LYP/def2-SVP level of theory. The structures of Au-Cu-doped isomers optimized at the PBE/def2-SVP and transitions with orbitals analysis corresponding to S_1 and S_2 states are shown below.

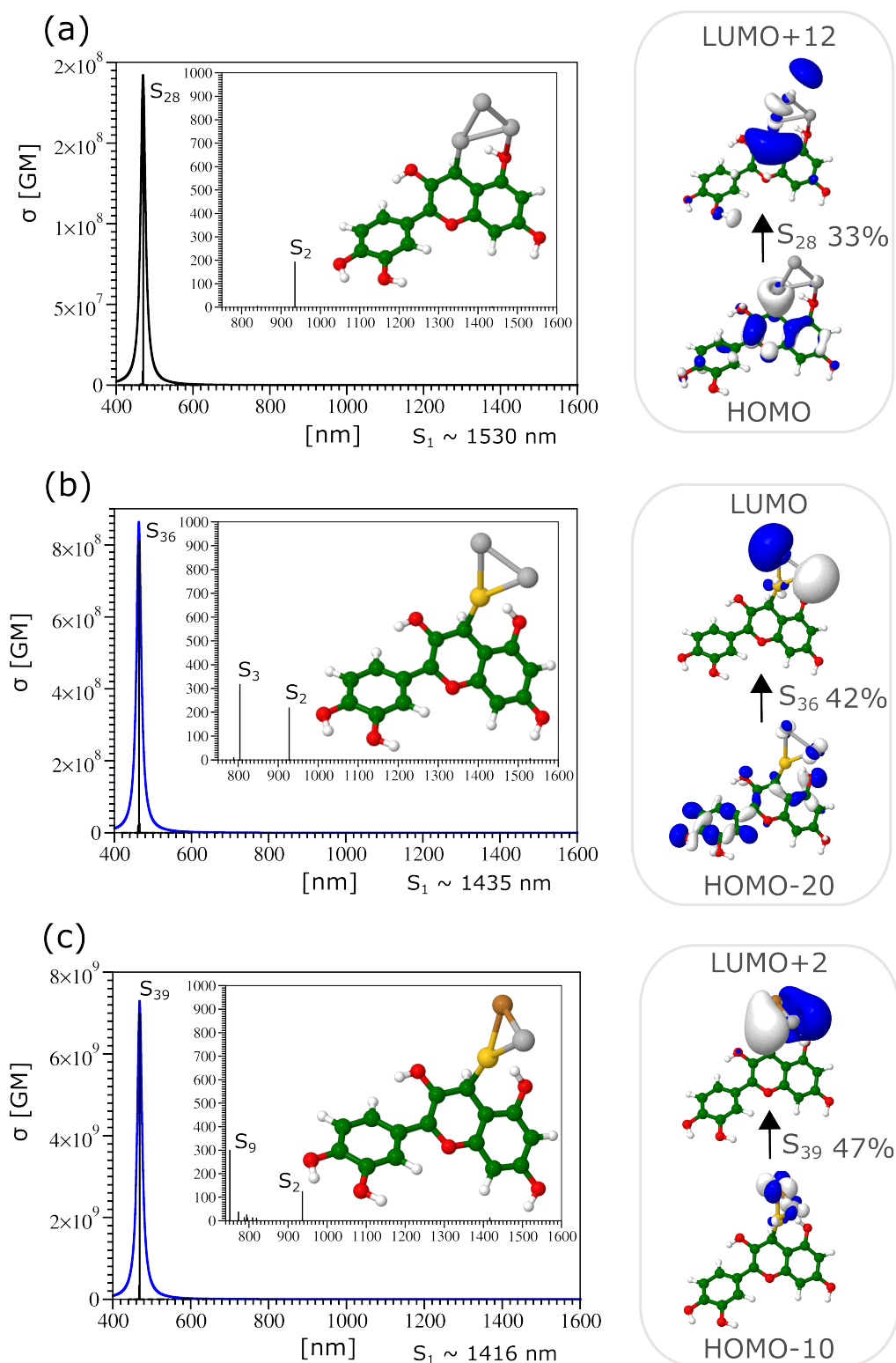


Figure S4. TPA spectra obtained by TDDFT at CAM-B3LYP/def2-SVP level of theory for (a) cyanidin- Ag_3 , (b) cyanidin- Ag_2Au isomer I, and (c) cyanidin- AgAuCu isomer V. TPA cross sections for states in IR/NIR regime are presented as insets. The molecular orbital analysis for leading excitations is shown on the right.

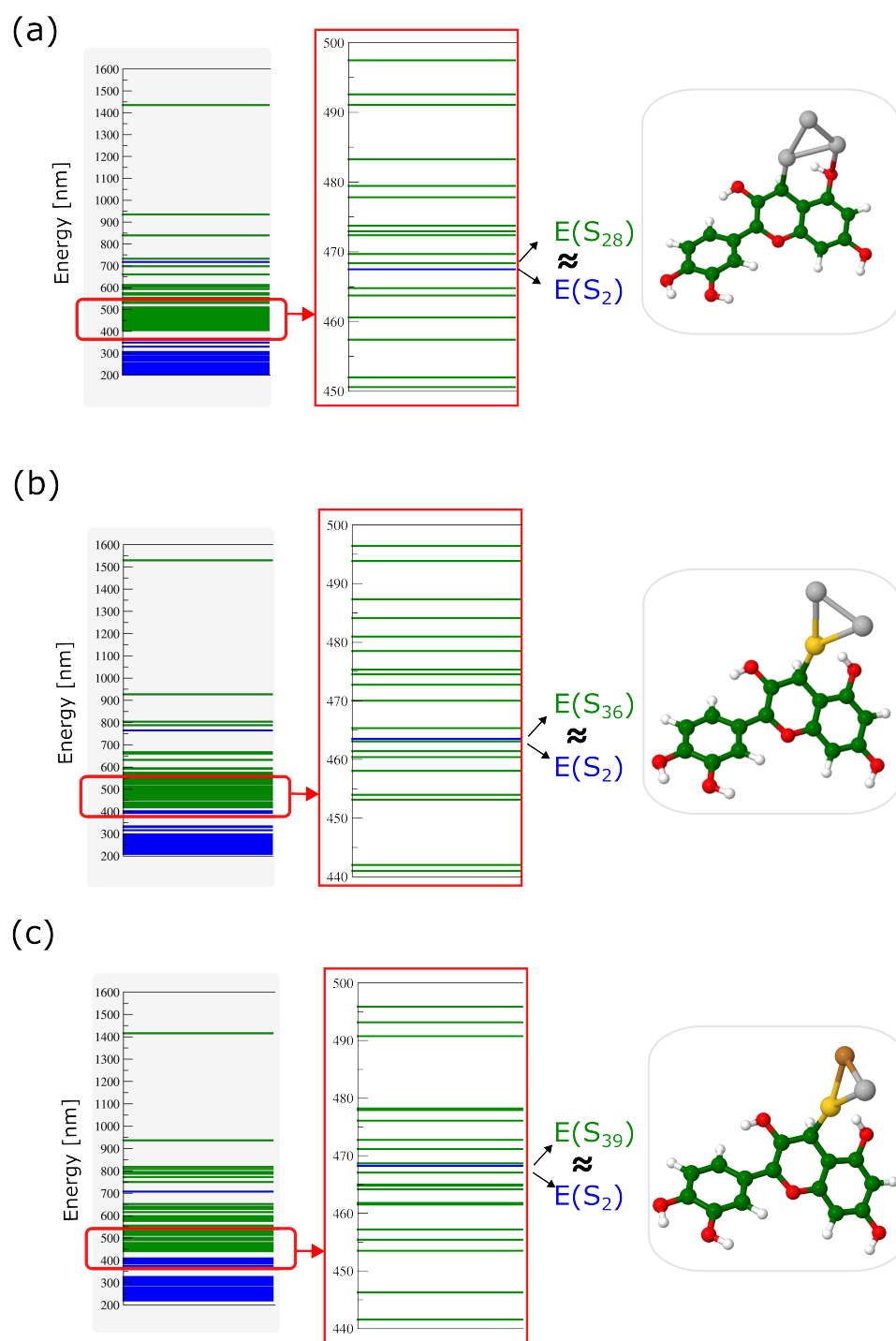


Figure S5. Energies of one-photon OPA (blue) and two-photon TPA (green) states illustrating the resonance between (a) cyanidin- Ag_3 , (b) cyanidin- Ag_2Au isomer I, and (c) cyanidin- AgAuCu isomer V.

Table S2. Analysis of the key excited states of {cyanidin-Ag₂Au}-TiO₂ at CAM-B3LYP/def2-SVP level of theory.

| Excited state | λ [nm] | f_e | Transitions |
|-----------------|----------------|--------|---|
| S ₁ | 765 | 0.0134 | H → L+9 (100%) |
| S ₄ | 550 | 0.0718 | H → L+1 (27%) H → L+13 (21%) |
| S ₁₀ | 479 | 0.4592 | H → L+43 (25%) H → L+6 (25%) H → L+18 (11%) |

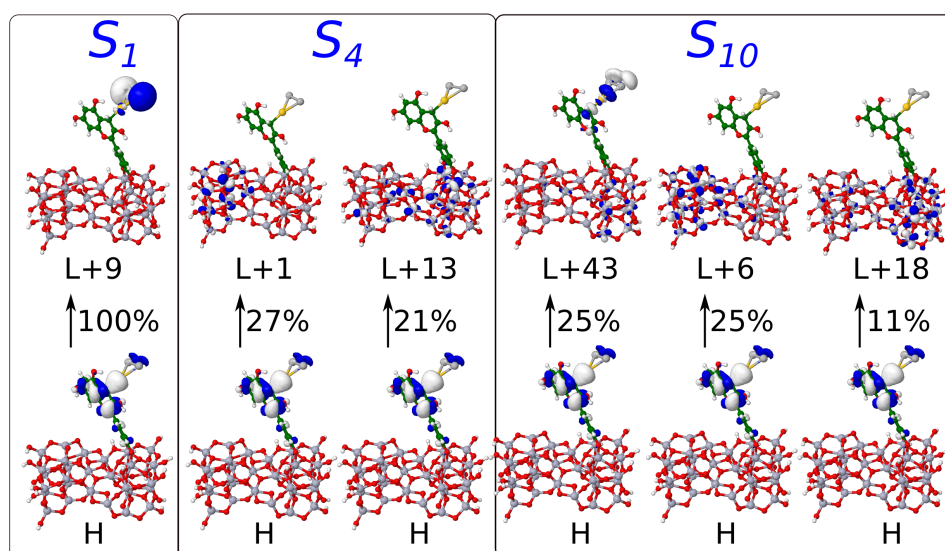
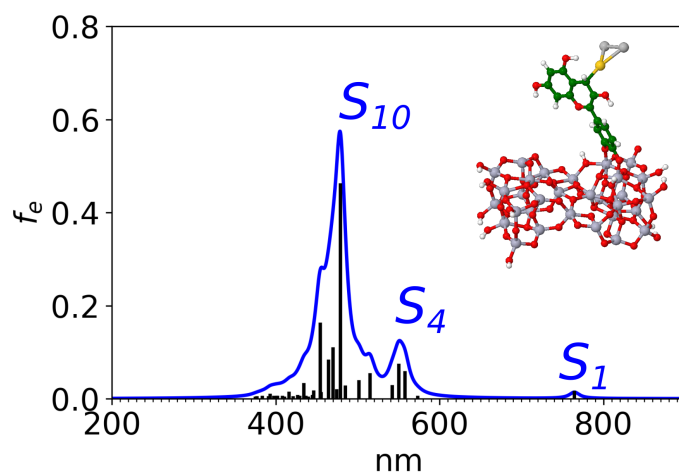


Figure S6. Absorption spectrum of {cyanidin-Ag₂Au}-TiO₂ at CAM-B3LYP/def2-SVP level of theory with the main transitions.

Appendix to Chapter 3

Supporting Material: Predicting fluorescence quantum yields for molecules in solution: A critical assessment of the harmonic approximation and the choice of the lineshape function

| Coumarin (Solvent) | $E(S_1)$ | $E(T_2)$ | E_{T-S} | SOC |
|-----------------------|----------|----------|-----------|----------------|
| | / eV | | | / 10^{-6} eV |
| 102 (MeCN) | 3.28 | 3.46 | 0.18 | 25.8 |
| 102 (cyhex) | 3.39 | 3.46 | 0.071 | 24.0 |
| 102 (EtOH) | 3.28 | 3.46 | 0.18 | 25.8 |
| 102 (water) | 3.28 | 3.45 | 0.17 | 25.8 |
| 343 (EtOH) | 3.14 | 3.11 | -0.035 | 27.3 |
| 522 (MeCN) | 3.03 | 3.34 | 0.31 | 61.1 |
| 522 (cyhex) | 3.16 | 3.39 | 0.23 | 56.3 |
| CIMMC (cyhex) | 4.04 | 3.68 | -0.36 | 5.4 |
| CIMMC (water) | 4.01 | 3.68 | -0.33 | 4.6 |

TABLE I. Vertical excitation energies of S_1 and T_2 , singlet-triplet energy gap $E_{T-S} = E(T_2) - E(S_1)$ and spin orbital coupling matrix elements $\text{SOC} = |\langle S_1 | H^{\text{SOC}} | T_2 \rangle|$, computed at the PBE0/def2SVP level of theory as implemented in the ORCA software package¹.

¹F. Neese, WIREs Comput. Mol. Sci. **2**, 73 (2012).

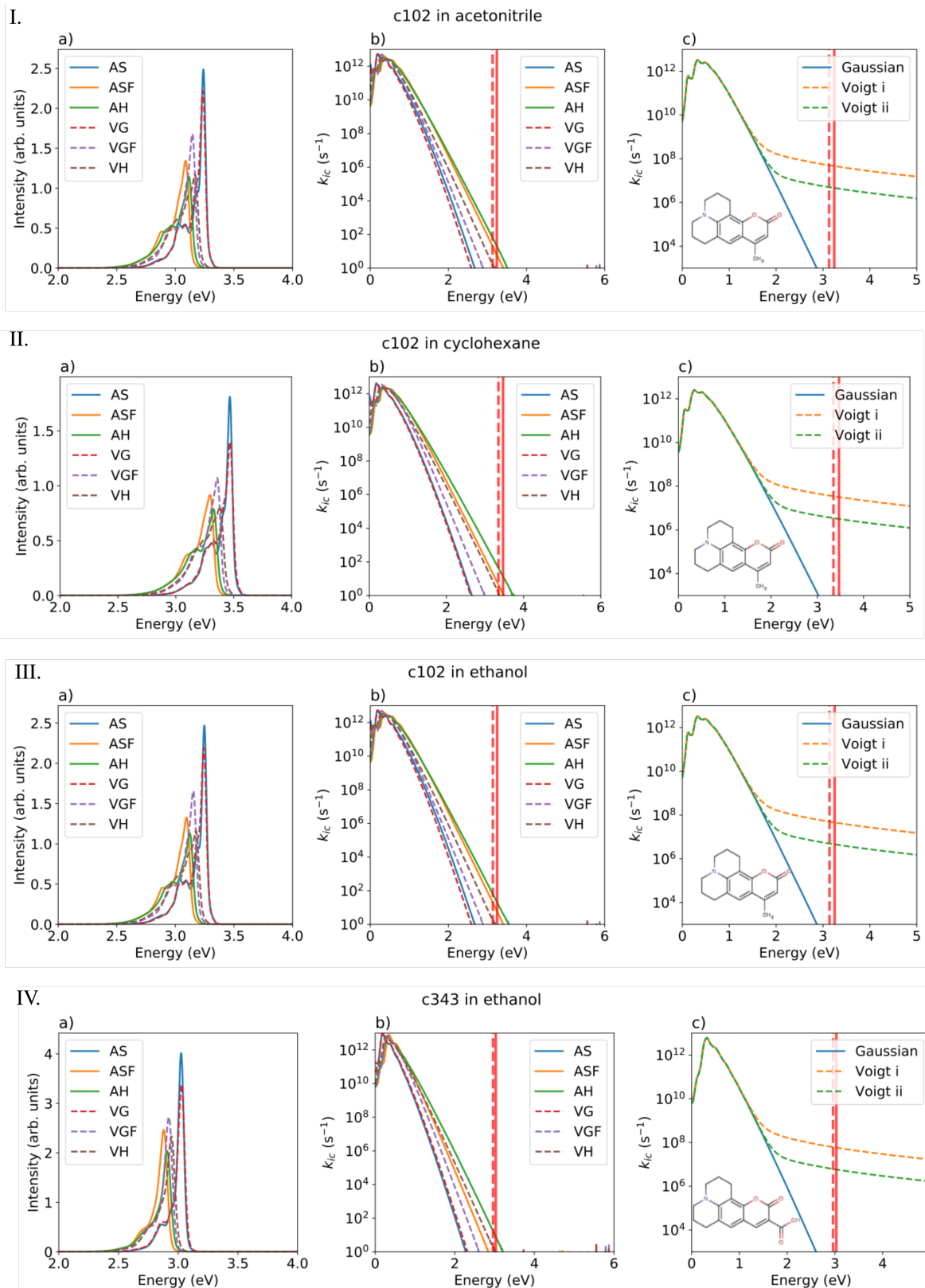


FIG. 1. **c102** in acetonitrile (I.), cyclohexane (II.) and ethanol (III.) and **c343** in ethanol (IV.), all at $T = 300$ K. a) Vibrational resolved emission spectrum for different harmonic models (with Gaussian broadening of $\text{HWHM}_G = 0.02$ eV). b) IC rate versus emission energy for different models and Gaussian broadening. c) IC rate with AH model for different broadening functions: Gaussian ($\text{HWHM}_G = 0.02$ eV), Voigt i ($\text{HWHM}_G = 0.02$ eV, $\text{HWHM}_L = 0.001$ eV) and Voigt ii ($\text{HWHM}_G = 0.02$ eV, $\text{HWHM}_L = 0.0001$ eV). The solid (dashed) red line marks the adiabatic (vertical) emission energy.

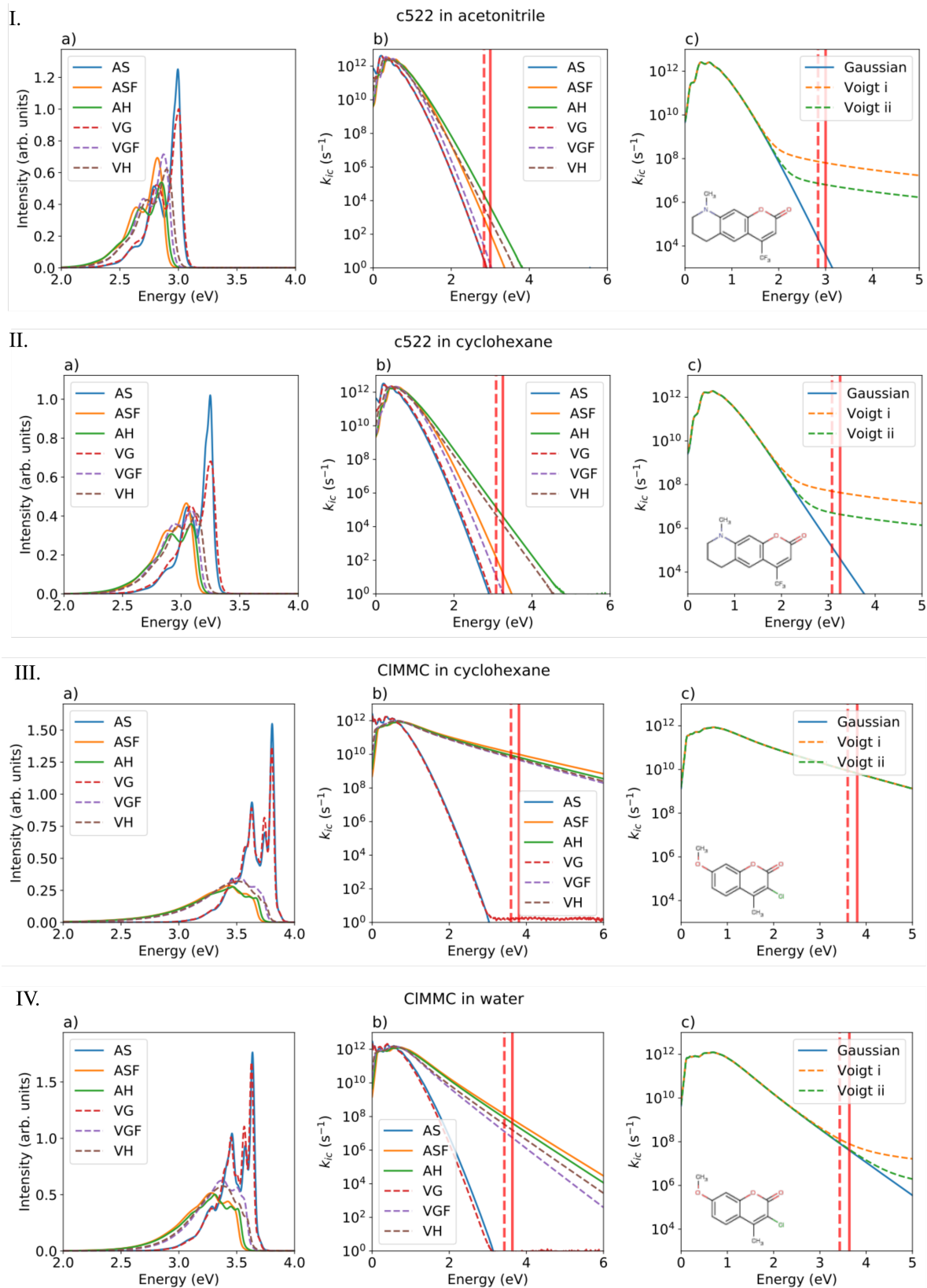


FIG. 2. **c522** in acetonitrile (I.), cyclohexane (II.) and **CIMMC** in cyclohexane (III.), water (IV.), all at $T = 300$ K. a) Vibrationally resolved emission spectrum for different harmonic models (with Gaussian broadening of $\text{HWHM}_G = 0.02$ eV). b) IC rate versus emission energy for different models and Gaussian broadening. c) IC rate with AH model for different broadening functions: Gaussian ($\text{HWHM}_G = 0.02$ eV), Voigt i ($\text{HWHM}_G = 0.02$ eV, $\text{HWHM}_L = 0.001$ eV) and Voigt ii ($\text{HWHM}_G = 0.02$ eV, $\text{HWHM}_L = 0.0001$ eV). The solid (dashed) red line marks the adiabatic (vertical) emission energy.

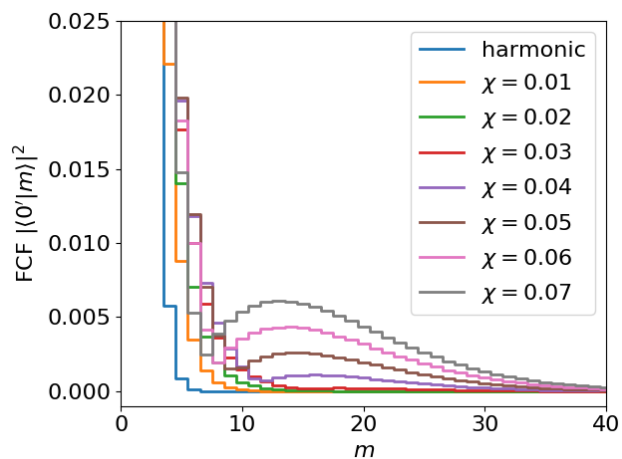


FIG. 3. Franck–Condon factors for a C=C stretching mode at $T = 300$ K. As the anharmonicity χ increases, the overlap between the initial vibrational state and highly excited final vibrational states becomes larger.

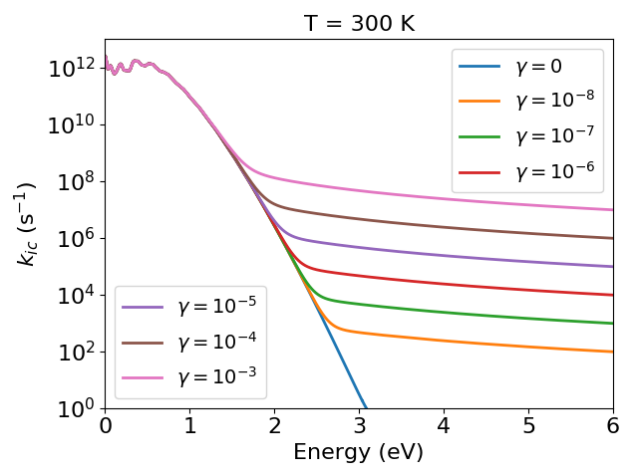


FIG. 4. CIMMC in cyclohexane (PCM). Internal conversion rates from harmonic AS model with Voigt broadening function. The Gaussian part of the Voigt profile was set to $\text{HWHM}_G = 0.02$ eV, while the Lorentzian part was varied between $\gamma = \text{HWHM}_L = 0$ and 10^{-3} eV.

Supporting Material: Design of J-aggregates-like oligomers built from squaraine dyes exhibiting transparency in the visible regime and high fluorescence quantum yield in the NIR region

Margarita Bužančić Milosavljević¹ and Vlasta Bonačić-Koutecký^{1,2,3,*}

¹Center of Excellence for Science and Technology-Integration of Mediterranean Region (STIM), Faculty of Science, University of Split, Ruđera Boškovića 33, 21000 Split, Croatia.

²Interdisciplinary Center for Advanced Science and Technology (ICAST) at University of Split, Meštrovićevo šetalište 45, 21000 Split, Croatia

³Department of Chemistry, Humboldt Universität zu Berlin, Brook-Taylor-Strasse 2, 12489 Berlin, Germany.

Table S1: Comparison of experimental¹ and theoretical absorption maxima for J-aggregates formed by squaraine dyes in toluene solvent.

| | $\lambda_{max}(exp)^1$ | | $\lambda_{max}(theor)$ | |
|--------|------------------------|--------|------------------------|--------|
| | nm | (eV) | nm | (eV) |
| dSQA | 690 | (1.80) | 625 | (1.98) |
| dSQB | 747 | (1.66) | 681 | (1.82) |
| tSQA | 714 | (1.74) | 652 | (1.90) |
| tSQB | 773 | (1.60) | 707 | (1.75) |
| tetSQA | | | 662 | (1.87) |
| tetSQB | | | 719 | (1.72) |

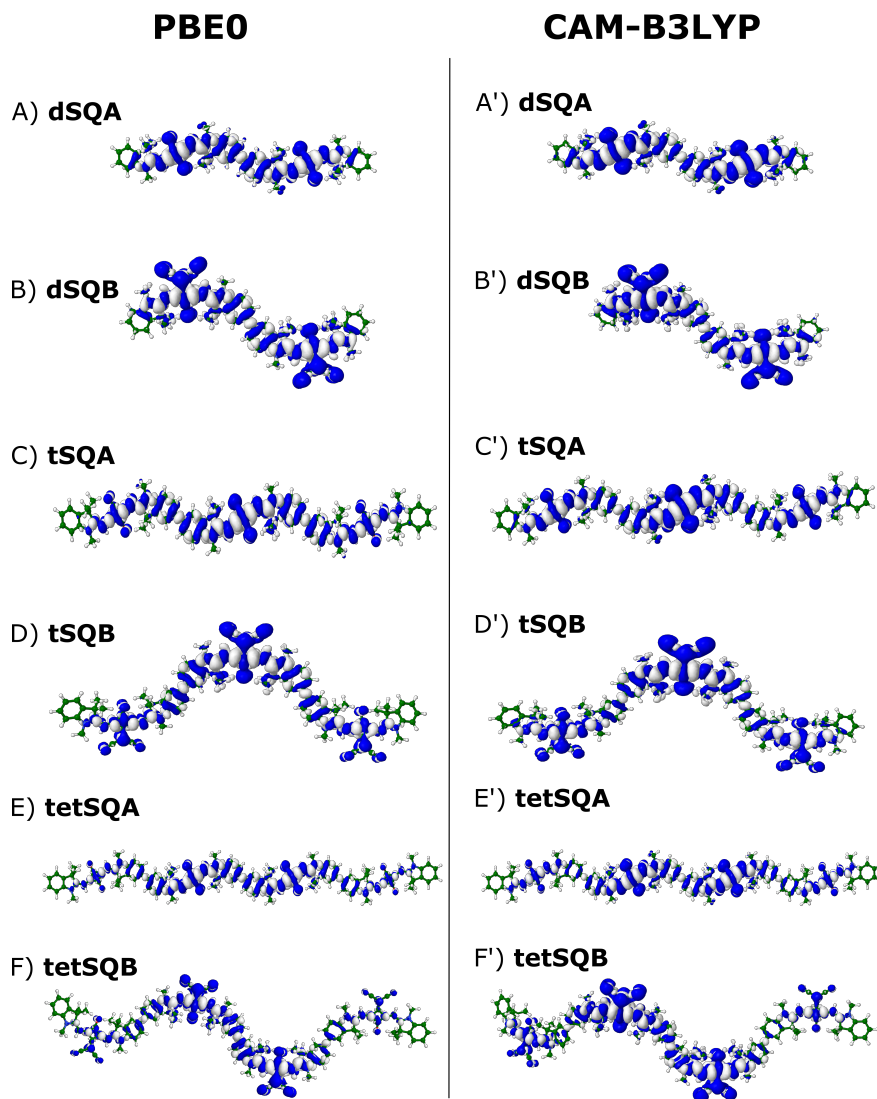


Figure S1: Comparison of calculated electron density difference (EDD) between first excited (S_1) and ground (S_0) state for squaraine J-aggregates in toluene solvent, for functionals PBE0/def2-SVP and CAM-B3LYP/def2-SVP in Multiwfn 3.6 software program.² Blue/white regions label the loss/gain of electronic charge during the transition.

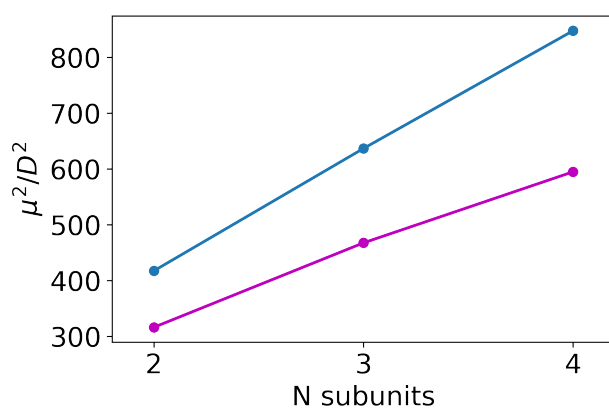


Figure S2: The calculated squared transition dipole moments (μ^2 =dipole strength) for SQA (blue) and SQB (violet) J-aggregates in toluene solvent as a function of the number of subunits N.

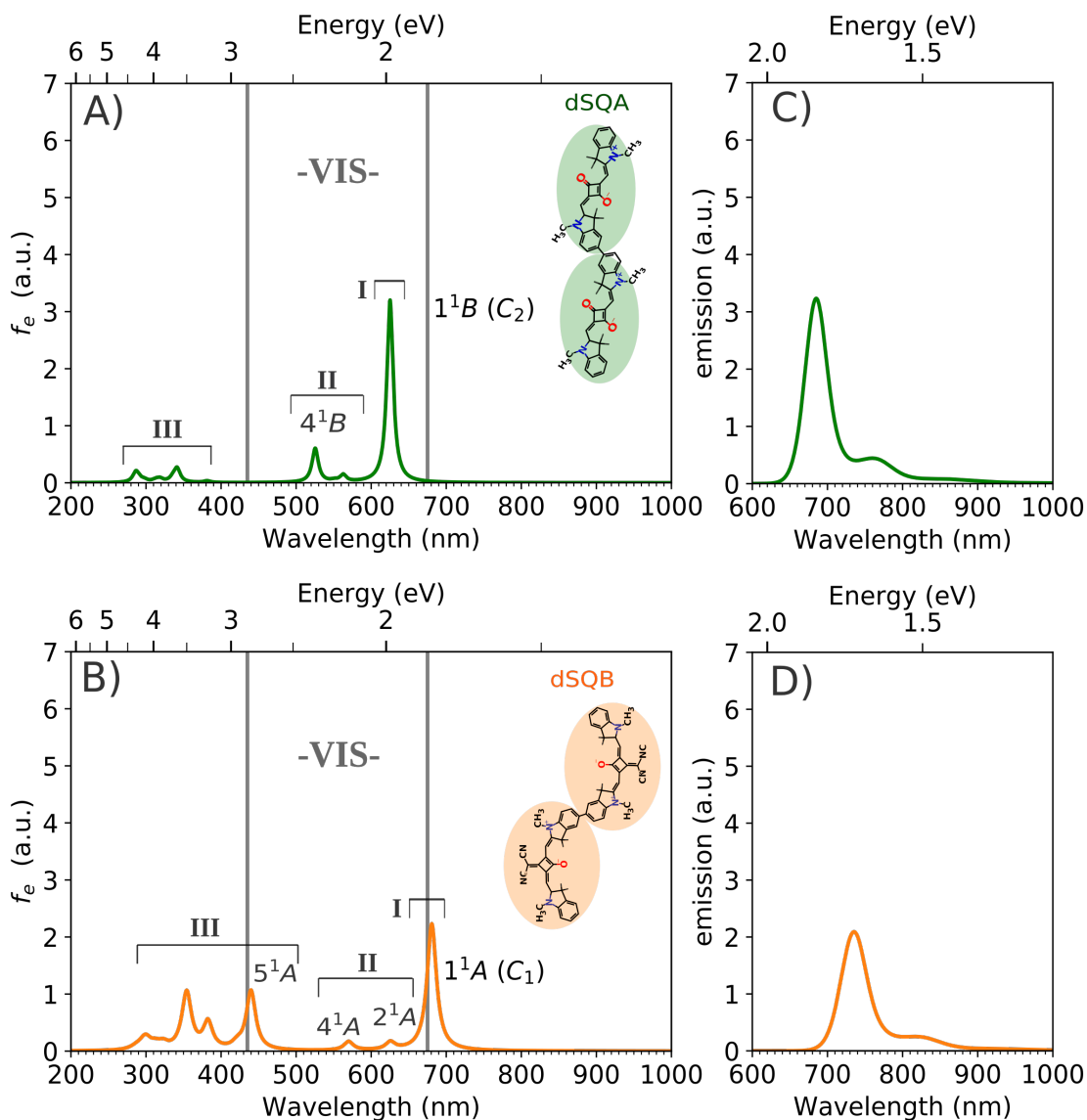


Figure S3: TD-DFT absorption spectra of J-aggregates forming dimers in toluene solvent: A) dSQA (green) built from squaraine dyes with the central squaric acid ring and oxygen atoms, and B) dSQB (orange) built from squaraine dyes with the central squaric acid ring substituted with the dicyanovinylene group. Transitions are divided into groups I, II, and III. The most intense transitions (I) are labeled according to symmetry point groups. f_e labels oscillator strengths. The visible regime (VIS) is shown within gray lines. HOMO-LUMO gaps are 2.35 eV for dSQA and 2.22 eV for dSQB J-aggregates. Comparison between emission spectra of C) dSQA and D) dSQB J-aggregates in toluene solvent (cf. Computational). Notice that monomer subunits forming J-aggregates are covalently bound (1.5Å).

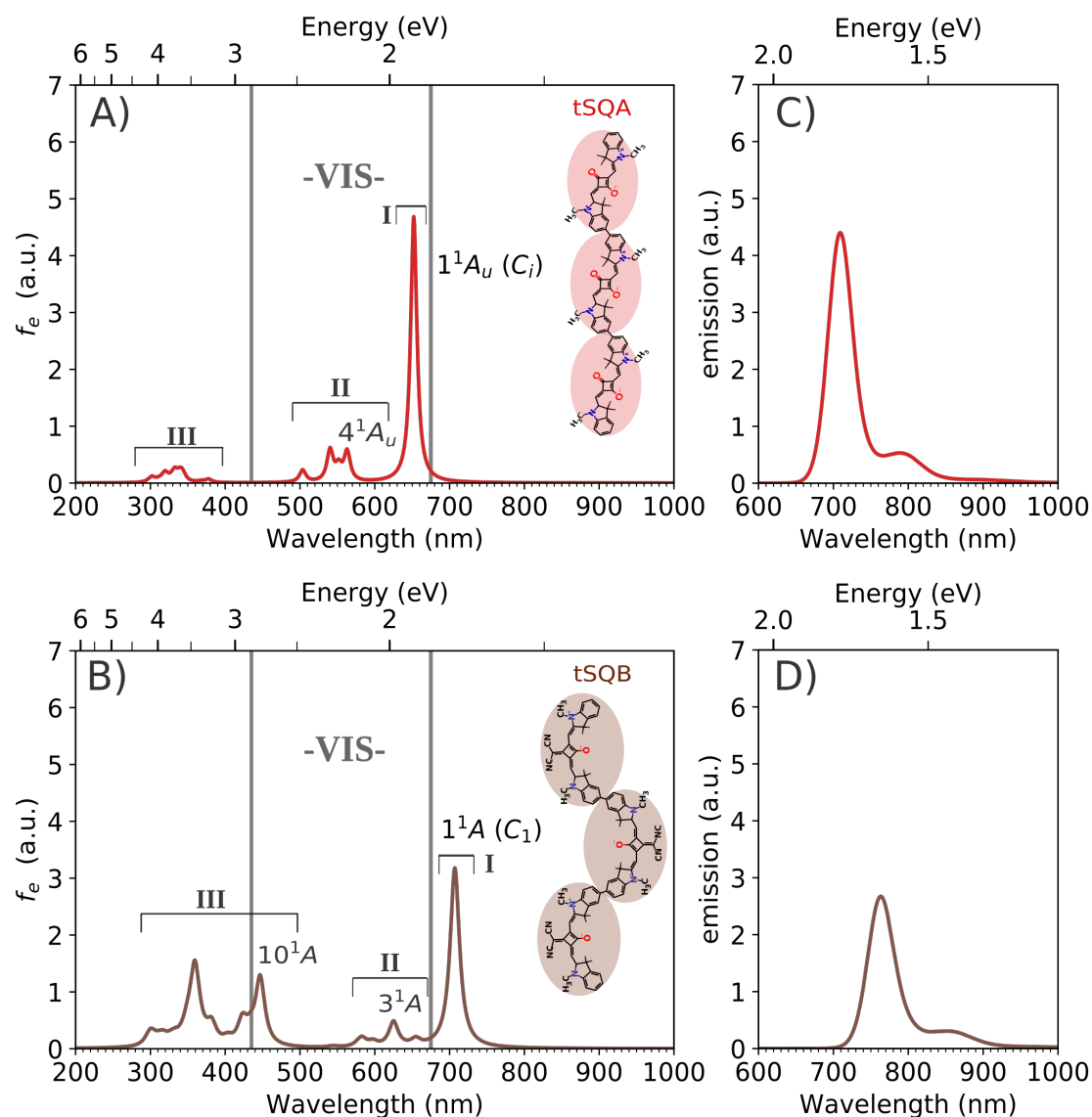


Figure S4: TD-DFT absorption spectra of J-aggregates forming trimers in toluene solvent: A) tSQA (red) built from squaraine dyes with the central squaric acid ring and oxygen atoms, and B) tSQB (brown) built from squaraine dyes with the central squaric acid ring substituted with the dicyanovinylene group. Transitions are divided into groups I, II, and III. The most intense transitions (I) are labeled according to symmetry point groups. f_e labels oscillator strengths. The visible regime (VIS) is shown within gray lines. HOMO-LUMO gaps are 2.29 eV for tSQA and 2.15 eV for tSQB J-aggregates. Comparison between emission spectra of C) tSQA and D) tSQB J-aggregates in toluene solvent (cf. Computational). Notice that monomer subunits forming J-aggregates are covalently bound (1.5Å).

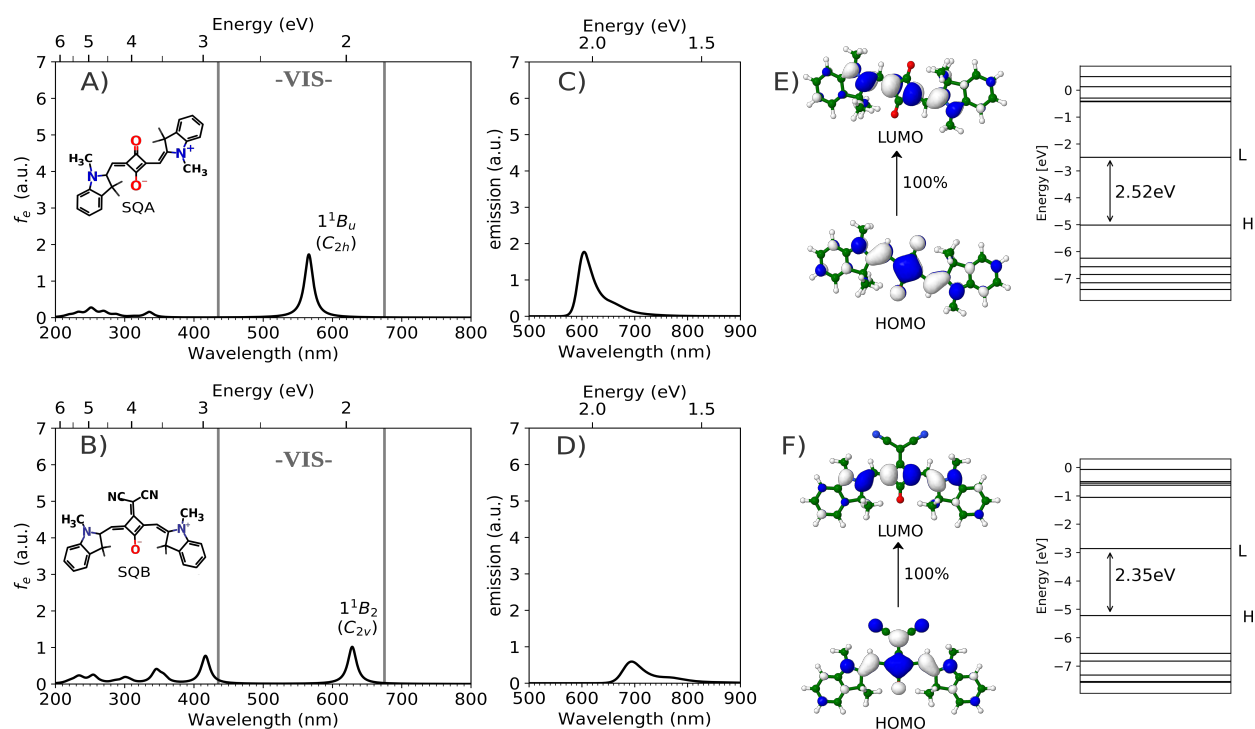


Figure S5: TD-DFT absorption spectra of monomer squaraine dyes in toluene solvent: A) SQA squaraine dye with the central squaric acid ring and oxygen atoms, and B) SQB squaraine dye with the central squaric acid ring substituted with the dicyanovinylene group. The most intense transitions (I) are labeled according to symmetry point groups. f_e labels oscillator strengths. The visible regime (VIS) is shown within gray lines. Comparison between emission spectra of C) SQA and D) SQB in toluene solvent (cf. Computational). HOMO and LUMO molecular orbitals involved in excitations within the first excited state together with the energies of Kohn-Sham orbitals and HOMO-LUMO gap are shown for E) SQA and F) SQB squaraine dyes. Both monomers have the first excited state with a bright π - π^* character within the VIS regime which is separated from higher excited states. Therefore no mixing of states nor breaking of Born-Oppenheimer approximation occurs.

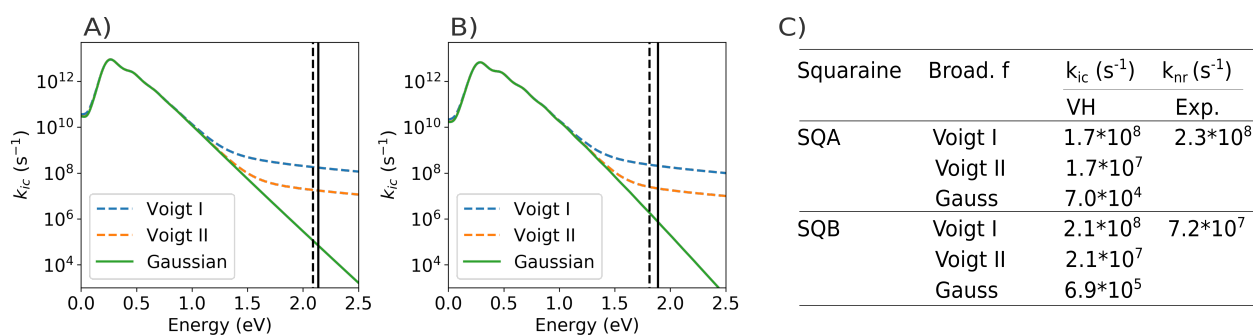


Figure S6: IC rate vs. adiabatic energy profiles (VH model) for: A) SQA, and B) SQB squaraines in toluene solvent. The broadening functions are a Gaussian ($HWHM_G = 0.02$ eV), Voigt I ($HWHM_G = 0.02$ eV, $HWHM_L = 0.001$ eV) and Voigt II ($HWHM_G = 0.02$ eV, $HWHM_L = 0.0001$ eV). The solid black line marks the adiabatic energy and dashed black line vertical emission energy. C) IC rates squaraine dyes calculated within vertical hessian model (VH) in toluene solvent (at 300K) using FCclasses3 program. k_{nr} labels the experimental non-radiative rate taken from Ref.¹ Internal conversion rates k_{ic} for monomers show larger dependence on different broadening in comparison with J-aggregates.

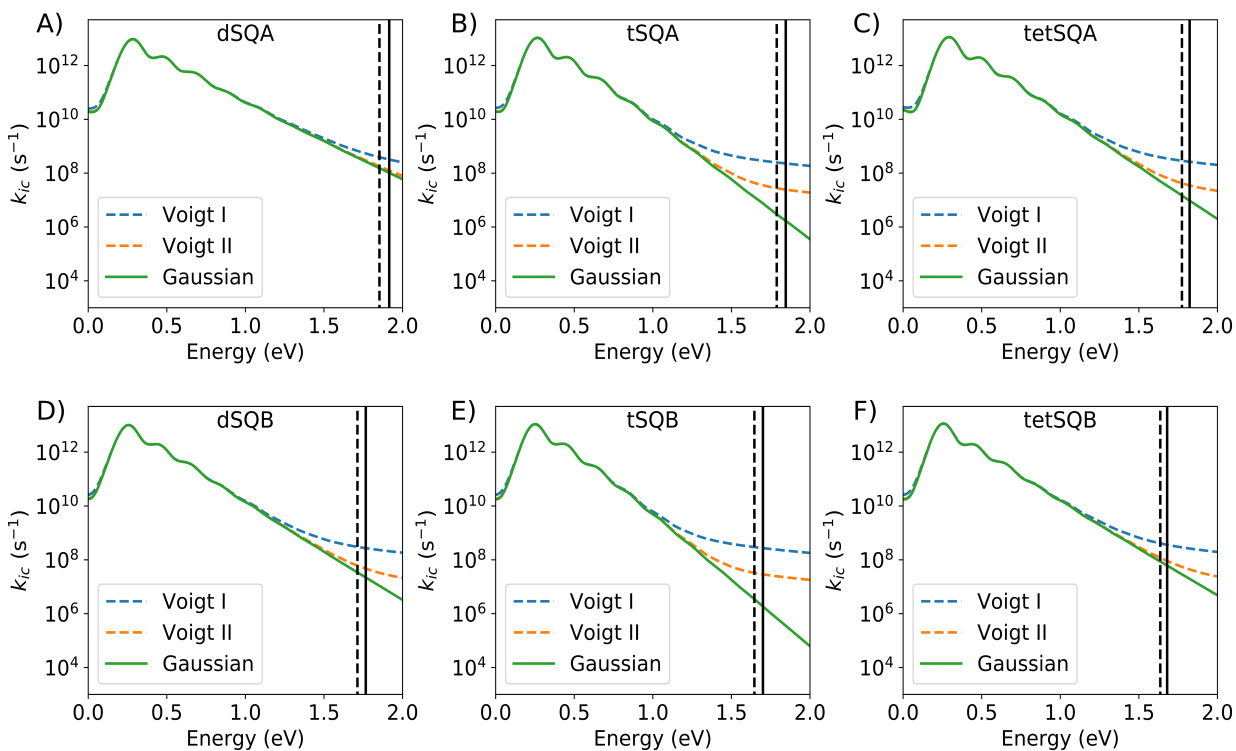


Figure S7: k_{ic} rates vs. emission energy (VH model) for: A) dSQA, B) tSQA, C) tetSQA, D) dSQB, E) tSQB and F) tetSQB J-aggregates in toluene solvent for different broadening functions: Voigt I ($\text{HWHM}_G = 0.02$ eV and $\text{HWHM}_L = 0.001$ eV), Voigt II ($\text{HWHM}_G = 0.02$ eV and $\text{HWHM}_L = 0.0001$ eV) and Gaussian ($\text{HWHM}_G = 0.02$ eV). The solid black line marks the adiabatic emission energy and the dashed black line vertical emission energy. The broadening has been described in the Computational part and has been investigated in Ref.³

Table S2: Parameters for scaling relations obtained from DFT and TD-DFT calculations for SQA and SQB monomers in toluene solvent.

| | N_v | $S(1)$ | $ \vec{\tau}(1) $ [$Bohr^{-1}$] | $\Delta\epsilon(1)$ [eV] | ω_{eff} [cm^{-1}] | J_{ge} [cm^{-1}] |
|-----|-------|--------|-----------------------------------|--------------------------|------------------------------|------------------------|
| SQA | 174 | 0.006 | 1.39 | 2.09 | 1579 | -881 |
| SQB | 186 | 0.009 | 1.24 | 1.81 | 1568 | -645 |

N_v labels the number of vibrational modes, S the average Huang-Rhys factor, $|\vec{\tau}|$ the non-adiabatic coupling vector, and $\Delta\epsilon$ excitation energy. The effective vibrational mode ω_{eff} corresponds to the C-C stretch vibration. $S(1)$, $|\vec{\tau}(1)|$, and $\Delta\epsilon(1)$ are monomer values, as indicated in brackets. The excitonic couplings J_{ge} are determined from calculations of Davydov splitting for dSQA and dSQB.

The following expression for internal conversion rate⁴ k_{ic} is used:

$$k_{ic} = u_{ic} \sqrt{\frac{\pi}{2}} |\vec{\tau}(1)|^2 \left[1 + 2 \frac{J_{ge}}{\Delta\epsilon(1)} \cos\left(\frac{\pi}{N+1}\right) \right]^{-2} \frac{1}{\sqrt{X}} \exp\left(-X \left[\log\left(\frac{NX}{N_v S(1)}\right) - 1 \right] - \frac{N_v S(1)}{N}\right) \quad (1)$$

where electronic excitation is:

$$X = \frac{\Delta\epsilon(1)}{\omega_{eff}} + 2 \frac{J_{ge}}{\omega_{eff}} \cos\left(\frac{\pi}{N+1}\right) \quad (2)$$

N is the number of monomer units in J-aggregate, and the factor for the conversion of atomic units in s^{-1} is $u_{ic} = 4.13 \times 10^{16} s^{-1}$.

References

- ¹ H. Ceymann, A. Rosspeintner, M. H. Schreck, C. Mützel, A. Stoy, E. Vauthey, and C. Lambert. *Phys. Chem. Chem. Phys.*, 2016, **18**, 16404.
- ² T. Lu and F. Chen. *Journal of Computational Chemistry*, 2012, **33**, 580-592.
- ³ A. Humeniuk, M. Bužančić, J. Hoche, J. Cerezo, R. Mitrić, F. Santoro, and V. Bonačić-Koutecký. *The Journal of Chemical Physics*, 2020, **152**, 054107.
- ⁴ A. Humeniuk, R. Mitrić, and V. Bonačić-Koutecký. *The Journal of Physical Chemistry A*, 2020, **124**, 10143–1015.

Curriculum Vitae

MARGARITA BUŽANČIĆ MILOSAVLJEVIĆ

Date and place of birth: 1st September 1992. Zagreb, Croatia

e-mail: margarita@stim.unist.hr

EDUCATION

- 2018.-2024.
Doctoral study of Biophysics, Faculty of Science, University of Split
- 2014.-2016.
Graduate university study of Chemical Engineering, Faculty of Chemical Engineering and Technology, University of Zagreb
- 2011.-2014.
Undergraduate university study of Chemical Engineering, Faculty of Chemical Engineering and Technology, University of Zagreb
- 2007.-2011.
Archdiocesan Classical Gymnasium "Don Frane Bulić", Split

EMPLOYMENT

- 2018.-2024.
Research Asistent/PhD student at Center of Excellence for Science and Technology-Integration of Mediterranean region (STIM), University of Split, Croatia
- 2017.
Intern at the Public Institution RERA S.D. for Coordination and Development of the Split-Dalmatia County
- 2014.-2015.
Teaching assistant at Department of Reaction Engineering and Catalysis, Faculty of Chemical Engineering and Technology, University of Zagreb

- 2013.
Internship at the Neir company specialised for restoration and conservation of cultural property, Split

CONFERENCES, WORKSHOPS

- 2023. University of Split, STIM, Croatia, “Joint event: Cluster of Excellence Matters of Activity (MoA), Humboldt-Universität zu Berlin and Center of Excellence - STIM, University of Split”
Poster: “Design of new materials for aggregation induced emission of light and Model systems for dye-sensitized solar cells”
- 2021. MedILS, Split, Croatia, “System approaches in cancer”
- 2021. MedILS, Split, Croatia, “Advances in biomedical research IV”
- 2020. Ruđer Bošković Institute, Zagreb, Croatia, “11th Symposium on Computing π -conjugated Compounds”
Poster: ”Predicting fluorescence quantum yields for molecules in solution: A critical assessment of the harmonic approximation and the choice of the lineshape function “
- 2019. University of Split, STIM, Croatia “Interdisciplinary endeavour in technology at nanoscale, water and environment”
Poster: “Design of new efficient materials based on organic dyes for Transparent Luminescent Solar Concentrators - reliability of theoretical prediction”
- 2019. University of Split, Croatia, “4th Grandmaster Early-Career Workshop in Physics”
Poster : “Design of new efficient materials based on organic dyes for Transparent Luminescent Solar Concentrators”
- 2018. Lyon, France, “Annual International associated laboratory NCBA workshop”
Presentation: “Structural Properties of $\text{Ag}_{60}\text{Cl-L}_{12}$; Towards new materials for Transparent Luminescent Concentrators”

AWARDS

- Dean’s Award for a prestigious student research work, Faculty of Chemical Engineering and Technology, University of Zagreb, 2015.
- Poster award, 1st place, at “24th Croatian Meeting of Chemists and Chemical Engineers”, University of Zagreb, 2015.

Publications

MARGARITA BUŽANČIĆ MILOSAVLJEVIĆ

1. Margarita Bužančić Milosavljević, Martina Perić Bakulić, Željka Sanader Maršić, Antonija Mravak and Vlasta Bonačić-Koutecký. Enhancing efficiency of dye sensitized solar cells by coinage metal doping of cyanidin-silver trimer hybrids at TiO₂ support based on theoretical study. *Nanomaterials*, 14, 1034, 2024. doi:10.3390/nano14121034
2. Margarita Bužančić Milosavljević and Vlasta Bonačić-Koutecký. Design of J-aggregates-like oligomers built from squaraine dyes exhibiting transparency in the visible regime and high fluorescence quantum yield in the NIR region. *Phys. Chem. Chem. Phys.*, 26, 1314-1321, 2024. doi:10.1039/D3CP05291E
3. Margarita Bužančić Milosavljević, Antonija Mravak, Martina Perić Bakulić and Vlasta Bonačić-Koutecký. Model systems for dye-sensitized solar cells: cyanidin-silver nanocluster hybrids at TiO₂ support. *RSC Advances*, 13 (9), 6010-6016, 2023. doi: 10.1039/D3RA00165B
4. Alexander Humeniuk, Margarita Bužančić, Joscha Hoche, Javier Cerezo, Roland Mitrić, Fabrizio Santoro and Vlasta Bonačić-Koutecký. Predicting fluorescence quantum yields for molecules in solution: A critical assessment of the harmonic approximation and the choice of the lineshape function. *The Journal of Chemical Physics*, 152 (5), 054107, 2020. doi:10.1063/1.5143212
5. Athanasios Zavras, Antonija Mravak, Margarita Bužančić, Jonathan M. White, Vlasta Bonačić-Koutecký, and Richard A. J. O'Hair. Structure of the ligated Ag₆₀ nanoparticle [Cl@Ag₁₂@Ag₄₈(dppm)₁₂] (where dppm = bis(diphenylphosphino)methane). *Chinese Journal of Chemical Physics*, 32 (2); 182-186, 2019. doi:10.1063/1674-0068/cjcp1812285